Dissertation

submitted to the
Combined Faculties for the Natural Sciences and for Mathematics
of the Ruperto-Carola University of Heidelberg, Germany
for the degree of
Doctor of Natural Sciences

presented by

Diplom-Physiker Jens Rodmann
Born in Zerbst, Germany

Oral examination: 15 February 2006

Dust in Circumstellar Disks

Referees: Prof. Dr. Thomas Henning
Prof. Dr. Rainer Spurzem

Abstract – Zusammenfassung

Dust in circumstellar disks
This thesis presents observational and theoretical studies of the size and spatial distribution of dust particles in circumstellar disks. Using millimetre interferometric observations of optically thick disks around T Tauri stars, I provide conclusive evidence for the presence of millimetre- to centimetre-sized dust aggregates. These findings demonstrate that dust grain growth to pebble-sized dust particles is completed within less than 1 Myr in the outer disks around low-mass pre-main-sequence stars. The modelling of the infrared spectral energy distributions of several solar-type main-sequence stars and their associated circumstellar debris disks reveals the ubiquity of inner gaps devoid of substantial amounts of dust among Vega-type infrared excess sources. It is argued that the absence of circumstellar material in the inner disks is most likely the result of the gravitational influence of a large planet and/or a lack of dust-producing minor bodies in the dust-free region. Finally, I describe a numerical model to simulate the dynamical evolution of dust particles in debris disks, taking into account the gravitational perturbations by planets, photon radiation pressure, and dissipative drag forces due to the Poynting-Robertson effect and stellar wind. The validity of the code it established by several tests and comparison to semi-analytic approximations. The debris disk model is applied to simulate the main structural features of a ring of circumstellar material around the main-sequence star HD 181327. The best agreement between model and observation is achieved for dust grains a few tens of microns in size locked in the 1:1 resonance with a Jupiter-mass planet (or above) on a circular orbit.

Staub in zirkumstellaren Scheiben
Die vorliegende Arbeit beschreibt Beobachtungen sowie theoretische Untersuchungen der Partikelgröße und räumlichen Verteilung von Staub in zirkumstellaren Scheiben. Interferometrische Beobachtungen von T-Tauri-Sternen im Millimeterbereich belegen die Existenz von millimeter- bis zentimetergroßen Staubteilchen im Außenbereich der Scheiben. Die Ergebnisse weisen darauf hin, dass Teilchenwachstum bis zu diesen Dimensionen in weniger als 1 Millionen Jahre erfolgt. Die Modellierung der spektralen Energieverteilung mehrerer sonnenähnlicher Hauptreihensterne mit Infrarotexzess zeigt, dass die Innenregionen vieler Scheiben staubfrei sind. Dies lässt sich auf den gravitativen Einfluß eines massereichen Planeten und/oder eine verringerte Staubproduktion im Innenbereich der Scheibe zurückführen. Ein Modell zur Simulation der dynamischen Entwicklung von Staub in gasfreien Scheiben wird beschrieben. Es berücksichtigt den Einfluss von Planeten, Strahlungsdruck sowie Reibungskräfte durch Poynting-Robertson-Effekt und Sonnenwind. Das Modell wird angewendet, um den Staubringes von HD 181327 zu simulieren. Die beste Übereinstimmung zwischen Simulation und Beobachtung wird für rund 30-μm große Teilchen erzielt, die sich in 1:1 Resonanz mit einem Planeten mit mehr als einer Jupitermasse befinden.

Sterne

Zu wenig Zeit genommen
für die Betrachtung der Sterne.
Ich rede nicht von Teleskopen.
Ich spreche von einer Dachluke
in einer ganz gewöhnlichen
wolkenlosen Nacht.
Vom Heimweg zu später Stunde,
nur flüchtig aufschauend,
den Schlüssel schon im Schloß.
Nicht, was ich weiß,
reut mich.
Mich reut
der nachlässige Gebrauch
meiner Augen.

Rainer Malkowski

Contents

List of Figures

List of Tables

Chapter 1
Introduction

... чем глупее, тем ближе к делу.
Чем глупее, тем и яснее.
(... the stupider one is, the closer one is to reality.
The stupider one is, the clearer one is.)

FYODOR M. DOSTOEVSKY, The Brothers Karamazov

To an outsider it may seem that the topics of planet and star formation research over the past 20 years or so are dealing with strange, remote objects. In fact, quite the opposite is true. The main driving force behind the scientific interest in molecular clouds, young stars and dusty disks, to name only a few fields of active research, is the fundamental desire to understand the formation of the solar system, and in particular of our home planet Earth. This is clearly seen in the introductory section of almost every article published in the star and planet formation branch. Every astronomer tries to put his or her work, be it observational or theoretical, into context to the origin of the solar system.

Uniformitarism is a powerful concept in the natural sciences. It is very likely that what we find here, will also exist somewhere else. Since our sun is an ordinary main-sequence star, this principle has led astronomers to believe that other stars should harbour planetary systems too. The first extrasolar planet has been discovered a decade ago, and since then the tally has risen to about 150 planetary systems, some of them with two or three planets (Schneider 2005). These findings provided fresh impetus to the research on the formation of planets and the evolution of planetary system.

The link between both fields, young stars on one side and extrasolar planets on the other, is established by the study of circumstellar disks. The presence of these objects is a natural outcome of the birth of a new star. Planets are thought to form within the circumstellar disks in the first few million years of the system. The details of the picture are still uncertain, but it seems clear that the growth of submicron-sized dust grains to larger particles is the necessary prerequisite to form larger bodies. At a much later evolutionary stage, most of the circumstellar disk has been cleared. Collisions between large bodies, however, constantly release new dust to the system. On the following pages I will briefly describe the current knowledge about dust in young circumstellar disks (§1.1). The changes in physical nature that occur during the transition from young disks to debris disks and the influence of planets on the disk are addressed in §1.2. Finally, the scientific goals of this thesis are defined (§1.3).

1.1 Dust in protoplanetary disks

Solar-mass pre-main-sequence stars In the 1940s, a particular group of variable stars showing irregular and often large photometric variations caught the attention of astronomers. In a series of articles, Joy (1942, 1945, 1949) described the observational properties of these stars, naming the class T Tauri, after the brightest member in the Taurus-Auriga dark cloud. Based on the apparent proximity of associations of T Tauri stars with those of brighter OB stars, Ambartsumian proposed that T Tauri stars are the low-mass analogues of the more massive OB stars. Since the latter have only a short lifespan (a few Myr), their counterparts are also likely to be young. The early suggestion that these young objects formed in the molecular clouds they are associated with was bolstered by their similar radial velocities and proper motions (Herbig 1977; Jones and Herbig 1979). In the current view, T Tauri stars are low-mass ($M_\star \lesssim 2\ \mathrm{M}_\odot$) pre-main-sequence stellar objects whose optical emission is sufficient to penetrate the surrounding, natal molecular cloud (Bertout 1989).

T Tauri stars display a wealth of observational features that allow to infer the astrophysical properties of young stars and to study conditions and processes governing low-mass star formation. The infrared excess emission of T Tauri stars is one of the most compelling arguments for the existence of circumstellar disks (Cohen 1983; Rucinski 1985; Strom et al. 1989). The brightness of T Tauri stars in the infrared wavelength range can be several orders of magnitude higher than expected from a main-sequence star having a similar effective temperature. The same is true for ultraviolet, radio, and X-ray emission (Calvet et al. 2000; Güdel 2002; Feigelson and Montmerle 1999, and references therein). Spectroscopic observations reveal strong optical emission lines that probe diverse mechanisms in the vicinity of the central star, e. g. infall, outflows, and photospheric activity (Alencar and Basri 2000; Calvet and Hartmann 1992; Hirth et al. 1997). Multi-scale temporal variations exhibited by T Tauri stars convey information on stellar rotation, surface temperature inhomogeneities (cool or hot spots), and magnetic fields (Herbst et al. 1994; Johns-Krull et al. 2001).

Dust in circumstellar disks Although dust grains constitute only a minor fraction of the disk material around young stars ($\sim$1 Myr), they play a pivotal role in the complicated multi-stage process of planet formation. The growth of submicron-sized dust particles as found in the interstellar medium (ISM) to larger aggregates by coagulation (collisional sticking) is the first essential step towards building larger rocky bodies (planetesimals) that may eventually accrete into terrestrial planets and planetary cores (Beckwith et al. 2000).

Statistical analysis of the near-infrared excess of young stellar clusters shows that emission from the inner disk disappears within a few Myr (Strom et al. 1989; Haisch et al. 2001). The bulk of the circumstellar matter, however, is located in the outer parts of the circumstellar disk, and does not contribute significantly to the near-infrared emission. Sub-millimetre and millimetre observations thus far show no clear trend comparable with the near-infrared results, but there is evidence suggesting a decrease in the amount of cold circumstellar dust during the post T-Tauri phase ($\sim$10–30 Myr) (Carpenter et al. 2005). The decline of dust emission can be interpreted as a consequence of gradual mass loss through disk dissipation and/or opacity changes due to particle growth. It is important to stress that such studies only trace the evolution of the dust disk. The evolution of the gaseous disk, containing the bulk of the disk mass, is at present only poorly understood.

Probing circumstellar dust The observational characterisation of dust grain properties, e. g., particle composition and size relies on the wavelength-dependent opacity of dust grains. Since dust opacity information can only be gained from optically thin regions, the observational study of dust grain size has concentrated on two different wavelength regimes that sample different regions of the circumstellar disks. First, on infrared spectroscopy carrying information from the disk surface, and, second, millimetre continuum observation probing the cold outer zone where most of the disk mass is locked up.

Mid-infrared spectroscopy Mid-infrared spectroscopy of pre-main-sequence stars, especially of intermediate-mass Herbig Ae stars, show a rich circumstellar dust mineralogy (Molster and Waters 2003). Through the analysis of the position, shape, and relative strengths of solid-state spectral features one can derive the chemical/mineralogical composition, particle size, and crystallinity of the constituent dust grains. The most salient mid-infrared spectral features are the broad bands at 10 and 18 μm, connected to stretching and bending modes of silicon-oxygen bonds (Knacke 1968; Dorschner 1971; Woolf and Ney 1969). Medium-resolution spectroscopy has enabled the detection of crystalline dust in circumstellar disks around intermediate- and low-mass pre-main-sequence stars (e. g. Malfait et al. 1998; Honda et al. 2003). Dust particle growth to micron-sized aggregates is frequently found (Bouwman et al. 2001; Meeus et al. 2003; Przygodda et al. 2003). Recent interferometric observations of three Herbig Ae stars (the massive counterparts of T Tauri stars) with the mid-infrared interferometer MIDI showed that the inner region (1–2 AU) contained processed dust of larger sizes and higher crystallinity, while the outer disk region (2–20 AU) contains unprocessed, smaller grains (van Boekel et al. 2004).

Millimetre continuum observations Turning our attention to dust continuum observations in the millimetre range, the case for unambiguous signs of dust particle growth is less clear cut. For many years there has been little sound observational evidence identifying grain growth processes in disks around pre-main-sequence stars. The analysis of spectral energy distributions showed that the sub-mm/mm fluxes of T Tauri stars decline more slowly towards longer wavelengths than expected for ISM-sized dust (e. g. Beckwith and Sargent 1991). It was tempting to interpret a shallow spectral slope as an indication of the presence of particles much larger than in the ISM ($\gg 0.1\,\mu$m). It was soon realised, however, that spatially unresolved disk observations cannot be used to distinguish between small, optically thick disks containing sub-micron ISM dust and extended, optically thin disks with larger dust particles. Spatially resolved images are needed to break this parameter degeneracy (Koerner et al. 1995; Dutrey et al. 1996).

Major technical improvements at the Very Large Array (VLA) allowed the resolution of the disk around the young star TW Hya at 7 mm and the determination of the dust opacity index (Wilner et al. 2000; Calvet et al. 2002). Testi et al. (2003) resolved the dusty disk around the pre-main-sequence star CQ Tau and concluded that millimetre- and even centimetre-sized dust particles must be present in the outer disk. In a similar study of six isolated intermediate-mass (Herbig Ae) stars by Natta et al. (2004), dust grain growth was inferred for two objects.

In Chapter 2 of this dissertation I present the results from VLA 7-mm continuum observations of 14 T Tauri stars located in the Taurus-Auriga star-forming region. This set of sources currently constitutes the largest sample of low-mass pre-main-sequence stars investigated for signs of dust grain growth to the millimetre/centimetre size regime.

1.2 Debris disks

The circumstellar disks described in §1.1 only survive for about 6 to 10 Myr. As the disk is losing mass, its physics and observational appearance are changing significantly. The massive protoplanetary disk (0.01–0.1 $M_\odot$) transgresses into a phase characterised by a depletion in gas and dust. With the bulk of the gaseous material gone, the particle dynamics is no longer governed by gas drag. The motion of dust grains and other bodies is largely determined by stellar gravitation and radiation as well as by mutual collisions. Due to the high orbital velocities of the impactors, such encounters may result in their complete destruction. Large amounts of dust and fragments of different sizes are the debris of a destructive collision. Hence the name *debris disk* describing this evolutionary phase of the circumstellar disk.

Observing debris disks The bulk mass of dust in debris disks is rather cold, and re-emits stellar radiation primarily at far-infrared wavelengths and beyond. Therefore, the major breakthrough in the observational study of debris disks was achieved by the advent of space-based infrared telescopes and sub-millimetre detector technology. The IRAS mission discovered mid- and far-infrared excess emission for many nearby main-sequence stars. One of the most prominent representatives is the A 0 star Vega (Aumann et al. 1984), and the whole class of IR-excess main-sequence stars is often referred to as Vega-type. The existence of optically thin disks with cool, passively heated dust particles appears to be a common phenomenon among nearby main-sequence stars (Habing et al. 2001). The first optical image of a debris disk has been taken around β Pictoris (Smith and Terrile 1984), and progress on the front of coronagraphic imaging from ground and space has led to the discovery of several more such systems.

Dust production by collisions Early on it was recognised that the dusty material seen in thermal re-emission cannot be primordial material left over from the star/disk formation phase (Harper et al. 1984). Such material would be removed from the system on time scales smaller than the stellar age by stellar radiation and winds. The dust, therefore, must be constantly replenished by collisions of unseen planetesimals and/or sublimation of volatile material from comet-like bodies. This reservoir of dust-producing bodies is large enough to supply second-generation dust to the debris disks for several hundred Myr. The interplanetary dust observed in the solar system demonstrates that this process is still on-going, albeit at a lower level, for main-sequence stars several Gyr old (Grün 1999). As a result of reduced dust production, the strength of infrared excess emission decreases with stellar age. The quantitative nature of the decline is not well understood, and stars of the same age show a large spread in the fractional infrared luminosity (Decin et al. 2003).

The planetary hypothesis The collision-induced dust production strongly relies on the dynamical perturbations by (proto)planets embedded in the debris disks, and episodes of strong gravitational "stirring" may boost the dust production, and hence the infrared/sub-millimetre brightness of the disk (Kenyon and Bromley 2002; Dominik and Decin 2003). The gravitational influence of one or more planets also affects the dynamics of dust particles, and many structural features observed in debris disk have been attributed to the presence of a planet (Augereau 2004).

Two chapters of this work are dedicated to debris disks. The analysis of spectral energy distributions of debris disks observed by the Spitzer Space Telescope are set forth in Chapter 3. In Chapter 4, I describe the development of a numerical model to simulate the dynamics of dust particles under the simultaneous influence of planets, radiation forces, and stellar wind.

1.3 Scientific objectives

The main scientific objective of this dissertation is a better understanding of the physical properties, distribution, and dynamics of dust particles in circumstellar disks. The following questions are addressed:

Investigation of dust particle growth in disks around T Tauri stars (Chapter 2)

1. What is the dust opacity index in circumstellar disks around T Tauri stars?
2. Is there evidence for grain growth?
3. If yes, are there correlations with stellar parameters like age or mass?
4. Can other factors that influence the opacity index be ruled out?
5. How do the results compare to findings for higher-mass stars?

SED modelling of debris disks observed by the Spitzer Space Telescope (Chapter 3)

1. How frequent are inner disk gaps?
2. What is the minimum dust grain size?
3. What is the mass of dust particles emitting in the infrared?
4. How well can these parameters be constrained?

Dynamical models of debris disks with planets (Chapter 4)

1. Is the Hermite integration scheme able to model a debris disk for more than 10^6 orbits?
2. What are the model limitations in terms of planet numbers and orbit geometry?
3. Is the orbital evolution of dust grains under the influence of drag forces treated correctly?
4. What is the efficiency of resonant trapping in exterior and interior mean motion resonances, respectively?
5. What is the minimum number of test particles needed to resolve density structures?
6. What is the optimal approach to assess the orbital dynamics of debris disks: dust density plots, distributions of orbital elements, or animated simulations?
7. Can the surface density asymmetry of HD 181327 be explained by the influence of a planet?

Chapter 2
Dust grain growth in circumstellar disks around T Tauri stars

In dust we trust.

AIGEN LI, University of Arizona, USA

2.1 Dust continuum observations

2.1.1 Very Large Array

The NRAO[1] Very Large Array is a radio interferometer consisting of 27 antennas, each 25 m in diameter. It is located on the Plains of San Agustin in western New Mexico, USA, at approximately 2100 m above sea level. The antennas are arranged in a Y-shaped fashion (Figure 2.1). The resolution of the array can be changed by moving the antennas on rail tracks along the arms. There are four basic antenna arrangements, called configurations, that cover a factor of $\sim$30 in scale. The array is reconfigured biannually, going from the most extended A configuration, through the B and C configurations, to the most compact D configuration. For a time span of, typically, two to three weeks there are three additional hybrid configurations available that combine larger antenna spacings on the north arm with shorter ones on the southwest and southeast arms. These configurations provide decent (u, v)-coverage even for sources outside the optimal declination range of $-15^\circ < \delta < 75^\circ$. All 27 antennas are equipped with receivers designed for eight wavelength (or frequency) bands. From low to high frequencies these bands are designated 4, P, L, C, X, U, K, Q, corresponding to observing wavelengths of 400, 90, 20, 6, 3.6, 2, 1.3, and 0.7 cm, respectively.

2.1.2 Stellar sample

The sample consists of 14 low-mass pre-main-sequence stars located towards the Taurus-Auriga star formation region (Table 2.1). This molecular cloud complex is a well-studied testbed for the low-mass mode of star formation in the Milky Way (Lada et al. 1993). The region, extending over some 50 square degrees on the sky, shows prominent dark lanes that obscure background stars

[1]The National Radio Astronomy Observatory is operated for the National Science Foundation by Associated Universities, Inc., under a cooperative agreement.

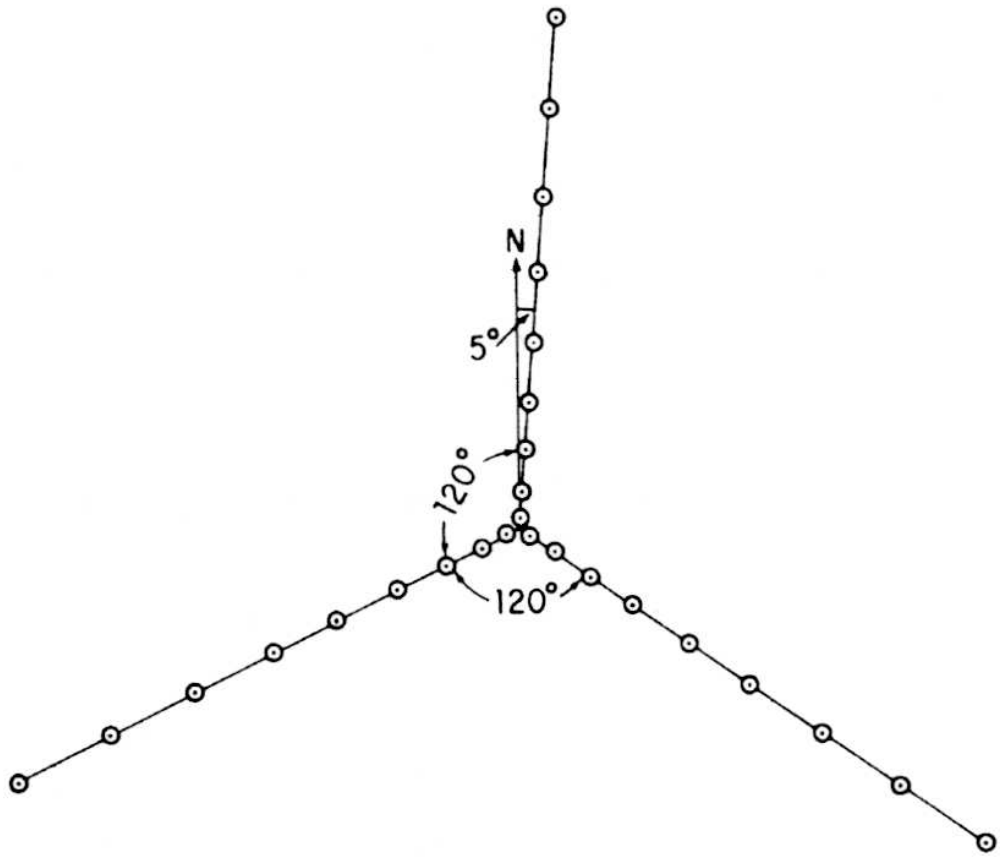

Figure 2.1. Antenna arrangement of the Very Large Array, featuring a Y-shape design of 27 antennas, 9 on each arm. The distance of an antenna from the centre of the array scales as power law. The array is rotated by 5° with respect to North to avoid exact East-West baselines between antennas on the Southern arms.

lying behind the complex (Barnard 1927). Molecular gas associated with the dark dust lanes can be traced by CO line measurements (Ungerechts and Thaddeus 1987; Mizuno et al. 1995). The estimated total mass in molecular hydrogen is of the order $10^4\ \mathrm{M}_\odot$ (Stahler and Palla 2004).

All sample stars are catalogued as classical T Tauri stars, based on the equivalent width of their Hα emission line $\gtrsim$10 Å (Herbig and Bell 1988). The strength of the Hα emission attests an increased chromospheric activity and accretion of hot, circumstellar gas. All sources are classified as Class II young stellar objects, as derived from the slope of their near- to mid-infrared spectral energy distributions, $\alpha_{\mathrm{IR}} = \mathrm{d}\log(\lambda F_\lambda)/\mathrm{d}\log\lambda$, with $-2 \lesssim \alpha_{\mathrm{IR}} \lesssim 0$ (Adams et al. 1987; Kenyon and Hartmann 1995; Hartmann 2002). The excess emission above the photospheric value stems from irradiation-heated dust. The fact that the central stars are detectable in the optical argue a disk configuration.

Table 2.1. Properties of sample stars.

Star	Coordinates (J2000.0) $\alpha\,(^{\rm h}\ ^{\rm m}\ ^{\rm s})$	$\delta(^\circ\ '\ '')$	Type[a]	SED[b] class	Spectral type[a]	$T_{\rm eff}^{\rm (b)}$ (K)	$M_\star^{\rm (c)}$ ($\mathrm{M}_\odot$)	$L_\star^{\rm (b)}$ ($\mathrm{L}_\odot$)	Age[c] (Myr)
CY Tau	4 17 33.74	+28 20 46.5	II	cTTS	M1	3720	0.48	0.47	0.7
RY Tau	4 21 57.42	+28 26 35.5	II	cTTS	K1	5080	1.69	7.60	0.2
FT Tau	4 23 39.19	+24 56 14.2	II	cTTS	cont.	3890[c]	—	—	—
DG Tau B	4 27 02.56	+26 05 30.4	II	cTTS	—	—	—	—	—
DG Tau	4 27 04.69	+26 06 16.1	II	cTTS	M	3890[c]	0.56	1.7[c]	0.3
HL Tau	4 31 38.41	+18 13 57.6	II	cTTS	K7–M2	4060	0.55	0.9[c]	1.0
GG Tau	4 32 30.39	+17 31 40.1	II	cTTS	K7	4060	0.65	1.50	0.3
UZ Tau E	4 32 43.10	+25 52 31.0	II[e]	cTTS	M1–3	3680	0.44	2.94[c]	$<$0.1
DL Tau	4 33 39.09	+25 20 37.9	II	cTTS	K7	4060	0.56	0.77[c]	1.2
DM Tau	4 33 48.74	+18 10 10.0	II	cTTS	M1	3720	0.62	0.25	3.2
CI Tau	4 33 52.03	+22 50 30.2	II	cTTS	K7	4060	0.70	0.87	0.8
DO Tau	4 38 28.59	+26 10 49.4	II	cTTS	M0	3850	0.72	1.20	0.6
LkCa 15	4 39 17.81	+22 21 03.6	II	cTTS[f]	K5	4350	—	0.74	1.0[d]
GM Aur	4 55 10.98	+30 21 59.5	II	cTTS	K3	4730	0.72	0.83	1.8

References — (a) Herbig and Bell (1988); (b) Kenyon and Hartmann (1995); (c) Beckwith et al. (1990); (d) Duvert et al. (2000). (e) Hartmann (2002); (f) Herbig and Bell (1988) classifi ed LkCa 15 as a weak-line T Tauri star.

There are copious dust continuum observations of the sample stars at millimetre wavelengths (Table 2.4), confirming the presence of circumstellar dust around the central T Tauri stars. Estimating the amount of circumstellar matter is an intricate task. Disk mass estimates from continuum emission suffer from severe uncertainties concerning the dust properties, most notably the dust opacity. The commonly applied "standard" opacity law, e. g. from Hildebrand (1983), may result in figures off by one order of magnitude. A further uncertainty is introduced by the gas-to-dust ratio, which in the absence of reliable data is customarily assumed to be equal to the interstellar value (100:1). Having these caveats in mind, the disk masses of the sources range from 0.02 to 0.7 $\mathrm{M}_\odot$ (Beckwith et al. 1990; Dutrey et al. 1996). For the majority of the stars in our sample, emission from circumstellar CO gas has been detected, often tracing a disk in Keplerian rotation (Koerner et al. 1993; Dutrey et al. 1994; Koerner and Sargent 1995; Handa et al. 1995; Dutrey et al. 1996; Jensen et al. 1996; Mitchell et al. 1997; Duvert et al. 2000; Najita et al. 2003). For the majority of sources there are no X-ray detections; HL Tau and UZ Tau being the only exceptions (Neuhäuser et al. 1995). Classical T Tauri stars show intrinsically less X-ray activity than weak-line objects due to their slower rotation.

The stellar ages and masses have been determined by fitting pre-main-sequence isochrones to loci of the stars in the Hertzsprung-Russell diagram; they range from 0.1 to 3.2 Myr and from 0.4 to 1.7 $\mathrm{M}_\odot$, respectively (Beckwith et al. 1990; Duvert et al. 2000). The uncertainties of the age determinations are considerable and preclude a meaningful correlation with the opacity indices β.

The average distance to the Taurus-Auriga molecular cloud as found in the literature varies between 135 pc (Cernicharo et al. 1985) and 160 pc (Strom et al. 1989). Using optical spectrophotometry of reddened stars projected onto the cloud, Kenyon et al. (1994) derive a distance of 140 ± 10 pc to the extincting region. Preibisch and Smith (1997) analysed the rotation properties of stars and found a slightly larger value of 152 ± 10 pc. HIPPARCOS measurements for RY Tau give a parallax of $\pi = 7.49 \pm 2.18$ mas, corresponding to 134 ± 39 pc. We adopt the standard value of 140 pc (Elias 1978; Kenyon et al. 1994; Loinard et al. 2005) to convert angular scales into physical sizes.

2.1.3 Observations and Data Reduction

7-mm continuum observations The Very Large Array (VLA) was used to observe the dust continuum emission of 14 T Tauri stars at 43.34 GHz (7 mm). The total receiver bandwidth was 100 MHz, divided into two 50 MHz bands centred at 43.3149 GHz and 43.3649 GHz. The observations were carried out in D configuration on 22–23 March 2003 and again on 12 May 2003. The 27 VLA antennas provided $27 \times (27-1)/2 = 351$ baselines from 35 m to 1.03 km, corresponding to 5–150 kλ at 7 mm (Figure 2.2). The May observations took place during array reconfiguration (D to A), and only 26 antennas were available.

The nominal sizes of the antenna primary beam and the synthesised beam of the array were $1'$ (HPBW) and $1.5''$ (HPBW), respectively. Phase calibration was accomplished by sandwiching the on-source observations between pointings of nearby secondary calibrators (radio sources

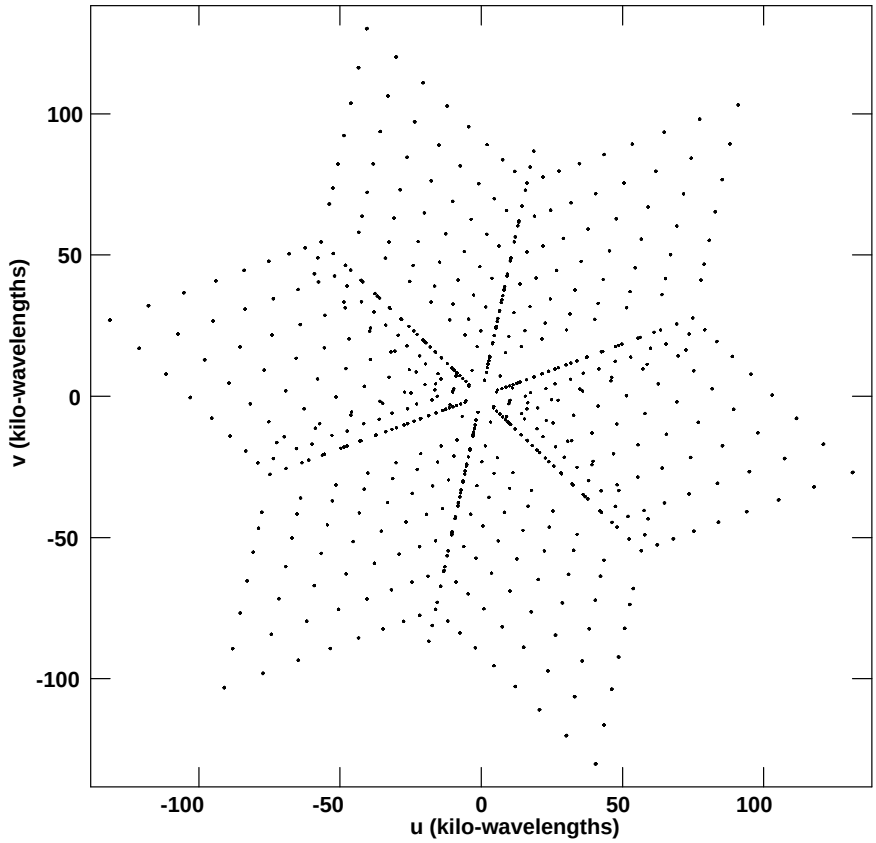

Figure 2.2. (u, v) plane coverage in a 7-mm "snapshot" observation of GM Aur on 22 March 2003. Each visibility point $V(u, v)$ corresponds to one baseline vector $\boldsymbol{b}_{ij}$ between the antennas i and j. The reverse vector $\boldsymbol{b}_{ji} = -\boldsymbol{b}_{ij}$ contains the complex conjugated visibility, $V(-u, -v) = V^*(u, v)$. Note the lack of information at small (u, v) distances, in particular the absence of zero-spacing data. Earth's rotation and merging of (u, v) data from different observations results in denser coverage.

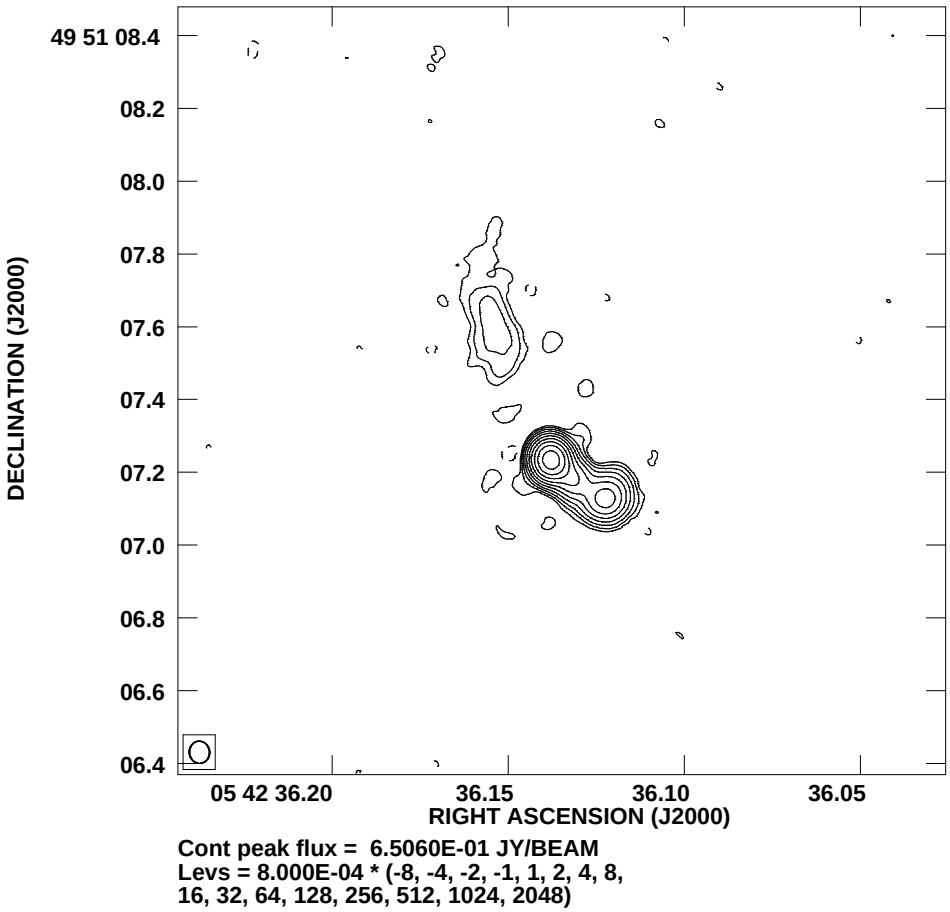

Figure 2.3. 7-mm image of the flux calibrator J0542+4951 (3C 147).

J0431+2037, J0403+2600, J0443+3441). The typical source/phase calibrator cycle time was 5–10 minutes. Absolute flux calibration was obtained from observation of the quasar J0542+4951 (3C 147) which is assumed to have a flux density of 0.91 Jy (Figure 2.3). The estimated uncertainty in the absolute flux calibration is $\sim$10%. Reference pointing measurements were made approximately every hour.

In order to mitigate opacity variations by different antenna elevations, we only used secondary calibrators within 5° the elevation of the primary calibrator. The total on-source integration times were between 30 minutes and 2 hours, depending on the predicted source brightness.

The (u, v) data sets for the three observing dates were merged using the $\mathcal{AIPS}$ task DBCON. CLEANed images were obtained with IMAGR using a ROBUST parameter of 0, which is intermediate between natural and uniform weighting of the visibility data and optimises for spatial resolution and sensitivity. Three weak sources (DM Tau, CI Tau, and LkCa 15) were CLEANed using natural weighting (ROBUST=5) to increase signal-to-noise ratio and allow secure detection. The extended emission of GG Tau is also best imaged using natural weighting. Figures 2.4 and 2.5 show the corresponding contour plots for the 7-mm images.

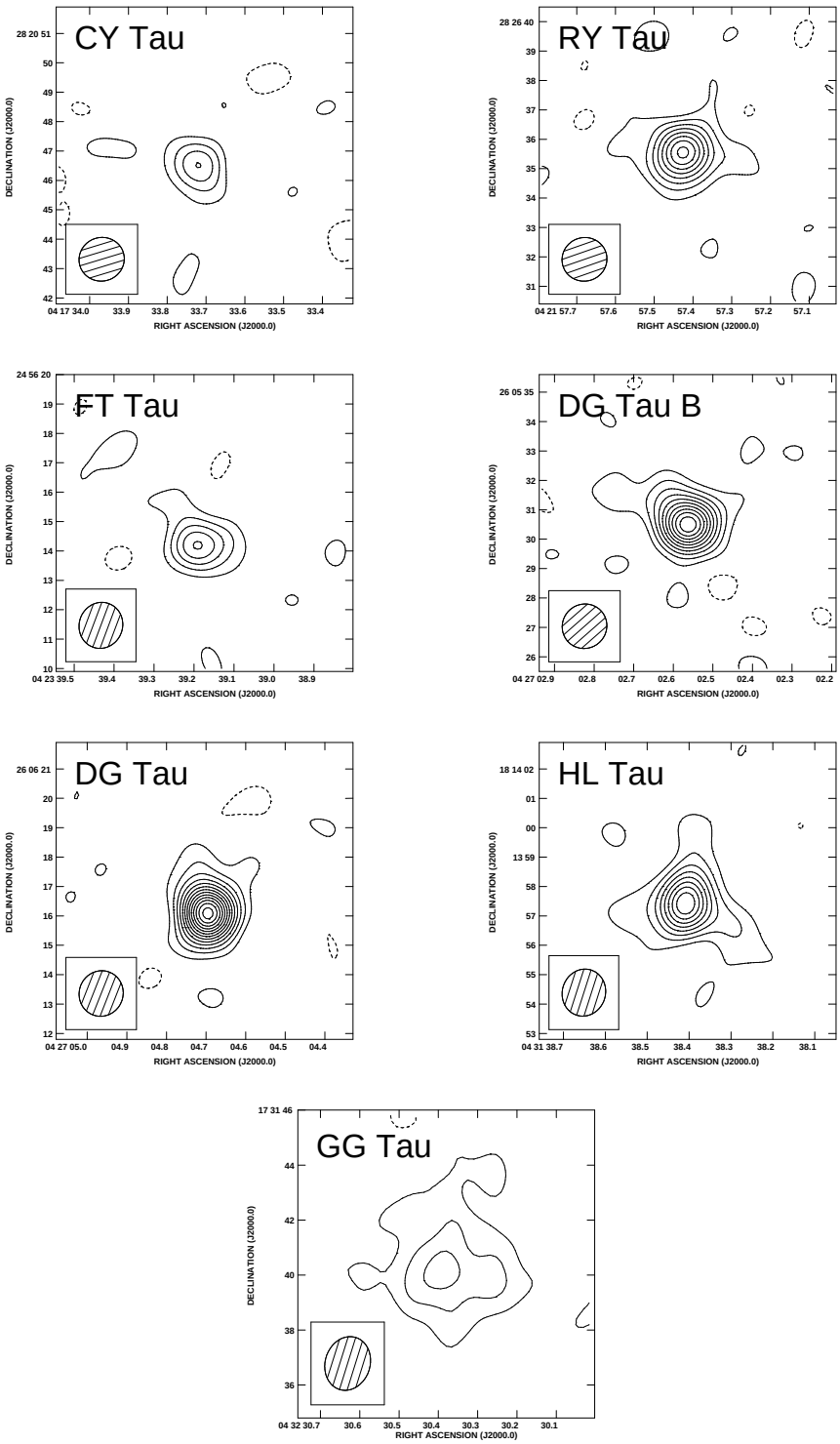

Figure 2.4. VLA D-confi guration images of the $\lambda = 7$ mm continuum emission. Contour levels are drawn in steps of the corresponding 2σ rms noise level; the average 1σ rms noise level is $\sim$0.15 mJy/beam. The synthesised beam is shown in the bottom left corner of each panel; the average beam size is $\sim 1\farcs5$.

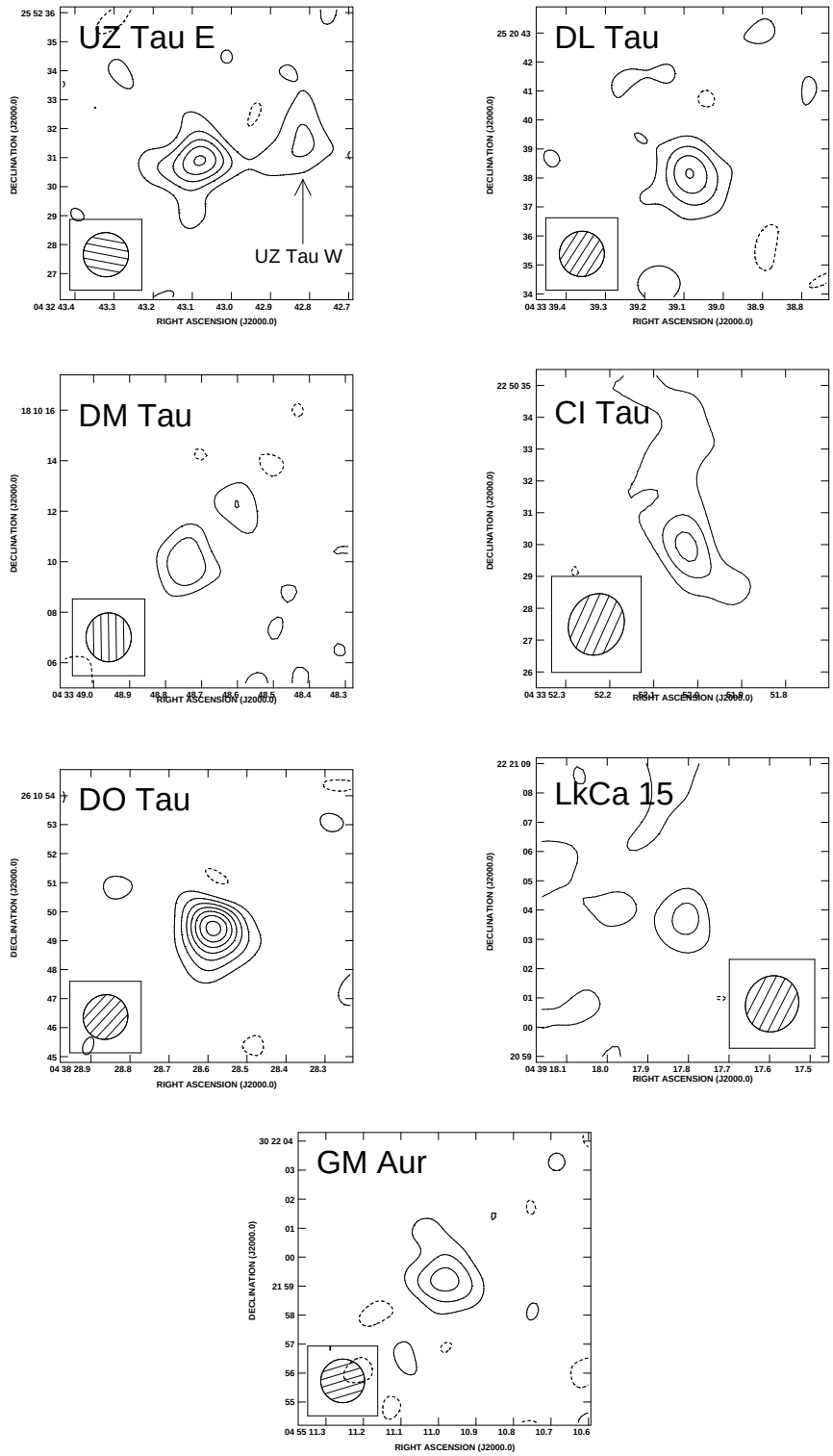

Figure 2.5. Same as Figure 2.4. Given their low signal-to-noise ratios, the two sources DM Tau and LkCa 15 are considered as undetected.

Centimetre observations Five of the sources have poor-quality archival VLA detections at 8 GHz (Wilner 1998). All five sources were re-observed at 3.6 cm (8.46 GHz), 2.0 cm (14.94 GHz), and 1.3 cm (22.46 GHz). The total bandwidth was again 100 MHz, with two 50 MHz channels 50 MHz apart. The 1.3-cm observations were carried out on 17 March 2003; the 2.0- and 3.6-cm observations on 21 March 2003. All observations were made in the compact D configuration, covering baselines of 3–77 kλ, 2–50 kλ, and 1–30 kλ in the (u, v)-plane at 1.3, 2.0, and 3.6 cm, respectively.

The flux density scale was set by observations of the calibrator J0542+4951 with known flux densities of 1.80, 2.71, and 4.74 Jy at 1.3, 2.0, and 3.6 cm, respectively. CLEANed images were produced with `IMAGR` and natural weighting of the visibilities (`ROBUST`=5). Finally, primary beam corrections were performed using the $\mathcal{AIPS}$ task `LTESS` to compensate for the non-uniform single-antenna response across the field-of-view of the entire array. The contour maps are shown in Figures 2.6 and 2.7; note that DG Tau and DG Tau B appear in the same image.

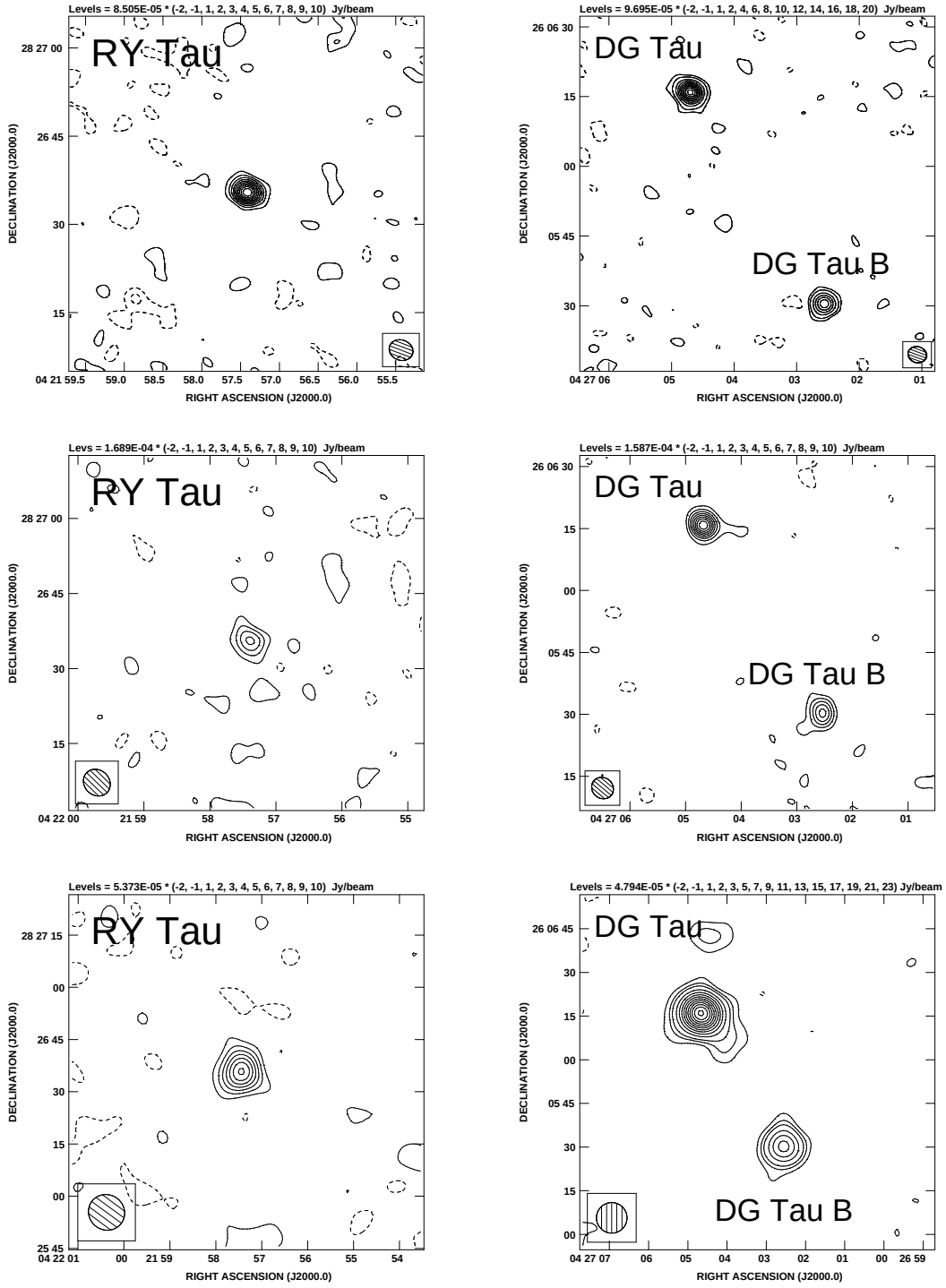

Figure 2.6. VLA D-confi guration images at $\lambda = 1.3$ cm (top), $\lambda = 2.0$ cm (centre), and $\lambda = 3.6$ cm (bottom) for RY Tau (left column), DG Tau, and DG Tau B (right column). Contour levels are given for each panel separately in multiples of 2σ rms noise level. The average 1σ rms noise levels are approximately 50, 80, and 30 μJy/beam at 1.3, 2.0, and 3.6 cm, respectively.

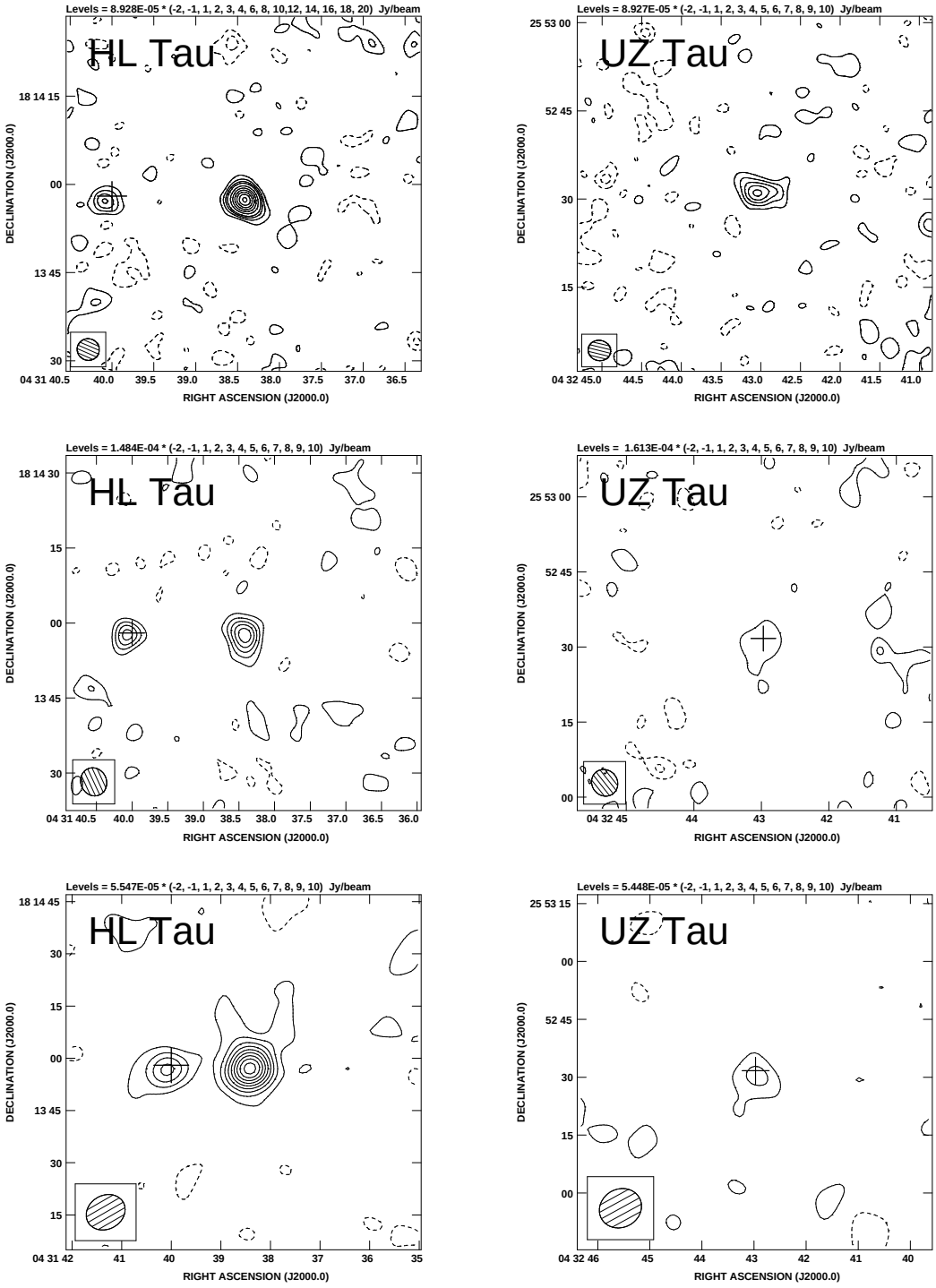

Figure 2.7. VLA D-confi guration images at $\lambda = 1.3$ cm (top), $\lambda = 2.0$ cm (centre), and $\lambda = 3.6$ cm (bottom) for HL Tau (left column) and UZ Tau (right column). Contouring and noise levels as in Figure 2.6. About 30″ to the east of HL Tau lies XZ Tau (indicated by cross-hairs). XZ Tau is an interesting binary system featuring an extremely young Herbig-Haro outfbw (Krist et al. 1999).

2.1.4 Radio seeing

Short-term variations in precipitable water vapour lead to changes in the path length of an electromagnetic wave travelling through the troposphere, causing phase fluctuations when observed by radio interferometers (Figure 2.8). Tropospheric phase noise negatively affects spatial resolution and coherence, especially at mm wavelengths (Carilli et al. 1999).

In order to estimate the amount of smearing introduced by tropospheric phase noise, we compared self-calibrated and standard-calibrated images of two bright radio sources. Images of self-calibrated sources are corrected for the radio seeing on short timescales (3.3 seconds integration time), and deconvolution will give the intrinsic source size. The same procedure applied to images obtained from ordinary calibration gives the 'seeing disk'. By using two test sources, one unresolved (J0426+2327), the other extended (J0412+2305), we checked the flux reduction by phase-noise induced smearing for point sources and extended sources, respectively.

The analysis of the merged 7-mm data showed that the overall radio seeing was $\sim 0\farcs5$. Inspection of the single-day data revealed that the seeing on the second day (23 March 2003) was the

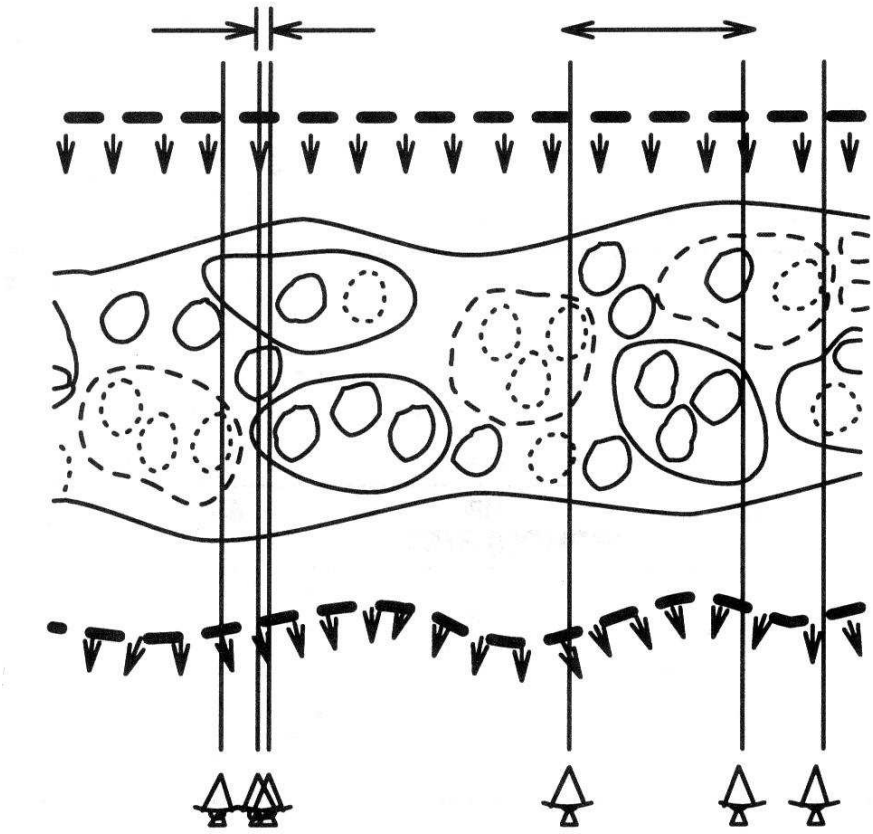

Figure 2.8. Effect of tropospheric water vapour on wave phase. The phase of the incoming plane is distorted by large- and small-scale spatial variations of the water vapour content in the Earth's troposphere. Regions of increased precipitable water vapour (solid lines) have a larger refraction index than pockets of diminished water vapour content (dotted lines). A higher index of refraction retards the wave propagation, leading to a loss of phase information. (Taken from Carilli et al. 1999.)

worst ($\sim$0.″7), while on 22 March and 12 May better water vapour conditions prevailed (about 0.″1 and 0.″4, respectively). The integrated 7-mm fluxes are reduced by 4–5%, and are within 2% for each day. The seeing at 1.3 cm was about 0.″5. The peak fluxes might be reduced by up to 5%; the integrated fluxes were affected less than 1%. Tropospheric seeing effects at longer centimetre wavelengths are expected to be negligible.

2.2 Results

2.2.1 7-mm maps and fluxes

We detected the continuum emission from cold circumstellar dust at 7 mm for all 14 T Tauri stars comprising our sample. Two sources (DM Tau and LkCa 15) have signal-to-noise ratios < 5, and we do not consider these sources further in our analysis. The integrated fluxes were measured on the combined maps using the $\mathcal{AIPS}$ routine `IMSTAT`, and corrected for seeing reduction. In the light of the radio seeing analysis, we decided to use the excellent conditions of the first-day data set to determine source sizes. The task `IMFIT` was used to check if the source was spatially resolved or unresolved by fitting a two-dimensional Gaussian function to the emission peak. The deconvolved disk sizes are of the order 100–200 AU, representing typical dimensions for protoplanetary disks. The major and minor axes can, in principle, be used to derive the inclination angle of the disks. Their uncertainties, however, are very large, and the disk orientations are poorly constrained. Table 2.2 summarises the results derived from the 7-mm maps.

The extended dust emission of three sources is of particular interest. The map of HL Tau shows a prominent "finger" pointing in south-western direction. The measured position angle of $235^\circ \pm 10^\circ$ is roughly co-aligned with the counter-jet of HL Tau (Mundt et al. 1988; Wilner and Lay 2000). The knobby feature northwest of DG Tau B appears to have the orientation of the protostellar jet found by Mundt & Fried (1983). In the case of DG Tau, a similar feature does not coincide with the known jet position angle.

We detected extended dust emission and resolved circumstellar material around the northern binary ($\sim$0.″3 separation) of the quadruple system GG Tau (Leinert et al. 1993). Previous ^{13}CO line emission and 1.4-mm continuum observations demonstrated that the circumbinary disk consists of two structural components: an 80-AU wide ring at a radius of $\sim$220 AU, and a fainter, more extended disk (Dutrey et al. 1994; Guilloteau et al. 1999). At 7 mm we most likely observe a combination of the two components. Given the complicated source geometry of GG Tau we have not attempted to deconvolve a simple Gaussian model from the 7-mm map.

The quadruple system UZ Tau could be resolved into the bright eastern and the (marginally detected) western components, both of which are known to harbour a binary system. Speckle and direct imaging observations resolved UZ Tau W into a binary system with a projected separation of $\sim$50 AU (Ghez et al. 1993; Simon et al. 1995). Radial-velocity measurements showed UZ Tau E to be a spectroscopic binary with a projected semi-major axis of $\sim$0.1 AU (Mathieu et al. 1996; Prato et al. 2002). We confirm the findings of Jensen et al. (1996), who noted a substantial reduction of millimetre emission around UZ Tau W compared to the tight binary UZ Tau E. In the former system, the two components have a separation comparable to a typical protoplanetary disk, leading to disk truncation and therefore smaller and less massive disks. The two components of UZ Tau E, on the other hand, apparently do not affect the common circumbinary disk in which they reside (Mathieu et al. 2000).

Table 2.2. Seeing-corrected 7-mm flux densities, spatial resolutions, and estimated source sizes. The stated uncertainties for the flux densities do not contain the uncertainty of the absolute flux calibration.

Source	Integrated flux (mJy)	Disk resolved?	Deconvolved source size (AU)	P.A. (°)
CY Tau	1.19 ± 0.26	no		
RY Tau	2.97 ± 0.29	yes	180 (±30) × 40 (±50)	140 ± 10
FT Tau	1.62 ± 0.27	partially	170 (±50) × —	60 ± 20
DG Tau B	3.57 ± 0.29	yes	130 (±30) × 40 (±50)	50 ± 30
DG Tau	5.30 ± 0.37	partially	110 (±30) × —	10 ± 10
HL Tau	4.92 ± 0.43	yes	140 (±40) × 80 (±40)	170 ± 30
GG Tau	3.24 ± 0.42	yes		
UZ Tau E	1.84 ± 0.28	partially	120 (±50) × —	80 ± 20
DL Tau	1.49 ± 0.25	yes	210 (±60) × 140 (±100)	110 ± 40
DM Tau	0.74 ± 0.20	—		
CI Tau	0.76 ± 0.17	partially	220 (±60) × —	40 ± 10
DO Tau	2.47 ± 0.29	partially	60 (±50) × —	70 ± 30
LkCa 15	0.44 ± 0.17	—		
GM Aur	1.05 ± 0.23	yes	200 (±50) × 60 (±70)	10 ± 20

2.2.2 Centimetre fluxes

Centimetre emission could be detected for all five sources observed at 1.3, 2.0, and 3.6 cm (Table 2.3). The integrated fluxes of UZ Tau at 2.0 and 3.6 cm are below the 4-σ level.

The counter-jet of HL Tau mentioned in Section 2.2.1 can also be seen in the corresponding 1.3-cm image. Its position angle has been measured to $225° \pm 20°$, in agreement with the value measured from the 7-mm map. The UZ Tau multiple system is not resolved into its eastern and western components.

Radio emission from low-mass pre-main-sequence stars is a common phenomenon (Güdel 2002). VLA observations of classical T Tauri stars at radio wavelengths revealed rising spectral indices and large angular sizes, interpreted as signs of wind emission (Cohen et al. 1982). Observational evidence and theoretical arguments favour focused anisotropic outflows and collimated jets rather than uniform, isotropic mass flows from T Tauri stars (Cohen 1982; Cohen and Bieging 1986). Wind emission is likely to contribute to the 7-mm continuum emission and has to be subtracted from the measured 7-mm flux densities in order to accurately derive dust opacity indices from spectral slopes at millimetre wavelengths.

Güdel (2002) emphasises that the observation of thermal radio emission conveys no information on the presence or absence of magnetic fields close to or on the stellar surface. Only polarisation or line-splitting (Zeeman) measurements can establish the presence of magnetic fields (White et al. 1992; Johns-Krull et al. 1999).

Table 2.3. Summary of centimetre observations. 1.3-cm values corrected for seeing-related flux reduction. The uncertainty in the absolute flux density calibration is not included.

Wavelength	Source	Integrated flux (mJy)	Detection (σ)
1.3 cm	RY Tau	0.92 ± 0.08	12
	DG Tau B	1.23 ± 0.09	14
	DG Tau	2.17 ± 0.11	20
	HL Tau	1.63 ± 0.11	15
	UZ Tau	0.77 ± 0.11	7
2.0 cm	RY Tau	0.63 ± 0.13	5
	DG Tau B	0.80 ± 0.13	6
	DG Tau	1.33 ± 0.15	9
	HL Tau	0.88 ± 0.14	6
	UZ Tau	0.48 ± 0.14	3
3.6 cm	RY Tau	0.31 ± 0.04	8
	DG Tau B	0.46 ± 0.05	9
	DG Tau	1.27 ± 0.05	25
	HL Tau	0.57 ± 0.05	11
	UZ Tau	0.10 ± 0.03	3

2.3 Analysis

2.3.1 Estimate of β from millimetre spectral energy distribution

The large outer disk radii derived suggest that the emission is mostly optically thin at 7 mm, i. e. $\tau_\nu \ll 1$. While optically thick emission originates from the disk surface (analogous to a stellar photosphere one might speak of a disk photosphere), optically thin emission stems from the thermal radiation of all dust particles within the instrument beam. The flux density F_ν received from an optically thin disk at distance D can be written as:

$$F_\nu = \frac{1}{D^2} \int_{R_{\rm in}}^{R_{\rm out}} B_\nu(T(r)) \tau_\nu 2\pi r \, {\rm d}r \; . \tag{2.1}$$

The optical depth τ_ν can be expressed as the product of the surface density $\Sigma(r)$ and the mass opacity coefficient κ_ν, $\tau_\nu = \Sigma(r)\kappa_\nu$. Furthermore, since we observe the disk at very long wavelengths, the Rayleigh-Jeans limit of the Planck function is applicable, i. e. $B_\nu \approx 2k_{\rm B}T\nu^2/c^2$. We can therefore simplify Equation 2.1 to:

$$F_\nu \approx \frac{2k_{\rm B}}{c^2} \frac{\kappa_\nu \nu^2}{D^2} \int_{R_{\rm in}}^{R_{\rm out}} T(r)\Sigma(r) 2\pi r \, {\rm d}r \; . \tag{2.2}$$

The frequency dependence of Equation 2.2 is given by the factor preceding the integral. Assuming that the dust opacity index κ_ν declines with a fixed power β of the frequency at long wavelengths, the millimetre spectral energy distribution scales as

$$F_\nu \propto \nu^{\beta+2} \tag{2.3}$$
$$F_\lambda \propto \lambda^{-\beta-2} \, . \tag{2.4}$$

One can therefore directly use the slope $\alpha_{\rm mm}$ of the millimetre spectral energy distribution (see Figures 2.9 and 2.10) to derive a first estimate of the dust opacity index via the relation $\beta = \alpha_{\rm mm} - 2$ (Beckwith and Sargent 1991; Testi et al. 2003; Natta et al. 2004).

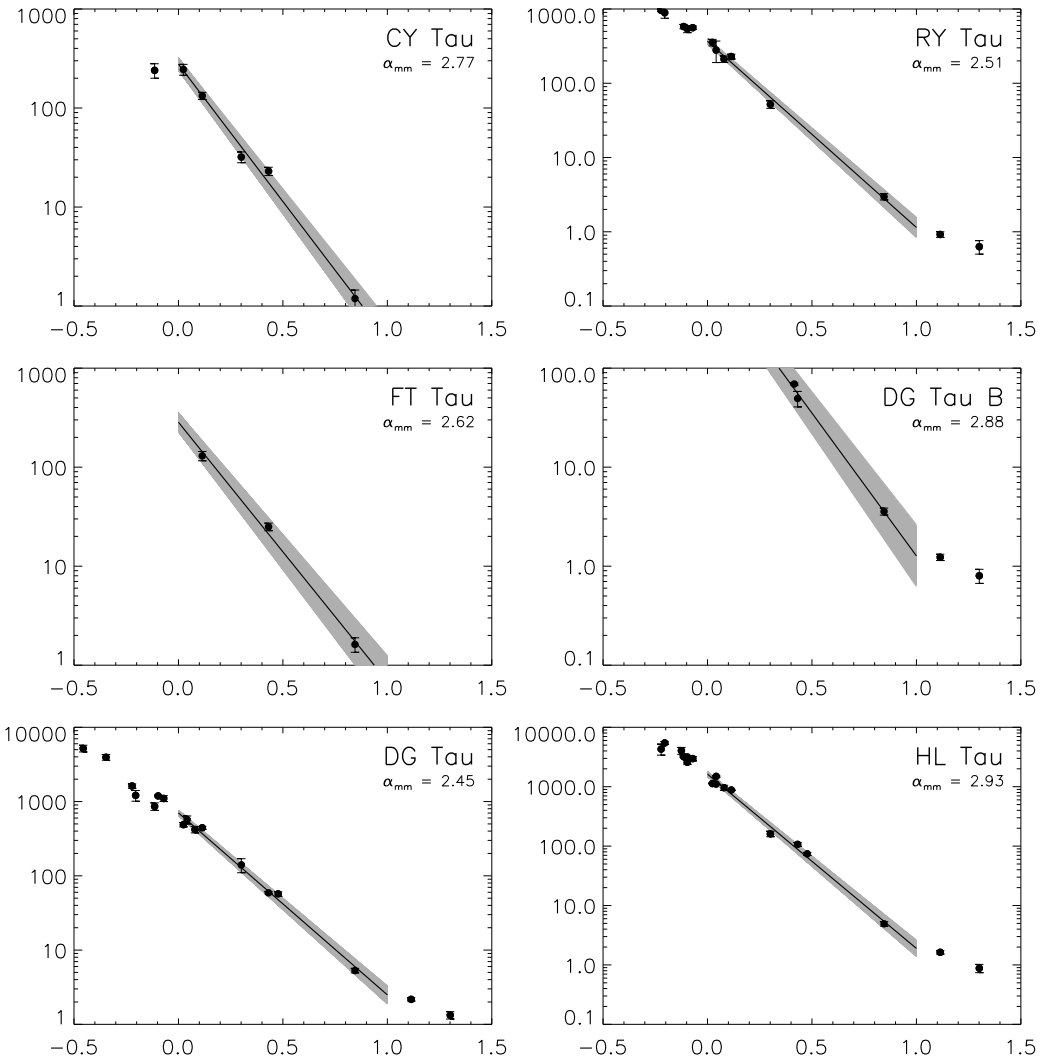

Figure 2.9. Spectral slopes $\alpha_{\rm mm}$ derived by fitting a power law to literature values (Table 2.4) and our 7-mm datum in the range $\lambda = 1$ to 7 mm. Flux densities (in mJy) are plotted as a function of $\log_{10}(\lambda/{\rm mm})$. We find $\alpha_{\rm mm} < 4$ for all sources; $\alpha_{\rm mm} = 4$ is expected for ISM-sized dust particles radiating in the Rayleigh-Jeans limit of the Planck function.

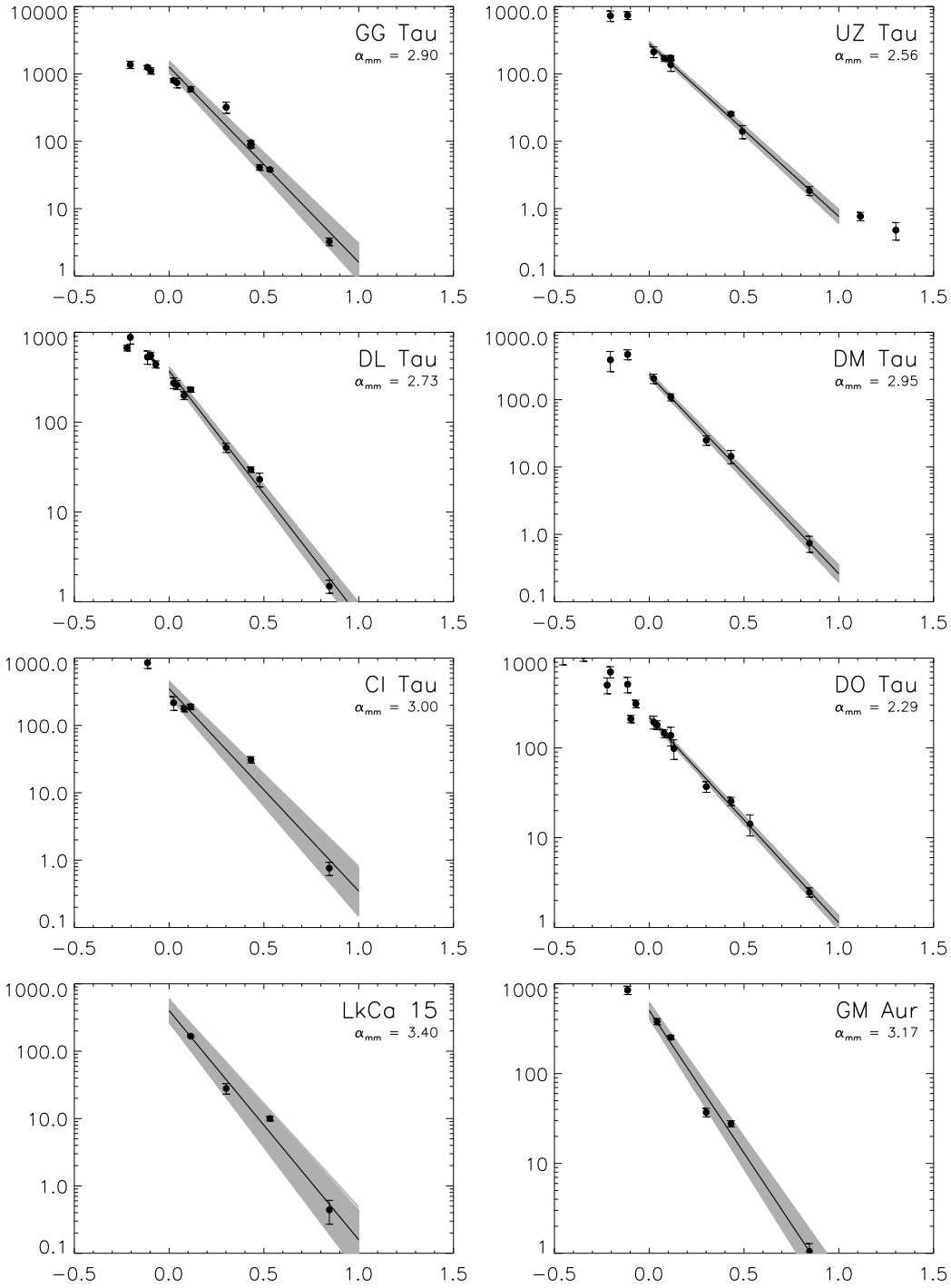

Figure 2.10. Spectral slopes $\alpha_{\rm mm}$ derived by fitting a power law to literature values (Table 2.4) and our 7-mm datum in the range $\lambda = 1$ to 7 mm, cont'd.

Table 2.4. Millimetre measurements and IRAS photometry compiled from the literature. The columns θ_B list the HPBW; note that the PSF sizes of the IRAS bands (12, 25, 60, and 100 μm) are given in arcmin.

λ	Flux	Error	θ_B	Ref.	Flux	Error	θ_B	Ref.	Flux	Error	θ_B	Ref.	Flux	Error	θ_B	Ref.	Flux	Error	θ_B	Ref.
(mm)	(Jy)	(Jy)	($''$)		(Jy)	(Jy)	($''$)		(Jy)	(Jy)	($''$)		(Jy)	(Jy)	($''$)		(Jy)	(Jy)	($''$)	
	RY Tau				**FT Tau**				**DG Tau B**				**DG Tau**				**HL Tau**			
0.012	17.74	0.027	1′	(a)	0.36	0.045	1′	(a)									9.74	0.031	1′	(a)
0.025	26.48	0.054	1′	(a)	0.57	0.037	1′	(a)					30.39	0.065	1′	(a)	31.18	0.073	1′	(a)
0.060	18.91	0.066	2′	(a)	0.82	0.041	2′	(a)					31.28	0.039	2′	(a)	76.26	0.810	2′	(a)
0.100	13.50	2.501	4′	(a)									39.86	0.840	4′	(a)	77.95	1.394	4′	(a)
1.056	0.354	0.036	22	(b)									0.489	0.033	22	(b)	1.13	0.02	22	(b)
1.1	0.28	0.09	18.5	(f)									0.57	0.07	18.5	(f)	1.11	0.02	18	(k)
1.2	0.212	0.021	12	(g)									0.420	0.042	12	(g)	0.961	0.096	12	(g)
1.3	0.229	0.017	11	(c)	0.130	0.014	11	(c)					0.443	0.020	11	(c)	0.879	0.019	11	(c)
2.0	0.052	0.006	5	(d)									0.14	0.03	27.5	(f)	0.161	0.017	5	(d)
2.6									0.0691	0.0017	4	(h)								
2.7					0.025	0.0022	3	(e)	0.0494	0.0088	0.7	(i)	0.059	0.0020	3	(e)	0.1069	0.0078	0.6	(i)
3.0													0.057	0.0040	6	(j)	0.074	0.0040	3	(j)
	UZ Tau E				**DL Tau**				**CI Tau**				**DO Tau**				**GM Aur**			
0.012	1.38	0.031	1′	(a)	0.97	0.034	1′	(a)	0.78	0.025	1′	(a)					0.25	0.031	1′	(a)
0.025	1.76	0.043	1′	(a)	1.32	0.045	1′	(a)	1.30	0.046	1′	(a)	4.07	0.041	1′	(a)	1.07	0.042	1′	(a)
0.060	2.37	0.069	2′	(a)	1.39	0.084	2′	(a)	2.15	0.071	2′	(a)	6.33	0.106	2′	(a)	3.08	0.112	2′	(a)
0.100													8.55	1.483	4′	(a)				
1.056	0.213	0.039	22	(b)	0.273	0.037	22	(b)	0.217	0.050	22	(b)	0.194	0.032	22	(b)				
1.1					0.26	0.03	18.5	(f)					0.18	0.02	18.5	(f)	0.38	0.03	18	(k)
1.2	0.170	0.017	12	(g)	0.198	0.020	12	(g)	0.177	0.018	12	(g)	0.145	0.015	12	(g)				
1.3	0.137	0.028	1.1	(l)	0.230	0.014	11	(c)	0.190	0.017	11	(c)	0.1375	0.032	3	(m)	0.253	0.012	11	(c)
1.35													0.0986	0.024	4	(m)				
2.0					0.12	0.03	27.5	(f)					0.037	0.005	5	(d)	0.037	0.004	5	(d)
2.7	0.0255	0.0016	3	(e)	0.0296	0.0020	3	(e)	0.0310	0.0033	3	(e)	0.0255	0.0027	3	(e)	0.0277	0.0022	3	(e)
3.0					0.023	0.0040	8	(j)												
3.1	0.014	0.0031	2.1	(l)																
3.4													0.0142	0.0007	1	(m)				

References —(a) Weaver and Jones (1992); (b) Beckwith and Sargent (1991); (c) Beckwith et al. (1990); (d) Kitamura et al. (2002); (e) Dutrey et al. (1996); (f) Mannings and Emerson (1994); (g) Altenhoff et al. (1994); (h) Mitchell et al. (1997); (i) Looney et al. (2000); (j) Ohashi et al. (1996); (k) Adams et al. (1990); (l) Jensen et al. (1996); (m) Koerner et al. (1995).

2.3.2 Free-free emission

At centimetre wavelengths the radio continuum of young stars is expected to be dominated by free-free radiation from ionised winds or outflows. Free-free emission arises from electron–atom/electron–ion interactions in the ionised stellar atmosphere or plasma wind. The electrons lose kinetic energy in the positive electric field of atomic nuclei while emitting bremsstrahlung.

With the exception of RY Tau, all other sources observed at 1.3 cm appear to be resolved, at least in one spatial direction. The position angles roughly match (within 20°) those derived from the 7-mm images. This supports the hypothesis that dust emission rather than wind emission is the main contribution at low centrimetre wavelengths (Rodriguez et al. 1994; Wilner et al. 1996, 2005). For HL Tau the position angles differ by $\sim$40°, probably as a result of the bright counter-jet.

In the following, we measured the free-free spectrum for four sources by fitting a power law to the centimetre flux values (Figure 2.11). The 2.0-cm and 3.6-cm fluxes are assumed to originate from free-free radiation only. At higher frequencies, a reliable quantification of the corresponding contribution of thermal dust emission and free-free radiation is difficult; we assumed an equal mixture of dust and wind emission at 1.3 cm. The spectral index $\alpha_{\rm ff}$ ($F_\nu \propto \nu^{\alpha_{\rm ff}}$) was found to be in the range -0.1 to $+0.4$. A symmetric, ionised, and opaque wind with constant velocity has a spectral power index of 0.6 (Panagia and Felli 1975; Wright and Barlow 1975; Olnon 1975). $\alpha_{\rm ff} = -0.1$ is expected for totally transparent free-free emission (Shang et al. 2004).

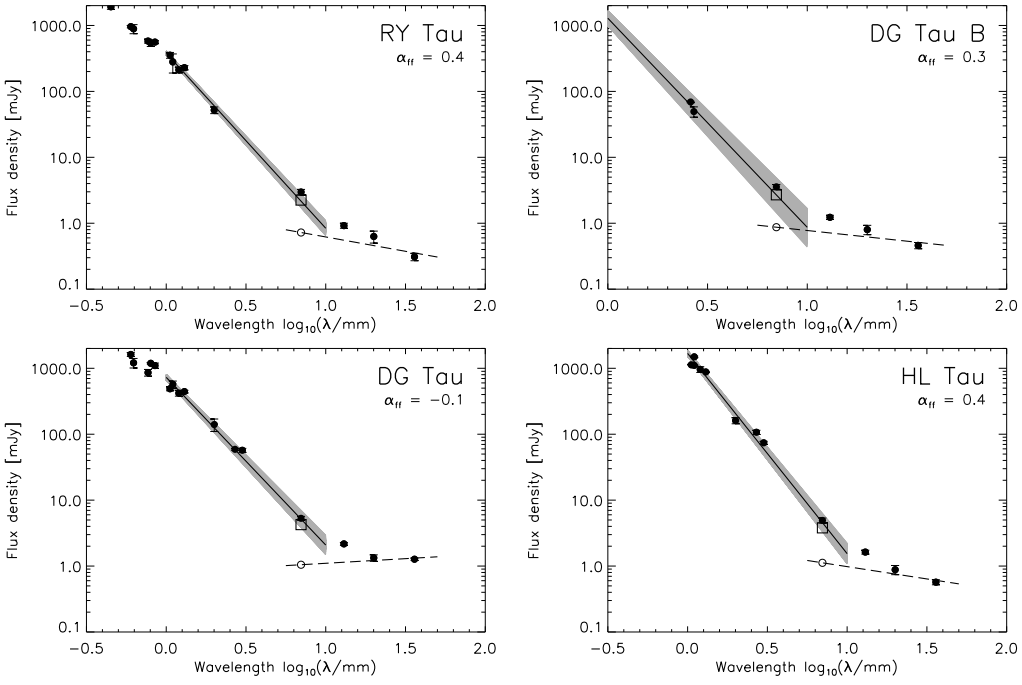

Figure 2.11. Free-free emission contribution to 7-mm flux densities. The dashed line represents the fit to the centimetre fluxes, assuming that 50% of the 1.3-cm emission arises from free-free radiation. The squares depict the corrected 7-mm fluxes after subtraction of the estimated free-free contributions (open circles). The thick line shows the power-law fits to the millimetre data; the shaded region indicates the uncertainty range for the 1–7 mm slopes. Data points below λ=7 mm were compiled from the literature (Table 2.4).

For all four objects we extrapolated the free-free radio spectrum to λ=7 mm to estimate the contribution of wind emission to the 7-mm fluxes. Subtracting the estimated free-free emission from the measured 7-mm value one obtains the thermal dust emission. We found that about 20% of the 7-mm emission originates from free-free radiation; 80% are due to dust continuum emission. For sources where no centimetre data were available, we used these numbers to correct the 7-mm fluxes.

2.3.3 Optical thickness correction

Were the millimetre emission completely optically thin, i.e. without any contribution from the optically thick inner disk, one could simply read off the opacity index β from the (free-free radiation corrected) spectral index $\alpha_{\rm corr}$ using the relation $\tilde{\beta} = \alpha_{\rm corr} - 2$, as explained in §2.3.1. There is, however, a non-negligible contribution to the measured fluxes from optically thick emission. Knowing this contribution will enable an improved estimate for the emissivity index β.

For simplicity, we assume that the surface density distribution $\Sigma(r)$ and temperature distribution $T(r)$ of the disk depend on the radial distance from the star alone and are of power-law forms $\Sigma(r) = \Sigma_0 \, (r/R_0)^{-p}$ and $T(r) = T_0 \, (r/R_0)^{-q}$, respectively. The ratio of optically thick to optically thin emission is then given by

$$\Delta = \frac{1}{\tau_0 R_0^p} \frac{2-p-q}{2-q} \frac{R_1^{2-q} - R_0^{2-q}}{R_{\rm disk}^{2-p-q} - R_1^{2-p-q}} \tag{2.5}$$

$$\approx -\frac{p}{(2-q) \ln\{(1-p/2)\,\bar{\tau}\}} \, , \tag{2.6}$$

where R_1 and $\bar{\tau}$ are the radius at which the disk changes from being optically thick to optically thin ($\tau(R_1) \approx 1$) and the average optical depth, respectively (Beckwith et al. 1990).

For the surface-density profile we adopt a value of $p = 1.5$ throughout. The temperature profile index q is uniquely determined by the slope of the spectral energy distribution in the optically thick regime, given by the relation $q = 2/(3 - \alpha_{\rm IR})$. We measured the spectral slope at far-infrared wavelengths, and derived temperature indices in the range of $q \approx 0.5 - 0.7$ (Table 2.6). Since Δ depends only weakly, that is logarithmically on the average optical depth $\bar{\tau}$, an order-of-magnitude estimate for this quantity will suffice. $\bar{\tau}$ is a function of the opacity, mass, outer radius, and orientation of the disk (Beckwith et al. 1990). We estimate its approximate value by taking characteristic numbers for these parameters, i. e. disk masses from Beckwith et al. (1990) and disk radii from Table 2, for a circumstellar disk seen at random orientation. We found that $\bar{\tau}$ is of the order of $\sim 10^{-2}$.

The ratio of optically thick to optically thin emission can now be employed to arrive at an improved estimate of the dust opacity index β, yielding (Beckwith and Sargent 1991)

$$\beta = (1 + \Delta)\tilde{\beta} \approx (\alpha_{\rm corr} - 2) \times (1 + \Delta) \, . \tag{2.7}$$

After inserting the relevant parameters for the sources where the disk could be spatially resolved, correction values $\Delta \approx 0.2$ were derived. The optical-depth correction slightly increases the opacity indices; the final β values are given in Table 2.5.

Table 2.5. Spectral slopes derived from power-law fitting in the range 1–7 mm (Col. 2), and values corrected for free-free radiation (Col. 4). For objects without centimetre measurements, a 20% contribution of free-free emission was assumed (denoted by brackets). The estimated dust opacity indices $\tilde{\beta}$ (Col. 5) were corrected for optical depth ($\Delta = 0.2$), yielding the final β values (Col. 6).

Source	mm slope $\alpha_{\rm mm}$	f-f contribution at 7 mm (%)	f-f corrected $\alpha_{\rm corr}$	β estimate $\tilde{\beta}=\alpha_{\rm corr}-2$	Opacity index $\beta=(1+\Delta)\tilde{\beta}$
RY Tau	2.51 ± 0.10	24	2.66 ± 0.09	0.66 ± 0.09	0.8 ± 0.1
FT Tau	2.62 ± 0.17	(20)	2.76 ± 0.24	0.76 ± 0.24	0.9 ± 0.3
DG Tau B	2.88 ± 0.20	24	3.17 ± 0.19	1.17 ± 0.19	1.4 ± 0.2
DG Tau	2.45 ± 0.09	20	2.54 ± 0.11	0.54 ± 0.11	0.7 ± 0.1
HL Tau	2.93 ± 0.10	23	3.04 ± 0.12	1.04 ± 0.12	1.3 ± 0.1
UZ Tau E	2.56 ± 0.08	(20)	2.66 ± 0.09	0.66 ± 0.09	0.8 ± 0.1
DL Tau	2.73 ± 0.11	(20)	2.82 ± 0.14	0.82 ± 0.14	1.0 ± 0.2
CI Tau	3.00 ± 0.27	(20)	3.12 ± 0.30	1.12 ± 0.30	1.3 ± 0.4
DO Tau	2.29 ± 0.06	(20)	2.38 ± 0.07	0.38 ± 0.07	0.5 ± 0.1
GM Aur	3.17 ± 0.20	(20)	3.29 ± 0.20	1.29 ± 0.20	1.6 ± 0.2

2.3.4 Opacity indices

One can use the millimetre spectral slope of circumstellar disks around pre-main-sequence stars to gain information on the characteristic dust grain size, provided the observed emission is largely optically thin. The magnitude of the dust opacity index indicates whether dust aggregates are small or large compared to the observing wavelength. At 7 mm one largely observes the thermal emission of cold dust in the outer parts of the disk midplane, and the β values are a robust measure of the characteristic grain size in this region.

For dust grains with sizes of the order of a few tenths of a micron ($\ll \lambda_{\rm obs}/2\pi$), as present in the interstellar medium and in protostellar cores, the opacity index has been found to be $\beta \approx 2$ (Hildebrand 1983; Draine and Lee 1984; Ossenkopf and Henning 1994). For very large bodies ($\gg \lambda_{\rm obs}/2\pi$) that block radiation by virtue of their geometrical cross-section, the opacity is frequency-independent (grey opacity), $\beta = 0$.

Particles of about the same size as the observing wavelength of $\lambda = 7$ mm, i. e. pebble-sized particles, are expected to be in an intermediate regime (Beckwith et al. 2000). Strictly speaking, one has to include the refractive index $m = n + {\rm i}k$ of the absorbing material. At millimetre wavelengths, the optical constants for silicate grains are $n \approx 3$ and $k \simeq 0$, thus $|m| \approx 3$ (Laor and Draine 1993; Henning and Mutschke 1997; Mutschke et al. 1998). Thus opacity indices $\beta \lesssim 1$ suggest the presence of dust particles with sizes $\gtrsim \lambda/2\pi|m|$, i. e. with sub-millimetre/millimetre dimensions.

After correcting for free-free radiation and optically thick emission, we determined dust opacity indices β in the range 0.5–1.6 for 10 sources where the circumstellar disk could be spatially resolved (Figure 2.12). Six objects have $\beta \lesssim 1$, a robust indication of agglomerated dust particles in the millimetre size regime. Four other sources have β values between 1.3 and 1.6, lower than the dust opacity index $\beta \simeq 2$ of submicron-sized particles as found in the interstellar medium. β values smaller than 2 may also be explained by grain properties like shape, compo-

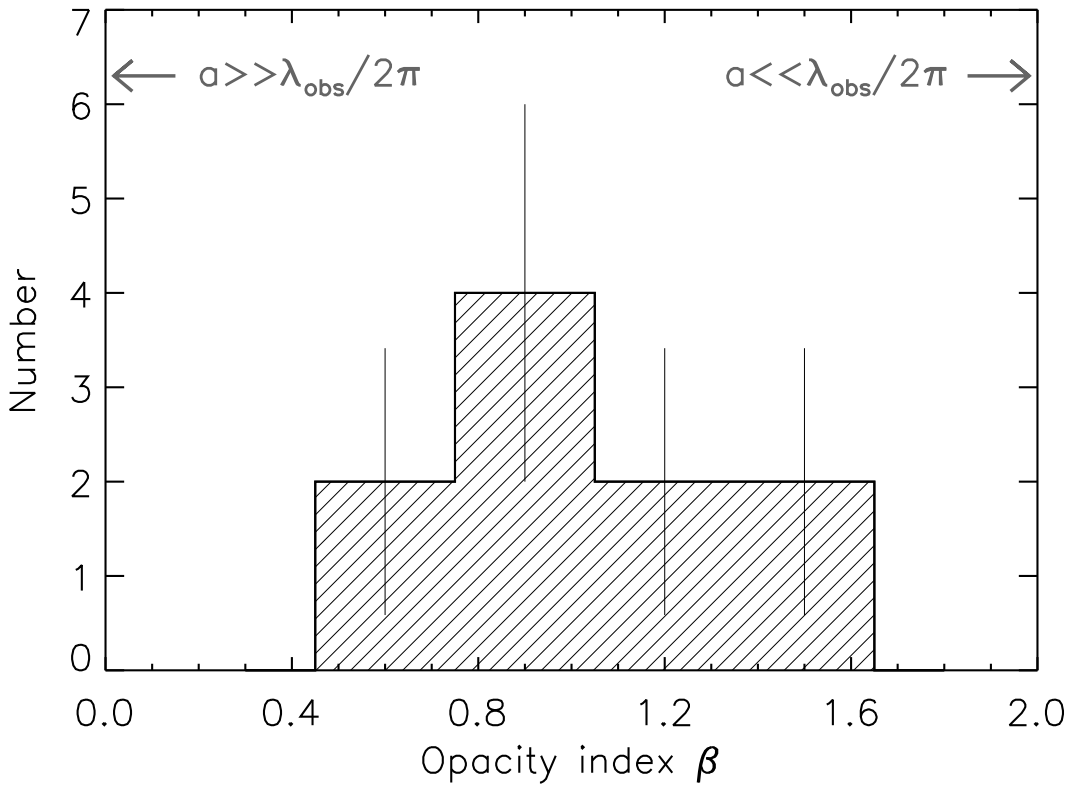

Figure 2.12. Distribution of dust opacity indices. ISM-sized dust grains have $\beta \simeq 2$, while particles much larger than the observing wavelength λ=7 mm have a frequency-independent opacity law ($\beta = 0$). The populated intermediate regime is indicative for the presence of millimetre-sized dust aggregates.

sition, conductivity, porosity, and crystallinity of the dust particles (Henning et al. 1995). Size, however, is the most important parameter influencing dust opacity indices. We deem unlikely the possibility that extreme dust compositions or particle structures cause the observed low β values (Koerner et al. 1995; Draine 2005).

We underline the importance of proper free-free correction of the millimetre slopes, without which the opacity indices would be systematically smaller. The detection of emission at centimetric wavelengths remains the only safe method to estimate the contribution of free-free radiation to the millimetre emission observed.

Millimetre observations trace the cold outer disk midplane where most of the disk mass is locked up. The grain-size indicator β therefore only conveys information on that disk region. Due to higher densities and collision frequencies, the characteristic particle size in the inner disk may be even larger. The surface layer of the inner disk is accessible through mid-infrared spectroscopy. Mid-infrared observations of pre-main-sequences stars and analysis of their 10-μm silicate feature demonstrated grain growth to micron-sizes (Bouwman et al. 2001; Meeus et al. 2003; Przygodda et al. 2003).

2.4 Disk masses

The flux density originating from an optically thin disk is proportional to the total mass of the thermally emitting dust particles. The total mass of the disk, comprising gas and dust, can then be estimated by assuming the canonical gas-to-dust ratio as found in the interstellar medium, i. e. 100-times more gaseous constituents than solid particles.

The dust mass of a disk can be expressed by

$$M_{\rm dust} = \int_{R_{\rm in}}^{R_{\rm out}} \Sigma(r) 2\pi r {\rm d}r = 2\pi \Sigma_0 R_{\rm in}^2 \left[\frac{(R_{\rm out}/R_{\rm in})^{2-p} - 1}{2-p} \right] , \tag{2.8}$$

where the previously used power-law form of the surface density has been put in. Using this relation, we see that the integral in Equation 2.2 represents a temperature-weighted disk mass. The thermal emission from a ring at distance r and width ${\rm d}r$ is the product of the local surface density weighted by the temperature of the ambient material. Since the disk temperature drops with distance to the central star, the inner disk regions contribute more dust emission than the outer part to the total flux observed.

Following Beckwith (1999), one can replace the integral in Equation 2.2 by $T_{\rm av} M_{\rm dust}$, where $T_{\rm av}$ is the sought-after average temperature of the disk. Making use of the expression for the disk temperature first given §2.3.3, we write:

$$\begin{aligned}
\int_{R_{\rm in}}^{R_{\rm out}} T(r)\Sigma(r) 2\pi r {\rm d}r &= \int_{R_{\rm in}}^{R_{\rm out}} T_0 \Sigma_0 \left(\frac{r}{R_{\rm in}} \right)^{-p-q} 2\pi r \, {\rm d}r \\
&= 2\pi T_0 \Sigma_0 R_{\rm in}^{p+q} \int_{R_{\rm in}}^{R_{\rm out}} r^{1-p-q} \, {\rm d}r \\
&= 2\pi T_0 \Sigma_0 R_{\rm in}^{p+q} \left[\frac{R_{\rm out}^{2-p-q} - R_{\rm in}^{2-p-q}}{2-p-q} \right] \\
&= 2\pi T_0 \Sigma_0 R_{\rm in}^{2} \left[\frac{(R_{\rm out}/R_{\rm in})^{2-p-q} - 1}{2-p-q} \right] \\
&= T_0 M_{\rm dust} \left\{ \frac{(R_{\rm out}/R_{\rm in})^{2-p} - 1}{2-p} \right\}^{-1} \left[\frac{(R_{\rm out}/R_{\rm in})^{2-p-q} - 1}{2-p-q} \right] \\
&= T_0 M_{\rm dust} \left(\frac{2-p}{2-p-q} \right) \left[\frac{(R_{\rm out}/R_{\rm in})^{2-p-q} - 1}{(R_{\rm out}/R_{\rm in})^{2-p} - 1} \right] .
\end{aligned} \tag{2.9}$$

Hence, one obtains for the average disk temperature:

$$T_{\rm av} = T_0 \left(\frac{2-p}{2-p-q} \right) \left[\frac{(R_{\rm out}/R_{\rm in})^{2-p-q} - 1}{(R_{\rm out}/R_{\rm in})^{2-p} - 1} \right] . \tag{2.10}$$

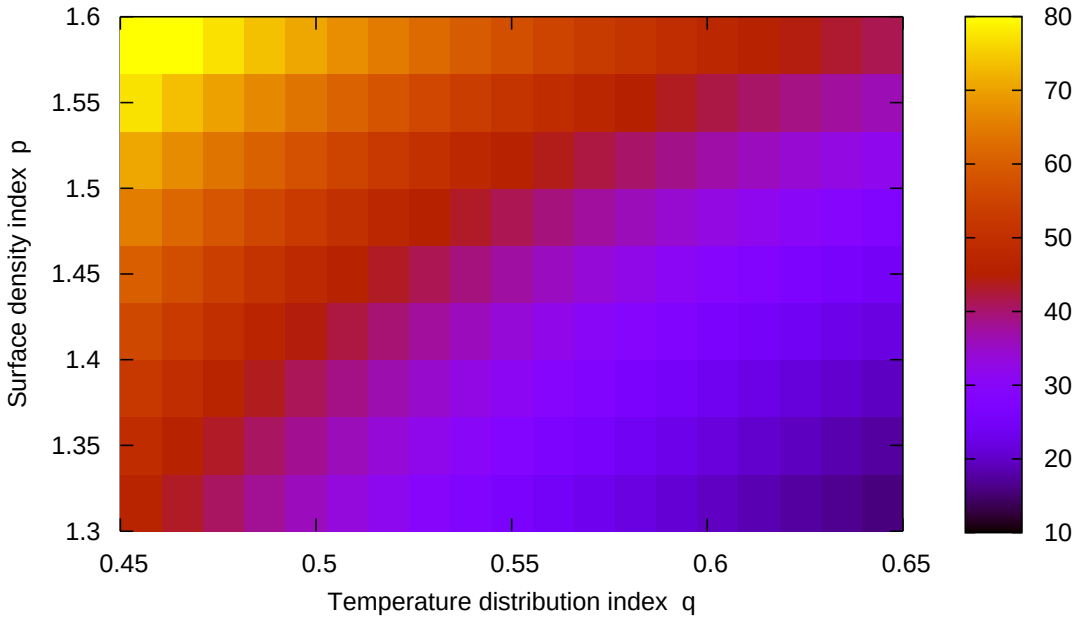

Figure 2.13. Average temperature of a T Tauri disk (in K) as a function of the power-law index of the temperature distribution q and the exponent of the surface density power-law p.

Figure 2.13 shows the average disk temperature as a function of the power-law indices q and p of the temperature and surface density distribution, respectively. Physically, it is clear that $T_{\rm av}$ is proportional to p, and inversely proportional to q. The steeper the temperature gradient with distance from the central star, the colder the dust in the outer parts, and, hence, the lower the average temperature. Conversely, the steeper the surface density drops, the smaller the contribution of thermal emission from cold dust compared to warm dust, leading to a higher average temperature. Assuming that the inner edge of the disk extends to the sublimation radius, the average disk temperature is approximately $T_{\rm av} \approx 50$ K. This value is consistent with existing estimates for circumstellar disks around T Tauri stars (Beckwith 1999). Returning to Equation 2.2, we arrive at:

$$M_{\rm dust} \approx \frac{D^2 c^2}{2 k_{\rm B} \nu^2} \frac{F_\nu}{T_{\rm av} \kappa_\nu} \tag{2.11}$$

$$M_{\rm dust} \approx \frac{D^2 \lambda^2}{2 k_{\rm B}} \frac{F_\nu}{T_{\rm av} \kappa_\nu} \, . \tag{2.12}$$

The dust opacity law is parametrised as a power-law function of frequency (or wavelengths) via the relations $\kappa_\nu = \kappa_0 (\nu/\nu_0)^\beta$ or $\kappa_\lambda = \kappa_\nu = \kappa_0 (\lambda/\lambda_0)^{-\beta}$, respectively. The fiducial values of Hildebrand (1983) were chosen, with $\kappa_0 = 1.0$ cm^{2}g^{-1} at $\lambda_0 = 1.3$ mm. After the insertion of

Table 2.6. Dust mass and total disk mass derived from Equations 2.13 and 2.14 using the average disk temperature as estimated from Equation 2.10. Numbers in brackets could not be inferred from the data; in these cases the mean value of the corresponding quantity was adopted.

Source	q	$R_{\rm in}(=R_{\rm subl})$ (AU)	$R_{\rm out}$ (AU)	$T_{\rm av}$ (K)	$M_{\rm dust}$ ($\mathrm{M}_\oplus$)	$M_{\rm disk}$ ($\mathrm{M}_\odot$)
CY Tau	0.575	0.005	(100)	33	130	0.04
RY Tau	0.649	0.022	90	48	140	0.04
FT Tau	0.570	(0.01)	85	47	90	0.03
DG Tau B	(0.6)	(0.01)	65	47	460	0.14
DG Tau	0.629	0.010	55	46	210	0.06
HL Tau	0.499	0.008	70	62	400	0.12
GG Tau	(0.6)	0.010	(100)	39	360	0.11
UZ Tau E	0.599	0.014	60	56	70	0.02
DL Tau	0.622	0.007	105	30	150	0.05
DM Tau	(0.6)	0.004	(100)	26	140	0.04
CI Tau	0.551	0.007	110	40	100	0.03
DO Tau	0.566	0.009	60	52	60	0.02
LkCa 15	(0.6)	0.007	(100)	33	160	0.05
GM Aur	0.461	0.007	100	64	140	0.04

convenient units, the dust mass reads as:

$$M_{\rm dust} \approx \frac{10}{T_{\rm av}} \left(\frac{D}{100\ \mathrm{pc}}\right)^2 \left(\frac{F_\nu}{1\ \mathrm{mJy}}\right) \left(\frac{\lambda}{1.3\ \mathrm{mm}}\right)^{2+\beta} \mathrm{M}_\oplus \qquad (2.13)$$

$$M_{\rm disk} \approx 100 \times M_{\rm dust} \approx \frac{0.003}{T_{\rm av}} \left(\frac{D}{100\ \mathrm{pc}}\right)^2 \left(\frac{F_\nu}{1\ \mathrm{mJy}}\right) \left(\frac{\lambda}{1.3\ \mathrm{mm}}\right)^{2+\beta} \mathrm{M}_\odot\ . \qquad (2.14)$$

As already mentioned in §2.1.2, calculating the disk mass is prone to serious uncertainties, and estimates of $M_{\rm disk}$ are only reliable to an order of magnitude or so. Having this caveat in mind, we estimated the disk masses by assuming a gas-to-dust ratio of 100:1. The values thus determined fall in the range from a few percent to a tenth of a solar mass (Table 2.6). An attempt to correlate the disk mass and the opacity index is precluded by the huge inherent uncertainties. The same considerations are valid for a supposed relation between disk mass and the age of the star.

The average disk mass of $\approx 0.05\ M_\odot$ is comparable to the value assumed for the early solar nebula. The so-called minimum-mass solar nebula, $M_{\rm MMSN} \approx 0.01\ \mathrm{M}_\odot$, contains the mass of today's planetary system augmented to solar abundances to account for the loss of volatile (mainly gaseous) elements during the formation of the solar system (Weidenschilling 1977). This number, however, represents a lower limit of the actual mass of the solar nebula. Hubble Space Telescope observations of the Orion Trapezium Cluster demonstrated that a substantial fraction of the proto-planetary disk surrounding pre-main-sequence stars may be dissipated through photoionisation by nearby OB stars (O'Dell and Wen 1994; Bally et al. 1998; Henney and O'Dell 1999).

Chapter 3
Modelling the spectral energy distributions of debris disks

Modeling in science remains, partly at least, an art.
Some principles exist, however, to guide the modeler.
The first is that all models are wrong;
some though, are better than others
and we can search for the better ones.

MCCULLAGH & NELDER, Generalized Linear Models

3.1 The Spitzer Space Telescope

Every new generation of infrared space telescopes brought a substantial progress to our understanding of the formation and evolution of circumstellar disks. The Infrared Astronomical Satellite (IRAS), a joint American-Dutch-British project launched in 1983, conducted the first complete survey of the infrared sky. The IRAS mission revealed the ubiquity of dusty material around young stars. A decade later, the European Infrared Space Observatory (ISO) was put into space. Among its prime results is the discovery of the rich mineralogy of the dusty circumstellar material. With the exception of very nearby stars, neither IRAS nor ISO were sensitive enough to detect dust around main-sequence stars older than a few hundred Myr.

The Spitzer Space Telescope, launched in August 2003, is the latest member of the family of infrared space telescopes (Figure 3.1, Table 3.1). It is equipped with advanced infrared detector technology, offering an effective enhancement in sensitivity by a factor of ~ 100, compared to its predecessor ISO. The space observatory utilises a novel type of heliocentric orbit. Seen from the Earth, Spitzer falls behind at about 0.12 AU per year. This Earth-trailing orbit configuration minimises the detrimental effects of the terrestrial thermal radiation on the spacecraft. As a consequence, passive cooling alone can lower the temperature of the outer shell to 40 K, and the quantity of cryogen required to reach the working temperature of the telescope and the instruments can be reduced significantly. These and other improvements of the heat budget also allowed for a warm-launch architecture, where only the science instruments are enclosed in a cryostat while the telescope section itself is at ambient temperatures, beginning to cool in-orbit. Therefore, smaller and more lightweight vacuum vessels could be designed for Spitzer.

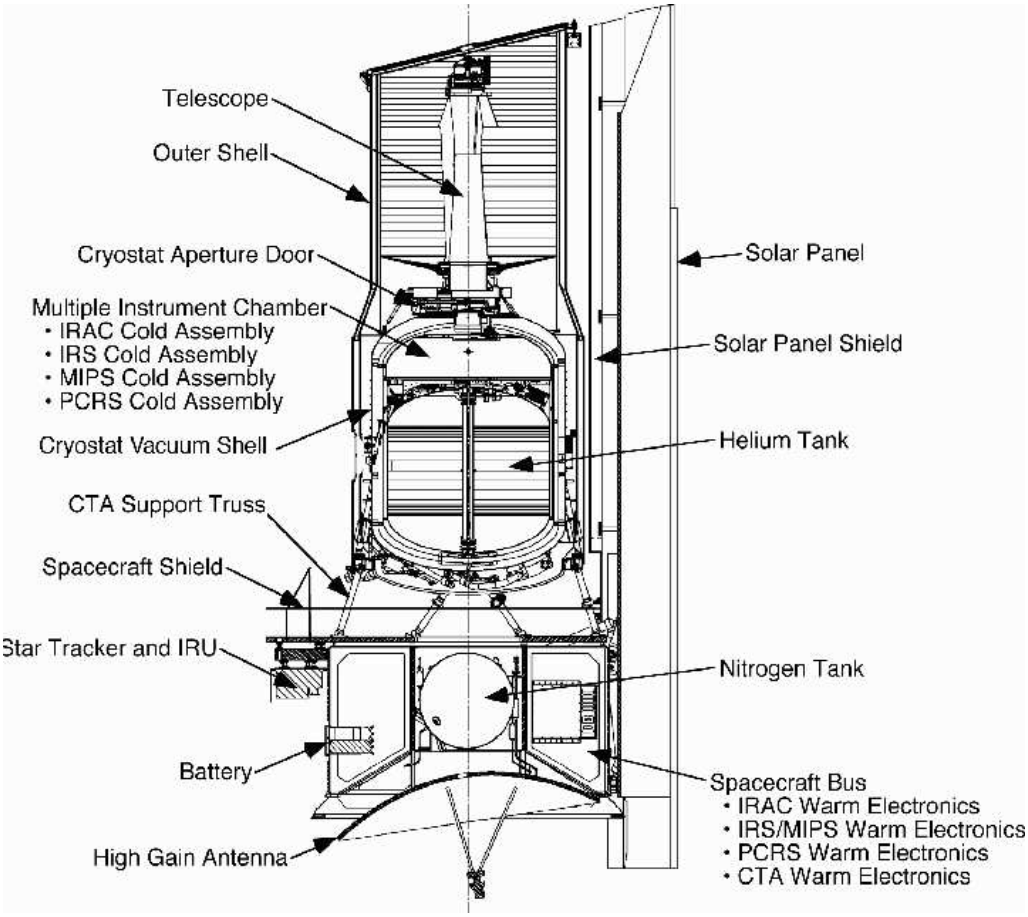

Figure 3.1. Cutaway view of the Spitzer Space Telescope. The flight hardware is composed of three main sections. The cryogenic telescope assembly (CTA) at the front end of the observatory contains the telescope, the scientific instruments, and the helium tank. The rear end consists of a spacecraft operating at ambient temperature, housing computers, instrument electronics, thrusters, and antenna. The third section is the solar panel that covers the whole length of the observatory. The solar panel array can generate ~ 500 W of power, and also serve as a passive radiation shield. (From Werner et al. 2004).

Spitzer features an 85-cm Ritchey-Chrétien telescope operated at a nominal temperature of 5.5 K. The observatory's focal plane houses three scientific instruments:

- The Infrared Array Camera (IRAC) is a near/mid-infrared imager for simultaneous imaging in band pairs at 3.6/5.8 μm and 4.5/8.0μm (Table 3.2; Fazio et al. 2004).
- The Multiband Infrared Photometer for Spitzer (MIPS) has three detector arrays providing imaging at central wavelengths of 24, 70, and 160 μm as well as measurements of spectral energy distributions between 52 and 100 μm (Table 3.2; Rieke et al. 2004).
- The Infrared Spectrograph (IRS) comprises four separate spectrograph modules covering the wavelength range from 5.3 to 38 μm with spectral resolution $\lambda/\Delta\lambda$ from $\sim$100 to 600. (Table 3.3; Houck et al. 2004).

Table 3.1. Technical parameters of the Spitzer Space Telescope. (Adapted from Werner et al. 2004.)

Parameter	Value
Dimensions (height × diameter)	4.5 m × 2.1 m
Total Observatory mass at launch	861 kg
Superfluid helium at launch	337 ℓ
Telescope primary diameter	0.85 m
Telescope temperature	5.5 K
Temperature of science instruments	$\sim$ 1.4 K
Estimated nominal cryogenic lifetime	5.3 years

Table 3.2. Basic instrument characteristics of the infrared imagers IRAC and MIPS. In the SED mode the MIPS instrument works as a low resolution spectrometer, providing a spectral resolution $\lambda/\Delta\lambda = 15$–$25$. (Adapted from Werner et al. 2004.)

Instrument	Channel/ band	Wavelength range (μm)	Field of view (arcmin)	Detector size (pixel) and detector material
IRAC	1	3.19–3.94	5.2 × 5.2	256 × 256 InSb
	2	4.00–5.02	5.2 × 5.2	256 × 256 InSb
	3	4.98–6.41	5.2 × 5.2	256 × 256 Si:As
	4	6.45–9.34	5.2 × 5.2	256 × 256 Si:As
MIPS	24 μm	21.5–26.2	5.4 × 5.4	128 × 128 Si:As
	70 μm	62.5–81.5	5.2 × 5.2	32 × 32 Ge:Ga
	160 μm	139.5–174.5	5.3 × 0.5	2 × 20 stressed Ge:Ga
	SED	51–106	2.7 × 0.34	32 × 24 Ge:Ga

Table 3.3. Characteristics of the Infrared Spectrograph IRS. (Adapted from Werner et al. 2004.)

Module	Wavelength range (μm)	Slit dimension (arcsec)	Spectral resolution $\lambda/\Delta\lambda$
Short-Low (SL)	5.2–7.7, second order	3.6 × 57	80–128
	7.4–14.5, first order	3.7 × 57	64–128
Long-Low (LL)	14.0–21.3, second order	10.5 × 168	80–128
	19.5–38.0, first order	10.7 × 168	64–128
Short-High (SH)	9.9–19.6	4.7 × 11.3	$\sim$600
Long-High (LH)	18.7–37.2	11.1 × 22.3	$\sim$600

3.2 Legacy Science project "Formation and Evolution of Planetary Systems"

Six large science projects were selected for the Spitzer Legacy Science Program. The driving idea behind the Legacy Program was to maximise the scientific return from the Spitzer Space Telescope in the light of its limited cryogenic lifetime. The selected Legacy projects were awarded a substantial amount of Spitzer's observing time (a total of 3160 hours), especially during the first year of operation. The scientific topics of the Legacy Science projects cover the breadth of infrared astronomy, from the study of star formation and the evolution of circumstellar disks, through a survey of the galactic plane to the observation of nearby galaxies and high-z galaxies at infrared wavelengths.

The Legacy project "Formation and Evolution of Planetary Systems: Placing Our Solar System in Context" (FEPS) (Meyer et al. 2002) performed spectrophotometric observations of a large sample of 328 solar-type stars (Figure 3.2) in order to study the pivotal phase of planet formation and to follow the evolution of the circumstellar disks as they grow older. This required the precise measurement of infrared spectral energy distributions for a statistically robust sample that spans a wide range of stellar ages. For the majority of the sources, photometric observations from 4 to 70 μm have been obtained using the IRAC camera and MIPS photometer. About 40 stars have additional MIPS observations in the 160-μm band. Furthermore, 5 to 38 μm low-resolution IRS spectra were taken for all stars. Therefrom 50 stars have been surveyed at higher spectral resolution ($R \approx 600$) from 10 to 37μm.

The target stars have been selected in such a way to comprise to subsamples with ages from approximately 3 to 100 Myr and from about 100 Myr to 3 Gyr (Figure 3.3). The former selection primarily contains pre-main-sequence and young main-sequence stars located in various OB associations (e. g. Scorpius-Centaurus, Upper Centaurus Lupus, Lower Centaurus Crux) and open clusters (e. g. Hyades, Pleiades, α Per). The other subsample mostly contains older field stars within ~ 50 pc from the Sun (Figure 3.4).

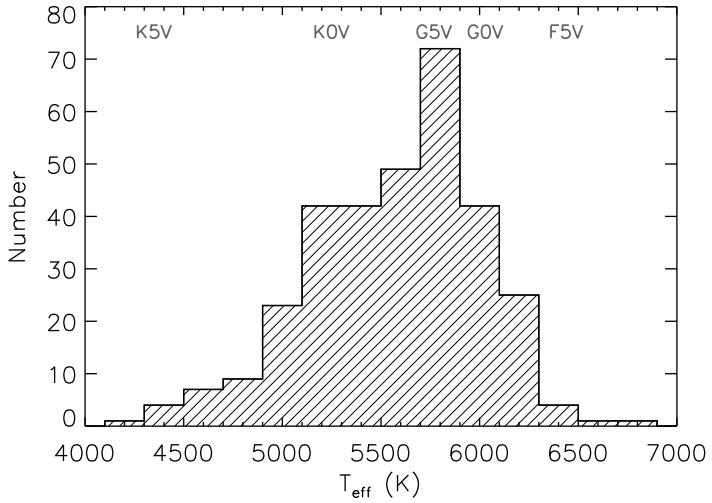

Figure 3.2. Distribution of effective temperatures and spectral types. The sample contains mostly solar-type stars; stellar masses and luminosities cover ranges from 0.85 to 1.45 $M_\odot$ and 0.4 to 6 $L_\odot$, respectively.

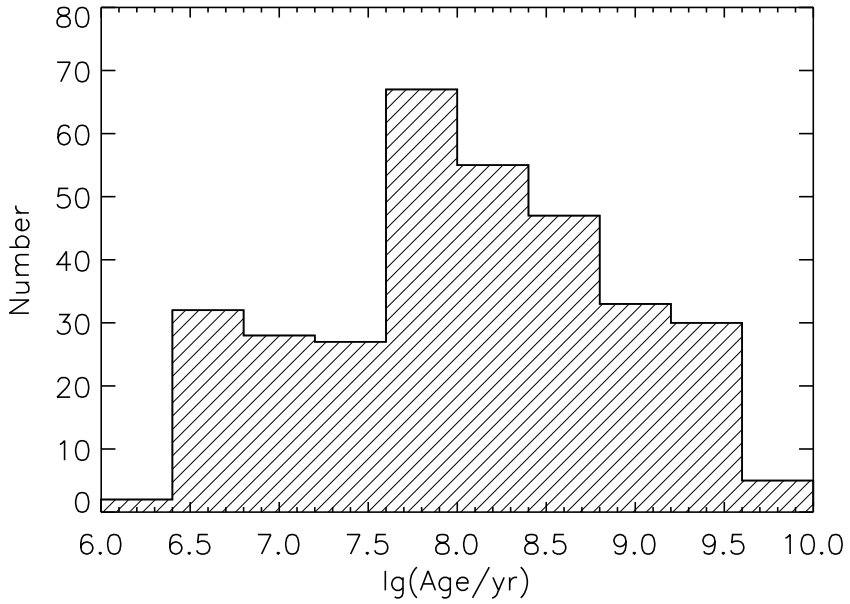

Figure 3.3. Age distribution of the stars in the FEPS sample. The majority of the stars is older than ∼30 Myr, i. e. the circumstellar material, if present, is likely to be optically thin (debris disk phase).

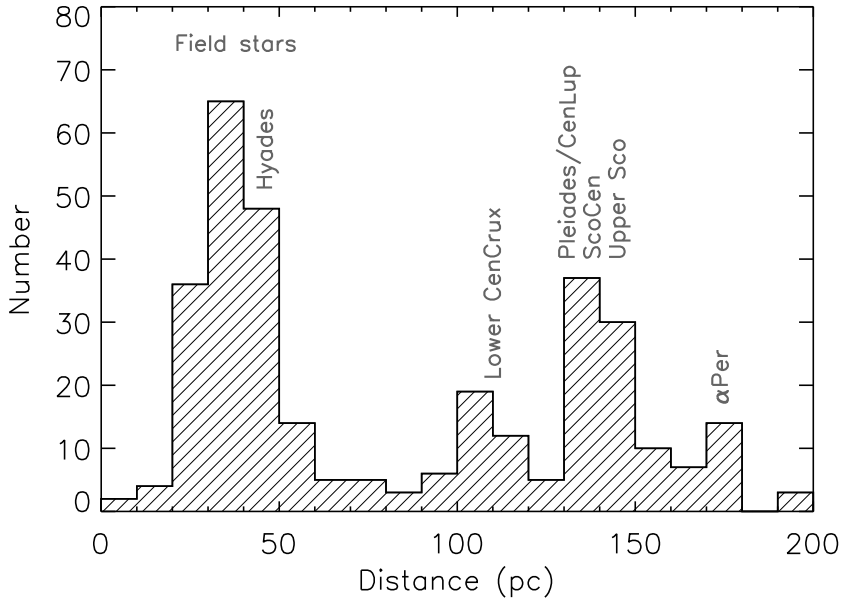

Figure 3.4. Distribution of distances of FEPS stars. About one third of the sample stars are members of stellar groups and open clusters (indicated in the plot); the remainder are field stars. Three stars have distances in excess of 200 pc.

3.3 Modelling of spectral energy distributions

The spectral energy distribution (SED) is the most important diagnostic of the fundamental properties of circumstellar debris disks in the case of spatially unresolved observations. Of particular importance are the infrared, sub-millimetre and millimetre part of the SED. In this wavelength range dust grains re-emit most of the incident stellar radiation.

3.3.1 Model description

For the modelling of the spectral energy distribution of debris disks obtained from Spitzer observations, the analytic model of Wolf and Hillenbrand (2003) has been used. The basic principle of the Debris Disk Radiative Transfer Simulation Tool (DDS) is based on three assumptions.

First, the disk configuration is assumed to be optically thin for both stellar radiation and dust re-emission. The optical depth is measured along a line of sight from the central star along the disk midplane at visual wavelengths (~ 0.5 μm). In the optically thin regime, dust particles are heated by the incident stellar radiation only. The emergent spectral energy distribution is then determined by scattering, absorption, and re-emission of stellar radiation by dust grains. The effects of multiple scattering and additional grain heating by dust re-emission can be neglected, leading to a significant simplification of the radiation transfer problem.

Second, the dust grains are compact spherical objects with homogeneous physical, chemical, and mineralogical properties. In this case, the interaction of the stellar radiation with the dust particles can be described by Mie theory (e. g. Bohren and Huffman 1983). The detailed scheme used to calculate the absorption and scattering efficiency factor is given in Wolf and Voshchinnikov (2004). Finally, we assume that the dust grains are in a state of thermal equilibrium with the ambient radiation field. In particular, this condition demands that dust grains are large enough ($\gg 1$ nm) to rule out stochastic heating. For very small grains (some ten Å in diameter), there is no equilibrium temperature, and the dust re-emission varies on short timescales (Krügel 2003).

Calculation of spectral energy distribution Since the disk is assumed to be optically thin, one can express the net SED as a simple summation of the re-emission and scattering contributions from all grains. After Wolf and Hillenbrand (2003), the contributions from a single dust particle can be calculated as follows. The monochromatic luminosities absorbed, re-emitted, and scattered by a dust grain of radius a, temperature $T_{\rm grain}$, and distance r to the star are given by:

$$L_{\rm grain}^{\rm abs}(\lambda) = \pi a^2 Q_{\rm abs}(\lambda) \frac{L_\star(\lambda)}{4\pi r^2} \tag{3.1}$$

$$L_{\rm grain}^{\rm emis}(\lambda) = 4\pi a^2 Q_{\rm abs}(\lambda)\ \pi B_\lambda(T_{\rm grain}) \tag{3.2}$$

$$L_{\rm grain}^{\rm sca}(\lambda) = A Q_{\rm sca}(\lambda) L_\star(\lambda) \left(\frac{a}{2r}\right)^2 , \tag{3.3}$$

where $Q_{\rm abs}(\lambda)$, $Q_{\rm sca}(\lambda)$, and A are the efficiencies for absorption and scattering of the dust grain and its albedo, respectively. These quantities are grain-size dependent, and can be obtained from Mie theory. $L_\star(\lambda)$ is the luminosity of a star with radius $R_\star$ and effective temperature $T_{\rm eff}$ at a certain wavelength λ, given as $L_\star(\lambda) = 4\pi R_\star^2\, \pi B_\lambda(T_{\rm eff})$.

Using the fact that the emission of the grain integrated over all wavelengths is equal to the total amount of bolometric flux absorbed by the particle, i. e.

$$\int_0^\infty L_{\rm grain}^{\rm abs}(\lambda)\ {\rm d}\lambda = \int_0^\infty L_{\rm grain}^{\rm emis}(\lambda)\ {\rm d}\lambda\ , \tag{3.4}$$

one derives the distance r corresponding to a grain temperature $T_{\rm grain}$ via the relation

$$r(T_{\rm grain}) = \frac{R_\star}{2}\left(\frac{\int_0^\infty Q_{\rm abs}(\lambda)B_\lambda(T_{\rm eff}){\rm d}\lambda}{\int_0^\infty Q_{\rm abs}(\lambda)B_\lambda(T_{\rm grain}){\rm d}\lambda}\right)^{1/2}\ . \tag{3.5}$$

The contribution of a single dust grain to the SED is then simply given by integrating the re-emission and scattering terms over all possible grain temperatures. Finally, the emergent spectral energy distribution results from adding the contribution from all grains, taking into account the prescribed disk geometry, the grain size distribution, and the total dust mass.

3.3.2 Model parameters

The spectral energy distribution of a star surrounded by a debris disk depends on the stellar properties, the extension and density distribution of the circumstellar disk, and the size and optical parameters of the dust grains. Below we will briefly introduce the key parameters of the DDS and discuss their relevance to the SED modelling of debris disks observed by Spitzer. For more detailed considerations the reader is referred to the paper of Wolf and Hillenbrand (2003).

- Central star —The radiative input into the disk is specified by a model spectral energy distribution of the stellar photosphere. Alternatively, a blackbody radiation source can be used by setting stellar luminosity and effective temperature.

- Disk mass —The total mass of dust particles. Since the disk is optically thin, the dust re-emission scales linearly with the disk mass $M_{\rm dust}$.

- Disk size —The size of the disk is defined by the inner and outer disk radius, $R_{\rm\ in}$ and $R_{\rm out}$. The former determines the wavelength at which the SED departs from the stellar photosphere (onset of infrared excess). The outer disk radius only influences the net flux, while preserving the shape of the SED. A larger value of $R_{\rm out}$ may always be compensated by a higher dust mass. That means both quantities are degenerate and impossible to constrain in the absence of sub-millimetre/millimetre flux measurements.

- Radial density distribution —The assumed radial density distribution follows a power law, $n(r) \propto r^{-q}$. We used $q = 1$ throughout, corresponding to a disk with constant surface density $\Sigma(r) \propto r^0$. A constant surface density is expected for a collision-less disk with no planetary perturbers (Briggs 1962).

- Minimum grain radius —The size of the smallest dust particles present in the disk, $a_{\rm\ min}$, governs the shape and strength of the mid-infrared spectral bands due to silicate dust. In the absence of collisional processes the minimum grain size is set by stellar radiation pressure (see §4.2.2).

- Maximum grain radius —The maximum grain size, $a_{\max}$, is a very uncertain parameter. Similar to the outer disk radius, the net flux of the SED is decreasing for larger parameter values. Due to this limitation and the fact that particles larger than ~ 1 mm contribute little to the infrared SED, we set $a_{\max} = 1$ mm, unless specified otherwise.

- Grain size distribution —The power-law exponent of the grain size distribution $n(a) \propto a^{-p}$ is set to the canonical value $p = 3.5$, characteristic for a size distribution initially produced by a collisional cascade (Dohnanyi 1969; Tanaka et al. 1996).

- Dust mineralogy —The interaction of dust particles with radiation also depends on their chemical composition and crystallinity. Given the lack of any distinct dust features in the IRS spectra for most of the stars modelled, we adopted the optical constants of "astronomical silicate" (Draine and Lee 1984; Weingartner and Draine 2001).

3.3.3 Model fitting

Our goal is to determine the values for the parameters of the DDS debris disk model that best describe an observed spectral energy distribution. Since the model depends on a set of physical parameters in a complicated fashion that can not be expressed in terms of linear functions, we are dealing with the nonlinear model fitting problem. In contrast to linear models where parameter estimates can be obtained analytically, the fitting of nonlinear models requires the use of an iterative solution procedure. A huge amount of literature exists on fast and reliable solution methods (see Press et al. 1992, and references therein).

Definition of the problem We want to find the DDS model that matches the observed spectral energy distribution $F_{\rm obs}(\lambda_i)$ best. Let $F_{\rm mod}(\lambda_i, \boldsymbol{p})$ be the spectral energy distribution computed by the model, where $\boldsymbol{p} = (p_1, p_2, \ldots, p_M)$ is the vector of fit parameters. In practice, the number of fit parameters is always much smaller than the number of available model parameters. Given a typical number of 10 to 15 SED data points, the number of fit parameters should not be larger than 3 or 4, otherwise the best-fit solution will be poorly constrained. For example, we may fit simultaneously for the inner disk radius, the minimum grain size, and the dust mass. In this case the fit parameter vector reads as $\boldsymbol{p} = (p_1, p_2, p_3) = (R_{\rm in}, a_{\rm min}, M_{\rm dust})$.

We then need a quantity that measures the level of agreement (or disagreement) between the observed and model SED. Conventionally, this so-called figure of merit is chosen in such a way that small values represent a close agreement, i. e. a good fit, between data and model. The best fit is then found by minimising the merit function. We adopted the standard chi-square statistic defined as:

$$\chi^2(\boldsymbol{p}) = \sum_{i=1}^{N} \left[\frac{F_{\rm obs}(\lambda_i) - F_{\rm mod}(\lambda_i, \boldsymbol{p})}{\sigma_i} \right]^2 , \tag{3.6}$$

where N and σ_i are the number of data points and the corresponding measurement errors, respectively.[1] The agreement is measured as the sum of N squared weighted differences between data and model. The quantity $\nu = N - M$ is the number of degrees of freedom, and for a good fit one expects $\chi^2 \approx \nu$. We define the so-called reduced chi-square value by normalising the merit

[1] Chi-square fitting is a maximum likelihood estimator only if the measurement errors are independent and normally distributed (Press et al. 1992).

function to the number of degrees of freedom, $\chi^2_\nu = \chi^2/\nu$. Hence, the reduced chi-square value is of the order of unity near or at the fit solution.

Minimisation of $\boldsymbol{\chi^2}$ So far so good. It appears that in order to determine the best-fit solution one only needs to find the parameters that minimise the χ^2 function. In a multi-dimensional parameter space, however, that is a formidable task. As mentioned above, a solution can only be obtained by an iterating procedure. Therefore, the initial parameters are crucial for ensuring that the minimisation converges to a useful answer. As a rule of thumb, the model corresponding to the starting parameters should not be too far off from the observed SED.

Having such an educated guess $\boldsymbol{p}_0$ at hand, we move in the parameter space in the direction in which χ^2 is decreasing most rapidly, that is

$$\boldsymbol{p}_{\rm new} = \boldsymbol{p}_0 - \alpha \boldsymbol{\nabla} \chi^2(\boldsymbol{p}_0) \; , \tag{3.7}$$

where α determines the size of the step. The components of the gradient of χ^2 with respect to the parameters $\boldsymbol{p}$ are given by

$$\frac{\partial \chi^2}{\partial p_k} = -2 \sum_{i=1}^{N} \left(\frac{F_{\rm obs}(\lambda_i) - F_{\rm mod}(\lambda_i, \boldsymbol{p})}{\sigma_i^2} \right) \frac{\partial F_{\rm mod}(\lambda_i, \boldsymbol{p})}{\partial p_k} \; , \tag{3.8}$$

with $k = 1, 2, \ldots, M$. Iterating Equation 3.7 is called the method of steepest descent or gradient descent, and will successively refine the parameter set until a minimum of χ^2 is reached. Unfortunately, while approaching a best-fit solution, this method becomes increasingly inefficient since the gradient is disappearing (Gershenfeld 1999).

If, on the other hand, the current parameters result in a good approximation of the observed SED, one can use Newton's method to reach the best-fit solution. The underlying idea is easily explained. Around the current point $\boldsymbol{p}_0$ in the parameter space, χ^2 can be expanded to second order,

$$\chi^2(\boldsymbol{p}) = \chi^2(\boldsymbol{p}_0) + \left[\boldsymbol{\nabla} \chi^2(\boldsymbol{p}_0) \right] (\boldsymbol{p} - \boldsymbol{p}_0) + \frac{1}{2} (\boldsymbol{p} - \boldsymbol{p}_0) \cdot \mathbf{H} \cdot (\boldsymbol{p} - \boldsymbol{p}_0) \; , \tag{3.9}$$

where $\mathbf{H}$ is an $M \times M$ matrix containing the second derivatives of χ^2 with respect to the parameters. This so-called Hessian matrix describes the curvature of the χ^2 surface over the M-dimensional parameter space. The components of the Hessian are given by

$$\begin{aligned}
{\rm H}_{kl} &= \frac{\partial^2 \chi^2}{\partial p_k \partial p_l} \\
&= 2 \sum_{i=1}^{N} \frac{1}{\sigma_i^2} \left\{ \frac{\partial F_{\rm mod}(\lambda_i, \boldsymbol{p})}{\partial p_k} \frac{\partial F_{\rm mod}(\lambda_i, \boldsymbol{p})}{\partial p_l} - \left[F_{\rm obs}(\lambda_i) - F_{\rm mod}(\lambda_i, \boldsymbol{p}) \right] \frac{\partial^2 F_{\rm mod}(\lambda_i, \boldsymbol{p})}{\partial p_k \partial p_l} \right\} \\
&\approx 2 \sum_{i=1}^{N} \frac{1}{\sigma_i^2} \left\{ \frac{\partial F_{\rm mod}(\lambda_i, \boldsymbol{p})}{\partial p_k} \frac{\partial F_{\rm mod}(\lambda_i, \boldsymbol{p})}{\partial p_l} \right\} \; .
\end{aligned} \tag{3.10}$$

The second-derivative terms are proportional to the residual between data and model, and will be small for a good approximation. Furthermore, the residuals should have alternating signs, and the

terms will generally cancel out. The gradient of Equation 3.9 reads

$$\boldsymbol{\nabla}\chi^2(\boldsymbol{p}) = \boldsymbol{\nabla}\chi^2(\boldsymbol{p}_0) + \mathbf{H}\cdot(\boldsymbol{p}-\boldsymbol{p}_0)\ . \tag{3.11}$$

At the minimum one has $\boldsymbol{\nabla}\chi^2(\boldsymbol{p}) = \mathbf{0}$, and the best-fit parameter vector can be found by iterating

$$\boldsymbol{p}_{\mathrm{new}} = \boldsymbol{p}_0 - \mathbf{H}^{-1}\cdot\boldsymbol{\nabla}\chi^2(\boldsymbol{p}_0)\ , \tag{3.12}$$

where $\mathbf{H}^{-1}$ is the inverse of the Hessian. Comparing the iteration prescription of the method of steepest descent (Equation 3.7) to that of Newton's method (Equation 3.12) one recognises a basic similarity. For both methods we must be able to compute the gradient of the χ^2 function with respect to any parameter vector $\boldsymbol{p}_0$. This is done by calculating the derivatives numerically via a finite difference approximation. To use Newton's method, we further need to evaluate M^2 second derivatives and then find the inverse of the Hessian.

Newton's method is very powerful in the final stage of the iteration when $\chi^2(\boldsymbol{p})$ is close to its minimum. Far away from the minimum, however, the quadratic form (3.9) may not be a good approximation of the χ^2 surface. In this regime, Equation 3.12 is unreliable, and the method of steepest descent should be used. It would be desirable to have a method that combines the best of both worlds. In the initial stages of the minimum search, this method would follow the steepest descent down to smaller χ^2 values. Closer to the minimum it would switch to Newton's method to quickly reach the best-fit solution.

Levenberg-Marquardt method Such a scheme is due to Marquardt (1963). Based on a earlier work (Levenberg 1944), the so-called Levenberg-Marquardt method unites the strong points of the steepest descent and inverse-Hessian method, while avoiding their weaknesses.

The basic idea of the Levenberg-Marquardt method relies on an ingenious application of dimensional analysis. The reader might have noticed that we did not specify how to determine the step size α in Equation 3.7. Clearly, one needs to find the right order of magnitude for α. If it is too large, one overshoots the minimum mark. If it is too small, the convergence to the best-fit solution will be unnecessarily slow. Comparing again the Equations 3.7 and 3.12, we see that α must be somehow related to the inverse of the Hessian $\mathbf{H}^{-1}$. Where is the relation one might say: The former is a scalar quantity; the latter a matrix?

Let X be the dimension of the k-th component of the parameter vector $\boldsymbol{p}$. Since the quantity χ^2 is non-dimensional, the corresponding component of the gradient (Equation 3.8) has dimension $1/\mathrm{X}$. The constant of proportionality between p_k and $\partial\chi^2/\partial p_k$ must therefore have the dimension X^2. Marquardt (1963) realised that the reciprocal of the diagonal element H_{kk} has the same dimension, so that quantity will, approximately, determine the scale for α. Equation 3.7 can then be rewritten component-wise as

$$p_k^{\mathrm{new}} = p_k^0 - \frac{1}{\lambda \mathrm{H}_{kk}}\frac{\partial\chi^2}{\partial p_k}\ , \tag{3.13}$$

where λ is a new non-dimensional scale factor. In other words, in regions of the parameter space where the χ^2 surface has a large curvature with respect to one particular parameter p_k, one should apply a small parameter increment to refine the solution. Conversely, for a flat χ^2 function, we can afford large steps.

Using this prescription, we can combine the method of steepest descent and Newton's method by defining a matrix $\mathbf{M}$

$$\mathrm{M}_{kl} = \begin{cases} \frac{1}{2}\mathrm{H}_{kl}(1+\lambda) & = \frac{1}{2}\frac{\partial^2\chi^2}{\partial p_k^2}(1+\lambda) \quad , \text{if } k=l \\ \frac{1}{2}\mathrm{H}_{kl} & = \frac{1}{2}\frac{\partial^2\chi^2}{\partial p_k \partial p_l} \quad , \text{otherwise} \end{cases} \tag{3.14}$$

Finally, we replace the Hessian from Equation 3.12 with the new matrix $\mathbf{M}$, arriving at

$$\boldsymbol{p}_{\mathrm{new}} = \boldsymbol{p}_0 - \mathbf{M}^{-1} \cdot \boldsymbol{\nabla}\chi^2(\boldsymbol{p}_0) \; . \tag{3.15}$$

If $\lambda = 0$ we have just Newton's method. For large values of λ, on the other hand, $\mathbf{M}$ will become diagonally dominant, and the iteration scheme passes into looking like Equation 3.13, i. e. the method of steepest descent. The control parameter λ determines the transition from one method to the other.

Levenberg-Marquardt recipe Starting off with some meaningful initial parameter set $\boldsymbol{p}_0$, the flow chart of the Levenberg-Marquardt algorithm looks like (Press et al. 1992):

(1) Compute $\chi^2(\boldsymbol{p}_0)$.

(2) Choose a moderate value for λ.

(3) Solve the set of M linear equations given by $\mathbf{M} \cdot \delta\boldsymbol{p} = -\boldsymbol{\nabla}\chi^2(\boldsymbol{p}_0)$ for the parameter increment $\delta\boldsymbol{p} = \boldsymbol{p}_{\mathrm{new}} - \boldsymbol{p}_0$ and evaluate $\chi^2(\boldsymbol{p}_0 + \delta\boldsymbol{p})$.

(4) If $\chi^2(\boldsymbol{p}_0 + \delta\boldsymbol{p}) \geq \chi^2(\boldsymbol{p}_0)$, increase λ by a substantial factor and repeat step (3). This will change the minimum search strategy more towards the method of steepest descent.

(5) If $\chi^2(\boldsymbol{p}_0 + \delta\boldsymbol{p}) < \chi^2(\boldsymbol{p}_0)$, decrease λ by a substantial factor, take $\boldsymbol{p}_0 + \delta\boldsymbol{p}$ as the new trial parameter solution, and go back to step (3). Smaller λ makes the minimum search more like Newton's method.

(6) Terminate iteration once χ^2 decreases and the difference $\chi^2(\boldsymbol{p}_0) - \chi^2(\boldsymbol{p}_0 + \delta\boldsymbol{p})$ is below some (small) threshold value.

Error estimate on best-fit parameters and confidence limits After an acceptable minimum has been found, one obtains the set of model parameters $\boldsymbol{p}_{\mathrm{fit}}$ that matches the observational data best. We profit from another feature of the Levenberg-Marquardt method in order to estimate the parameter uncertainties. Setting λ one can compute the covariance matrix $\mathbf{C}$ by inversion of $\mathbf{M}$, $\mathbf{C} = \mathbf{M}^{-1}$. The square root of the diagonal element $\sqrt{C_{kk}}$ gives the formal standard error for the fitted parameter p_k (Press et al. 1992).

The use of the chi-square minimisation to estimate the best-fit parameters also enables us to define confidence limits. At the solution, the merit function assumes some minimal value χ^2_{min}. The region of the parameter space around $\boldsymbol{p}_{\mathrm{fit}}$ where χ^2 increases by no more than a given $\Delta\chi^2$ defines a natural confidence region. Depending on the number of fit parameters, the usual 1-σ, 2-σ, and 3-σ confidence limits can be drawn. For instance, for $M = 2$ one obtains $\Delta\chi^2$ values of 2.30, 6.17, and 11.8, respectively (Avni 1976). The confidence intervals for each parameter separately are given by $\Delta p_k = \sqrt{\Delta\chi^2 C_{kk}}$ (Press et al. 1992); see Figure 3.7 for an example.

Implementation A graphical user interface has been developed in the Interactive Data Language (IDL) to control the fitting of observed spectral energy distributions with DDS models (Figure 3.5). A publicly available IDL Levenberg-Marquardt package was implemented to solve the nonlinear least-square problem.[2] This particular version of the Levenberg-Marquardt algorithm allows the definition of upper and lower bounding constraints to be placed on each parameter.

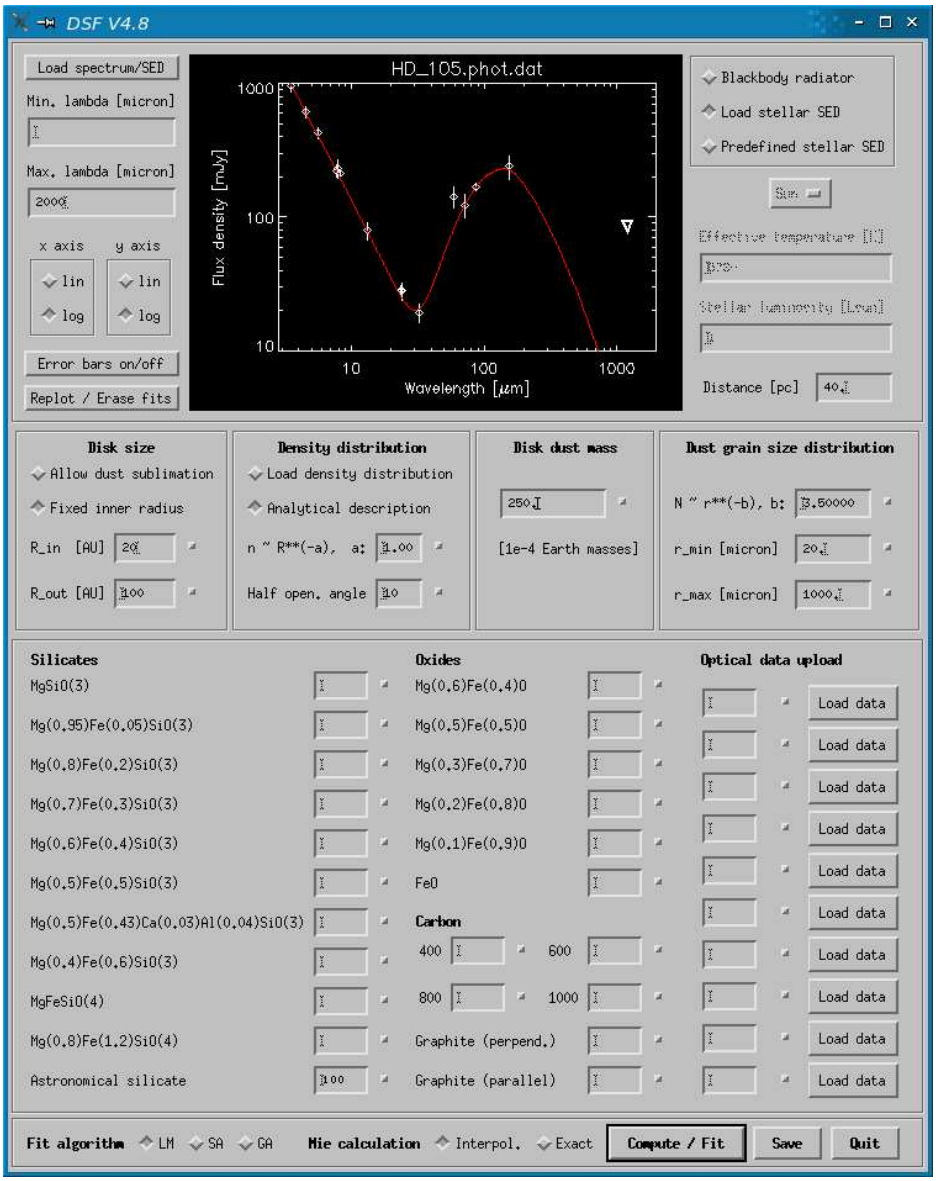

Figure 3.5. Screenshot of the graphical user interface of the Debris Disk SED and Spectrum Fitting (DSF) tool.

[2]Written by Craig B. Markwardt (NASA/GSFC, USA), based upon the MINPACK-1 function `lmdif.f` by More and collaborators. The source codes and descriptions are available at `http://cow.physics.wisc.edu/~craigm/idl/fitting.html`

3.3.4 Treatment of upper limits and bandpass correction

Treatment of upper limits Let $F_{\rm obs} = F_{\rm meas} \pm \Delta F_{\rm meas}$ be the best estimate of the flux density at some wavelength λ, consisting of the measured value and the associated uncertainty. If $|F_{\rm meas}/\Delta F_{\rm meas}| \lesssim 3$, the source is usually considered to be not detected. In this case, the measurement is quoted by a 3-σ upper limit $F_{\rm meas} + 3 \times \Delta F_{\rm meas}$ (Carpenter 2004). To give a working example, consider the SEST 1.2-mm observation of HD 105. The measured flux density was 11 mJy, while the rms noise was 27 mJy. We quoted the 3-σ upper limit as 92 mJy.

The only exception from this rule applies to (formally) negative fluxes, commonly encountered for dust-continuum observations at sub-mm/millimetre wavelengths. For a non-detected source with negative flux measured, the 3-σ upper limit is given by $3 \times \Delta F_{\rm meas}$. Upper-limit data points are not included in the SED fitting procedure. However, it is checked that the best-fit model is consistent with the constraint from the upper limit.

Bandpass correction In order to compare the model spectral energy distribution $F_{\rm mod}(\lambda)$ with the observed flux values $F_{\rm obs}(\lambda_i)$, one has to take into account the spectral response functions of the photometric band. Given a spectral response $S(\lambda)$ over some filter window, the following prescription is used:

$$F_{\rm corr}(\lambda_i) = \frac{\int F_{\rm mod}(\lambda) S(\lambda)\,{\rm d}\lambda}{\int S(\lambda)\,{\rm d}\lambda}\ . \tag{3.16}$$

The spectral response curves for the bands of the IRAC and MIPS instruments were taken from the instrument web pages.[3] For the synthetic IRS bandpasses at 8, 13, 24, and 33 μm, uniform response curves were applied.

3.4 HD 105 – first results from Spitzer

HD 105 is a G0 main-sequence star located 40 $\pm$ 1 pc away from the Sun. The large equivalent width of its Li I λ6707 line and its position in the Hertzsprung-Russell diagram attest the youth of the star (Wichmann et al. 2003). This is supported by the analysis of chromospheric and coronal activity indicators such as Ca II HK and X-ray emission (Wright et al. 2004; Cutispoto et al. 2002). Furthermore, it is a kinematic member of the Tucana-Horologium moving group (Mamajek et al. 2004). This membership suggests an age estimate of 30 $\pm$10 Myr for HD 105 (Meyer et al. 2004).

Prior to the Spitzer observation, HD 105 was known to have an infrared excess based on ISO/ISOPHOT measurements at 60 and 90 μm (Silverstone 2000). Photometric measurements obtained with the Spitzer Space Telescope from 4 to 160 μm confirmed infrared emission above photospheric levels at 70 and 160 μm, but no excess emission shortward of $\sim$35 μm (Meyer et al. 2004). The fractional luminosity $L_{\rm IR}/L_\star$ of the total excess is $\sim 3.9 \times 10^{-4}$. The search for dust continuum emission at sub-millimetre (350 μm) and millimetre wavelengths (1.2 mm) resulted only in upper limits (Mazin 2004 as cited in Hollenbach et al. 2005; Carpenter et al. 2005). Low-resolution spectra obtained with the IRS instrument over the entire wavelength range available (5.2–38 μm) showed no distinct features that could be attributed to emission bands of dust. A search for gas emission from the disk using the high spectral resolution mode of the

[3] Data files are available at `http://ssc.spitzer.caltech.edu/irac/spectral_response.html` and `http://ssc.spitzer.caltech.edu/mips/spectral_response.html` for IRAC and MIPS, respectively.

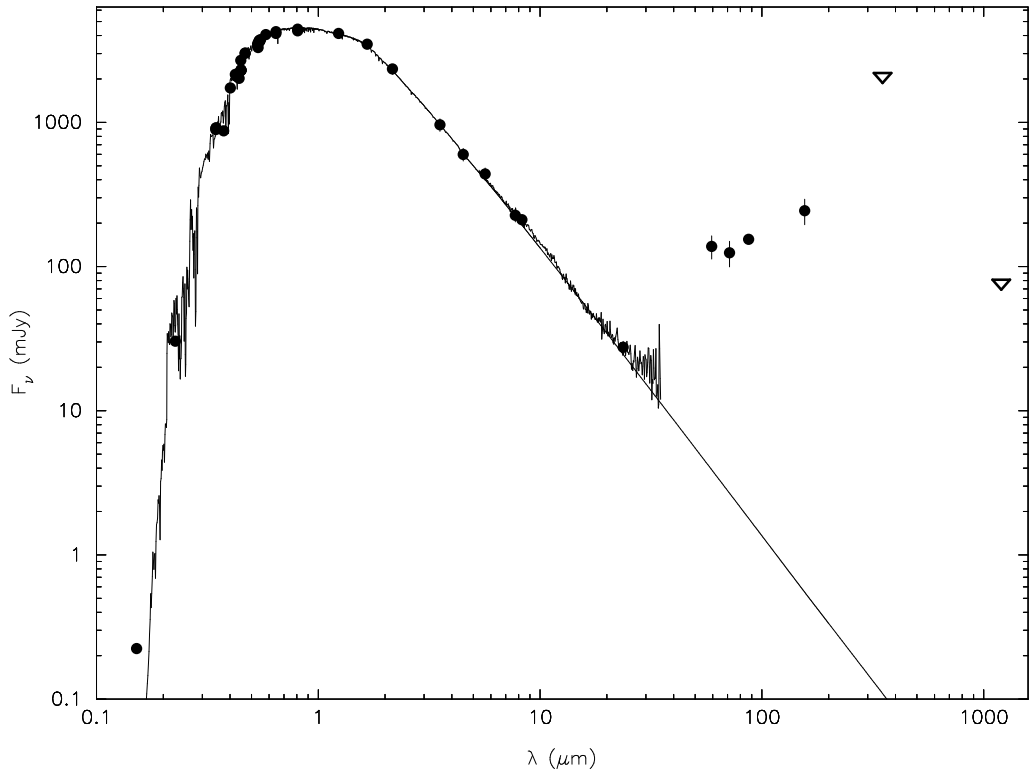

Figure 3.6. Spectral energy distribution of HD 105, containing photometric measurements and the IRS low-resolution spectrum. The solid curve shows the best-fi t Kurucz model of the stellar photosphere with $T_{\rm eff} = 6063$ K, $\log g = 4.47$, and $A_{\rm V} = 0.0$ (Cohen et al. 2003). The triangles denote upper limits at 350 μm and 1.2 mm (see text).

IRS instrument aboard Spitzer yielded upper limits on the amount of warm molecular gas present around HD 105 (Hollenbach et al. 2005). The values suggest that less than 1 $\mathrm{M_J}$ of gas exists in the 1–40 AU region. The complete spectral energy distribution of HD 105 is plotted in Figure 3.6.

SED modelling Infrared fluxes above the expected photospheric levels are an unambiguous sign of the presence of circumstellar dust around the main-sequence star HD 105. The predominance of the far-infrared excess emission as compared to shorter wavelengths is explained by the thermal emission of cold dust grains with characteristic temperatures of 40 K, or thereabouts. The lack of excess emission at wavelengths shorter than ~ 35 μm implies that only small amounts of circumstellar dust are present in the inner part ($\lesssim$ 10–20 AU) of the debris disk. Early modelling of the spectral energy distribution of HD 105 by Meyer et al. (2004) yielded a minimum grain radius of ~ 5 μm and an inner disk radius of ~ 45 AU. They reported a dust mass between 9×10^{-8} and 4×10^{-7} $\mathrm{M_\odot}$.

Here we present more detailed modelling, applying the Levenberg-Marquardt method to determine the best-fit debris disk model and to estimate the statistical uncertainties of the parameters. Following the choice of parameters by Meyer et al. (2004), we also adopted the minimum dust grain radius, $a_{\rm min}$, and the inner disk radius, $R_{\rm in}$, as the fit parameters. Both quantities greatly

influence the shape of the dust re-emission and the wavelength at which the disk emission begins to depart from the photosphere.

Since the IRS low-resolution spectra offer no constraining information on the mineralogical composition of the dust particles, we assumed the grains to be composed of "astronomical silicate" (Draine and Lee 1984; Laor and Draine 1993; Weingartner and Draine 2001). The power-law index of the radial density profile has been set to $n(r) \propto r^{-1}$, corresponding to a steady-state disk with constant surface density $\Sigma(r) \propto r^0$. Despite the fact that perturbations by embedded massive planets as well as collision processes may complicate this simple picture (Gor'kavyi et al. 1997), we note that the details are of little importance for the problem at hand because the SED models are relatively insensitive to the prescribed radial density distribution.

We assume a value of $p = 3.5$ for the power-law index of the grain size distribution $n(a) \propto a^{-p}$. A few considerations on this particular choice are in place. For quite some time, the adopted value has become the standard way to parametrise the grain size distribution in debris disks. Theoretical work on the emergent steady-state size distribution of an ensemble of colliding bodies led to $p = 3.5$ (Dohnanyi 1969). It could be demonstrated that the operating collisional cascade is self-similar, i. e. scale free, and can be extended to large planetesimal bodies to sub-micron size dust particles (Tanaka et al. 1996). Indeed, spatially-resolved sub-millimetre observations of Fomalhaut seem to be consistent with the canonical value, indicating that the size distribution of particles in these systems is produced by collisional cascades (Wyatt and Dent 2002; Holland et al. 2003). There are, however, physical processes that challenge this simple assumption. First, the frequency of collisions scales with the square of the object number density. Therefore, one expects a variation of the grain size distribution with the radial distance from the star. Furthermore, the lifetime of a particle in a debris disk depends on its size, where small grains are removed faster than larger ones. As a result, the grain size distribution is no longer a unique law (Krivov et al. 2000).

The difficulties connected to even a rough estimation or constraint on the maximum grain radius and the outer disk radius have been mentioned in the previous section. We assumed fiducial values of $a_{\max} = 1000\,\mu\mathrm{m} = 1$ mm and $R_{\mathrm{out}} = 100$ AU, respectively. The contribution of millimetre-sized (or larger) particles to the infrared SED sampled by Spitzer observations is negligible anyhow. Both quantities are poorly constrained in the absence of flux measurements at longer wavelengths. The total mass of the disk in dust grains smaller than 1 mm was adjusted to match the peak of the infrared emission, yielding a value of $M_{\mathrm{dust}} \approx 7.5 \times 10^{-8}\,\mathrm{M}_{\odot}$, corresponding to $0.025\,\mathrm{M}_{\oplus}$ or two times the mass of the Earth moon.

The wavelength at which the dust re-emission begins to depart significantly from the stellar photosphere was used to find the initial values for the inner disk radius R_{in} and the smallest grain radius $a_{\min}$. The computed best-fit values are $R_{\mathrm{in}} = 19 \pm 3$ AU and $a_{\min} = 22 \pm 3\,\mu$m. The corresponding SED model and σ-confidence regions are plotted in Figure 3.7. Some degree of degeneracy can be seen in the latter plot. A smaller inner disk radius can be compensated by larger dust grains, and vice versa. However, R_{in} cannot be smaller than ~ 13 AU because otherwise the dust becomes too hot, and produces excess emission at $\lambda \lesssim 35\,\mu$m.

Our findings suggest that the inner 15–30 AU of disk are relatively free of dust. Dust originating from outside this radius is prevented from entering the inner disk by the gravitational influence of one or more massive planets at or within 15–30 AU (Scholl et al. 1993; Liou and Zook 1999, see also §4.4.3). In addition, there must be only few dust-generating objects, e. g. colliding planetesimals, in the inner region of the disk (Meyer et al. 2004).

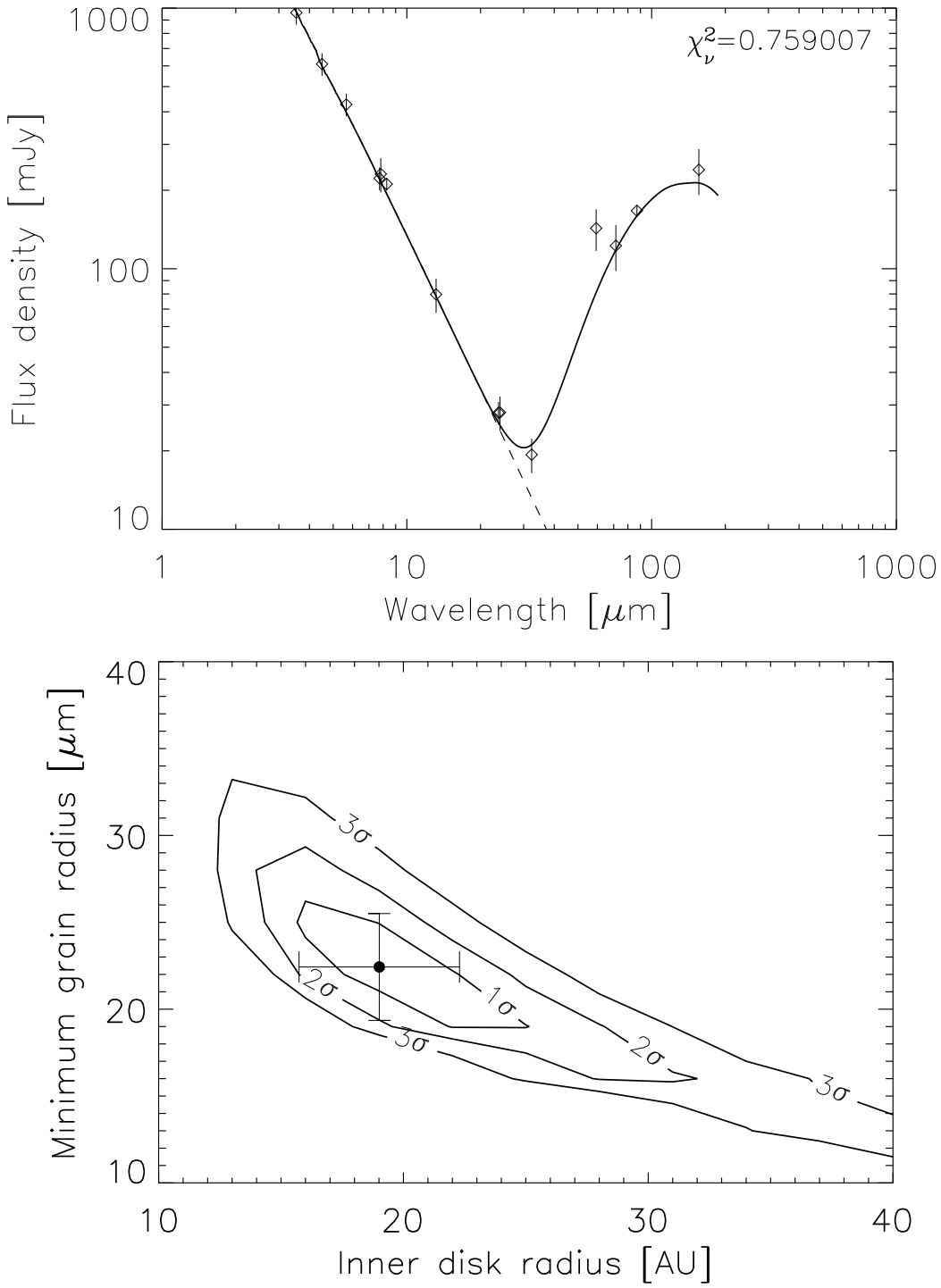

Figure 3.7. Best-fit SED model (top) and confidence contours on parameters (bottom). The best-fit model is consistent with the 350-μm and 1.2-mm upper limits (not shown). The confidence regions are delineated by lines of constant $\Delta\chi^2$.

3.5 HD 12039 – an unusual debris disk system

Hines et al. (2005) reported the discovery of a debris disk containing warm dust associated with HD 12039, a $\sim$ 30-Myr old G3/5 main-sequence star at 42 ± 2 pc. The IRAC and short wavelength IRS data for HD 12039 are consistent with the best-fit model of the stellar emission. Beyond ~ 14 μm the IRS spectrum begins to depart from the photosphere and continues to increase until at least 33 μm. The excess emission was also detected in the MIPS 24-μm band, and the flux value is consistent with the IRS spectrum. The object could not be detected in the two other far-infrared bands at 70 μm and at 160 μm. The excess emission is plotted in Figure 3.8.

Treating the grains as simple blackbody radiators, Hines et al. (2005) could derive important constraints on the dust temperature and its spatial distribution. The absence of significant excess continuum emission for wavelengths $\lesssim 14$ μm and the measured excess at 24 μm together imply a maximum dust temperature of $\sim$ 160 K. The slope between the MIPS 24 μm and IRS 33 μm broadband photometric points corresponds to colour temperatures of $\sim$ 110 K. Finally, the upper limit at 70 μm can be used to compute a lower limit for the dust temperature of $\sim$ 80 K. We see that the thermal emission is confined to a remarkably small temperature range, suggesting that the dust is distributed in a narrow ring located at 4–6 AU from the star (Hines et al. 2005).

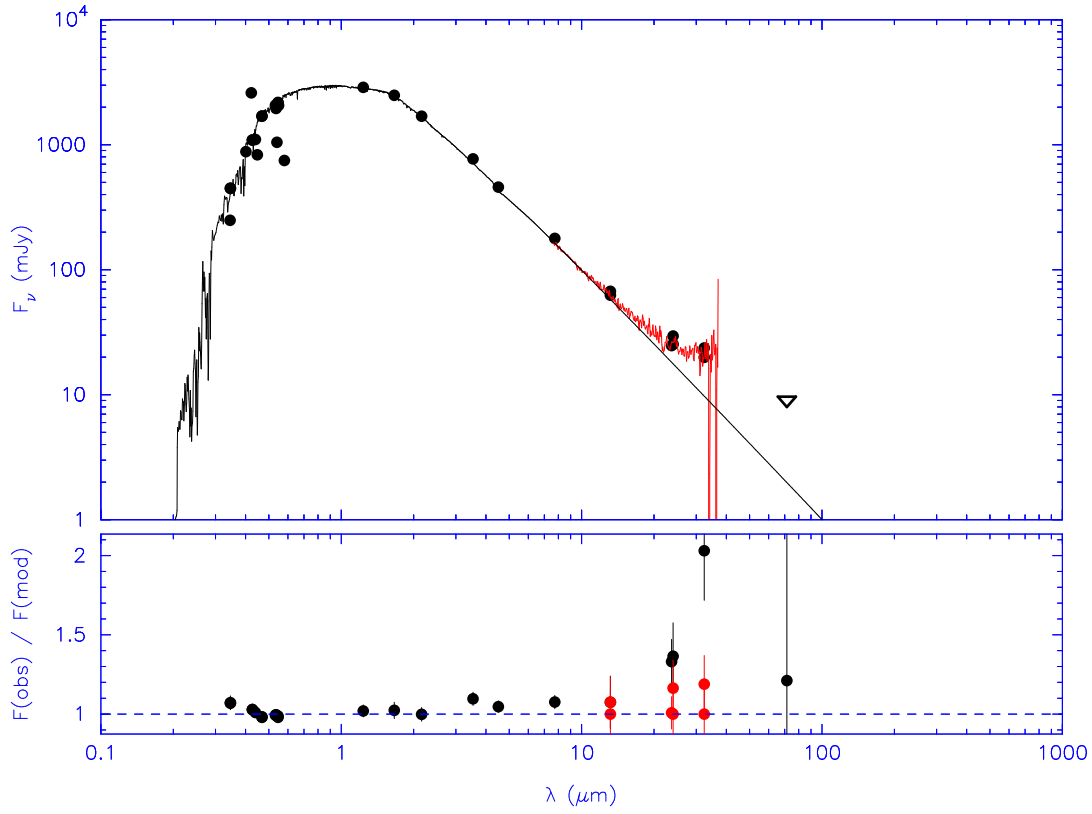

Figure 3.8. Spectral energy distribution of HD 12039, containing photometric measurements and the IRS low-resolution spectrum (red line). The solid curve shows the best-fi t Kurucz model of the stellar photosphere with $T_{\rm eff} = 5688$ K, $\log g = 4.0$, [Fe/H]=0.0, and $A_{\rm V} = 0.0$. The dust re-emission is plotted in the lower frame. The triangle at 70 μm denotes the 3-σ upper limit 6 times the expected photospheric flux.

SED modelling We further investigate the HD 12039 debris system using the dust disk models of Wolf and Hillenbrand (2003), which take into account absorption and emission from dust grains based on their optical properties as opposed to the simple blackbody assumption. Like for HD 105, we use "astronomical silicates", and a disk with constant mass surface density $\Sigma(r) \propto r^0$.

As discussed above, the wavelength at which the dust re-emission departs significantly from the stellar photosphere ($\lambda \sim 14$ μm) yields an initial estimate of the inner radius of the disk. To explain the spectrum of the infrared excess in HD 12039, we calculated the inner and outer disk radii and corresponding total dust mass for a suite of single-size grain models with particle radii $a = 0.1, 0.5, 1, 3, 7, 25, 50$ and 100 μm (Models 1a–h). We applied the Levenberg-Marquardt algorithm to find the models that best fit the observations of HD 12039. The parameters of these models are listed in Table 3.4 and illustrated in Figure 3.9. The best-fit model spectral energy distributions are shown in Figure 3.10.

Table 3.4. Model parameters for the debris system HD 12039

Model	Grain radius a (μm)	Inner disk radius $R_{\rm in}$ (AU)	Outer disk radius $R_{\rm out}$ (AU)	Dust mass $M_{\rm dust}$ (10^{-4} $M_\oplus$)
1a	0.1	40	50	0.26
1b	0.5	27	40	0.1
1c	1	20	31	0.08
1d	3	11	19	0.07
1e	7	4.0	6.0	0.02
1f	25	3.7	6.0	0.1
1g	50	3.8	6.1	0.2
1h	100	3.9	6.0	0.4
2	0.4 – 1000	28	40	4.5

Models assuming small grains require large orbital radii from the star ($R_{\rm in} \approx$ 10–40 AU, $R_{\rm out} \approx$ 20–50 AU), because these small grains have low radiative efficiencies compared with blackbody grains. For grain sizes $a \geq 7$ μm, we find values of $R_{\rm in} \approx 4$ AU and $R_{\rm out} \approx 6$ AU, approximately independent of particle size, consistent with the simple blackbody dust model. Table 3.4 and Figure 3.9 also show that a model assuming $a = 7\mu$m grains (located between 4–6 AU) yields the minimum dust mass. These single-size-grain models illustrate the inherent degeneracies in fitting spectral data alone without independent morphological information such as direct imaging of the systems in thermal emission or scattered light.

Real systems in which the dust is produced by collisions of parent bodies will likely exhibit a distribution of particle sizes. Therefore, we also modelled the infrared excess for HD 12039 using a power-law grain size distribution $n(a) \propto a^{-p}$ that included small grains of radius $a_{\rm min} = 0.4$ μm (just below the blowout size of 0.5 μm, see Hines et al. 2005) and a maximum grain size of $a_{\rm max} = 1000$ μm. Again the power-law exponent was set to $p = 3.5$. For such a distribution, most of the opacity is supplied by the smallest grains and most of the mass is contained in the largest grains. For these assumptions the best-fit inner and outer disk radii are $R_{\rm in} = 28$ AU and $R_{\rm out} = 40$ AU, respectively (Table 3.4). In general, more mass is required by this model than by

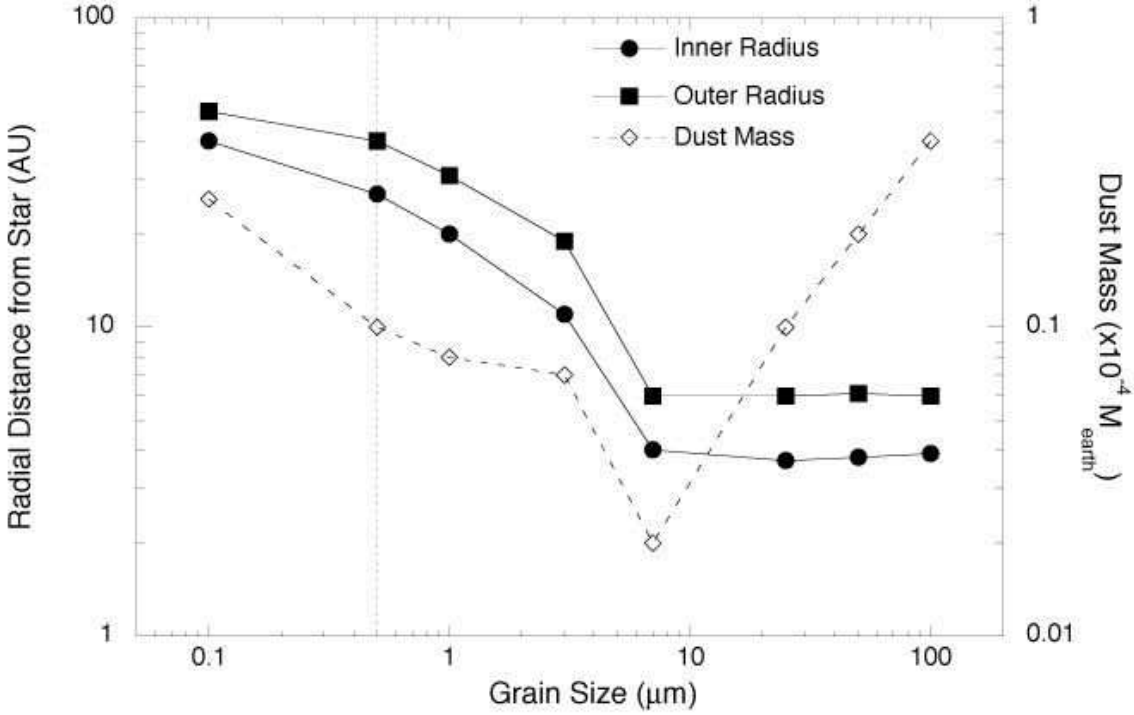

Figure 3.9. Plot of the best-fi t parameters for the single-size grain debris disk models (see Table 3.4). The inner and outer radial distances of the disk from HD 12039 and the associated dust mass for each disk model are plotted as a function of grain size. The vertical dotted line labels the blowout size ($a = 0.5$ μm) for silicate grains. Note that models with grains $a \geq 7\mu$m yield $R_{\rm in} \approx 4$ AU and $R_{\rm out} \approx 6$ AU, independent of particle radius. (Figure from Hines et al. 2005.)

the single-size grain models considered above because of the inclusion of very large grains with small ratios of emitting area to mass. Disk models and the photosphere-subtracted Spitzer data for HD 12039 are shown in Figure 3.11. All of the models require an inner hole radius $R_{\rm in} \gtrsim 4$ AU, but we are unable to choose between the various models from the spectral fitting alone.

Obviously, a range of possible models successfully fit the thermal excess, but two are of particular interest because they represent end points of a plausible range of grain physical characteristics. First, large grains ($a \geq 7$ μm) located between 4 and 6 AU from the star (Models 1e–h). Second, grains with sizes $0.4 \leq a \leq 1000$ μm characterised by a power-law distribution, and located between 28 and 40 AU. Without resolved images of the debris system or more sensitive searches for mineralogical features, we cannot distinguish between these models with confidence. Hines et al. (2005) argued that the surface area of Model 2, dominated by small grains near the blowout limit located at 30–40 AU, would require a large mass of parent bodies (> 100 M$_\oplus$) in collisional equilibrium to maintain the small-grain population against rapid blowout and Poynting-Robertson drift. Alternatively, we may observe a transient dust signature due to recent a collisional event, and observable for only about a few hundred years.

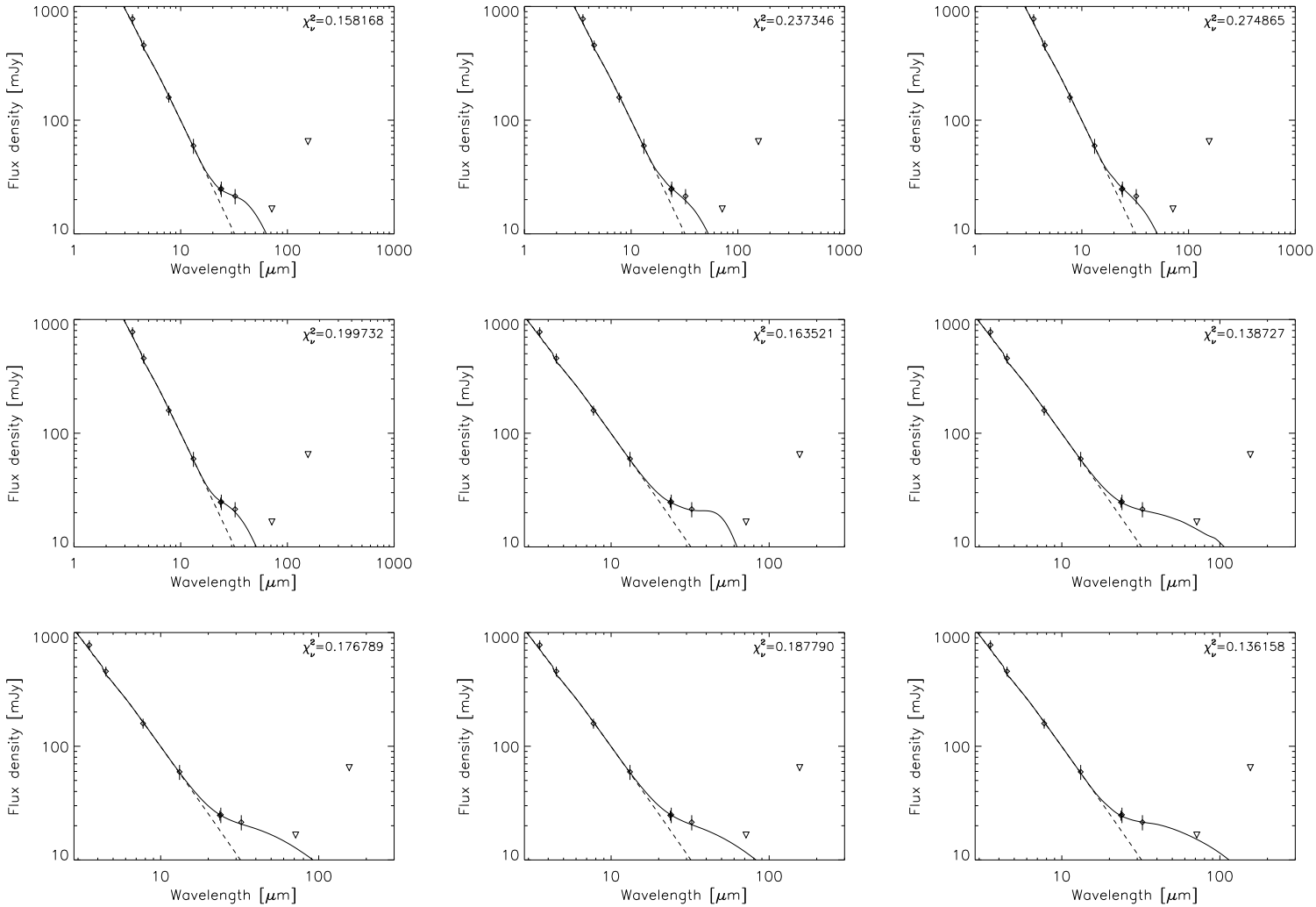

Figure 3.10. The best-fit model spectral energy distributions for particle radii $a = 0.1, 0.5, 1, 3, 7, 25, 50$ and 100 μm (arranged from left to right and top to bottom). The model for a grain size distribution with $0.4 \leq a \leq 1000$ μm is shown in lower right. All models fit the observed infrared excess emission equally well.

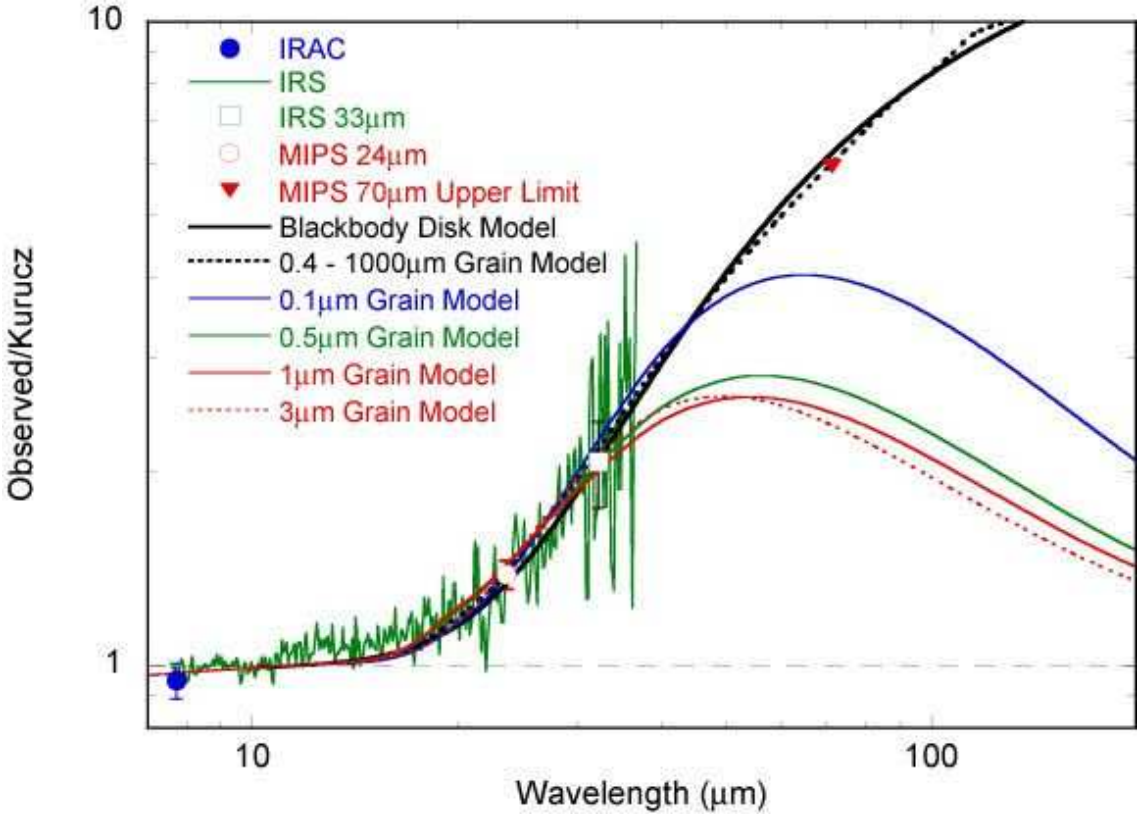

Figure 3.11. The spectrum of HD 12039 compared with the spectral energy distributions of the disk models (Table 3.4). All divided by the best-fi t stellar photosphere model (Kurucz model). Several single-size grain models are depicted as well as a model composed of grains with a power-law distribution of sizes from 0.4–1000 μm. The best fi t blackbody model is also shown for comparison. The single-size grain dust models with particle radii $a \geq 7$ μm are indistinguishable from the simple blackbody model, and are not plotted independently in this fi gure. (Taken from Hines et al. 2005.)

The lack of material much warmer than $\sim$ 110 K in the HD 12039 system could be explained by several mechanisms. First, this temperature is approximately equal to the threshold for the onset of rapid sublimation of micron-sized water ice grains. Thus, if the dust parent bodies are primarily icy, the inner edge of the observed debris distribution could be determined by grain evaporation. Second, the timescale on which grains collide and produce fragments small enough for rapid blowout is an order of magnitude shorter than the Poynting-Robertson timescale at 6 AU, but the timescales are comparable at 30 AU. This suggests that the inner belt model could be self-limited. Dust grains would collide 'in situ' before drifting inward a significant distance from their production location (Wyatt 2005), and the small grains would be blown out by radiation pressure. The existence of a planetesimal belt surrounding HD 12039 might require the presence of a nearby giant planet to stop the planet formation process, as is understood to be the case with Jupiter and the asteroid belt in our solar system. Third, a planet could exist at the inner edge of the debris annulus and consume/scatter inbound grains (e. g. Moro-Martín et al. 2005).

3.6 Far-infrared excess sources

Kim et al. (2005) used the unprecedented sensitivity of the Spitzer Space Telescope to search for cold debris disks around solar-type stars. The main aim being to find systems with characteristic dust temperatures in the range from 30 to 60 K, six stars where selected with 70-μm detections but no significant excess above the stellar photospheres for $\lambda \leq 33$ μm. For stars with luminosities comparable to the Sun, this criterion restricts the equilibrium temperature and inner radii of the debris disks to $T \lesssim 70$ K and $R_{\rm in} \gtrsim 10$ AU. Such debris disks offer the unique opportunity to study Kuiper-Belt analogues around other solar-like stars. In our solar system, the presence of a large reservoir of icy bodies beyond Neptune's orbit has been confirmed by the detection of many of those so-called Kuiper-Belt objects (Jewitt and Luu 1993, 2000). Dust grains released during mutual collisions among Kuiper-Belt objects are expected to account for a significant fraction of the interplanetary dust particles (Liou et al. 1996; Flynn 1996; Yamamoto and Mukai 1998). Furthermore, $\sim 10\%$ of the far-infrared luminosity of the solar system could by emitted by Kuiper-Belt dust.

Table 3.5. Stellar parameters of stars with cold debris disks. HD 13974 is a short period (10 days) binary system with a G0 V primary star (Duquennoy and Mayor 1988) and a companion with spectral type between G9 V and K4 V (Hummel et al. 1995). A two-component Kurucz model was fitted to the observed SED with derived temperatures of 6215 K and 4493 K for the primary and secondary components, respectively. (Table adapted from Kim et al. 2005.)

Source	Distance (pc)	Age (Gyr)	Spectral type	$T_{\rm eff}$ (K)	$L_\star$ ($L_\odot$)
HD 8907	34	1–3	F8 V	6250	2.05
HD 122652	37	1–3	F8 V	6157	1.55
HD 145229	33	0.3–1	G0 V	5893	0.96
HD 6963	27	1–3	K0 V	5517	0.55
HD 13974	11	1–3	G0 V/(G9−K4) V	6215/4493	1.18

SED modelling We modelled the spectral energy distributions of 5 stars that exhibit infrared excess at 70 μm but are consistent with photospheric emission at $\lambda \leq 33$ μm (Table 3.5, Figure 3.12). The fact that the SEDs do not significantly deviate from the photosphere for $\lambda \leq 33$ μm places the maximum temperature for the detected dust grains at $\sim$ 100 K. This suggests a minimum equilibrium distance from the stars $\gtrsim$ 10 AU, assuming the presence of grains a few μm in size or larger. Particles larger than $\sim$ 1 μm and beyond $\sim$ 10 AU are subject to slow Poynting-Robertson inward drift and will be destroyed on timescales of 1–10 Myr (timescale proportional to particle size). This time scale is very short compared to the age of the systems (see Table 3.5), which suggests that the debris in these systems is being replenished by a parent population of objects, a putative Kuiper Belt.

The same modelling approach as for HD 105 and HD 12039 has been used. Again the model disk is assumed to have constant surface density, while the dust particles are considered to be

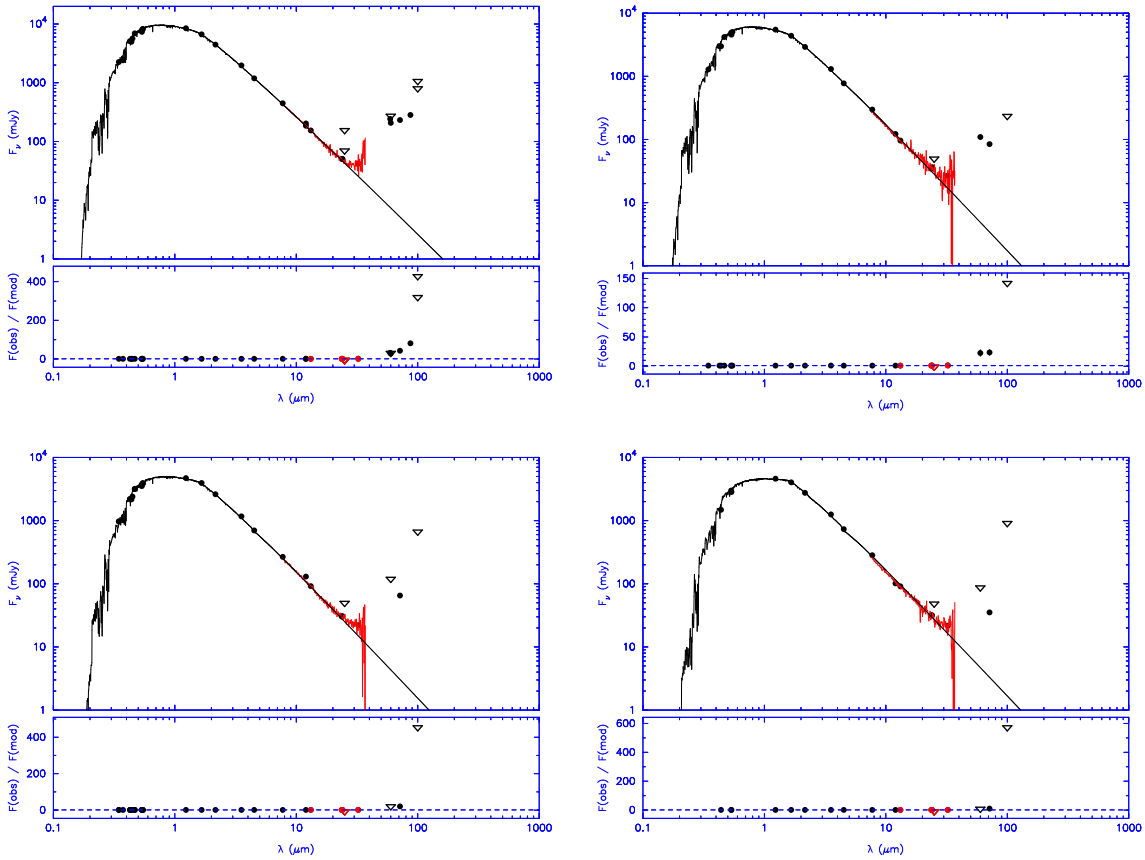

Figure 3.12. Spectral energy distributions of HD 8907 (upper left), HD 122652 (upper right), HD 145229 (lower left), and HD 6963 (lower right). In all cases, the IRS low-resolution spectra (red lines) follow the photospheric emission for $\lambda \leq 33$ μm.

composed of astronomical silicates. The power-law exponent of the grain size distribution has been set to the standard value of $p = 3.5$. For the maximum grain size ($a_{\rm max}$) and $R_{\rm out}$, we assume values of $a_{\rm max} = 1\,$mm and $R_{\rm out} = 100\,$AU. Upper limits, if available, were used to constrain the flux of the disk models in the sub-millimetre and/or millimetre wavelength range. Three parameters are fitted simultaneously by the Levenberg-Marquardt algorithm: $R_{\rm in}$, $a_{\rm min}$, and $M_{\rm dust}$ in grains smaller than 1 mm. The first two parameters influence the shape of the SED and the wavelength at which the disk emission begins to depart from the stellar photosphere; the latter only scales the dust re-emission to match the peak of the infrared emission.

Figure 3.13 shows the best-fit model spectral energy distributions of HD 8907, HD 122652, HD 145229, and HD 6963. The corresponding parameters are listed in Table 3.6. We find minimum dust grain sizes from a few μm to a few ten μm, while the inner disk radii are in the range 10–40 AU. The total mass of dust grains smaller than 1 mm is of the order of 10^{-3}–10^{-2} $M_\oplus$. HD 13974 is one of few cases in the FEPS sample with a 70 μm detection that is consistent with "bare" photospheres. An upper limit on the dust mass has been placed as $M_{\rm dust} \lesssim 1.6 \times 10^{-5}$ $M_\oplus$.

Table 3.6. Circumstellar disk properties from SED model fitting. In the case of HD 13974, $a_{\rm min}$ and $R_{\rm in}$ have been set to fiducial values, the dust mass being the only parameter varied during the fit.

Source	$a_{\rm min}$ (μm)	$R_{\rm in}$ (AU)	$M_{\rm dust}$ (10^{-2}M$_\oplus$)	log ($L_{\rm IR}/L_\star$)
HD 8907	6	43	1.7	-3.64
HD 122652	23	20	1.2	-4.10
HD 145229	5	19	0.4	-3.97
HD 6963	40	9	0.7	-4.17
HD 13974	(0.1)	(1)	$<$0.002	< -5.16

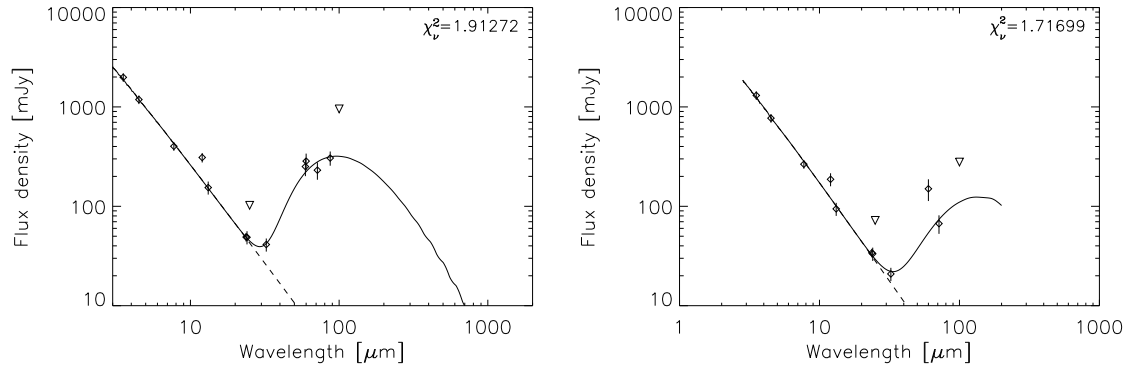

(a) HD 8907

(b) HD 122652

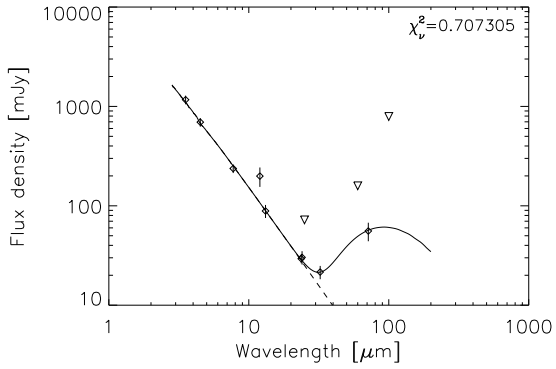

(c) HD 145229

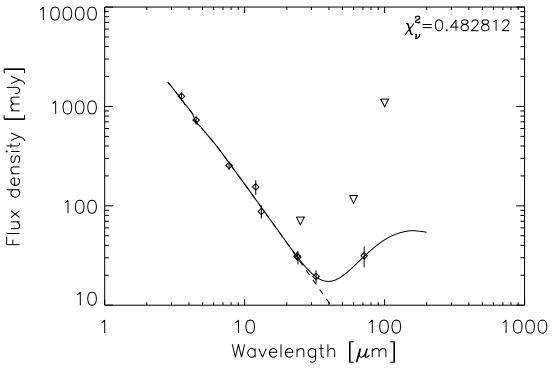

(d) HD 6963

Figure 3.13. Best-fit model SEDs of HD 8907, HD 122652, HD 145229, and HD 6963.

Chapter 4
Dynamical models of debris disks

Die Bewegung ist die Daseinsweise der Materie.
(Motion is the mode of existence of matter.)

FRIEDRICH ENGELS

4.1 Spatially resolved debris disks

The presence of planets has a great impact on the density distribution of dust particles in debris disks. There is a wide range of possible structures: over-dense rings, gaps, spiral structures and arcs, clumps, warped disks (Augereau 2004). Consequently, the observation of such features can serve as an indication for the presence of planetary perturbers. Unfortunately, only about 10 debris disks have been spatially resolved by visual/near-infrared coronagraphy, infrared imaging, or sub-millimetre observations (Table 4.1). Figure 4.1 shows a gallery of spatially resolved debris disk systems around young and evolved main-sequence stars; the figures are arranged with ascending stellar age. Below we introduce most of the debris disk systems.

HD 141569 A is the youngest spatially resolved debris disk and exhibits the highest fractional disk luminosity $f_{\rm disk} = L_{\rm disk}/L_\star$. Previously classified as a Herbig Ae/Be star with a stellar age ≥ 10 Myr (van den Ancker et al. 1998), it is now considered to be a transition object between the pre-main-sequence and main-sequence evolutionary stage. Lagrange et al. (2000) proposed the name "old pre-main-sequence stars" or "young main-sequence stars" for this class of objects. The disk around HD 141569 A displays a multitude of annular features: asymmetric rings at 200 AU and 325 AU (Augereau 2004) as well as a noticeable gap located at approximately 260 AU from the central star with a width of 60 AU (Lagrange et al. 2000). In addition, there are several open, extended spiral arms that might be explained by the secular perturbation of at least one of the two M-type companions located to the north-east (Clampin et al. 2003; Augereau and Papaloizou 2004).

The A0-star HR 4796 A also possesses an M-star companion about 500 AU away from the primary star. The disk appears as a narrow ring around a central gap 55 AU in radius, and it is oriented towards the secondary star (Koerner et al. 1998; Jayawardhana et al. 1998). Near-infrared coronagraphic images taken with the NICMOS instrument on-board the Hubble Space Telescope showed a sharp truncation of the disk's inner and outer edge (Schneider et al. 1999). This fact has been interpreted as indirect evidence for the existence of one or several unseen substellar/planetary companions that confine the dust to a narrow annulus. Takeuchi and Artymowicz (2001) advocated

Table 4.1. Spatially resolved debris disks around main-sequence stars. Adapted from a compilation of Williams et al. (2004).

Star	Spectral type	Age (Myr)	d (pc)	$L_{\rm disk}/L_*$ (10^{-5})	$R_{\rm in}$ (AU)	$R_{\rm out}$ (AU)	i ($^\circ$)	$T_{\rm dust}$ (K)	$M_{\rm dust}$ ($\mathrm{M}_\oplus$)	References
HD 141569 A	B9.5 V	5±3	99	800	200	310	55	60	3.56	o, p, q, r
HR 4796A	A0 V	8±2	67.1	500	50	200	73	110	0.250	a, b, c, d
β Pic	A5 V	$12\pm^{8}_{4}$	19.3	200	20	210	90	85	0.096	e, f, g, h, i
AU Mic	M1 Ve	$12\pm^{8}_{4}$	9.9	60	15	80	90	40	0.01	m, n, s
HD 107146	G2 V	140±60	28.5	120	>31	150		51	0.100	j
Fomalhaut	A3 V	$150\pm^{200}_{100}$	7.7	10	60	160	70	40	0.018	e, f, g
Vega	A0 V	$350\pm^{30}_{80}$	7.8	2	70	90	5	80	0.009	e, f, g, k
ε Eri	K2 V	730±200	3.2	8	30	60	30	35	0.005	f, g, l

References —(a) Jura et al. (1998); (b) Jayawardhana et al. (1998); (c) Greaves et al. (2000); (d) Schneider et al. (1999) (e) Holland et al. (1998); (f) Spangler et al. (2001); (g) Dent et al. (2000); (h) Lagage and Pantin (1994); (i) Pantin et al. (1997); (j) Williams et al. (2004); (k) Wilner et al. (2002); (l) Greaves et al. (1998); (m) Liu et al. (2004); (n) Liu (2004); (o) Augereau et al. (1999); (p) Weinberger et al. (1999); (q) Lagrange et al. (2000); (r) Li and Lunine (2003); (s) Barrado y Navascués et al. (1999); (t) Zuckerman (2001).

an alternative model where the migration and radial segregation of dust particles in a thin gaseous disk leads to the accumulation of small grains in a ring. No gas, however, has been detected around HR 4796 A; the upper-limit gas mass is 7 $\mathrm{M}_\oplus$ (Zuckerman et al. 1995; Greaves et al. 2000).

β Pic was the first star around which a debris disk, initially discovered by the IRAS satellite, could be spatially resolved by ground-based coronagraphy (Smith and Terrile 1984). Until today, the ∼12-Myr old A5 star (e. g. Ortega et al. 2002) remains one of the best studied examples of a debris disk system. High-resolution images of the edge-on disk revealed a number of asymmetries between the opposite wings (Kalas and Jewitt 1995). These features, as well as the central low-density region, are again explained most easily by the gravitational influence of unseen substellar companions (Artymowicz 1997; Heap et al. 2000). The inner disk of β Pic has been found to contain partially crystalline silicate dust whose 10-μm feature resembles closely that of solar system comets (Knacke et al. 1993). The time-variable absorption lines of ionised calcium have been interpreted as indirect evidence for infall of comet-like bodies onto the central star and subsequent evaporation (Beust et al. 1998). An upper limit on the gas mass has been derived by Thebault and Augereau (2005) to be 0.4 $\mathrm{M}_\oplus$. Taking into account the dust mass of $\sim 0.4\ \mathrm{M}_\oplus$ (Zuckerman and Becklin 1993), the gas-to-dust ratio of the β Pic disk is therefore of the order of 1, and might even be well below.

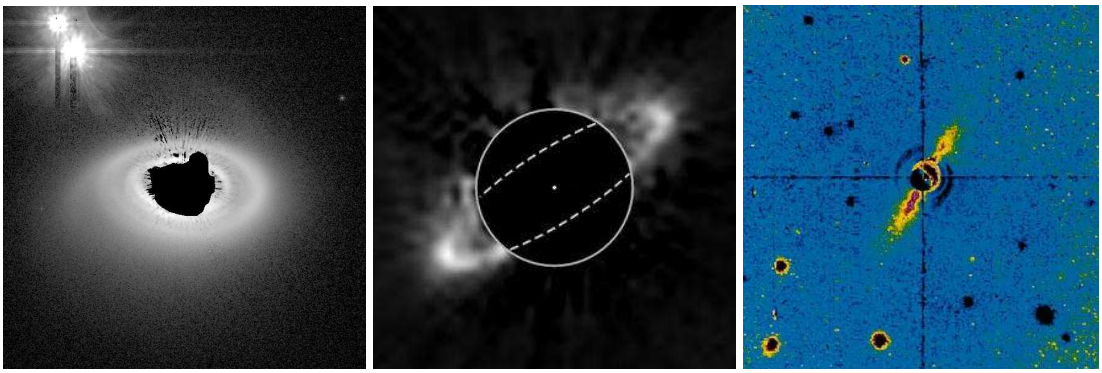

(a) HD 141569 A (b) HR 4796 A (c) β Pic

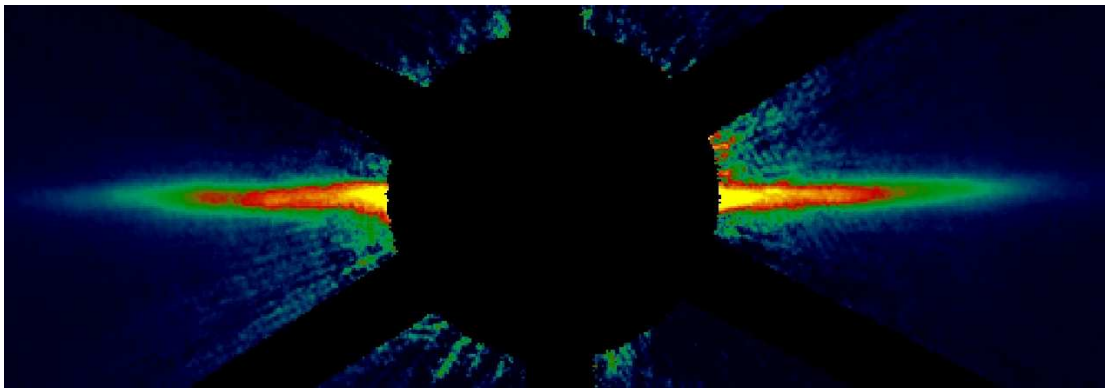

(d) AU Mic

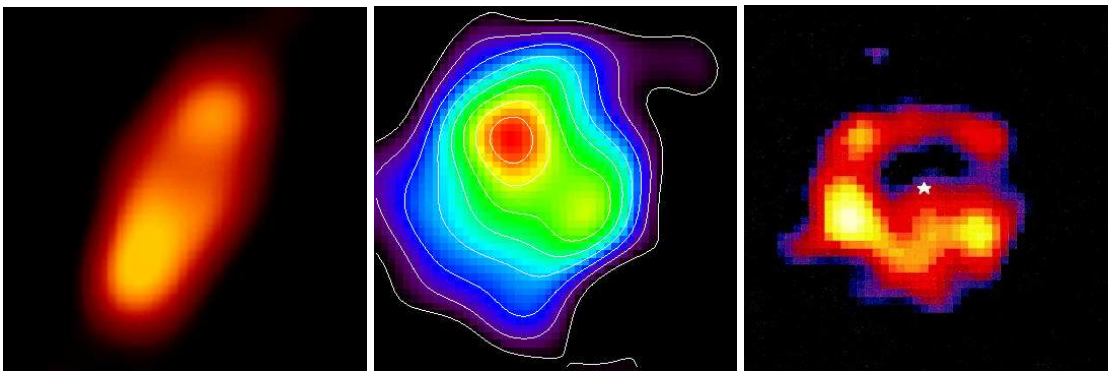

(e) Fomalhaut (f) Vega (g) ε Eri

Figure 4.1. Spatially resolved disks around main-sequence stars. The age of the sources is ascending from left to right, top to bottom. (a) HST/ACS V-band coronagraphic image (Clampin et al. 2003); (b) HST/NICMOS coronagraphic image at 1.1 μm (Schneider et al. 1999); (c) Coronagraphic image at 890 nm, Las Campanas Observatory (Smith and Terrile 1984); (d) Keck II coronagraphic AO observation, H-band (Liu 2004); (e) Spitzer Space Telescope MIPS image at 70 μm (Stapelfeldt et al. 2004); (f) JCMT/SCUBA 850-μm image (Holland et al. 1998); (g) JCMT/SCUBA 850-μm image (Greaves et al. 1998). See Table 4.1 for details.

We now come to stars a few hundred Myr old, shown in the bottom row of Figure 4.1. Fomalhaut (α Piscis Austrini) was resolved at far-infrared wavelengths by the Kuiper Airborne Observatory and the ISO satellite (Harvey et al. 1996; Fajardo-Acosta et al. 1997, respectively). The ISO 60-μm observations showed dust emission from about 200 AU extending to ~ 600 AU. On sub-millimetre 850-μm maps obtained by the SCUBA bolometer array, the disk appears as a highly inclined torus with two emission peaks at ~ 80 AU on either side of the star's position (Holland et al. 1998). So far, no circumstellar gas has been detected around Fomalhaut (Dent et al. 1995; Liseau 1999).

The two remaining debris systems, Vega and ε Eri, have low inclinations, and their disks appear nearly face-on. This fact makes them particularly suitable targets for a detailed modelling of their density distribution with or without planetary perturbers. Prior to the IRAS mission, the A0 star Vega (α Lyrae) used to be the standard star to which essentially all magnitude scales were tied. After that it became the defining prototype of the class of main-sequence stars having far-infrared excess emission due to cold dusty circumstellar disks. SCUBA sub-millimetre maps revealed an asymmetric 850-μm emission distribution (Holland et al. 1998). The possibility of a contamination by a background galaxy has been mentioned and rejected as being unlikely (Zuckerman 2001). Many authors tend to interpret the skewed peaks as the result of gravitational perturbation by an unseen planetary companion (Ozernoy et al. 2000; Wilner et al. 2002; Wyatt 2003; Deller and Maddison 2005).

ε Eri has a distance of only about 3 pc to the Sun. A ring-like density distribution between 35–75 AU around a central cavity has been resolved by sub-millimetre observations (Greaves et al. 1998). The emission appears to be highly non-uniform in azimuth, featuring a number of bright clumps interspersed with regions of lower flux. Again, several authors explained the substructure of the ring by the presence of a hypothetical planet (Ozernoy et al. 2000; Liou et al. 2000; Quillen and Thorndike 2002; Deller and Maddison 2005). Based on SEST 1.2-mm dust continuum observations, this interpretation has been called into question by Schütz et al. (2004), who noted that remnant noise in the sub-millimetre/millimetre maps may create spurious substructures. It is noteworthy that ε Eri does have a confirmed planetary companion, albeit with an orbital distance too small ($a_{\rm pl} = 3.4$ AU, $e_{\rm pl} = 0.6$) to affect the dust ring significantly (Hatzes et al. 2000). Similar to most of the other debris disks, no circumstellar gas could be detected (Dent et al. 1995; Liseau 1999).

The three last-mentioned debris disks, in particular Vega and ε Eri, have been the subjects of detailed numerical simulations aimed at deriving the orbital parameters of undetected planetary perturbers that are likely to be responsible for the observed structural features. In Table 4.2 we compare the modelling attempts of different authors for Vega and ε Eri; a recent model of Fomalhaut is also included for reference. All models roughly agree as far as the semi-major axis of the planet is concerned. The mass of the planet and its eccentricity, however, differ substantially from one model to another. Some general conclusions can nevertheless be drawn. With the exception of the work by Wyatt (2003), the mass of the planet required to reproduce the observed density distribution around Vega is higher than that for the ε Eri models. Furthermore, the dominant mean motion resonances are the low-order commensurabilities 2:1 and 3:2 between the orbital periods of the dust particles and the planet. Higher resonances like 5:3 are less important.

The disagreement among different models of the structure in the debris disks of Vega and ε Eri has two roots: one observational, the other numerical. First, the spatial resolution that can be achieved by infrared satellites and sub-millimetre telescopes is limited. The spatial resolution of the great majority of debris disk models can be, within CPU timing constraints, arbitrarily

Table 4.2. Comparison of different disk-planet models. The model parameters of the perturbing planet are mass, semi-major axis, and eccentricity. The dust grains considered are fully described by the β value (see § 4.2.2). The dominant mean motion resonances are indicated.

Star	$M_{\rm pl}$ ($M_{\rm J}$)	$a_{\rm pl}$ (AU)	$e_{\rm pl}$	β	Dominant MMRs	Reference
Fomalhaut	2	59	0.4	0.05	(1+q):1	(a)
Vega	2	50–60	0	0.3	(1+q):1	(b)
Vega	3	40	0.6	0.01	(1+q):1	(c)
Vega	0.054	60–70	0	0	2:1, 3:2	(d)
Vega	3	73.7	0.1	0.05	2:1, 3:2	(a)
ε Eri	0.2	55–65	0	0.002	2:1, 3:2	(b)
ε Eri	1	40	0.01	0.002–0.05	2:1, 3:2	(e)
ε Eri	0.084	40	0.3	0.1	3:2, 5:3	(f)
ε Eri	0.1	41.6	0.3	0.01, 0.1	3:2, 5:3	(a)

References —(a) Deller and Maddison (2005); (b) Ozernoy et al. (2000); (c) Wilner et al. (2002); (d) Wyatt (2003); (e) Liou et al. (2000); (f) Quillen and Thorndike (2002).

adjusted to study even sparsely populated resonances. The models, therefore, show many finer structures that are unresolved or undetectable with currently available observational technology. In order to compare models with an observed image, the modeller has to produce a synthetic image by convolving the model image with the instrument beam, thereby losing spatial information. The second cause, has to do with the adopted modelling procedure. Due to limited computing resources, the majority of the model fits was drawn from a small set of models, covering only a few particular parameter combinations (see, however, Deller and Maddison 2005). Bona-fide parameter scanning of the, at least, four-dimensional model space (mass of planet, semi-major axis, eccentricity, β value) combined with a simple χ^2 evaluation of the model-data fit would probably reveal large uncertainties as well as degeneracies of the model parameters.

4.2 Forces on dust particles

Dust particles in gas-free debris disk are subject to a wide range of forces. The interplay of the forces determines the spatial and temporal evolution of the dust particle orbit, thereby influencing the shape, size and structural features of a debris disk.

A first distinction can be made between gravitational and non-gravitational forces. The former are caused by the gravitational attraction of the central star, perturbations by planets or other massive bodies, and close encounters with other stars (e. g. in multiple systems or with interloping stars). Capture and trapping of a dust particle in mean motion resonances of the planets is of great consequence for the spatial distribution of dust in debris disks.

Non-gravitational forces result from the interaction with the stellar radiation field (radiation pressure, Poynting-Robertson effect), and the effect of the star's electromagnetic field on charged dust particles (Lorentz force). Furthermore, the corpuscular drag due to fast protons, electrons and heavy ions in stellar winds plays an important role for the dynamics of dust particles, especially during times of elevated stellar activity. Finally, mutual collision of dust particles may lead to partial or total destruction of the grains, thereby altering size distribution and trajectories. The thermal properties and spin of metre-sized objects may affect their long-term orbital evolution (Yarkovsky effect). The recently introduced photophoresis effect (Krauss and Wurm 2005) can be neglected because the gas density is assumed to be too low to affect the particle dynamics.

Owing to their different sources, the magnitude of the forces acting on dust grains varies significantly with particle size. Imagine a compact, spherical dust particle with size s. Gravitational forces are proportional to the mass of the particle, i. e. $F_{\rm G} \propto s^3$. Pressure forces are proportional to the cross-section of the particle, $F_{\rm P} \propto s^2$, whereas the electromagnetic Lorentz force scales with the particle's linear dimension, $F_{\rm L} \propto s$. From these simple arguments, we can already derive some important conclusions. The gravitational forces dominate for large particles, while radiation forces come into play for smaller grains. The Lorentz force is important only for very small particles, and it can govern the motion in this size range. For a quantitative overview of the magnitudes of the various forces, see Table 4.3. In the following sections, the relevant forces are discussed in detail.

Table 4.3. Quantitative comparison of various forces acting on dust grains with different sizes. The calculations were made for a radial distance of 1 AU from the Sun. The subscripts G, R, L, PR, and SW refer to stellar gravity, radiation pressure, Lorentz force, Poynting-Robertson effect, and solar-wind drag, respectively. (Adapted from Gr¨un 1999.)

Size (μm)	$F_{\rm G}$ (N)	$F_{\rm R}$ (N)	$F_{\rm L}$ (N)	$F_{\rm PR}$ (N)	$F_{\rm SW}$ (N)
0.01	9×10^{-23}	1.4×10^{-21}	1.5×10^{-20}	$1{,}4\times10^{-25}$	4×10^{-26}
0.1	9×10^{-20}	1.4×10^{-19}	1.5×10^{-19}	1.4×10^{-23}	4×10^{-24}
1	9×10^{-17}	1.4×10^{-17}	1.5×10^{-18}	1.4×10^{-21}	4×10^{-22}
10	9×10^{-14}	1.4×10^{-15}	1.5×10^{-17}	1.4×10^{-19}	4×10^{-20}
100	9×10^{-11}	1.4×10^{-13}	1.5×10^{-16}	1.4×10^{-17}	4×10^{-18}
1000	9×10^{-8}	1.4×10^{-11}	1.5×10^{-15}	1.4×10^{-15}	4×10^{-16}
	$F_{\rm G}/F_{\rm G}$	$F_{\rm R}/F_{\rm G}$	$F_{\rm L}/F_{\rm G}$	$F_{\rm PR}/F_{\rm G}$	$F_{\rm SW}/F_{\rm G}$
0.01	1	1.6×10^{1}	1.7×10^{2}	1.6×10^{-3}	4.4×10^{-4}
0.1	1	1.6×10^{0}	1.7×10^{0}	1.6×10^{-4}	4.4×10^{-5}
1	1	1.6×10^{-1}	1.7×10^{-2}	1.6×10^{-5}	4.4×10^{-6}
10	1	1.6×10^{-2}	1.7×10^{-4}	1.6×10^{-6}	4.4×10^{-7}
100	1	1.6×10^{-3}	1.7×10^{-6}	1.6×10^{-7}	4.4×10^{-8}
1000	1	1.6×10^{-4}	1.7×10^{-8}	1.6×10^{-8}	4.4×10^{-9}

4.2.1 Gravitational forces

Gravity of the central star The equation of motion of a body moving under the influence of gravitational attraction from a central object is known from Newtonian mechanics.

$$\frac{\mathrm{d}^2\boldsymbol{r}}{\mathrm{d}t^2} = \boldsymbol{a}_\mathrm{G} = -\frac{GM_\star}{r^3}\boldsymbol{r}, \tag{4.1}$$

where G is the gravitational constant, and $M_\star$ is the mass of the central star. The generic solutions of this second-order differential equation are conic sections, with the central star being located in one of the foci. Different families of solutions are distinguished by the eccentricity e. Elliptic orbits are characterised by $0 \leq e < 1$, the circle being a special case with $e = 0$. Particles on elliptic orbits are gravitationally bound to the system. Particles with $e = 1$ or $e > 1$, on the other hand, are not bound to the system and leave it on parabolic or hyperbolic trajectories, respectively. The size of the orbit is defined by the semi-major axis of the conic section a. The orientation of the orbit is fully prescribed by three angles with respect to an arbitrary reference coordinate system.

Gravitational perturbation by planets The presence of additional gravitating bodies, called planets henceforth, in the system causes perturbational forces. For the acceleration due to planets acting on a particle at $\boldsymbol{r}$ we write the vector sum of all perturbations:

$$\boldsymbol{a}_\mathrm{pl} = \sum_{i=1}^{P} \frac{Gm_i}{|\boldsymbol{r}_i - \boldsymbol{r}|^3}\left(\boldsymbol{r}_i - \boldsymbol{r}\right). \tag{4.2}$$

Generally, the problem is non-integrable, and the solutions of the equation of motion display a high complexity in the spatial and temporal domain. The resulting trajectory of the dust particle will no longer be a conic section, often the orbit shows a chaotic behaviour.

Mean motion resonances Resonant effects arise when the orbital period of the dust particle is a simple fraction of the planet's period. Since the orbital period T_orb of an object in the two-body problem is connected to the mean angular velocity n by the relation $n = 2\pi/T_\mathrm{orb}$, this type of resonance is called a mean motion resonance.

Let n' and n be the mean motion of a planet having a semi-major axis a_pl and the mean motion of a dust particle with a, respectively. The condition for a mean motion resonance are met when

$$\frac{T_\mathrm{orb}}{T'_\mathrm{orb}} = \frac{n'}{n} = \frac{p}{p+q}, \tag{4.3}$$

where p and q are integers with $p > 0$ and $p + q \geq 1$ (Murray and Dermott 1999). For $p = 1$ and $q = 1$, the orbital periods of particle T_orb and planet T'_orb are in a ratio of 1:2, and we speak of the particle being in the 1:2 resonance. The particle completes two orbits for every one orbit of the planet. Each object completes a whole number of orbits between successive defined configurations (e. g. conjunction or opposition), and every configuration occurs at the same longitude in a fixed reference frame. For $q = 2$, $q = 3$ and so on, a given planet-particle configuration only occurs every second, third, etc. time at the same location in space. The number $|q|$ is called the order of the mean motion resonance. So far we have only dealt with interior mean motion resonances, where the orbital period of the dust particle is smaller than the period of the planet, i. e. $a < a_\mathrm{pl}$. A well-known example of interior mean motion resonances is the asteroid belt in the solar system.

The distribution of asteroids as a function of semi-major axis shows gaps and concentrations at simple ratios with Jupiter's orbital period (Kirkwood 1867).

Of greater importance for the dynamics of dust particles in debris disks are exterior resonances. Dust particles that are held in an outer resonance with the planet receive orbital energy that can counteract the constant loss of energy due to dissipative forces discussed in §4.2.3 and §4.2.4 (Sicardy et al. 1993; Augereau 2004). An exterior mean motion resonance is characterised by $q < 0$, i. e. the orbital period of the particle is larger than the period of the planet. To take an example, let us consider the case $p = 3$ and $q = -1$. The orbital periods of particle and planet have now a ratio of 3:2, hence the name 3:2 mean motion resonance. This corresponds to the situation found in the solar system Kuiper Belt. About $^1/_3$ of the Kuiper Belt objects have semi-major axes around $a = 39.4$ AU, the exact location of the 3:2 mean motion resonance with Neptune at $a_{\rm pl} = 30$ AU (Jewitt and Luu 2000). Since Pluto is also located within this resonance, the 3:2-resonant Kuiper Belt objects are sometimes called "plutinos" (Jewitt and Luu 2000).

4.2.2 Radiation pressure

A dust particle orbiting the central star intercepts stellar radiation, hence receives the linear momentum the stellar photons carry. The resulting force, called radiation pressure, is proportional to the radiation flux density at the distance of the dust particle from the star $S(r)$, to the particle cross-section A, and depends on the efficiency factor $Q_{\rm pr}$, describing what fraction of the photons' momenta is imparted on the dust grain:

$$\boldsymbol{F}_{\rm R} = \frac{S(r) A Q_{\rm pr}}{c} \frac{\boldsymbol{r}}{r} \ . \tag{4.4}$$

For the time being, the finite orbital velocity of the particle has been neglected. We will come back to this point later when the Poynting-Robertson drag force is addressed (§4.2.3). Expressing $S(r)$ in terms of stellar luminosity $L_\star = 4\pi r^2 S(r)$, we can write

$$\boldsymbol{F}_{\rm R} = \frac{L_\star A Q_{\rm pr}}{4\pi c r^3} \boldsymbol{r}, \tag{4.5}$$

The radiation pressure varies with the inverse square of the distance to the star, similar to Equation 4.1. We can therefore introduce a dimensionless quantity β to describe the magnitude of the radiation pressure force in relation to the gravitational attraction of the central star. Since the dependence on r cancels out, β is independent of the particle's astrocentric distance.

$$\beta = \frac{|\boldsymbol{F}_{\rm R}|}{|\boldsymbol{F}_{\rm G}|} = \frac{L_\star A Q_{pr}}{4\pi c G M_\star m_{\rm grain}} \ , \tag{4.6}$$

where $m_{\rm grain}$ is the mass of the dust grain. With this relation one can rewrite Equation 4.5 as

$$\boldsymbol{F}_{\rm R} = \beta \frac{G M_\star m_{\rm grain}}{r^3} \boldsymbol{r} = -\beta \boldsymbol{F}_{\rm G}. \tag{4.7}$$

The resulting acceleration acting on a dust particle due to gravity and radiation pressure therefore reads as

$$\boldsymbol{a} = \boldsymbol{a}_{\rm G} + \boldsymbol{a}_{\rm R} = \boldsymbol{a}_{\rm G} - \beta \boldsymbol{a}_{\rm G} = -\frac{G M_\star (1-\beta)}{r^3} \boldsymbol{r} \ . \tag{4.8}$$

The net effect of the radiation pressure on a dust particle orbiting a star with mass $M_\star$ is to weaken the gravitational potential by the factor $1-\beta$. It is as though the grain "feels" only an apparent mass $M'_\star = (1-\beta)M_\star$ from the central star. The net force is a central force scaling as the inverse square of the distance. In particular, the solutions of the equation of motion are still conic sections. For $0 \leq \beta < 1$, the net acceleration is attractive and particles may assume elliptic, parabolic, or hyperbolic orbits depending on their initial position and velocity. If $\beta > 1$, however, the potential is repulsive and only hyperbolic orbits are possible. The trajectory of a particle with $\beta > 1$ differs from the ones in an attractive potential, inasmuch the star does not lie within the hyperbola branch.[1]

Influence of radiation pressure on particle orbits We will now investigate the conditions under which a dust particle is ejected from a system by radiation pressure, following the description of Burns et al. (1979). A particle leaves the system on an unbound orbit when its specific orbital energy E/m_{grain} becomes positive (Harwit 1963; Zook 1975),

$$E/m_{\mathrm{grain}} = \frac{v^2}{2} - \frac{GM_\star(1-\beta)}{r} \geq 0. \tag{4.9}$$

Consider a dust particle released from a large parent body, e. g. an asteroid or a comet, for which the effect of radiation pressure can be neglected. Let a and e be the orbital parameters of the parent body. A particle set free at periastron with zero velocity relative to the parent body has $r = a(1-e)$ and $v^2 = GM_\star(1+e)/(1-e)$ (Murray and Dermott 1999). Substituting these expressions into Equation 4.9 we obtain the ejection condition at periastron

$$\beta_{\mathrm{p}} \geq (1-e)/2. \tag{4.10}$$

Similarly, using distance and orbital velocity of the parent body at apoastron, $r = a(1+e)$ and $v^2 = GM_\star(1-e)/(1+e)$ (Murray and Dermott 1999), we find the corresponding ejection condition

$$\beta_{\mathrm{a}} \geq (1+e)/2. \tag{4.11}$$

A general expression for the β threshold, above which a dust particle is ejected from the system, at any point along the orbit of the parent body reads

$$\beta_{\mathrm{eject}} \geq \frac{1}{2}\left(\frac{1-e^2}{1+e\cos\phi}\right), \tag{4.12}$$

where ϕ is the true anomaly of the parent body's orbit. $\phi = 0$ and $\phi = \pi$ correspond to periastron and apoastron, respectively. Equation 4.12 is a monotonically increasing function, i. e. the β limit at perihelion is always smaller than at periastron (Figure 4.2). Figure 4.3 shows the trajectories of dust particles released from a parent body an a circular orbit. Since $e = 0$, all particles with $\beta \geq \frac{1}{2}$ have positive orbital energy and are ejected from the system on unbound orbits.

In the solar system, the stream of escaping, hyperbolic particles is collectively known as β-meteoroids (Zook and Berg 1975). They have been identified by several in-situ dust detectors (e. g. Pioneer 8 and 9, Ulysses, Galileo) through their high velocities, typically $v > 40$ km s^{-1} (Grün et al. 2001).

[1] Similar to the backscattering of α-particles from nuclei in Rutherford's famous experiment.

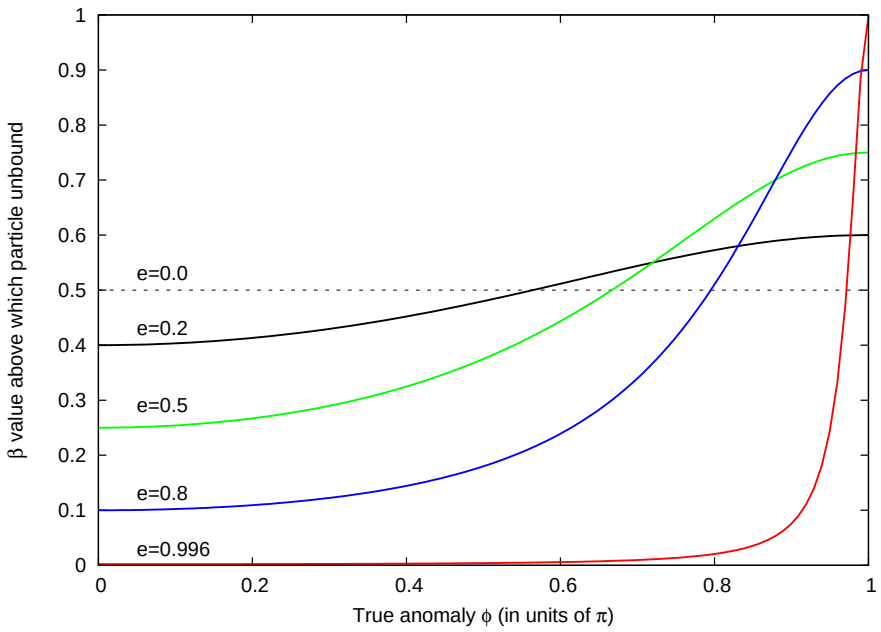

Figure 4.2. Limiting value for β as a function of the true anomaly of the parent body. The influence of the eccentricities is shown from $e = 0$ (circular orbit) to $e = 0.996$, the eccentricity of the comet C/1995 O1 (Hale-Bopp) (Bailey et al. 1996).

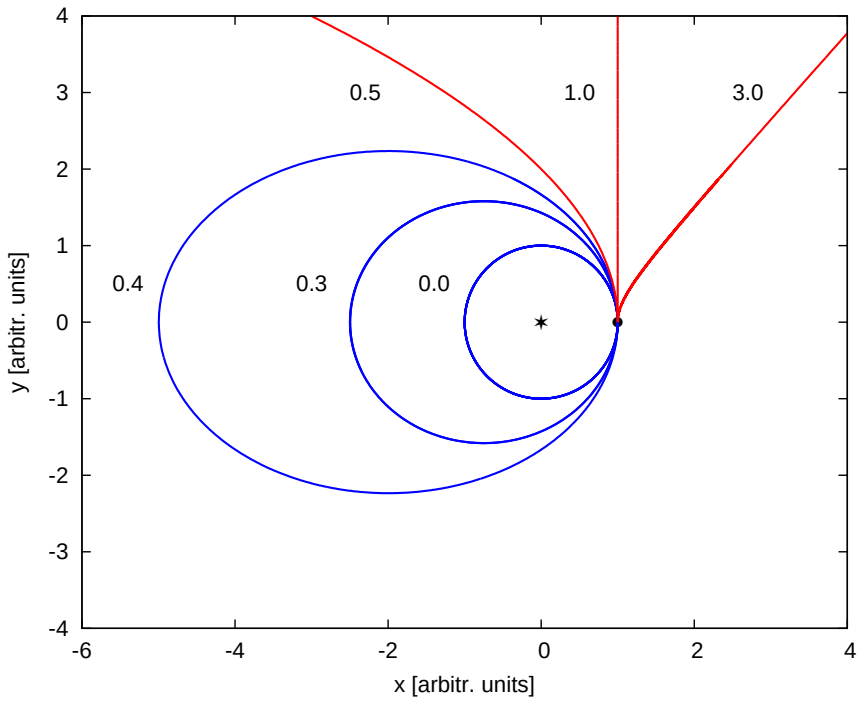

Figure 4.3. Influence of radiation pressure on particle orbits upon release from a parent body on circular orbit. Different β value are indicated. Bound orbits ($\beta < 0.5$) are shown in blue; unbound orbits in red.

β as a dust particle property So far we have used the quantity β to parametrise the effect of the radiation pressure on a dust particle without connecting it to any grain property. After Equation 4.6, β obviously depends on the particle's physical properties, like geometric cross-section and grain mass, the detailed interaction with radiation, and on stellar mass and luminosity.

Considering a compact, spherical grain with diameter s, we can the replace particle cross-section $A = \frac{1}{4}\pi s^2$ and $m_{\rm grain} = \rho V_{\rm grain} = \frac{1}{6}\pi\rho s^3$, and arrive at

$$\beta = \frac{3L_\star Q_{\rm pr}}{8\pi cGM_\star \rho s} = C_\star \frac{Q_{\rm pr}}{\rho s} \ . \tag{4.13}$$

We obtain an expression of the ratio of radiation pressure to gravity that only depends on dust properties and stellar parameters through the quantity $C_\star$. The radiation pressure due to luminous, early-type stars is several orders of magnitude stronger than for a solar-type star (Table 4.4).

Table 4.4. $C_\star$ factors for main-sequence stars in solar units, $C_\odot = 1.15 \times 10^{-3}$ kg m^{-2} (Burns et al. 1979). Stellar masses and luminosities from Binney and Merrifi eld (1998), as published in Schmidt-Kaler (1982).

Spectral type	$M_\star/M_\odot$	$\log\left(L_\star/L_\odot\right)$	$\log\left(C_\star/C_\odot\right)$
O3	120.	6.15	4.07
O5	60.	5.90	4.12
O8	23.	5.23	3.87
B0	17.5	4.72	3.48
B3	7.6	3.28	2.40
B5	5.9	2.92	2.15
B8	3.8	2.26	1.68
A0	2.9	1.73	1.27
A5	2.0	1.15	0.85
F0	1.6	0.81	0.61
F5	1.3	0.51	0.40
G0	1.05	0.18	0.16
G5	0.92	−0.10	−0.06
K0	0.79	−0.38	−0.28
K5	0.67	−0.82	−0.65
M0	0.51	−1.11	−0.82
M5	0.21	−1.96	−1.28
M7	0.12	−2.47	−1.55
M8	0.06	−2.92	−1.70

The radiation pressure efficiency $Q_{\rm pr}$ is a complex quantity connected to the chemical composition, mineralogical structure, and porosity of a dust particle. It is related to the absorption and scattering efficiency of a grain via the relation (Burns et al. 1979; Krügel 2003)

$$Q_{\rm pr} = Q_{\rm abs} + (1 - g)Q_{\rm sca}, \tag{4.14}$$

where g is the scattering asymmetry factor introduced by Henyey and Greenstein (1941). In the

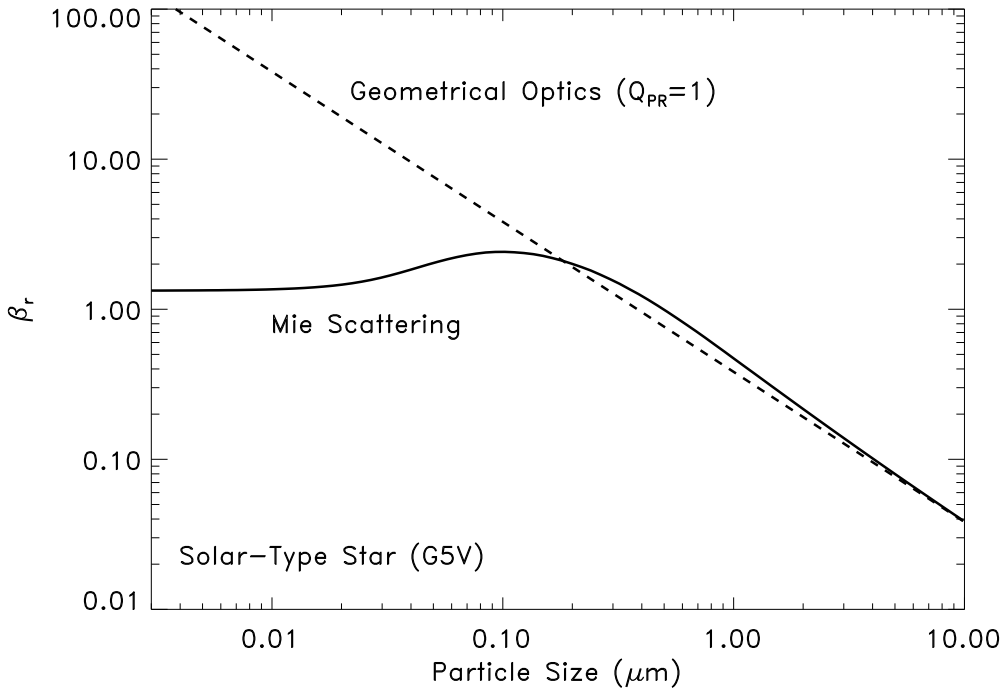

Figure 4.4. β as a function of particle size for a solar-type star and comparison of geometrical optics (dashed line) to a Mie scattering calculation (thick line) for composite interstellar grains (Mathis and Whiffen 1989). Above ~ 1 μm, β is inversely proportional to the particle size s; the two methods do not differ appreciably. For small grains Rayleigh scattering is dominant, and the Mie values level off at constant β. The turnover is at $\lambda_\star^{\max}/2\pi$, where $\lambda_\star^{\max}$ is the peak of the stellar emission. For other stars, it shifts with effective temperature according to Wien's law. (Figure by courtesy of Daniel Potter, University of Arizona.)

case of isotropic scattering $g = 0$, and $Q_{\rm pr} = Q_{\rm abs} + Q_{\rm sca}$. Perfect forward scattering and pure backscattering corresponds to $g = 1$ and $g = -1$, and the efficiency factors for radiation pressure assume the form $Q_{\rm pr} = Q_{\rm abs}$ and $Q_{\rm pr} = Q_{\rm abs} + 2Q_{\rm sca}$, respectively.

Absorption and scattering of radiation are size- and wavelength-dependent processes. Strictly speaking, one has to calculate the corresponding coefficients rigorously from Mie theory or other methods (e. g. Bohren and Huffman 1983). In the limit of geometrical optics, i. e. the particle is much larger than the wavelength of the incident radiation, the calculus simplifies. For large grains the radiation pressure efficiency averaged over the stellar spectrum yields

$$\overline{Q_{\rm pr}} = \frac{\int Q_{\rm pr}(s,\lambda) B_\lambda {\rm d}\lambda}{\int B_\lambda {\rm d}\lambda} \approx 1. \tag{4.15}$$

For a solar-type star, one can safely apply the geometrical-optics approximation for particles $\gtrsim 1$ μm (Figure 4.4). Wyatt et al. (1999) give a useful formula to express β in practical numbers:

$$\beta = 1150 \left(\frac{\rho}{\rm kg\,m^{-3}}\right)^{-1} \left(\frac{s}{\mu{\rm m}}\right)^{-1} \left(\frac{L_\star}{\rm L_\odot}\right) \left(\frac{M_\star}{\rm M_\odot}\right)^{-1}. \tag{4.16}$$

Shift of mean motion resonance As a particle subject to the radiation pressure effectively moves in a reduced gravitational potential, its orbital period reads

$$T_{\mathrm{orb}}^2 = \frac{4\pi^2}{GM'_\star}a^3 = \frac{4\pi^2}{GM_\star(1-\beta)}a^3. \tag{4.17}$$

From Kepler's third law one can determine the semi-major axis a corresponding to a p:$p+q$ resonance

$$a_{\mathrm{mmr}} = (1-\beta)^{1/3}\left(\frac{p}{p+q}\right)^{2/3} a_{\mathrm{pl}}, \tag{4.18}$$

where a_{pl} is the semi-major axis of the planet. Thus the location of a mean motion resonance moves inwards with increasing β, and particles locked in the resonance are "sorted" according to their β values, i. e. their sizes.

4.2.3 Poynting-Robertson effect

In the previous section we discussed the influence of the stellar radiation intercepted by a dust grain on the orbital dynamics of the particle. We saw that the momentum transfer of the incident stellar photons causes a radially-outward directed force. This radiation pressure counteracts gravity and is roughly inversely proportional to the size of the dust grains. Here we will show that the re-radiation of the energy intercepted by a moving grain gives rise to a transverse force that slowly brakes the motion of the particle.

Radiation pressure force on a moving particle The total radiative power received by a stationary, perfectly absorbing particle of geometric cross-section A is $AS(r)$, where $S(r)$ is the flux density of the stellar radiation field at a distance r. Now consider a particle with finite orbital velocity $\boldsymbol{v}$ moving relative to the star. Due to the Doppler effect, the intercepted power changes to

$$S' = S\left(1 - \frac{\dot{r}}{c}\right), \tag{4.19}$$

where $\dot{r} = \boldsymbol{v}\boldsymbol{r}/r$, and c is the speed of light (Burns et al. 1979). The radiation pressure force on a moving particle reads $S'AQ_{\mathrm{pr}}/c \times \boldsymbol{r}/r$ (see Equation 4.4). We used the tacit assumption that the star is a point source of radiation. For particles in the immediate vicinity of the star (only a few stellar radii or closer), the finite size of the radiation source has to be taken into account (Guess 1962).

Poynting-Robertson light drag The radiation energy intercepted by the particle heats up the dust particle and is continuously re-radiated. With the exception of very small grains (some ten Å) and very large bodies, the temperature distribution is nearly isothermal (Krügel 2003), and the re-radiation is isotropic in the rest frame of the particle (Figure 4.5a).

In the stellar frame of reference the particle appears to re-radiate more energy in the forward direction than in the backward direction (Figure 4.5b). As a result, a net force $-(S'AQ_{\mathrm{pr}}/c^2)\boldsymbol{v}$ is acting on the particle in the direction opposite to its instantaneous orbital velocity (Burns et al. 1979). The deceleration is proportional to $\boldsymbol{v}$, similar to the drag force exerted on a body moving through a laminar medium (Stokes flow). The force is called Poynting-Robertson drag force (Poynting 1903; Robertson 1937). The Poynting-Robertson force can also be explained as the

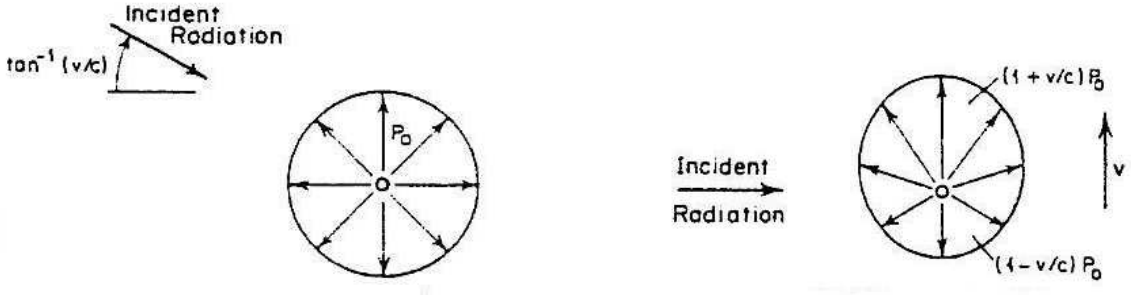

(a) Particle rest frame

(b) Rest frame of star

Figure 4.5. Schematic illustration of the Poynting-Robertson effect in the rest frame of the dust particle (a) and the rest frame of the star (b). Figure from Burns et al. (1979). The length of the arrows depicts the power of the re-radiated energy $P = AS$ in different directions.

transverse component of the radiation pressure force. In the particle's rest frame, there is a small angle $\arctan(v/c)$ between the radiation beam and the radial direction due to the aberration effect (Figure 4.5a). The stellar radiation seems to come from "slightly ahead"; the non-radial component of the imparted momentum slows down the particle.

The net force acting on a particle moving through a radiation field can then be expressed as the sum of radiation pressure force and Poynting-Robertson drag force

$$\begin{aligned}
\boldsymbol{F}_{\mathrm{R}} + \boldsymbol{F}_{\mathrm{PR}} &= \frac{S'(r) A Q_{\mathrm{pr}}}{c} \frac{\boldsymbol{r}}{r} - \frac{S'(r) A Q_{\mathrm{pr}}}{c^2} \boldsymbol{v} \\
&= \frac{S(r) A Q_{\mathrm{pr}}}{c} \left(1 - \frac{\dot{r}}{c}\right) \frac{\boldsymbol{r}}{r} - \frac{S(r) A Q_{\mathrm{pr}}}{c^2} \left(1 - \frac{\dot{r}}{c}\right) \boldsymbol{v} \\
&= \frac{S(r) A Q_{\mathrm{pr}}}{c} \left\{ \left(1 - \frac{\dot{r}}{c}\right) \frac{\boldsymbol{r}}{r} - \frac{\boldsymbol{v}}{c} + \frac{\dot{r}\boldsymbol{v}}{c^2} \right\} \\
&\approx \frac{S(r) A Q_{\mathrm{pr}}}{c} \left\{ \left(1 - \frac{\dot{r}}{c}\right) \frac{\boldsymbol{r}}{r} - \frac{\boldsymbol{v}}{c} \right\}, \qquad (4.20)
\end{aligned}$$

where the term of order $(v/c)^2$ has been dropped (Robertson 1937; Burns et al. 1979; Klačka 1992). Including the gravity of the star (Equation 4.1) and using the definition of β (Equation 4.6), we write the equation of motion of a particle as

$$\begin{aligned}
\boldsymbol{a} &= \boldsymbol{a}_{\mathrm{G}} + \boldsymbol{a}_{\mathrm{R}} + \boldsymbol{a}_{\mathrm{PR}} \\
&= -\frac{G M_\star}{r^3} \boldsymbol{r} + \beta \frac{G M_\star}{r^2} \left\{ \left(1 - \frac{\dot{r}}{c}\right) \frac{\boldsymbol{r}}{r} - \frac{\boldsymbol{v}}{c} \right\} \\
&= -\frac{G M_\star (1 - \beta)}{r^3} \boldsymbol{r} - \frac{\beta}{c} \frac{G M_\star}{r^2} \left(\frac{\dot{r}}{r} \boldsymbol{r} + \boldsymbol{v} \right). \qquad (4.21)
\end{aligned}$$

Secular changes of orbital elements The Poynting-Robertson force continuously removes orbital energy and angular momentum from the particle. As a consequence, the semi-major axis of the particle's orbit shrinks, and the dust grain spirals in towards the star (Figure 4.6). Since the drag is proportional to the particle's velocity, more momentum is lost near periastron than at greater distances to the star. That means that the particle's orbit becomes gradually circularised, i. e. its eccentricity decreases. (see again Figure 4.6). The secular evolution of the orbital elements is given by (Robertson 1937; Wyatt and Whipple 1950)

$$\frac{\mathrm{d}a}{\mathrm{d}t} = -\frac{A}{a}\frac{2+3e^2}{(1-e^2)^{3/2}} \tag{4.22}$$

$$\frac{\mathrm{d}e}{\mathrm{d}t} = -\frac{5A}{2a^2}\frac{e}{(1-e^2)^{1/2}}, \tag{4.23}$$

where $A = 6.24 \times 10^{-4}\ \beta\ (M_\star/\mathrm{M}_\odot)\ \mathrm{AU}^2\ \mathrm{yr}^{-1}$ (Wyatt et al. 1999). The orientation of the particle's orbital plane is not affected, i. e. inclination, longitude of ascending node, and the argument of pericentre remain constant (Grün et al. 2001). After dividing Equation 4.23 by Equation 4.22 and integrating, we obtain an invariant of motion for non-circular orbits:

$$\mathcal{C} = \frac{a(1-e^2)}{e^{4/5}} = \frac{a_0(1-e_0^2)}{e_0^{4/5}}. \tag{4.24}$$

Decay lifetimes For a particle on a circular orbit with $\beta < 1$, Equation 4.22 can be readily solved, and one finds the evolution of the semi-major axis, i. e. the distance to the star for circular orbits, as a function of time. Furthermore, we can determine the time it takes for the grain to spiral in from the distance a_0 to $a < a_0$ as a result of the Poynting-Robertson drag

$$a(t) = \sqrt{a_0^2 - 4A(t-t_0)} \tag{4.25}$$

$$t - t_0 = \frac{a_0^2 - a^2}{4A}. \tag{4.26}$$

Taking $a = 0$, we get the time elapsing until a particle initially at a distance of a_0 will fall into the star and be destroyed by sublimation (Gustafson 1994),

$$t_{\mathrm{PR}} \approx \frac{400}{\beta}\left(\frac{M_\star}{\mathrm{M}_\odot}\right)^{-1}\left(\frac{r_0}{\mathrm{AU}}\right)^2\ \mathrm{yr}. \tag{4.27}$$

Barring close encounters with and resonant trapping by planets as well as collisions between dust grains, t_{PR} gives the characteristic dust lifetime (Figure 4.7).

For $e \neq 0$ there is no analytical solution of the orbital evolution. However, by substituting a from Equation 4.24 in Equation 4.23, one finds a relation containing only eccentricity and time that can be integrated numerically (Wyatt and Whipple 1950),

$$t - t_0 = -\frac{2\mathcal{C}^2}{5A}\int_{e_0}^{e'} \frac{e^{3/5}}{(1-e^2)^{3/2}}\,\mathrm{d}e. \tag{4.28}$$

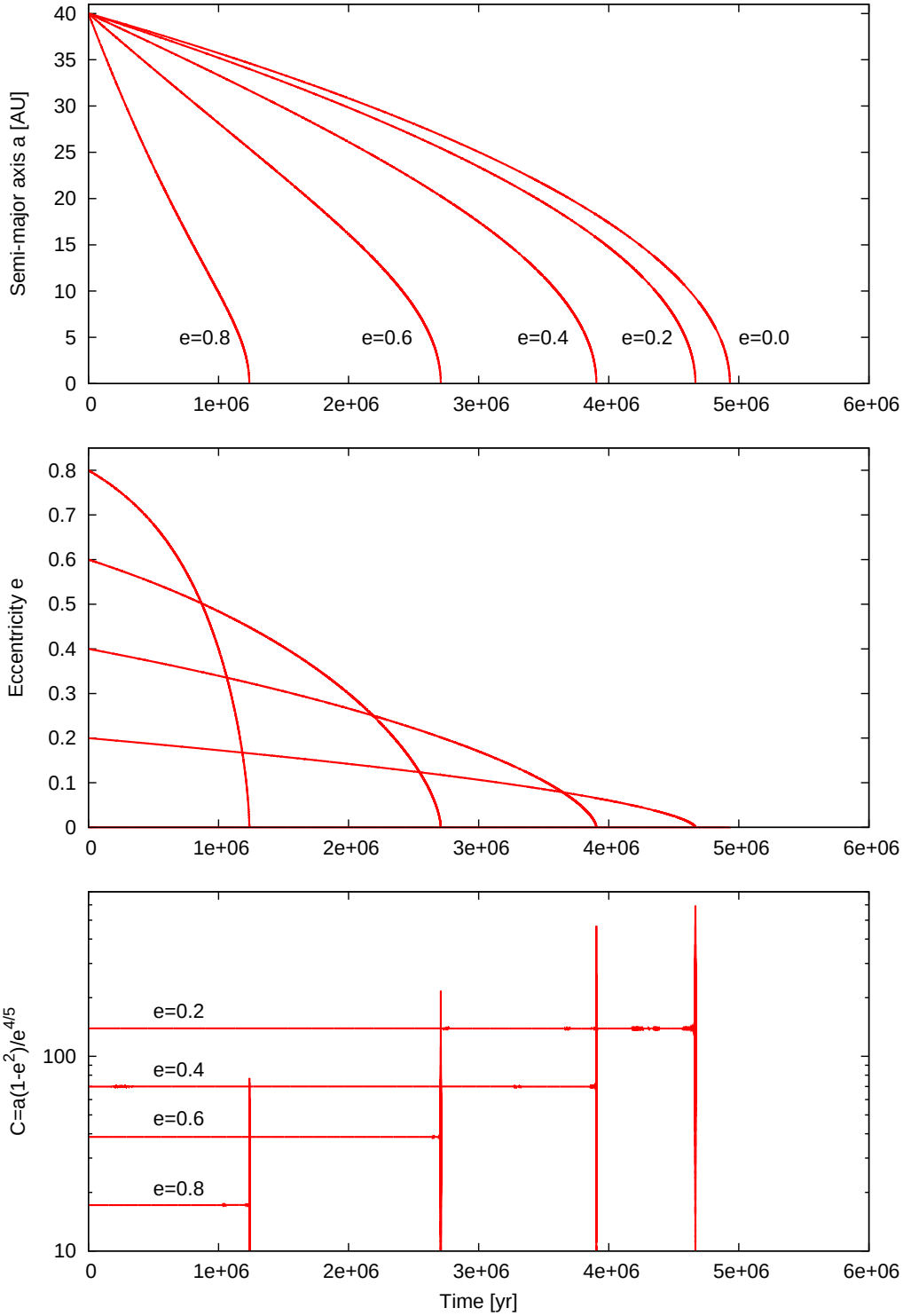

Figure 4.6. Time evolution of the particle's orbital elements as a function of the initial eccentricity. Plotted are the semi-major axis (top), the eccentricity (centre), and the motion invariant $\mathcal{C}$ (bottom) for different values of e_0. For all cases $\beta = 0.1$ and $a_0 = 40$ AU. The mass of the central star is 1 $\mathrm{M}_\odot$; the stellar wind is parametrised with $\xi = 0.3$.

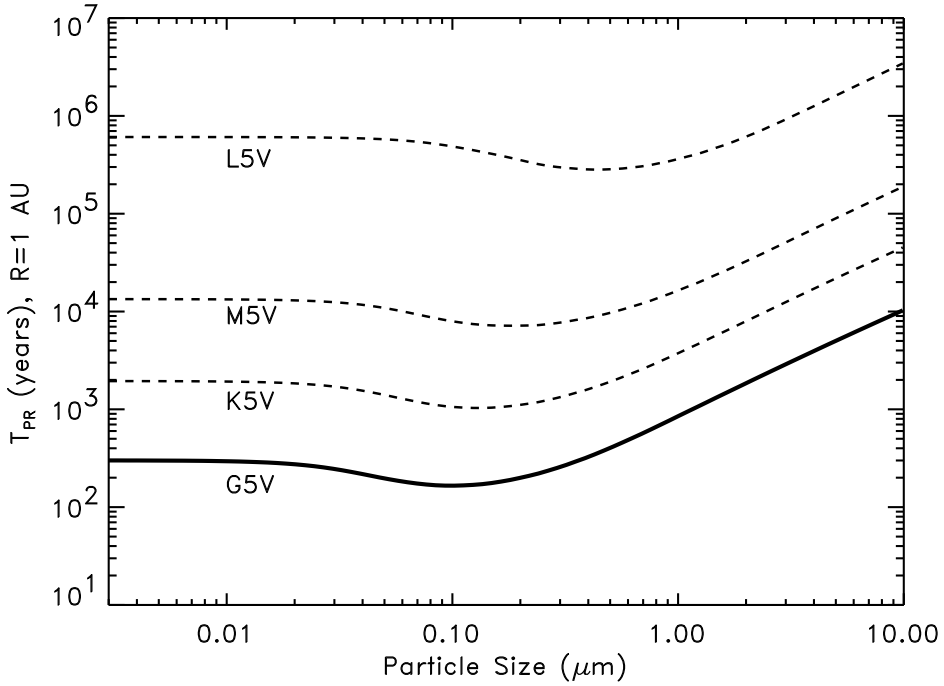

Figure 4.7. Poynting-Robertson lifetime as a function of particle size are shown for different main-sequence stars. The initial radial distance to the star is 1 AU; the decay lifetimes scale with the square of the initial distance. (Figure by courtesy of Daniel Potter, University of Arizona.)

4.2.4 Stellar wind forces

Not only stellar photons influence the orbit of a dust particle. The corpuscular radiation of the stellar wind, launched in the hot corona of stars and composed of protons, electrons, α-particles, and small admixtures of heavier ions, imparts momentum on a dust particle, thereby altering its orbit. Since the physical properties of the solar wind are well established, we use the sun as a proxy for other main-sequence stars.

Stellar-wind pressure force Typical flow speeds of ~ 400 km s^{-1} have been measured for the solar wind (Kallenrode 1998; Balogh et al. 2001). There are moderate fluctuations due to coronal structures and/or solar cycle (Gazis 1996). Owing to its comparatively low speed and small density, the momentum flux density carried by the solar wind is on average only $\sim 3 \times 10^{-4}$ times the amount transported by photons (Burns et al. 1979; Gustafson 1994). Thus, the solar-wind pressure force is several orders of magnitude weaker than the radiation pressure force. Hence, we can neglect the influence of the corpuscular pressure on the particle dynamics.

Stellar-wind drag In contrast, the corpuscular counterpart of the Poynting-Robertson effect caused by the stellar-wind particles is a significant additional drag force (Burns et al. 1979). Assuming typical values, the wind speed is only one to two orders of magnitude larger than the orbital velocity of the dust particle. The aberration angle of the corpuscular radiation seen by the grain is therefore much larger than for photons.

For the ratio of corpuscular drag to Poynting-Robertson drag force $\xi = F_{\rm SW}/F_{\rm PR}$ one finds $c/v_{\rm sw}$ times the ratio of their corresponding momentum flux densities. In the solar system, we have $\xi \approx 0.3$ for grains larger than ~ 0.1 μm (Gustafson 1994; Holmes et al. 2003). For submicron grains the corpuscular drag exceeds the Poynting-Robertson drag, and thus determines the long-term evolution of the particles' orbit (Lamy 1975; Burns et al. 1979; Minato et al. 2004). The drag ratio varies with solar wind speed, being ~ 0.4 during conditions of slow wind ($v_{\rm sw} < 400$ km s^{-1}) and decreasing to ~ 0.2 when the fast wind ($v_{\rm sw} > 600$ km s^{-1}) prevails (Schwenn and Marsch 1990). Additionally, the drag ratio depends on the latitude above the current sheet. At high ecliptic latitudes the solar-wind streams faster, resulting in a weaker corpuscular drag (Kojima and Kakinuma 1990). Since the dust disks we are going to model have typically only moderate vertical scale heights, we will neglect the latitude dependency of the stellar wind drag.

Equation 4.21 can now be augmented with the acceleration term due to stellar-wind drag, yielding (Burns et al. 1979; Liou et al. 1995)

$$\begin{aligned} \boldsymbol{a} &= \boldsymbol{a}_{\rm G} + \boldsymbol{a}_{\rm R} + \boldsymbol{a}_{\rm PR} + \boldsymbol{a}_{\rm SW} \\ &= -\frac{GM_\star(1-\beta)}{r^3}\boldsymbol{r} - \frac{\beta(1+\xi)}{c}\frac{GM_\star}{r^2}\left(\frac{\dot{r}}{r}\boldsymbol{r} + \boldsymbol{v}\right) \\ &= -\frac{GM_\star}{r^3}\left\{(1-\beta)\boldsymbol{r} + \frac{\beta(1+\xi)}{c}\left(\dot{r}\boldsymbol{r} + r\boldsymbol{v}\right)\right\}. \end{aligned} \tag{4.29}$$

The inclusion of the stellar wind drag will reduce the dust particle lifetimes from Equation 4.27, with $t_{\rm PR} \propto (1+\xi)^{-1}$. The timescale for grain removal by the stellar wind drag is proportional to the stellar mass loss rate. For $\dot{M}_{\rm sw}/\dot{M}_\odot \gtrsim 3 \times L_\star/L_\odot$ the corpuscular time scale is smaller than the one due to the Poynting-Robertson effect (Plavchan et al. 2005).

4.2.5 Other non-gravitational forces

There are several physical effects which we have not taken into account for the dynamical modelling of dust disks. The associated forces are often very small and/or have alternating directions, so only secular effects on the orbital evolution are expected to occur. This is the case for the Lorentz force and the Yarkovsky effect. Mutual grain collisions, however, are crucial for the evolution of grains a few 10 μm in size or larger. A detailed modelling of collision-related processes (grain erosion/destruction, velocity and size distribution of fragments) is extremely demanding. For this reason, no self-consistent treatment of grain collisions in debris disk simulations has been performed to date (e. g. Moro-Martín and Malhotra 2002; Deller and Maddison 2005).

Lorentz force Under normal circumstances, dust grains carry a positive charge due to photoemission of electrons (Goertz 1989), and their motion is influenced by electromagnetic forces. Unlike most of the forces discussed in the previous sections, the Lorentz force due to the interplanetary magnetic field acts mainly along the vertical direction (Gustafson 1994). It can thus change the inclination of a particle orbit.

For the solar system, the interplanetary magnetic field has the configuration of an Archimedian spiral (Parker 1958). At larger distances to the star, the $\boldsymbol{B}$-field is mostly toroidal; the dominant azimuthal component B_φ decreases with $1/r$ (Kallenrode 1998). Since the charge on a grain is

proportional to its size s, the ratio of Lorentz force to stellar gravity is

$$\frac{F_\mathrm{L}}{F_\mathrm{G}} \propto \frac{qB}{m_\mathrm{grain}/r^2} \propto \frac{s/r}{s^3/r^2} = r/s^2. \tag{4.30}$$

Thus the Lorentz force is of relevance only for small grains far away from the star. Furthermore, the field polarity changes within one stellar rotation, i. e. on shorter timescales than the characteristic orbital period of the dust particle (Grün et al. 2001). The successive upward and downward acceleration may cancel out, and the net effect of the Lorentz force is very small.

Collisions Collisions are a major complication of the grain dynamics, especially for large grains, whose Poynting-Robertson lifetimes are long and that have ample time to hit another dust particle. Gustafson (1994) gives an instructive order-of-magnitude estimation for the ratio of the collision and Poynting-Robertson timescales, denoted by t_coll and t_PR, respectively. Let $N(>m)$ be the number of grains with masses above m. Typically, there will be many more smaller grains than larger ones, e. g. $N(>m) \propto m^{1-q}$, equivalent to $N(>s) \propto s^{3-3q}$, with $q > 1$. For a destructive collision to occur, the mass of the impactor has to be above a minimum value proportional to the mass of the target (Fujiwara et al. 1989). Hence, the average time between catastrophic collisions is proportional to $N(>s)$. From Equation 4.27 we know that the Poynting-Robertson timescale is proportional to β^{-1}, i. e. $t_\mathrm{PR} \propto s$. The ratio of the two timescales now yields $t_\mathrm{coll}/t_\mathrm{PR} \propto s^{2-3q}$. The steady-state size distribution resulting from a collisional cascade has been found analytically as $N(>s) \propto s^{-5/2}$, corresponding to $q = 11/6$ (Dohnanyi 1969; Williams and Wetherill 1994). Using this value, one arrives at $t_\mathrm{coll}/t_\mathrm{PR} \propto s^{-7/2}$.

We immediately see that collisions play a paramount role for large particles, whereas the fast orbital decay of small particles prevents them from collision and destruction. For the solar system, critical grain sizes above which collisions dominate the long-term evolution are reported between $\gtrsim$ 10–80 μm (Dohnanyi 1978; Leinert et al. 1983; Grün et al. 1985).

Yarkovsky effect The diurnal warming and cooling of rotating bodies leads to a non-isotropic thermal re-emission. Since the object's ability to redistribute the absorbed stellar radiation is limited (thermal inertia), the "afternoon" hemisphere of the object will be warmer than the "morning" hemisphere (Burns et al. 1979). Consequently, the thermal emission from the warmer side is larger (Figure 4.8). The resulting reaction force may speed up or slow down the orbital motion of metre-sized objects, depending on the object's spin axis (Öpik 1951; Grün et al. 2001).

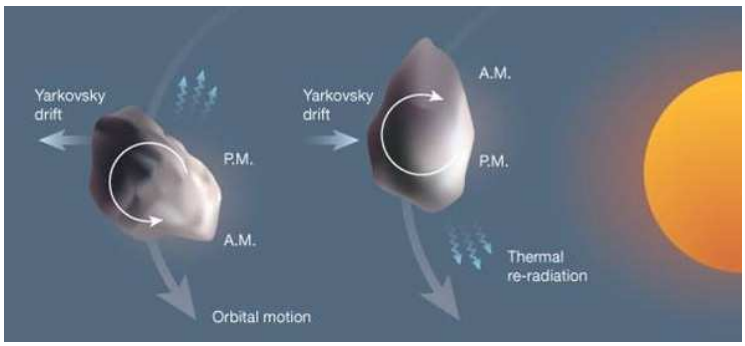

Figure 4.8. Illustration of the Yarkovsky effect. The recoil force results in an outward drift for objects in prograde rotation (left); retrograde rotation leads to an inward push (right). (Figure from Binzel 2003.)

4.3 Numerical method

The simulation of the dynamical evolution of a dust particle under the influence of stellar gravity, planetary perturbations, radiation and stellar-wind forces for, typically, 10^4 to 10^6 orbits requires an accurate numerical integration of the particles' equations of motion. Assuming no mutual interaction between the grains, i. e. no gravitational attraction and no collisions, one can treat the set of dust grains as mass-less test particles independently from one another. Methodologically, the system to be integrated can be described as as a few-body system with a large number of test particles. For this purpose the Fortran program `MODUST` has been developed.[2] The model components are:

- A central star, specified by its mass $M_\star$ and its bolometric luminosity $L_\star$. While $M_\star$ determines the depth of the gravitational potential, $L_\star$ is needed to convert β into a grain size s. The star is located at the centre of the coordinate system.
- P planets that move on Keplerian orbits around the central star. By virtue of their gravitational attraction, they perturb each other's motions and the orbits of the dust particles. Typically, only a few planets are modelled, and P is a small number. Radiation pressure, Poynting-Robertson effect, and stellar-wind drag do not influence the planetary orbits.
- N dust grains subject to the gravitational attraction of the star and the P planets. Furthermore, the motion of dust particles is affected by radiation forces, and corpuscular stellar-wind drag. In order to resolve potential density structures, N is chosen to be a large number, e. g. 10^3 or 10^4.

4.3.1 Hermite integration scheme

The Hermite scheme is a predictor-corrector method to solve the N-body problem. Originally described by Makino (1991), this integration method has found widespread application for the numerical simulation of the dynamical evolution of gravitational many-body systems.

For a particle i (with $i = 1, \ldots, P+N$) the momentary acceleration $\boldsymbol{a}_{0,i}$ and the first derivative thereof with respect to time $\dot{\boldsymbol{a}}_{0,i}$ are used to compute the future position $\boldsymbol{r}_i(t)$ and velocity $\boldsymbol{v}_i(t)$ at a desired time t from the corresponding instantaneous values $\boldsymbol{r}_{0,i}$ and $\boldsymbol{v}_{0,i}$ at time $t_0 < t$. In the first step, new position and velocity vectors are *predicted* for the next time step t by expanding $\boldsymbol{r}_0$ and $\boldsymbol{v}_0$ into Taylor series. For the sake of simplicity, we will drop the index i hereafter, bearing in mind that the below-mentioned prescriptions always deal with a certain particle. Furthermore, the positive time difference $t - t_0$ is written as Δt.

$$\boldsymbol{r}_\mathrm{p}(t) = \sum_{n=0}^{3} \frac{1}{n!} \frac{\mathrm{d}^n \boldsymbol{r}(t_0)}{\mathrm{d}t^n} (t - t_0)^n = \boldsymbol{r}_0 + \boldsymbol{v}_0 \Delta t + \frac{1}{2} \boldsymbol{a}_0 \Delta t^2 + \frac{1}{6} \dot{\boldsymbol{a}}_0 \Delta t^3 \tag{4.31}$$

$$\boldsymbol{v}_\mathrm{p}(t) = \sum_{n=0}^{2} \frac{1}{n!} \frac{\mathrm{d}^n \boldsymbol{v}(t_0)}{\mathrm{d}t^n} (t - t_0)^n = \boldsymbol{v}_0 + \boldsymbol{a}_0 \Delta t + \frac{1}{2} \dot{\boldsymbol{a}}_0 \Delta t^2 \tag{4.32}$$

Even if a small value of the time step Δt is chosen, this procedure generates an appreciable computational error that propagates with integration time. Higher-order derivatives of the acceleration

[2] **MO**delling of **DU**sty **ST**ars

have to be considered to improve the accuracy of the force polynomial. Making a Taylor series ansatz, one writes

$$\boldsymbol{a}(t) = \boldsymbol{a}_0 + \dot{\boldsymbol{a}}_0\Delta t + \frac{1}{2}\boldsymbol{a}_0^{(2)}\Delta t^2 + \frac{1}{6}\boldsymbol{a}_0^{(3)}\Delta t^3 \tag{4.33}$$

$$\dot{\boldsymbol{a}}(t) = \dot{\boldsymbol{a}}_0 + \boldsymbol{a}_0^{(2)}\Delta t + \frac{1}{2}\boldsymbol{a}_0^{(3)}\Delta t^2 \ , \tag{4.34}$$

where $\boldsymbol{a}_0^{(n)}$ denotes the n-th derivative of $\boldsymbol{a}$ with respect to time evaluated at $t = t_0$. The quantities $\boldsymbol{a}_0$, $\dot{\boldsymbol{a}}_0$ are already known, while $\boldsymbol{a}(t)$ and $\dot{\boldsymbol{a}}(t)$ are evaluated using the predicted values for the particle's position $\boldsymbol{r}_\mathrm{p}$ and velocity $\boldsymbol{v}_\mathrm{p}$. We therefore designate the left-hand sides of Equations 4.33 and 4.34 with $\boldsymbol{a}_\mathrm{p}$ and $\dot{\boldsymbol{a}}_\mathrm{p}$, respectively. Solving the latter equation for $\boldsymbol{a}_0^{(2)}$ and substituting it in Equation 4.33, we obtain (Makino and Aarseth 1992)

$$\boldsymbol{a}_0^{(3)} = 12\frac{\boldsymbol{a}_0 - \boldsymbol{a}_\mathrm{p}}{\Delta t^3} + 6\frac{\dot{\boldsymbol{a}}_0 + \dot{\boldsymbol{a}}_\mathrm{p}}{\Delta t^2}; \tag{4.35}$$

re-inserting this expression in Equation 4.33 yields

$$\boldsymbol{a}_0^{(2)} = -6\frac{\boldsymbol{a}_0 - \boldsymbol{a}_\mathrm{p}}{\Delta t^2} - 2\frac{2\dot{\boldsymbol{a}}_0 + \dot{\boldsymbol{a}}_\mathrm{p}}{\Delta t}. \tag{4.36}$$

That means the higher-order derivatives of the acceleration can be explicitly calculated in terms of $\boldsymbol{a}_\mathrm{p}$ and $\dot{\boldsymbol{a}}_\mathrm{p}$ by means of Hermite interpolation.[3]

The predicted position and velocity of particle i can now be refined by expanding Equations 4.31 and 4.32 up to fourth order.

$$\begin{aligned}
\boldsymbol{r}_\mathrm{c}(t) &= \boldsymbol{r}_\mathrm{p}(t) + \frac{1}{24}\boldsymbol{r}_0^{(4)}\Delta t^4 \\
&= \boldsymbol{r}_\mathrm{p}(t) + \frac{1}{24}\boldsymbol{a}_0^{(2)}\Delta t^4 \\
&= \boldsymbol{r}_\mathrm{p}(t) - \frac{1}{4}(\boldsymbol{a}_0 - \boldsymbol{a}_\mathrm{p})\Delta t^2 - \frac{1}{12}(2\dot{\boldsymbol{a}}_0 + \dot{\boldsymbol{a}}_\mathrm{p})\Delta t^3
\end{aligned} \tag{4.37}$$

$$\begin{aligned}
\boldsymbol{v}_\mathrm{c}(t) &= \boldsymbol{v}_\mathrm{p}(t) + \frac{1}{6}\boldsymbol{v}_0^{(3)}\Delta t^3 + \frac{1}{24}\boldsymbol{v}_0^{(4)}\Delta t^4 \\
&= \boldsymbol{v}_\mathrm{p}(t) + \frac{1}{6}\boldsymbol{a}_0^{(2)}\Delta t^3 + \frac{1}{24}\boldsymbol{a}_0^{(3)}\Delta t^4 \\
&= \boldsymbol{v}_\mathrm{p}(t) - \frac{1}{2}(\boldsymbol{a}_0 - \boldsymbol{a}_\mathrm{p})\Delta t - \frac{1}{12}(5\dot{\boldsymbol{a}}_0 + \dot{\boldsymbol{a}}_\mathrm{p})\Delta t^2,
\end{aligned} \tag{4.38}$$

where $\boldsymbol{a}_0^{(2)}$ and $\boldsymbol{a}_0^{(3)}$ have been substituted with the composite expressions derived previously. The remainder of the Taylor series is proportional to $\mathcal{O}(\Delta t^5)$. Taking the time derivative, we see that

[3]The name *Hermite* interpolation, as opposed to *Lagrange* interpolation, derives from the fact that both the functional value $\boldsymbol{a}$ and its derivative $\dot{\boldsymbol{a}}$ are given.

the error in the force calculation is of $\mathcal{O}(\Delta t^4)$. After re-grouping, the corrector reads:

$$\boldsymbol{v}_{\rm c}(t) = \boldsymbol{v}_0 + \frac{1}{2}(\boldsymbol{a}_0 + \boldsymbol{a}_{\rm p})\Delta t + \frac{1}{12}(\dot{\boldsymbol{a}}_0 - \dot{\boldsymbol{a}}_{\rm p})\Delta t^2 \tag{4.39}$$

$$\boldsymbol{r}_{\rm c}(t) = \boldsymbol{r}_0 + \frac{1}{2}(\boldsymbol{v}_{\rm c} + \boldsymbol{v}_0)\Delta t + \frac{1}{12}(\boldsymbol{a}_0 - \boldsymbol{a}_{\rm p})\Delta t^2. \tag{4.40}$$

The sequence of, first, evaluation of the acceleration and its first derivative and, second, correction of the position and velocity can be iterated to increase the accuracy of the orbit integration (§4.3.3).

4.3.2 Selection of time steps

As we have seen in the previous section, the choice of the time step size Δt_i between two Hermite scheme calculations of the particle i eventually determines the error of the integration. Using the aforementioned corrector, the accuracy of the method scales as Δt^4. The CPU time spent on the integration is proportional to the number of time steps in a given time interval, i. e. $\propto 1/\Delta t$. Therefore, an accurate long-term integration of the orbits of many particles in a reasonable computing time poses a dilemma. We may increase the accuracy of the integration only at the expense of lengthy CPU time, and vice versa. An intelligent selection of the time step is mandatory to ensure that a particle's motion is integrated as often as necessary and as rarely as possible to trade off between accuracy and speed.

The debris disk system to be modelled consists of a few planets and a great number of dust particles. The system is characterised by a wide range of distances to the central star and, accordingly, different orbital time scales. The spatial domain covers 4 to 5 orders of magnitude, from the sublimation region (~ 0.01 AU) to the outer edge of the disk and beyond (100 to 1000 AU). The corresponding orbital time scales ($T_{\rm orb} \propto R^{3/2}$) span ~ 7 orders of magnitude. Advancing all particles with a common time step is clearly an ill advice, which would result in either a too-coarse treatment of particles near the centre, or the needless waste of computing time in the outer parts of the system. The implementation of an individual time step selection seems advisable (Makino and Hut 1988).

The modeller has some freedom to choose how to calculate the size of the time step from the quantities that describe the particle's motion. As a first possibility, one could couple the time step to the orbital time scale via the relation $\Delta t_i = \eta T_{{\rm orb},i} = \eta R_i^{3/2}$, where η is a dimensionless control parameter that determines the number of force calculations per orbit. Similarly, one may relate the time step to the rate of change of the acceleration, $\Delta t_i \propto |\boldsymbol{a}_i/\dot{\boldsymbol{a}}_i|$. A prescription commonly adopted for N-body simulations has been given by by Aarseth (2003). It uses the acceleration and the first, second, and third time derivatives thereof to compute the time step by which the integration should be advanced in time:

$$\Delta t_i = \sqrt{\eta \, \frac{|\boldsymbol{a}_i| \left|\boldsymbol{a}_i^{(2)}\right| + |\dot{\boldsymbol{a}}_i|^2}{|\dot{\boldsymbol{a}}_i| \left|\boldsymbol{a}_i^{(3)}\right| + \left|\boldsymbol{a}_i^{(2)}\right|^2}} \, . \tag{4.41}$$

The formula has no direct physical interpretation, but it resembles the square of the curvature radius of the curve $\boldsymbol{a}(t)$ (Spurzem 1999).

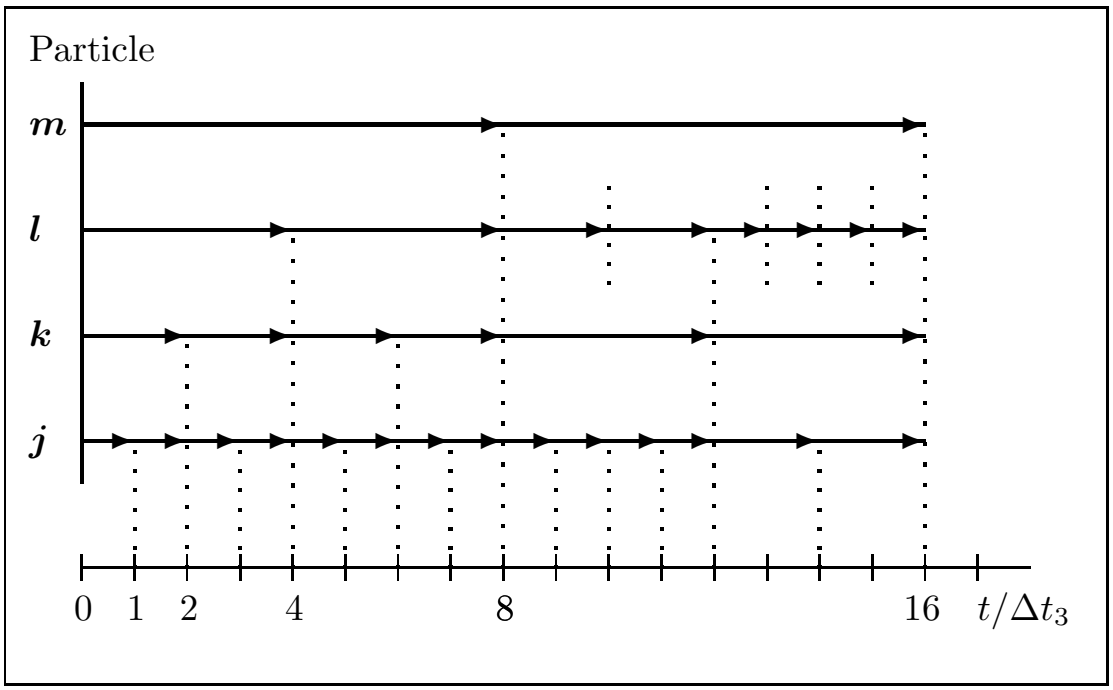

Figure 4.9. Illustration of the block time step scheme with four time-step levels and for four exemplary particles j, k, l, and m. Initially, particle j has the smallest time step, whereas particles k, l, and m need to be integrated only every second, fourth, and eighth step, respectively. The time step size may be adjusted after each integration, as illustrated for particles k and l at $t = 8$. Note that an increase by a factor of 2 is only allowed if $2\Delta t_i$ divides t_i without rest. For example, the time step for particle k may be increased to $\Delta t = 4$ at $t = 8$, but not already at $t = 6$. Figure by courtesy of Emil Khalisi.

To avoid the continuous distribution of particles along the time axis and to reduce some of the prediction overhead, the simulation time t and the time steps Δt_i can be "quantised" (McMillan 1986). Makino (1991) proposed a hierarchical order of time steps using successive powers of 2, $\Delta t_k = 2^{-k}$. The integer $k = 0, \ldots, k_{\max}$ describes the level depth, with $k = 0$ for the largest time step and $k = k_{\max}$ for the smallest one. We chose $k_{\max} = 31$, i. e. the range of possible time steps span ~ 10 orders of magnitude. Using discrete time steps, the basic mode of operation during the integration works as follows. For all particles a preliminary value of the time step $\Delta t_i^{\mathrm{pred}}$ is determined from Equation 4.41, and we search for the nearest power of two:

$$\Delta t_i = \max_k \left\{ \Delta t_k \mid \Delta t_k \leq \Delta t_i^{\mathrm{pred}} \right\} \tag{4.42}$$

Then a list is created containing all particles due for the next integration, $\mathcal{L} = \{i \mid t_i + \Delta t_i \leq t\}$, where t_i and t denote the proper and global time, respectively. The position of the planets that are needed for evaluating the gravitational force are predicted to the time t_i. Integration thus proceeds in chunks or blocks of particles that are treated simultaneously; therefore the procedure is often referred to as the block time step scheme. Once force calculation and correction are done, $\Delta t_i^{\mathrm{pred}}$ has to be updated according to the newly determined acceleration and its higher derivatives. The

new time step is then found by the following rule:

$$\Delta t_i^{\mathrm{new}} = \begin{cases} \frac{1}{2}\Delta t_i & \text{if } \Delta t_i^{\mathrm{pred}} < \Delta t_i \\ 2\Delta t_i & \text{if } \Delta t_i^{\mathrm{pred}} > 2\Delta t_i \ \text{ and } \ t_i \bmod (2\Delta t_i) = 0 \\ \Delta t_i & \text{otherwise} \end{cases} . \tag{4.43}$$

We see that a time step can be reduced by a factor of 2 after every integration. Doubling the time step is only possible if the accumulated proper time is commensurate with $2\Delta t$, i e. only every other integration cycle. The basic principle of the scheme is illustrated in Figure 4.9.

4.3.3 Accuracy

The relative difference of the system's total energy E from its initial value E_0 is used to measure the accuracy of the integration.[4] The total energy of the system is the sum of the kinetic and potential energy $T_i + U_i$ of all gravitating particles $i = 1, \ldots, P$ plus the stellar gravitational potential. The massless test particles do not contribute to the energy budget. Furthermore, the orbital energies of dust particles are not conserved because they are subject to dissipative forces (see §4.2.3 and §4.2.4).

Number of force calculations All numerical methods used for orbit integration rely on the extrapolation of the known position and velocity of a particle at time t to a future time $t + \Delta t$. The smaller the time step Δt, the more accurate the integration. As mentioned in the previous section, the size of Δt is set by Equation 4.41, but there is some freedom in choosing the average number of time steps per orbit N_{step} by adjusting the parameter η.

The other important parameter to affect the accuracy is the number of iterations of the predictor-corrector scheme. In order to reach a higher accuracy, one may repeat the sequence of prediction–evaluation–correction several times, where the corrected position and velocity computed by the Hermite scheme serve as prediction values for the next iteration. Figure 4.10 shows the relative energy error as a function of the number of time steps N_{step} and for different numbers of Hermite iterations N_{iter}.

The average number of force calculations can then be written as $N_{\mathrm{force}} = N_{\mathrm{step}}(N_{\mathrm{iter}} + 1)$. The computing time will be proportional to N_{force}, and one can envisage this quantity as the (orbital-averaged) computational work load. Many force calculations will ensure a small integration uncertainty, at the expense of a long computing time. Taking $\Delta E/E_0$ as the accuracy measure, one may look for the trade-off between work load and the corresponding accuracy. Defining an efficiency parameter by

$$\mathcal{E} = -\log\left(N_{\mathrm{force}} \times \frac{\Delta E}{E_0}\right), \tag{4.44}$$

we find the combination of least work load and smallest energy error by maximising $\mathcal{E}$. The optimal parameter settings for the integrator are $N_{\mathrm{iter}} \geq 3$ and $\lesssim 100$ time steps per orbit (Figure 4.11). If not stated otherwise, we applied these values for all further simulations.

[4] The relative energy error indicates the deviation of the calculated orbit from an equi-energy hyperplane in the 6-P dimensional phase of the system (Makino 1991). While a particle integration can be very accurate, i. e. close the surface with $E = E_0$, the corresponding orbital solution may be far off from the real one.

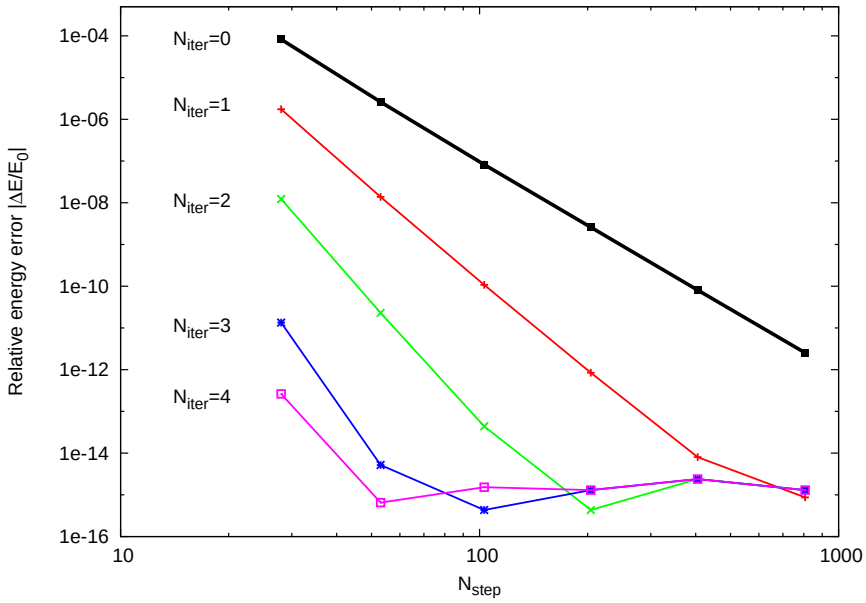

Figure 4.10. Relative energy error as a function of the number of time steps; each line corresponds to a different number of iterations of the Hermite scheme. The accuracy of the integration is bounded from below by the floating point arithmetic of the computer/compiler used. The smallest fraction representable in double precision mode (64 bit) is $2^{-52} \approx 2 \times 10^{-16}$.

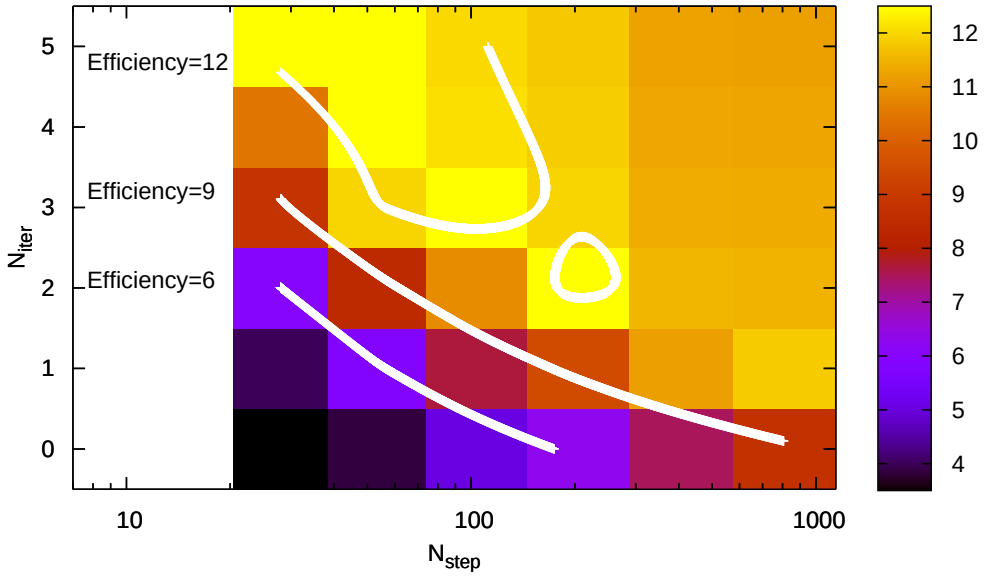

Figure 4.11. Optimal combination of time step size and number of Hermite iterations; the data points are the same as in Figure 4.10. The efficiency parameter $\mathcal{E}$ is defined in Equation 4.44.

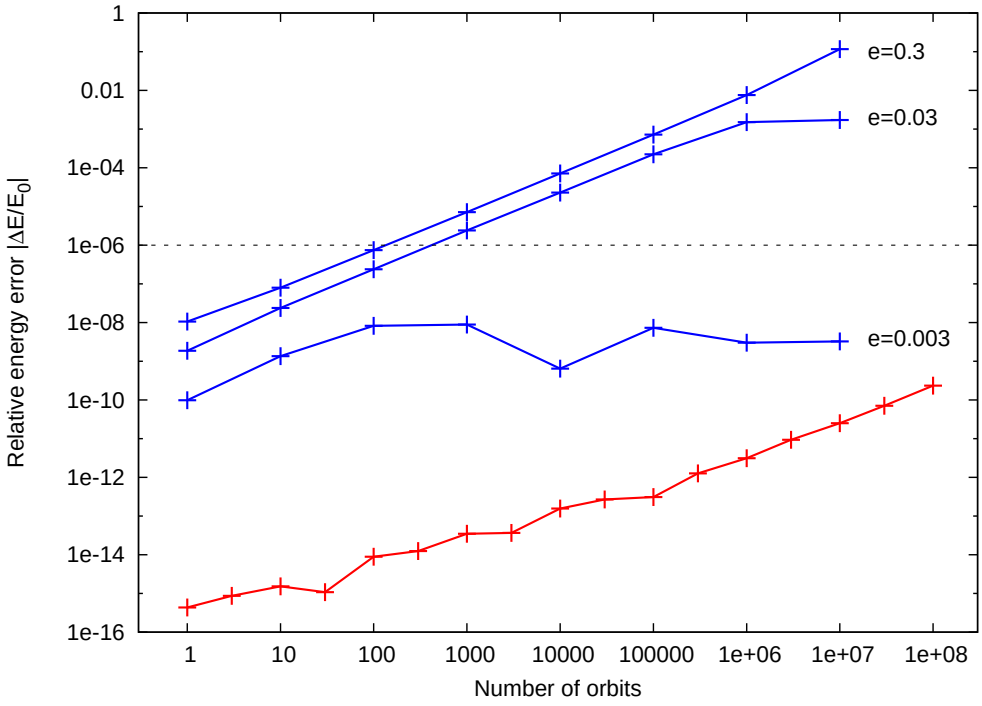

Figure 4.12. Accuracy during long-term integration. Plotted are the relative energy errors as functions of the number of planetary orbits for different eccentricities. For a circular orbit (red line), $\Delta E/E_0$ scales approximately as $N_{\mathrm{orbit}}^{0.7}$. The dashed line shows the maximum error $\Delta E/E_0 = 10^{-6}$ we deem acceptable.

Integration time Long-term integrations are especially important for the dynamical modelling of big dust particles at large distances to the central star. Their orbital elements only evolve slowly by the Poynting-Robertson drag. Furthermore, once trapped, large dust particle can remain locked in mean motion resonance for a long time.

We investigate the influence of the integration time on the final accuracy achieved. The relative energy error is expected to rise with the integration time. The steepness of the increase then determines the longest integration time that can be modelled below a certain error threshold. For a system with a planet on a circular orbit, the relative energy error grows less than linear with integration time (Figure 4.12). Up to 10^9 orbital time scales can be integrated with $\Delta E/E_0 \lesssim 10^{-9}$. Taking solar system numbers, this sufficient to trace the orbital evolution of millimetre-sized grains released in the outer Kuiper Belt ($\sim$50 AU, Jewitt and Luu 2000).

The situation is less favourable for planets on non-circular orbits. The relative energy errors of only slightly elliptic orbits turn out to be several orders of magnitude higher than in the circular case (Figure 4.12). In addition, the energy errors tend to increase more rapidly with integration time. The main reason for the different behaviour is the error propagation of the $\dot{\boldsymbol{a}}$ terms in the Hermite scheme. For non-circular orbits the first derivative of the force varies in time, and numerical errors in the evaluation of $\dot{\boldsymbol{a}}$ affect the corrected position and velocity of the planet. In order to obtain for elliptic orbits accuracies comparable to circular orbits, one needs to reduce the time step size considerably. For an orbit with $e = 0.3$, about 100 times more force evaluation are necessary. Accordingly, the computing time is prolonged by the same factor.

4.3.4 CPU timings

We performed timing experiments to study the dependence of the computing time on crucial model parameters. Knowing the scaling laws allows to plan many particle simulations as well as to predict the energy error achievable. All timings were performed on a commercial laptop PC powered by a Pentium-4M processor with 2.4 GHz.

Since the test particles do not interact with each other gravitationally, we expect the computing time to scale linearly with the number of test particles N. We set up a disk simulation with one planet on a circular orbit and integrated for 100 orbital time scales. We find that the total computing time scales slightly more than linear with increasing number of test particles, while the actual particle integration is proportional to N (Figure 4.13).

In order to test the influence of the number of planets, we modelled a system with P planets on coplanar, circular orbits. Their distances to the central star are spaced linearly, i. e. located at $r = 1, 2, \ldots, P$ astronomical units. (The semi-major axis of the fourth planet has been shifted by a small amount from $r = 4$ AU to avoid the (high-order) 8:1 mean motion resonance with the innermost planet. After 10^5 orbits for the innermost planet, the time required for the computation and the relative energy error was measured. In the configuration adopted for this test, the computing time is roughly linear to P. The final energy error jumps irregularly by several orders of magnitude (Figure 4.14).

4.4 Test calculations

The motion of a dust particle under the influence of radiation forces, stellar-wind drag, and the gravitational forces of a star and one or more planets is fully described by the acceleration terms given in Section 4.2. The equation of motion, however, cannot be solved analytically, and there is no general solution to the problem. Nevertheless, semi-analytic approximations exist in the case of only two bodies (star and particle) and for the circular restricted three-body problem. These specific cases will be used to conduct test calculations in order to check the validity of the code.

4.4.1 Two-body problem: particle on circular orbit

The variations of the osculating orbital elements of a test particle are given by Equations 4.22 and 4.23 (Robertson 1937; Wyatt and Whipple 1950). We have seen that both semi-major axis and eccentricity of the particle's orbit decrease until the grain sublimates in the vicinity of the star. Furthermore, the inclination of the particle's orbit is not changed since all force vectors lie in the orbital plane.

We tested the code repeatedly for dust particles on circular orbits, and compared the results to the semi-analytic solution of Wyatt and Whipple (1950). Here we show one simulation which was done for a single particle with $\beta = 0.1$ initially located at $a_0 = 61.4$ AU and with an inclination of $i = 6.7°$. The central star is assumed to have a mass of $1\ \mathrm{M}_\odot$, and we adopted $\xi = 0.3$ for the strength of the stellar wind drag. The numerical results from the `MODUST` code and the relative difference to the semi-analytic solution are plotted in Figure 4.15. Within numerical uncertainties, the orbital decay time $t_{\mathrm{PR}} = 11.6$ Myr matches closely the value calculated by Equation 4.27, where $\beta = \beta_{\mathrm{grain}}(1 + \xi)$. Comparing the evolution of the semi-major axis in time, the results of the code are in perfect agreement with the semi-analytic approximation.

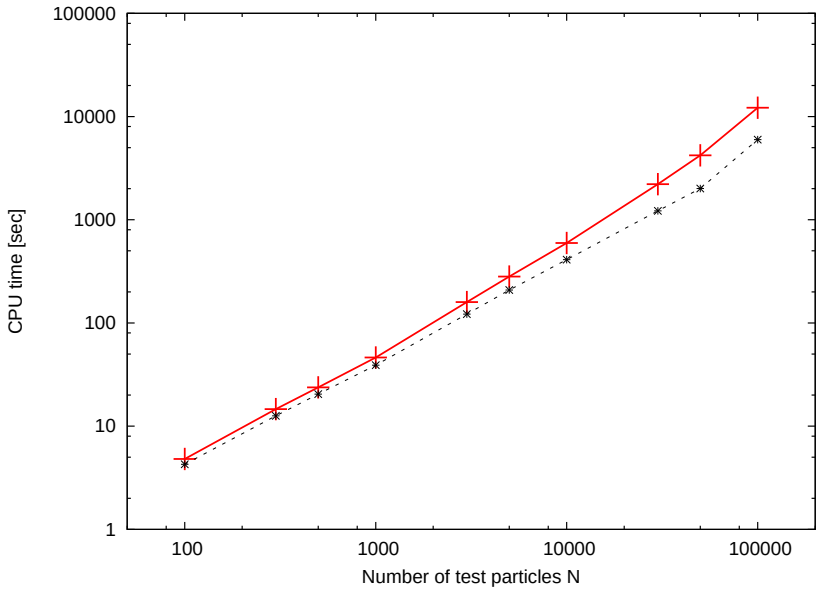

Figure 4.13. Total CPU time as a function of the number of test particles (red crosses and line); it is proportional to approximately $N^{1.12}$. The dotted line below shows the time spent on the actual Hermite integration, which scales linearly with N. The growing overhead is due to the time-costly search for the particle(s) to be integrated next.

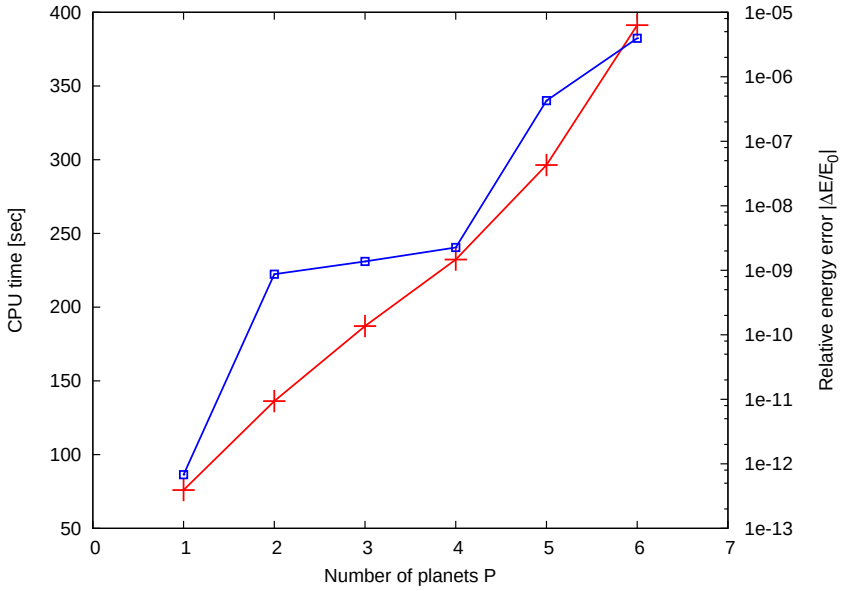

Figure 4.14. Total CPU time and relative energy error as a function of the number of planets (red and blue line, respectively). The computation time scales roughly linearly with P; the corresponding relative energy error $\Delta E/E_0$ rapidly increases several orders of magnitude.

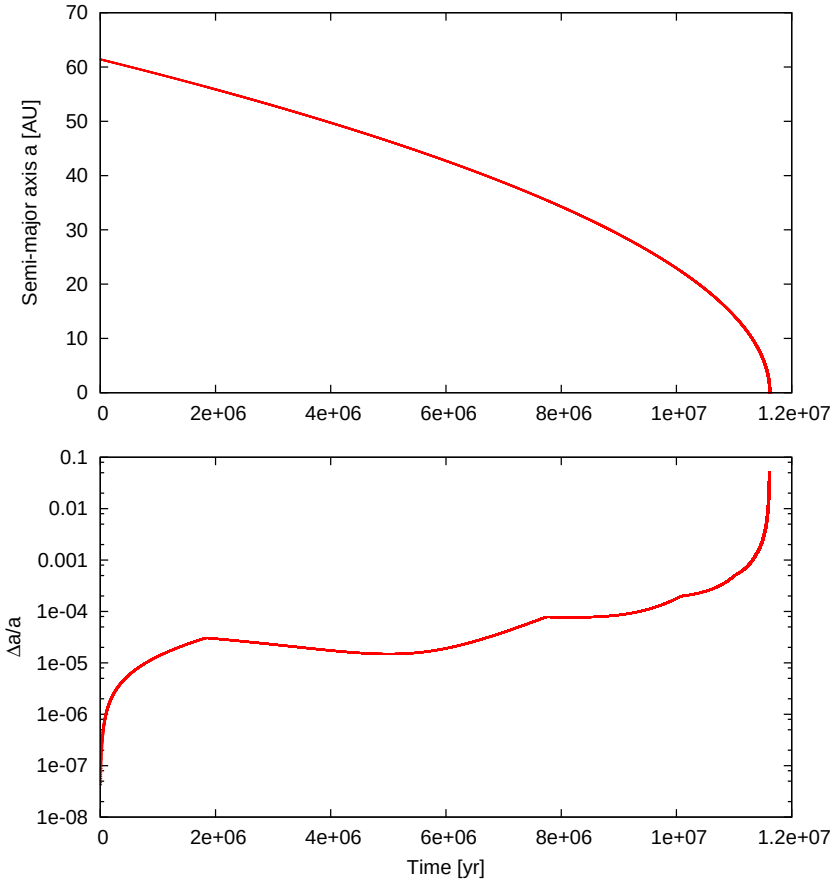

Figure 4.15. Test calculation for a dust particle on a circular orbit, and comparison to the semi-analytic solution of the secular evolution of the semi-major axis from Wyatt and Whipple (1950). The dust particle has $\beta = 0.1$; the stellar properties were set to solar values. *Top:* Semi-major axis as a function of time. *Bottom:* relative difference of numerical and semi-analytic solution. The agreement is better than one part in a thousand for most of the time. Only at small semi-major axes the difference is growing, mainly because Equation 4.22 has been solved with a fi xed time step.

4.4.2 Two-body problem: particle on eccentric orbit

Several test calculations were performed for dust particles on eccentric orbits. In Figure 4.16 we show one such test run around a solar-like star for a dust particle with, again, $\beta = 0.1$. The initial semi-major axis and eccentricity of the particle's orbit are $a_0 = 42.4$ AU and $e_0 = 0.71$, respectively. From the location where the curve $a(t)$ intercepts the time axis, one finds the orbital decay time. The value of 2.1 Myr is in excellent agreement with the semi-analytic result derived from Equation 4.28. The orbital evolutions of semi-major axis and eccentricity of the numerical simulation match well those predicted from the semi-analytic description. Since a is in the denominators of Equation 4.22 and 4.23, it is not surprising that larger deviations occur close to the star.

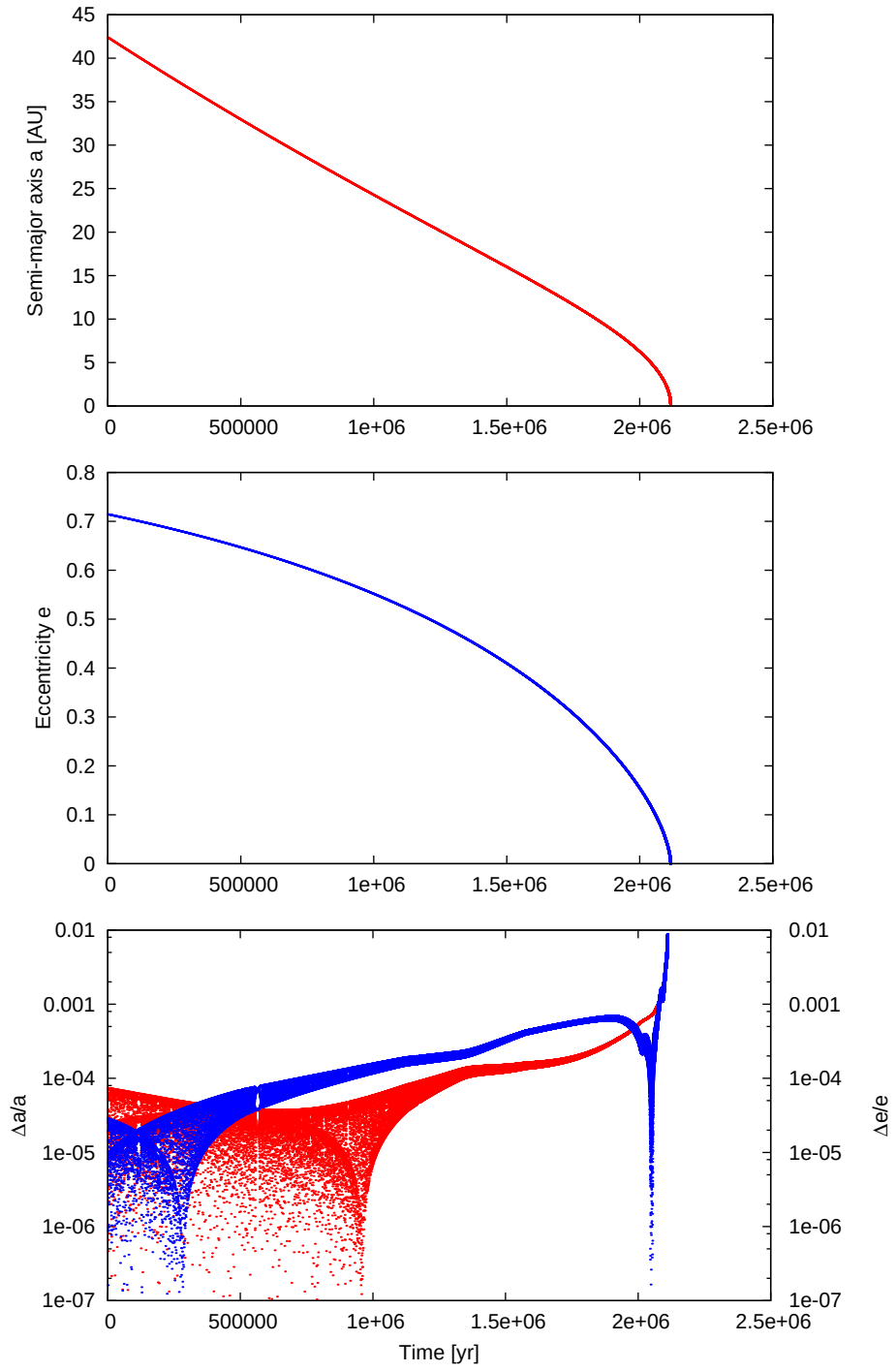

Figure 4.16. Test calculation for a dust particle on an eccentric orbit, and comparison to the secular evolution of semi-major axis and eccentricity from Wyatt and Whipple (1950). The parameters for dust particle and central star are the same as for Figure 4.15. *Top:* Semi-major axis as a function of time. *Centre:* eccentricity as a function of time. *Bottom:* Relative difference between the `MODUST` results and the semi-analytic solutions for semi-major axis and eccentricity, shown by the red and blue line, respectively.

4.4.3 Circular restricted three-body problem

The presence of a third, massive body introduces a further complication to the description of the particle's motion. The combined effects of energy dissipation by drag forces and energy gain inside mean motion resonances lead to a rich dynamics of the dust particle. Here we discuss a specific class of three-body systems, namely the circular, restricted three-body problem for which exist analytic approximations of the time dependence of the orbital elements (Liou and Zook 1997). In the circular, restricted three-body problem two bodies move in circular, coplanar orbits about their common centre of mass. The mass of the third body is negligible, hence does not affect the motion of the other two bodies (e. g. Murray and Dermott 1999). For the test calculations, we simulated a system with a solar-mass star, a Jupiter-mass planet on a circular orbit with $a = 30$ AU, and dust particles with β values 0.01, 0.1, 0.2, 0.3, and 0.4.

Exterior mean motion resonances We followed the evolution of several dust particles released at 50 AU and moving inwards due to radiative and corpuscular drag forces. The evolution of their semi-major axes and eccentricities are shown in Figure 4.17. The orbital decay rate is proportional to β (Equation 4.22), and at the beginning of the simulation small grains move in faster than larger ones. After a certain time, the decay of the particle's orbit halts, and evolves into a stationary phase. The semi-major axes obtained correspond to the 2:1 mean motion resonance with the planet; the exact values are given by Equation 4.18.

Inside the resonance the eccentricities increase rapidly towards a limiting value equal for all particles, regardless of the β value (Beauge and Ferraz-Mello 1993). We find $e_{\rm lim} \approx 0.48$, as expected for the 2:1 commensurability (Beauge and Ferraz-Mello 1994). Generally, the perihelion distance of a particle locked in an exterior mean motion resonance is smaller than the semi-major axis of the planet, $r_{\rm p} = (1 - e_{\rm lim})a_{\rm mmr} < a_{\rm pl}$ (Sicardy et al. 1993; Beauge and Ferraz-Mello 1994). This means that the particle orbit will cross that of the planet, leading to repeated close encounters with gravitational perturbations. Eventually the particle is ejected from the system (Weidenschilling and Jackson 1993; Lazzaro et al. 1994).

Interior mean motion resonances A completely different dynamical behaviour is found for interior mean motion resonances. We ran a simulation for the same particles released inside the orbit of the planet at 23 AU. As the dust grains move towards the central star, they encounter regions that are in resonances with the planet (Figure 4.18). Upon reaching a resonance, the semi-major axis of the particle decreases drastically, while the eccentricity increases sharply (Figure 4.19). Further in, the particle passes more resonances, and the pattern of drop in semi-major axis and lift in eccentricity is repeated several times. In between these events the orbital elements evolve similar to the two-body problem, i. e. with a gradual decrease of semi-major axis accompanied by a circularisation of the orbit. Although the eccentricity of the particle may reach high values (~ 0.4), the relatively small semi-major axis generally ensures that the orbit of the dust particle does not cross that of the planet. Finally, the orbital decay continues until sublimation.

As opposed to exterior mean motion resonances, interior commensurabilities can not compensate for the loss of orbital energy and angular momentum the particle suffers due to dissipative forces (Sicardy et al. 1993). Therefore, particles cannot be held in quasi-stationary orbits, as is the case for an exterior resonance (Liou et al. 1995). On the contrary, subsequent passages through these regions accelerate the orbital decay. Both dynamical effects together provide a mechanism to accumulate dust particles in exterior mean motion resonances with the planets, while constantly emptying the region inside the planet's orbit from dust (Scholl et al. 1993; Liou and Zook 1999).

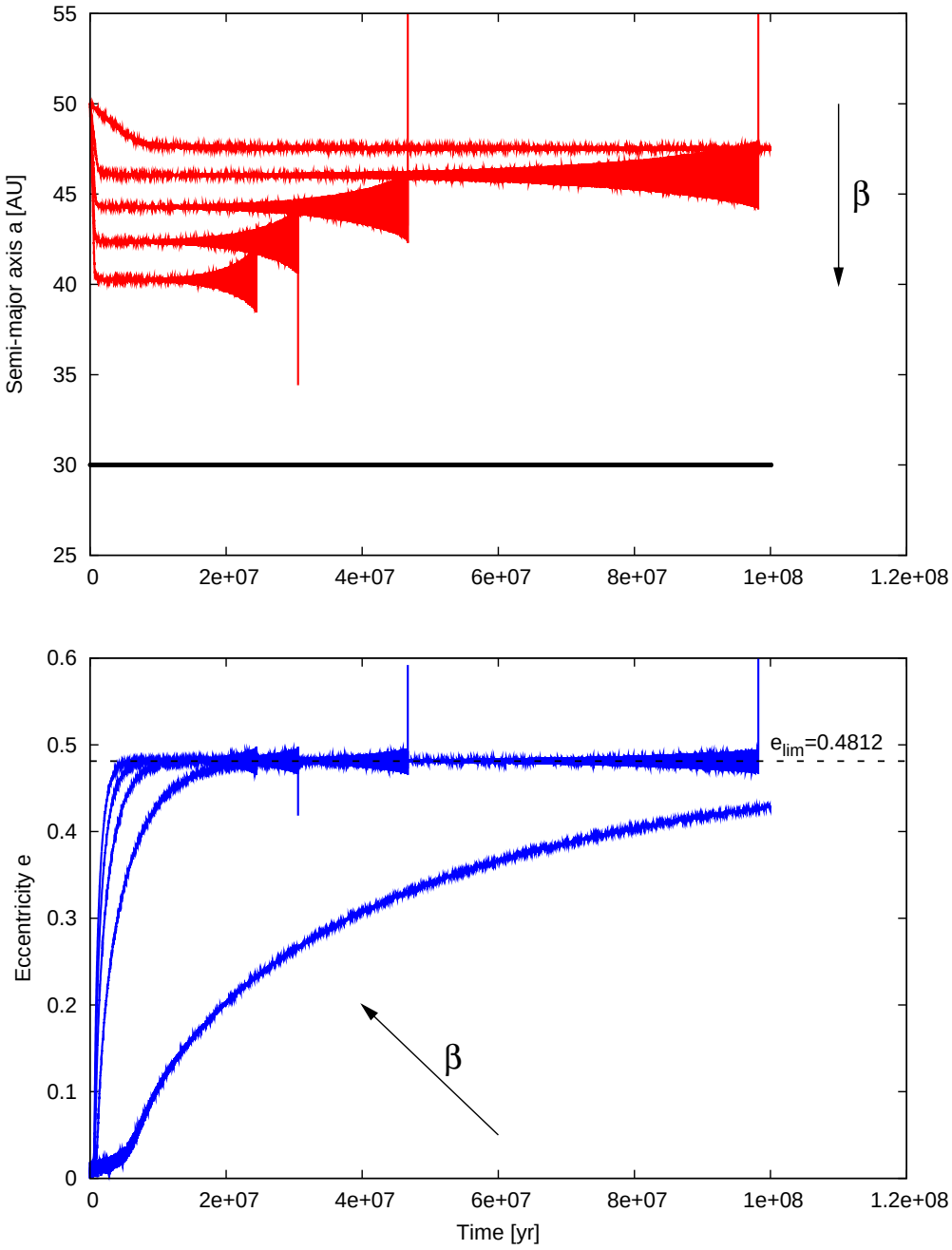

Figure 4.17. Orbital evolution of semi-major axis (top) and eccentricity (bottom) of dust particles trapped in the 2:1 exterior mean motion resonance with a planet at 30 AU (black line). Curves are plotted for β of 0.01, 0.1, 0.2, 0.3, and 0.4; arrows point in the direction of increasing β values. The "universal" eccentricity corresponding to the 2:1 commensurability is shown by the dashed line. Frequent close encounters with the planet lead to growing perturbations by the planet and, finally, ejection. Smaller grains are ejected earlier than larger ones.

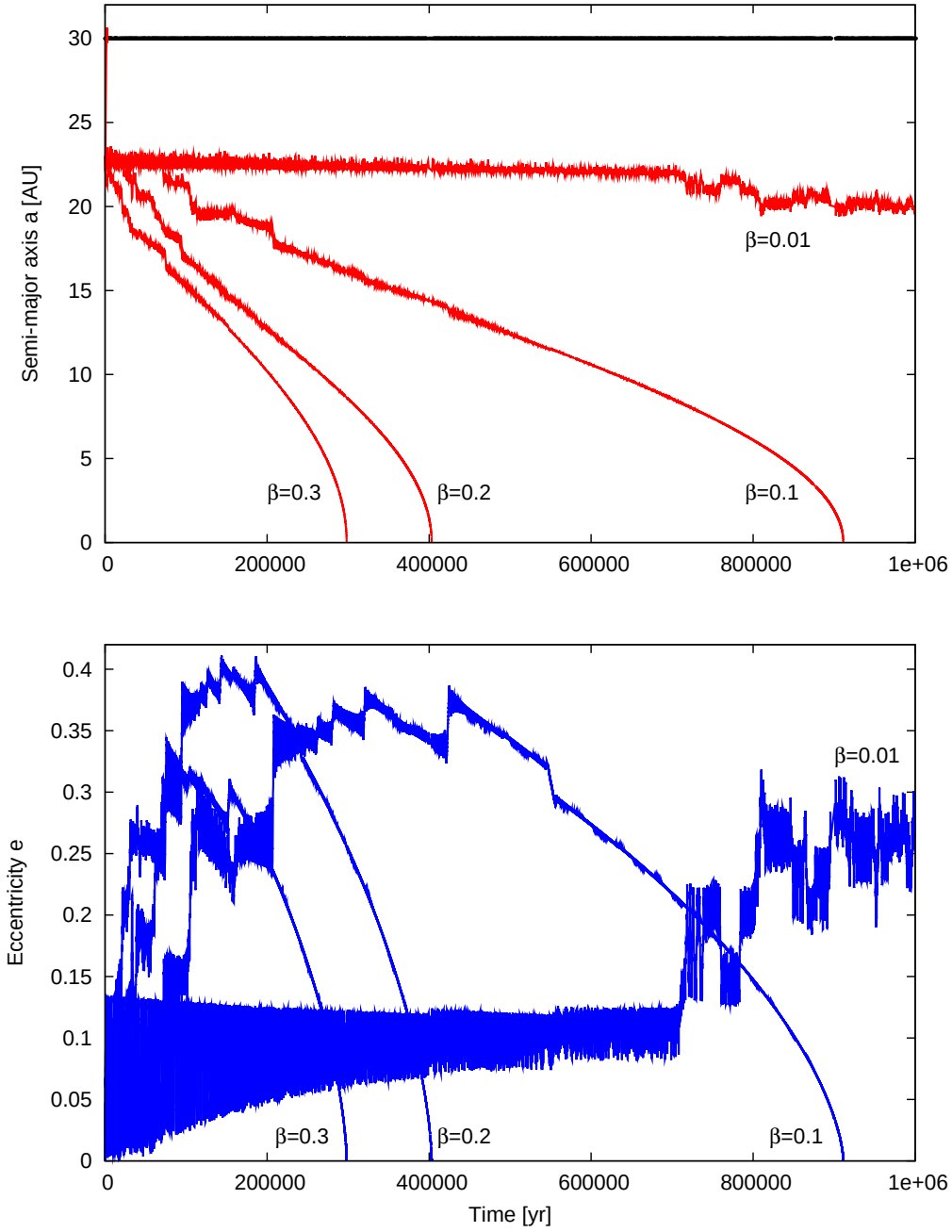

Figure 4.18. Orbital evolution of semi-major axis (top) and eccentricity (bottom) of dust particles released at 23 AU; the planet is at 30 AU (black line). Curves are shown for β of 0.01, 0.1, 0.2, and 0.3. The particle with $\beta = 0.4$ was ejected immediately. Every kink in the evolution of the orbital eccentricity designates the passage through an interior mean motion resonances.

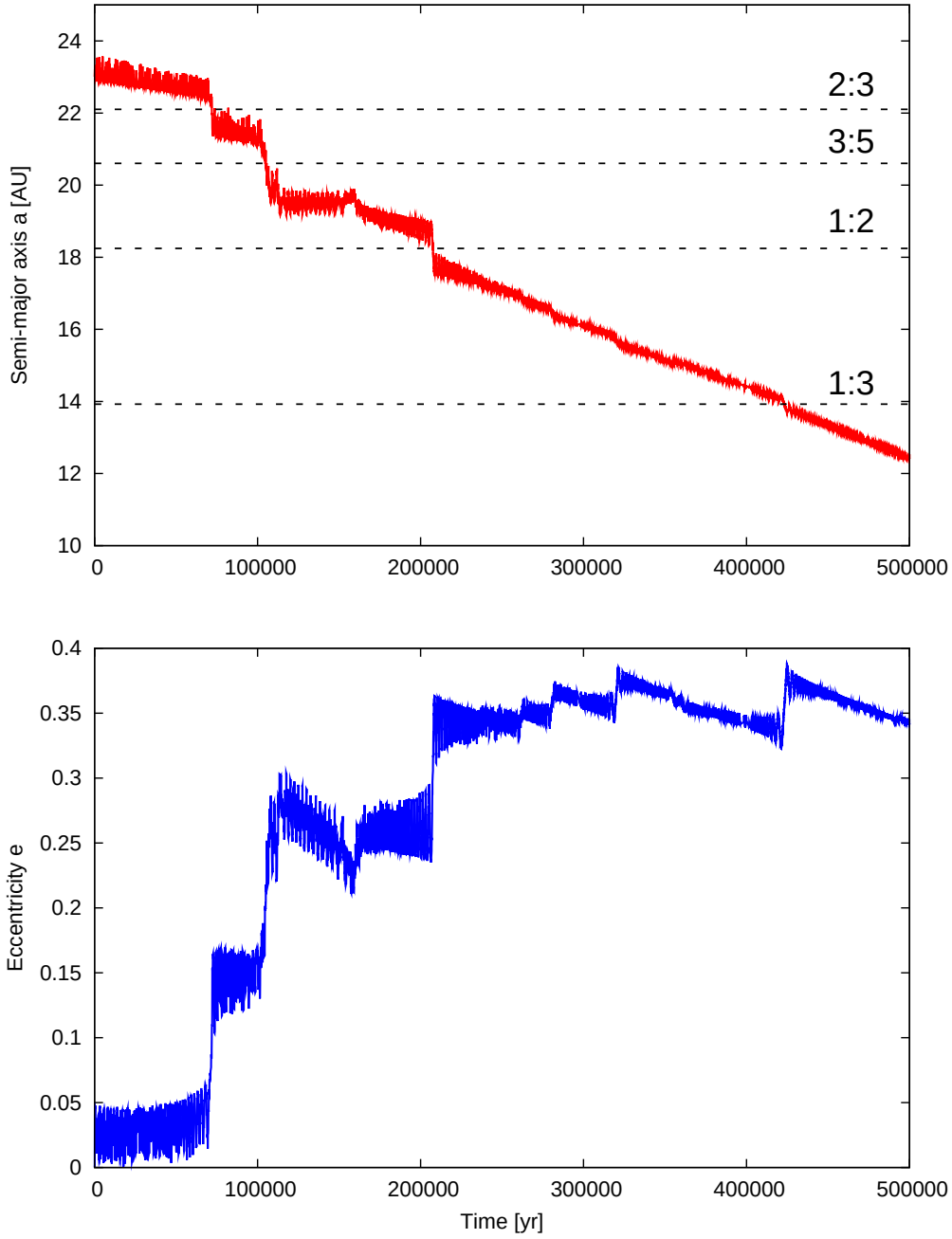

Figure 4.19. Change of the semi-major axis (top) and eccentricity (bottom) during passage of interior mean motion resonances. This plot shows the orbital evolution of the particle with $\beta = 0.1$ from Figure 4.18 in greater detail. The locations of the most important low-order commensurabilities are indicated by dashed lines.

4.5 Modelling the debris disk around HD 181327

Recently Schneider et al. (2006) discovered a ring of circumstellar debris around the F5.5 V star HD 181327, a known far-infrared excess source (Backman and Paresce 1993). It is a member of the relatively young (∼12 Myr) β Pic moving group (Zuckerman and Song 2004; Mamajek et al. 2004). Owing to its proximity (50 pc) and near-infrared brightness ($J = 6.20$ mag), HD 181327 was selected as a target for Hubble Space Telescope (HST) observations in the framework of the GO programme 10177 (Schneider 2005).

PSF-subtracted coronagraphic observations of HD 181327 obtained with the NICMOS instrument on-board the Hubble Space Telescope at 1.1 μm revealed the presence of a ring of circumstellar material located at a distance of 86.3 ± 3.9 AU from the central star (Schneider et al. 2006). Assuming a circular geometry, the inclination of the ring is 31.7° ± 1.6°. The 1.1-μm flux density in scattered light is 9.6 ± 0.8 mJy, corresponding to only ∼0.2% of the stellar flux density. The azimuthally-averaged width of the ring is ∼28 AU. The non-uniform surface brightness of the ring in azimuthal direction can be fitted by strong preferential scattering with a Henyey-Greenstein scattering phase function of $g \approx 0.3$. However, the overlying structures observed in scattered light may also be a result of the disk sculpting by a planetary perturber. We investigated this possibility and applied `MODUST` to model the debris disk around HD 181327.

4.5.1 Definition of the model grid

We sat up a grid of 40 models, varying the parameters that critically determine the structure of the debris disk, namely the distance of the planet to the star $a_{\rm pl}$, the mass of the planet $M_{\rm pl}$, and the β parameter. A shorthand notation is introduced to identify the different model families.

The planet's orbital radius with respect to the (initial) location of the disk will determine the dominant mean motion resonances. Two cases have been considered: First, the dust ring is assumed to be located at the 1:1 commensurability with the planet, i. e. $a_{\rm pl} = 86.3$ AU. In the second case, the bulk of the circumstellar debris is assumed to be locked in the 2:1 mean motion resonance, i. e. $a_{\rm pl} = 86.3 \text{ AU} \times 2^{-2/3} \approx 54.4$ AU. These models are denoted by the Roman numerals I and II, respectively.

The mass of the planetary perturber influences the trapping probability of dust particles in mean motion resonances. The limiting eccentricity below which particles can be captured is a steep function of the planetary mass, high-mass planets being much more efficient than low-mass ones (Beauge and Ferraz-Mello 1994). Based on previous studies (Table 4.2), we considered four different values for the mass of the planet: 0.1, 0.3, 1.0, and 3.0 $\mathrm{M_J}$. The corresponding model identifiers contain the Arabic numerals 1, 2, 3, and 4, respectively.

We have seen that the β parameter directly determines the locations of mean motion resonances, shifting them to smaller semi-major axes for increasing β values. Furthermore, it controls the orbital decay time and the average resonance lifetime of dust particles. The model grid has been defined to cover the β range from the blow-out limit ($\beta = 0.5$) to the Poynting-Robertson life times comparable to the age of HD 181327 ($\beta \approx 0.05$). The following logarithmically-spaced numerical values have been adopted: 0.48, 0.267, 0.15, 0.086, 0.048. Assuming silicate dust with a bulk density of 2 g cm^{-3}, and using $L_\star = 3.09$ $\mathrm{L_\odot}$ (Sylvester and Mannings 2000) and $M_\star = 1.35$ $\mathrm{M_\odot}$ (Nordström et al. 2004), these β values correspond to grain sizes of approximately 3, 5, 9, 15, and 27 μm (Equation 4.16). The actual β value used is designated by the letters a, b, c, d, and e, respectively. The model grid is listed for reference in Table 4.5.

Table 4.5. Overview of the grid of simulations that were used to model the debris disk around HD 181327. The models are labelled with a composite identifier, containing Roman numerals for the position of the planet, Arabic numerals for the planetary mass, and uncapitalised letters for the β value. The number of planetary orbits has been adjusted to integrate for at least one Poynting-Robertson time scale.

Model identifier	Position of planet $a_{\rm pl}$ (AU)	Mass of planet $M_{\rm pl}$ ($M_{\rm J}$)	β	Number of orbits
I-1a	86.3	0.1	0.48	1000
I-1b	86.3	0.1	0.267	2000
I-1c	86.3	0.1	0.15	3200
I-1d	86.3	0.1	0.086	6000
I-1e	86.3	0.1	0.048	10000
I-2a	86.3	0.3	0.48	1000
I-2b	86.3	0.3	0.267	2000
I-2c	86.3	0.3	0.15	3200
I-2d	86.3	0.3	0.086	6000
I-2e	86.3	0.3	0.048	10000
I-3a	86.3	1.0	0.48	1000
I-3b	86.3	1.0	0.267	2000
I-3c	86.3	1.0	0.15	3200
I-3d	86.3	1.0	0.086	6000
I-3e	86.3	1.0	0.048	10000
I-4a	86.3	3.0	0.48	1000
I-4b	86.3	3.0	0.267	2000
I-4c	86.3	3.0	0.15	3200
I-4d	86.3	3.0	0.086	6000
I-4e	86.3	3.0	0.048	10000
II-1a	54.4	0.1	0.48	1000
II-1b	54.4	0.1	0.267	2000
II-1c	54.4	0.1	0.15	3200
II-1d	54.4	0.1	0.086	6000
II-1e	54.4	0.1	0.048	10000
II-2a	54.4	0.3	0.48	1000
II-2b	54.4	0.3	0.267	2000
II-2c	54.4	0.3	0.15	3200
II-2d	54.4	0.3	0.086	6000
II-2e	54.4	0.3	0.048	10000
II-3a	54.4	1.0	0.48	1000
II-3b	54.4	1.0	0.267	2000
II-3c	54.4	1.0	0.15	3200
II-3d	54.4	1.0	0.086	6000
II-3e	54.4	1.0	0.048	10000
II-4a	54.4	3.0	0.48	1000
II-4b	54.4	3.0	0.267	2000
II-4c	54.4	3.0	0.15	3200
II-4d	54.4	3.0	0.086	6000
II-4e	54.4	3.0	0.048	10000

4.5.2 Initial conditions

After the model has been defined, we need to set up an initial particle distribution. A high number of test particles is desirable for resolving high-order resonances, that are normally less populated that low-order commensurabilities. We chose to model 10^4 test particles, which is a reasonable trade-off between resolution and computing time.

On the basis of the location and width of the circumstellar ring given by Schneider et al. (2006), the particles' semi-major axes were distributed randomly between 70 and 115 AU (Figure 4.21). A constant surface density distribution, $\Sigma(r) \propto r^0$, has been adopted. Such a surface density profile is expected for a collisionless debris disk configuration without sources or sinks of the dust particle population whose structure is determined primarily by gravitation, radiation pressure, and dissipative forces (Briggs 1962; Wolf and Hillenbrand 2003). Resonance effects by the gravitational perturbations of one or more planets may alter this simple power-law distribution significantly (Gor'kavyi et al. 1997). For the time being, we will neglect this specific aspect of the initial surface density distribution.

Gaussian distributions have been applied to set the initial eccentricities and inclinations of the test particles. At the start of the integration, the majority of dust grains have orbital eccentricities between 0 and ~ 0.4. The full width at half maximum of the inclination distribution has been set to $\sim 10°$, consistent with the apparent inclination distribution of dust parent bodies in the Kuiper Belt of the solar system (Jewitt et al. 1996). The distributions are shown in Figure 4.20

Stellar wind drag HD 181327 is a young main-sequence star of spectral type F, and one should expects a much more powerful stellar wind than around older solar-mass stars. We may get an estimate of the wind strength by means of x-ray observations that are a measure of the mass loss rate. For stars with spectral types in the range G–M, there is a fairly robust correlation between the these two quantities (Wood et al. 2005). Extrapolating to this relation to higher-mass stars, one obtains a stellar-wind drag 40–50 times stronger than in the solar system (Potter 2005), i. e. $\xi \approx 40\,\xi_\odot = 12$. That means that the orbital decay is dominated by corpuscular drag rather than by Poynting-Robertson effect.

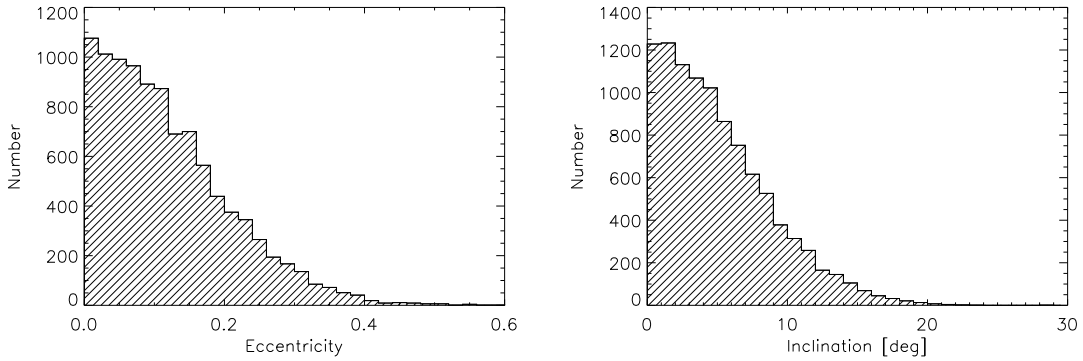

Figure 4.20. Initial eccentricity distribution (left) and inclinations (right) of the 10^4 test particles. The eccentricity and inclination values were drawn from Gaussian distributions with zero mean; only positive values have been considered. Since neither Poynting-Robertson effect nor stellar-wind drag have normal force components, there is no change in the orbital inclination of the particles.

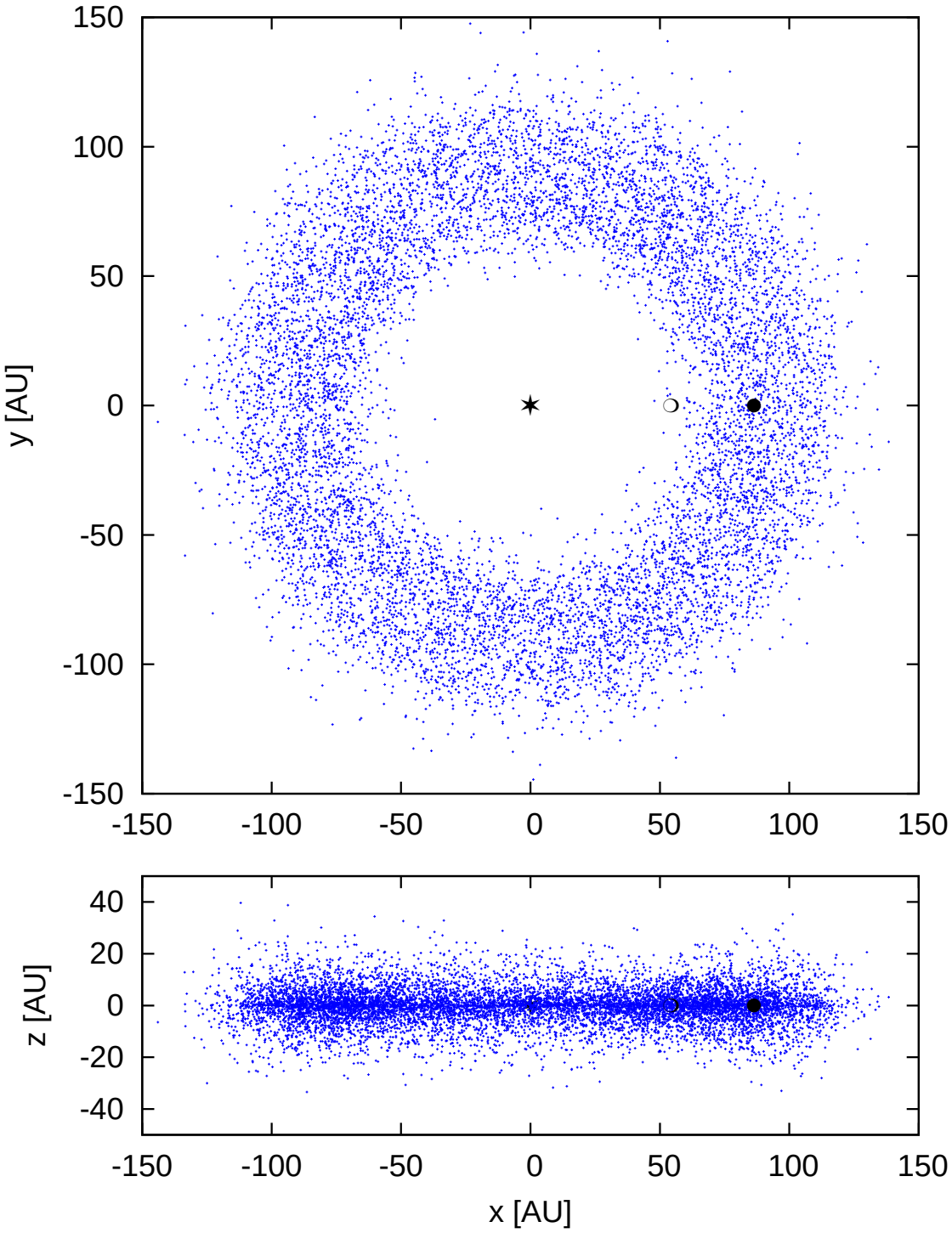

Figure 4.21. Face-on and edge-on views of the initial positions of 10^4 test particles. The semi-major axes of the particles are distributed randomly between 70 and 115 AU. The FWHM of the inclination distribution is $\sim 10°$. The initial positions of the planet are shown as a filled and open circle for the model families I and II, respectively.

4.5.3 Dust density distributions

The 40 debris disk simulations of the model grid were computed on eight dual-processor machines (2×1266 MHz) in the so-called processor-farming mode, where one or more separate jobs run on each processor and are executed in parallel with other processors. The computing times were between less than one hour and 29 hours, depending on the actual integration time (Table 4.5).

In order to enhance resonance features present in the dust density distributions, multiple snapshots of the disk configurations were made during the last 10% of the integration time. For each snapshot, the particle positions were transformed to the reference frame co-rotating with the planet, and their new coordinates were recorded and added up. With this method, we may artificially increase the resolution of the density distribution, without having to integrate more particles. This procedure, however, can only be applied when the disk has adapted to the gravitational influence of the planet and has settled in a quasi-stationary configuration. This condition has been checked independently by following the number of ejected particles.

The integrated two-dimensional dust density distributions are displayed in Figures 4.22 and 4.23. Several general trends can be observed:

- First of all, the density distributions of the model family I show striking horseshoe-shaped resonant structures, a direct indication that a considerable fraction of the disk particles are trapped in the 1:1 mean motion resonance with the planet. For the models of type II, on the other hand, this particular commensurability seems unoccupied.

- The distance of closest approach between the particles within the 1:1 resonance and the planet, i. e. the opening of the horseshoe, becomes wider with increasing planetary mass. This is a well-known result from the theory of the restricted three-body problem. A particle moving on a horseshoe orbit librates about one of the two equilibrium Lagrangian points L_4/L_5. The libration amplitude is decreasing with the mass of the secondary body (Murray and Dermott 1999).

- For a given β value, i. e. dust grain size, the shapes of the resonance features become more prominent with the mass of the planet. A similar trend is found for the size of the dust-free region around the planet, especially obvious for the type-II models.

- In the case of the model family I, the occupancy of the 1:1 mean motion resonance decreases for growing β. That means, smaller dust grains are less likely to be caught in the resonance (Weidenschilling and Jackson 1993; Dermott et al. 1994; Grün et al. 2001).

- The final disk configurations of the model family I appear somewhat larger than those of the model family II. Recalling that in the former case the planet's position is well inside the initial disk configuration (see Figure 4.21), this finding is explained by enhanced particle scattering through close encounters with the planet. In fact, the number of particles ejected from type-I systems is typically 2–3 times higher than for models of type II.

- All models display a particle accumulation near the orbital radius of the planet. According to Equation 4.18, the dust concentration extends slightly inside the planet's orbit due to radiation pressure. The inner parts of the disks show a more or less reduced dust density by the dynamical effects discussed in §4.4.3. (This inner clearing should not be confused with the central "hole" visible in the innermost region of the disk ($r \leq 15$ AU), which is empty for technical reasons.)

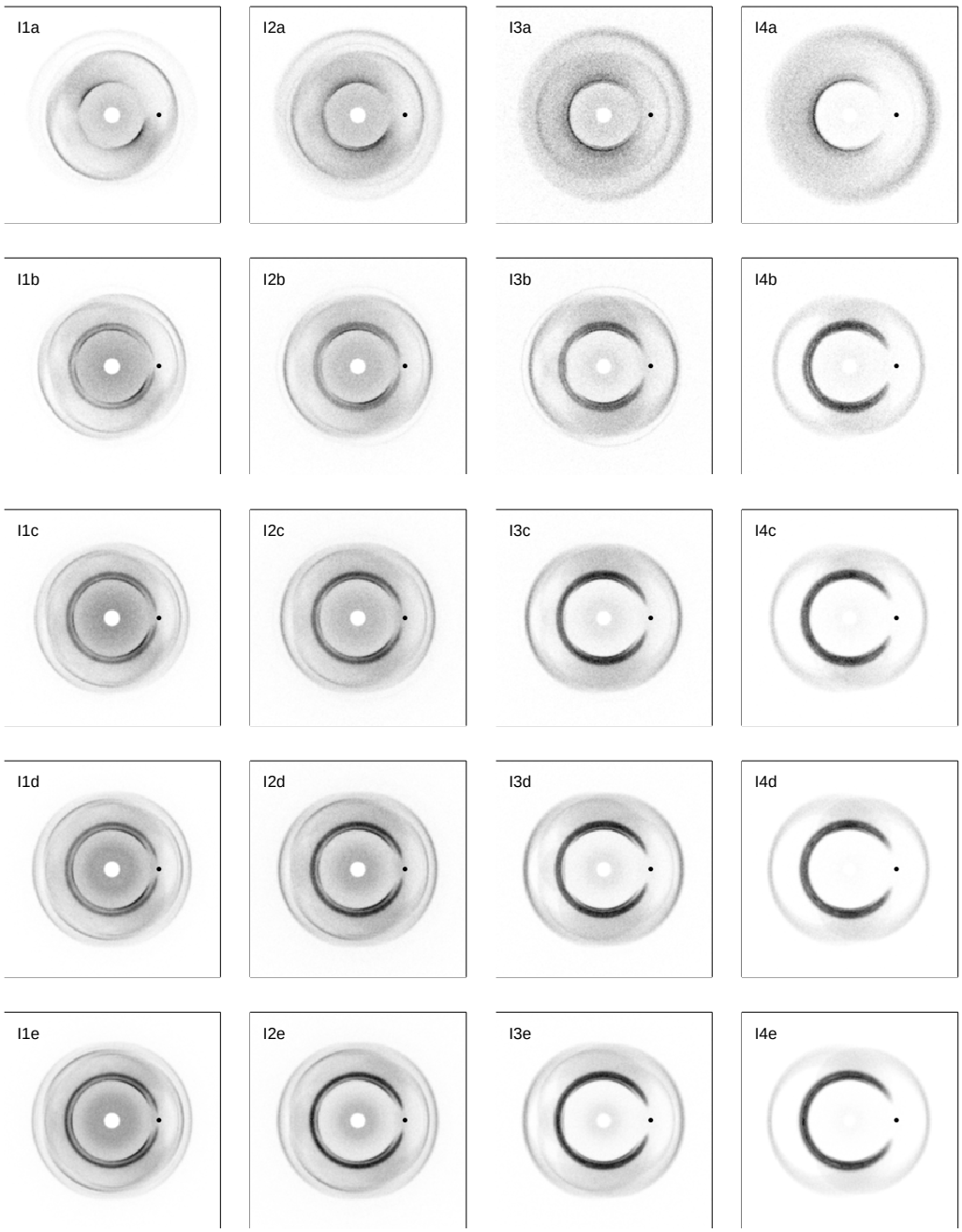

Figure 4.22. Integrated dust density distributions for the model family I shown in grey scale. The particle positions have been recorded during the last 10% of the integration time in the reference frame co-rotating with the planet; its position is marked by the black dot. The size of each panel is 400 by 400 AU, and the density distribution has been binned in 201×201 pixels.

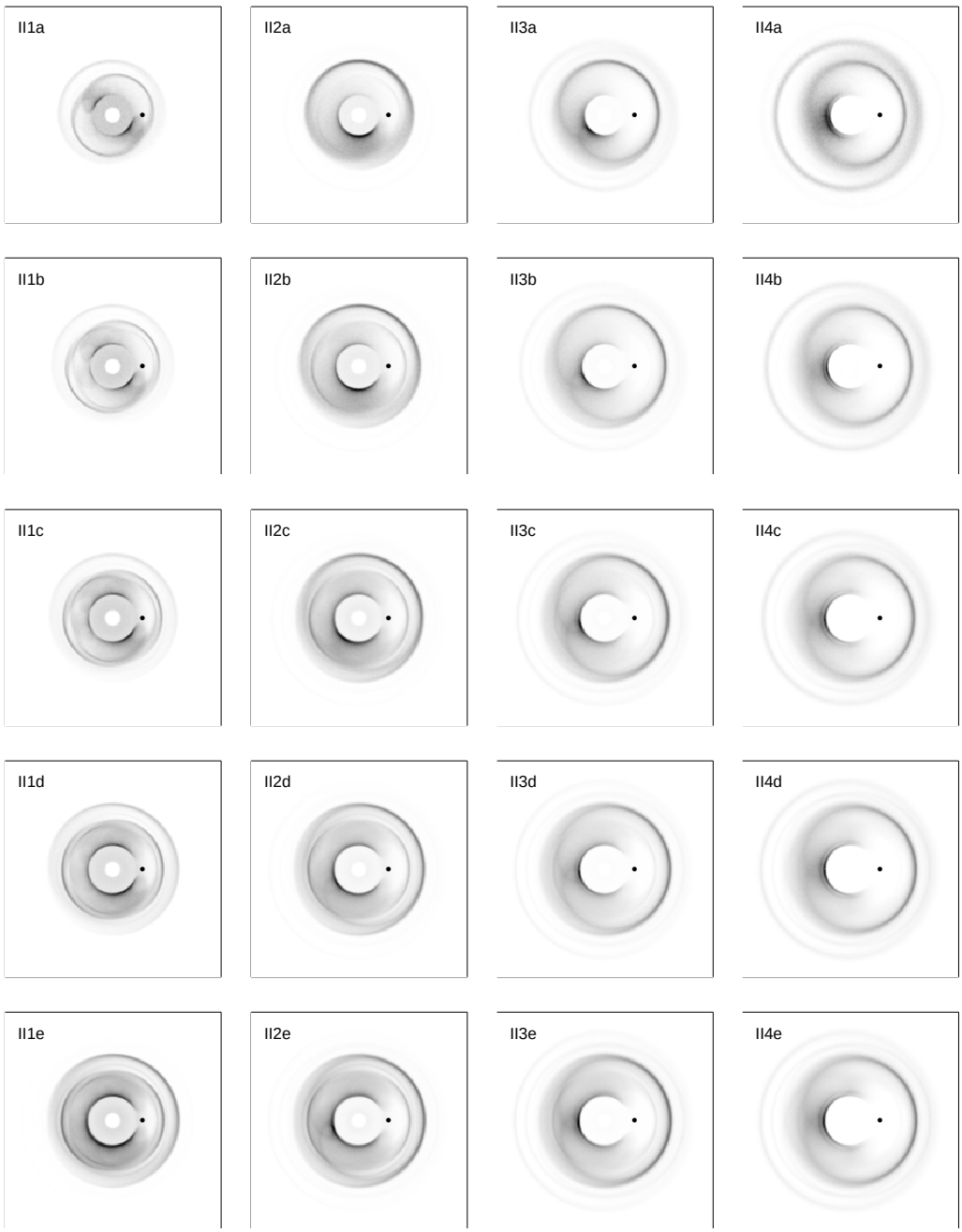

Figure 4.23. Integrated dust density distributions for the model family II, similar to Figure 4.22. The mass of the planet is increasing from left to right, while the β parameter is decreasing from top to bottom. Especially for low planetary masses, the density distributions display a marked lateral asymmetry with respect to the line star-planet. Since the coronagraphic mask used during the NICMOS observations has a diameter of $0.6''$, the particles were only followed until $r = 15$ AU.

4.5.4 Distribution of orbital elements

A more detailed analysis of the resonance structures present in the disks as a function of the planet's position, its mass, and the dust grain properties can be made by investigating the orbital element distributions of the particles. We are mainly interested in the semi-major axes and eccentricities of the dust particles, and will concentrate on their distributions. They are presented in Figures 4.24 through 4.27 and Figures 4.28 through 4.31 for the model families I and II, respectively. Starting the discussion with the first model family, the following conclusions can be drawn:

- The relative number of particles on horseshoe orbits increases with the mass of the planet and dust grain size. Except for the smallest grains ($\beta = 0.48$), where the 1:1 commensurability is nearly absent, the resonance peaks are fairly broad.
- The main exterior mean motion resonances are the 3:2, 4:3, and 2:1 commensurabilities. The latter resonance seems to play a role only for the largest β value, and its relative occupancy is increasing with the planetary mass. The same is true for the number ratio of 3:2 and 4:3 resonance.
- Comparing the final eccentricity distributions with the initial one (Figure 4.20), we note that the shapes of the particle orbits undergo substantial modification by the dynamical perturbation of the planet. The prominent peaks in the eccentricity distribution correspond to unique exterior mean motion resonances, as discussed in §4.4.3. Typically, the eccentricity values are below their limiting threshold $e_{\rm lim}$ (see Beauge and Ferraz-Mello 1994). With increasing planetary mass the eccentricity distribution becomes trimodal: First, a concentration around $e = 0$, these are the particles in the 1:1 commensurability; second, the highly occupied peaks of the exterior mean motion resonances; third, particles near $e = 1$ close to ejection from the system.

The dust density distributions of the type-II models display an entirely different geometry. This fact is reflected in the distributions of the orbital elements.

- The most important commensurabilities occupied are the two first-order resonances 2:1 and 3:2. Especially in the cases of higher planetary masses, also the second-order 3:1 and 5:2 resonances are populated. Interestingly, the 4:3 mean motion resonance seems of little importance. Particle trapping in the 1:1 resonance, i. e. with horseshoe- or tadpole-like orbits about the Lagrangian points, can not be discerned.
- The eccentricity distribution is again characterised by the resonance-specific population peaks. Due to the non-existent 1:1 resonance, very few dust grains move on circular orbits. Accordingly, there is no accumulation of zero-eccentricity particles as found for the type-I models.
- It has already been mentioned that the type-II disks appear smaller in size compared to the disks of the model family I. The semi-major axis distributions of the former only extend to $\sim$110 AU, whereas the distributions of the latter stretch out until 200 AU. Similarly, the reduced particle scattering in the case of the model family II leaves an imprint in the eccentricity distributions. In contrast to the type-I models, only a small number of particles move on high-e orbits.

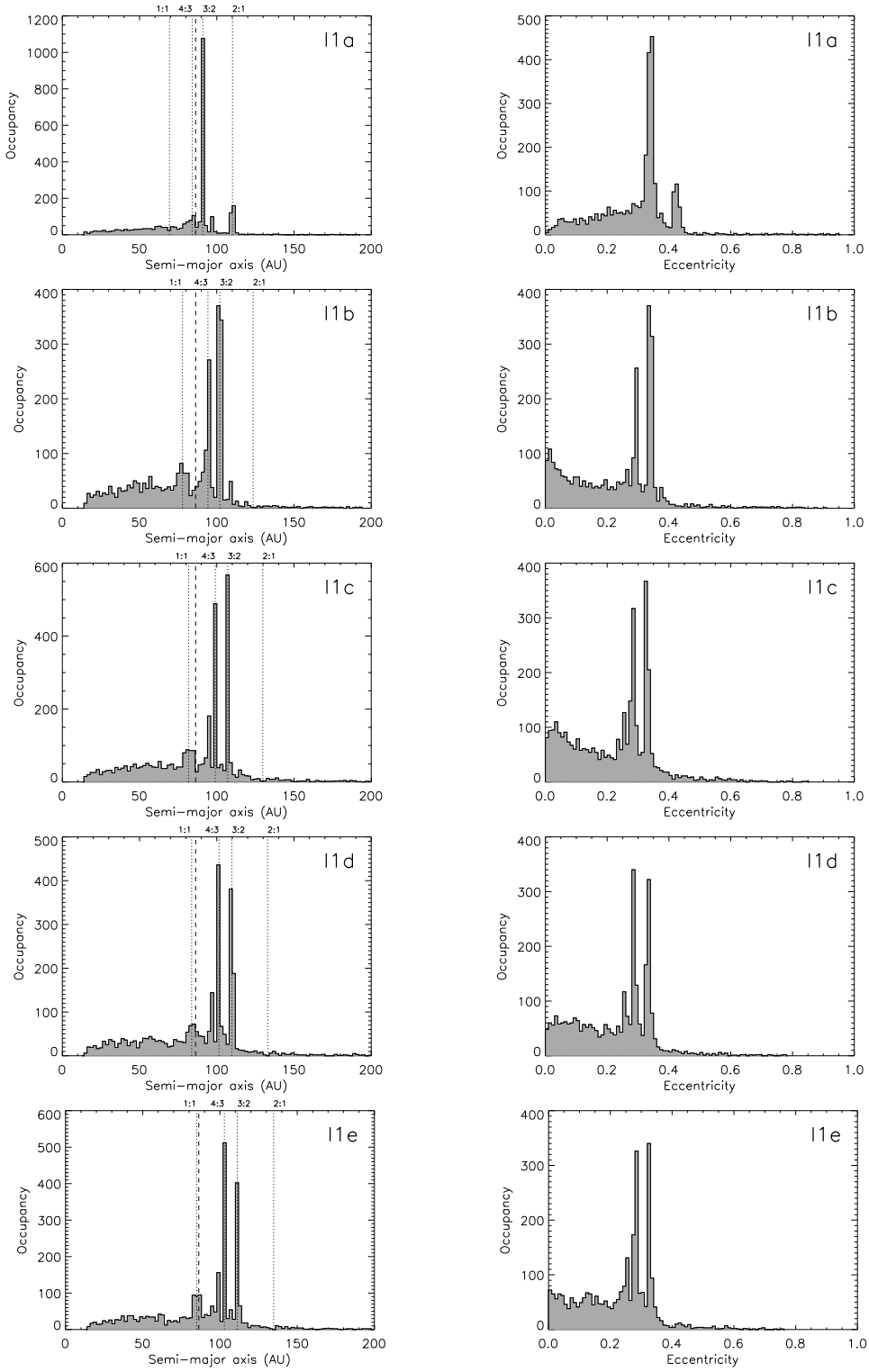

Figure 4.24. Distribution of semi-major axes (left) and eccentricities (right) for the model family I-1, showing the occupation of mean motion resonances. The dashed lines indicate the radial distance of the planet from the star, while major resonances are marked with dotted lines. The period commensurabilities are given at the top of the semi-major axis plots. Bin sizes of $\Delta a = 0.02$ AU and $\Delta e = 0.01$ were used.

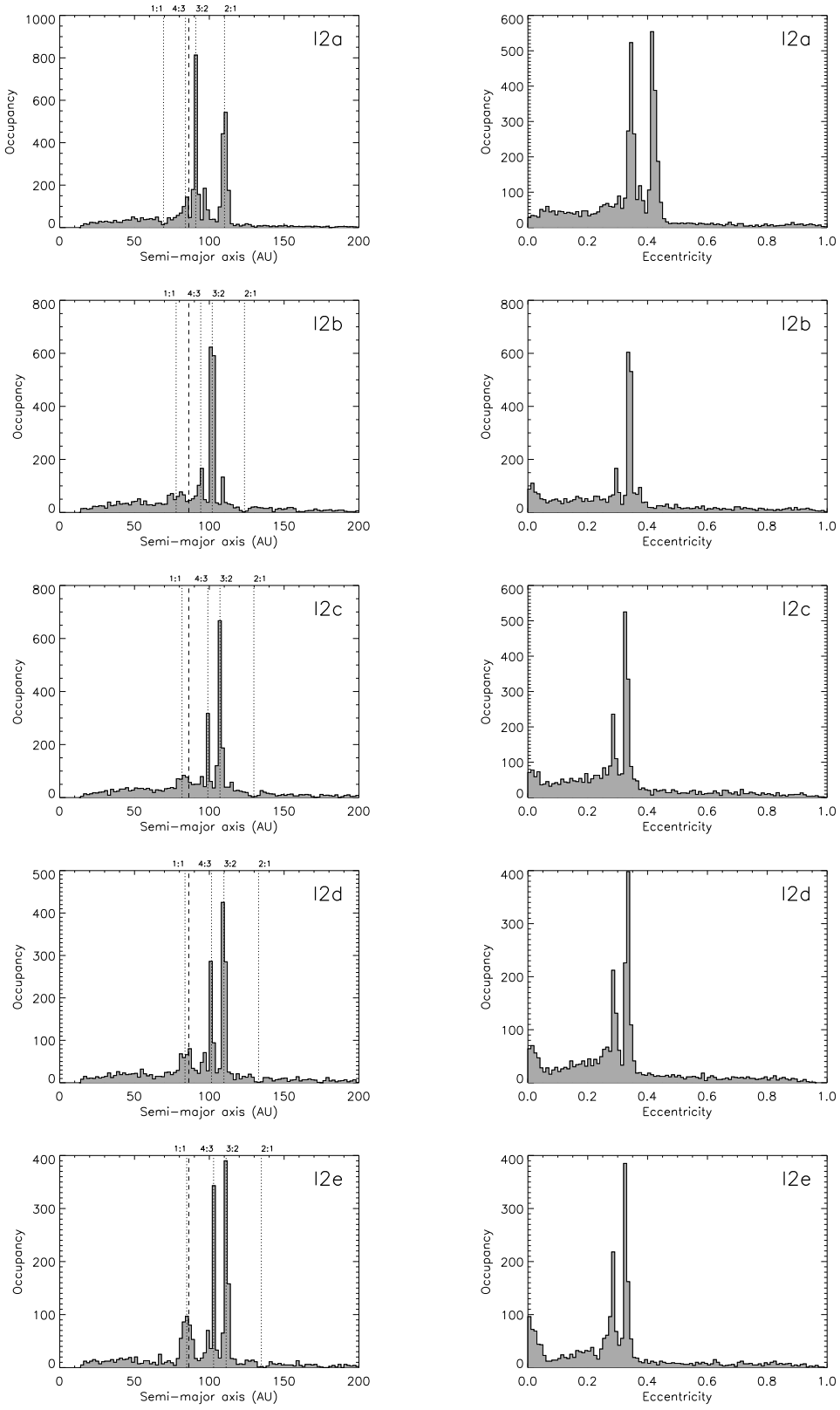

Figure 4.25. Distribution of semi-major axes and eccentricities for the model family I-2.

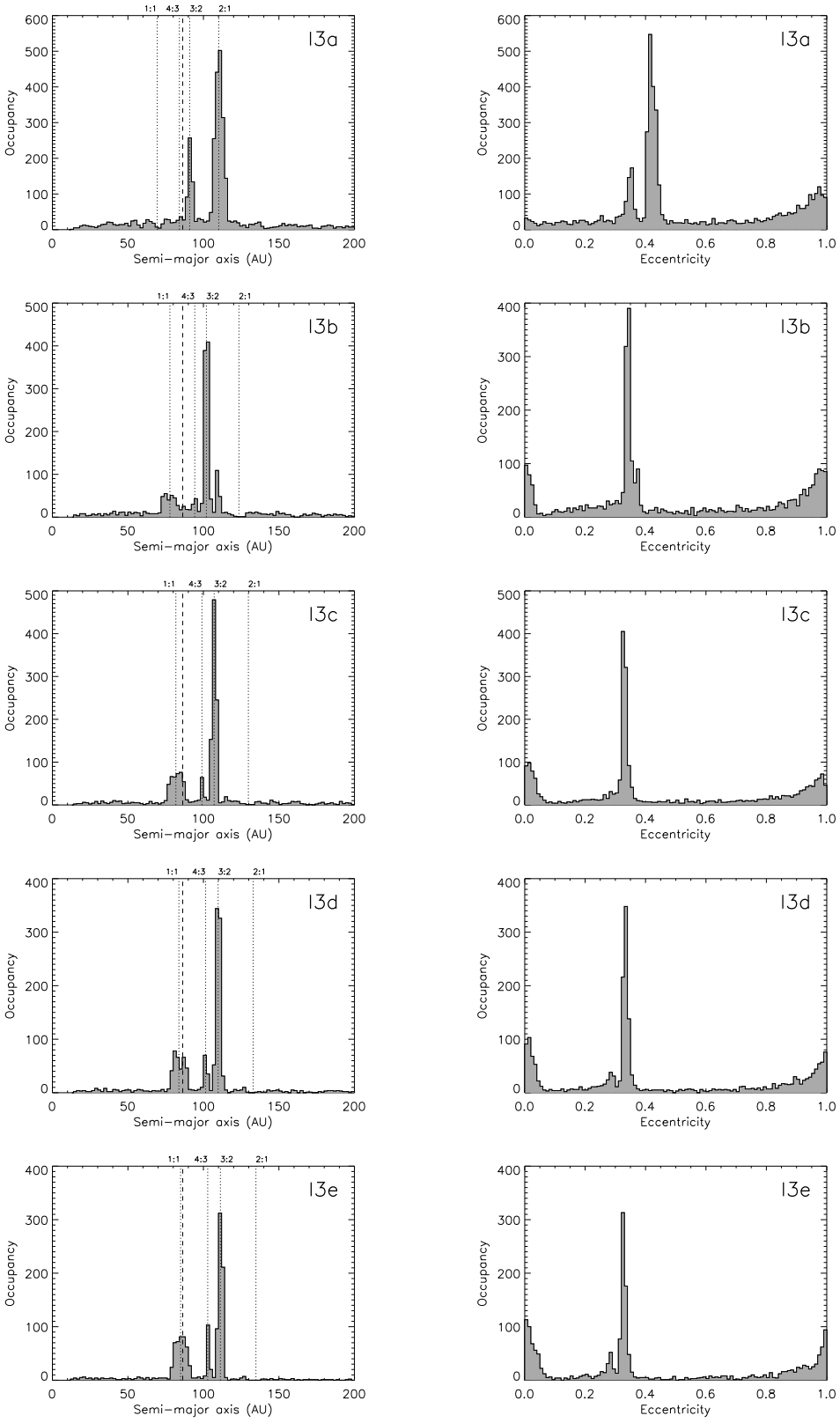

Figure 4.26. Distribution of semi-major axes and eccentricities for the model family I-3.

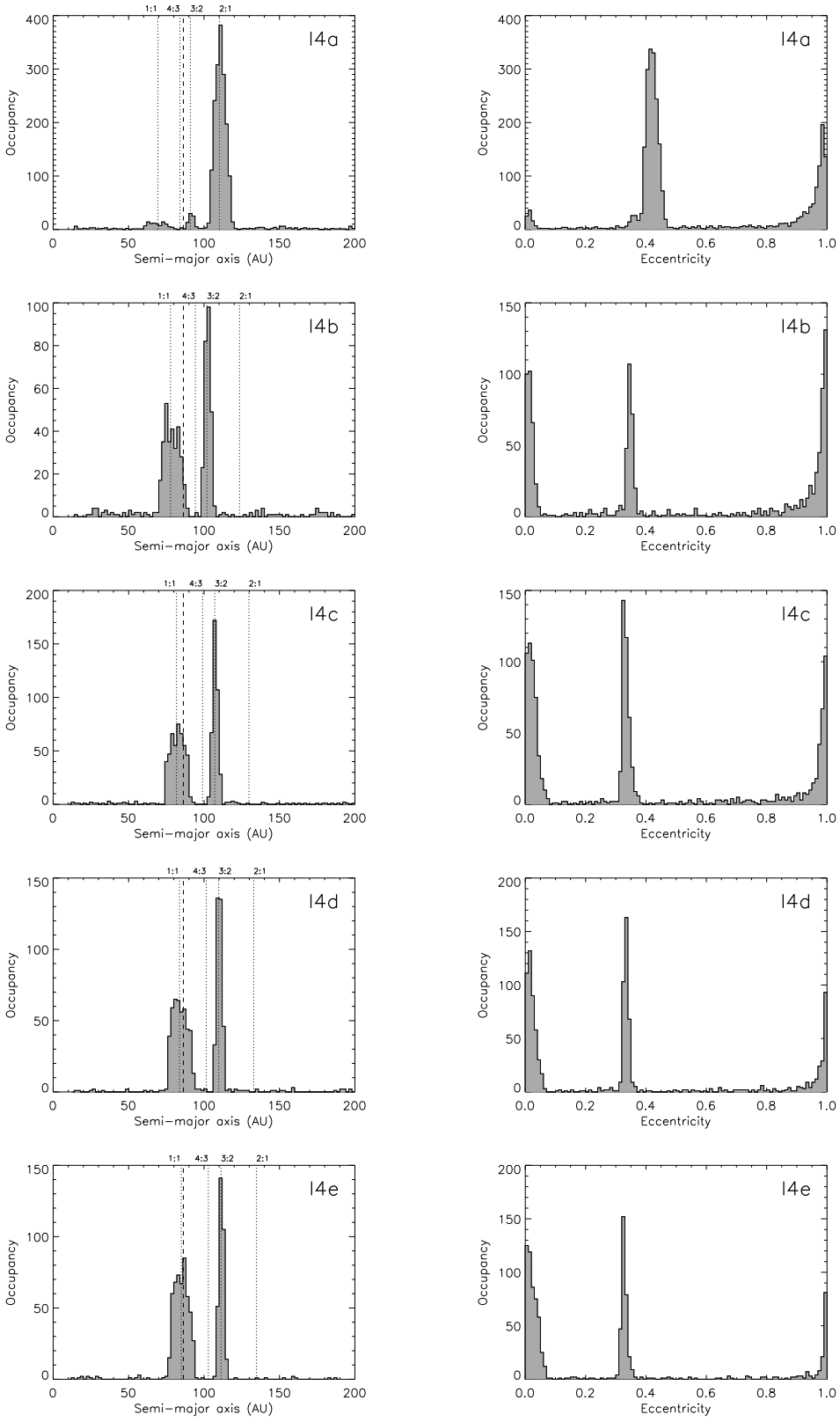

Figure 4.27. Distribution of semi-major axes and eccentricities for the model family I-4.

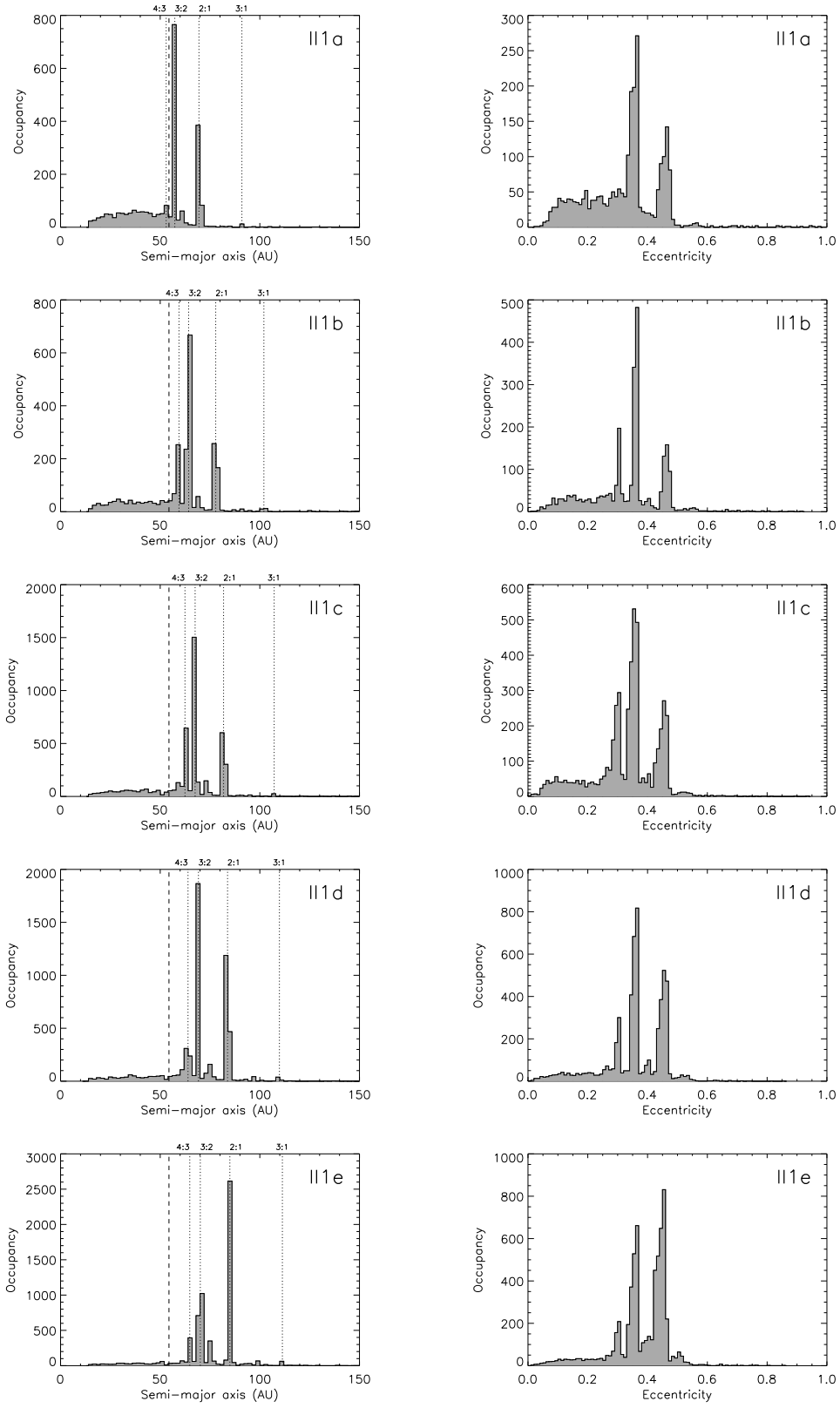

Figure 4.28. Distribution of semi-major axes and eccentricities for the model family II-1.

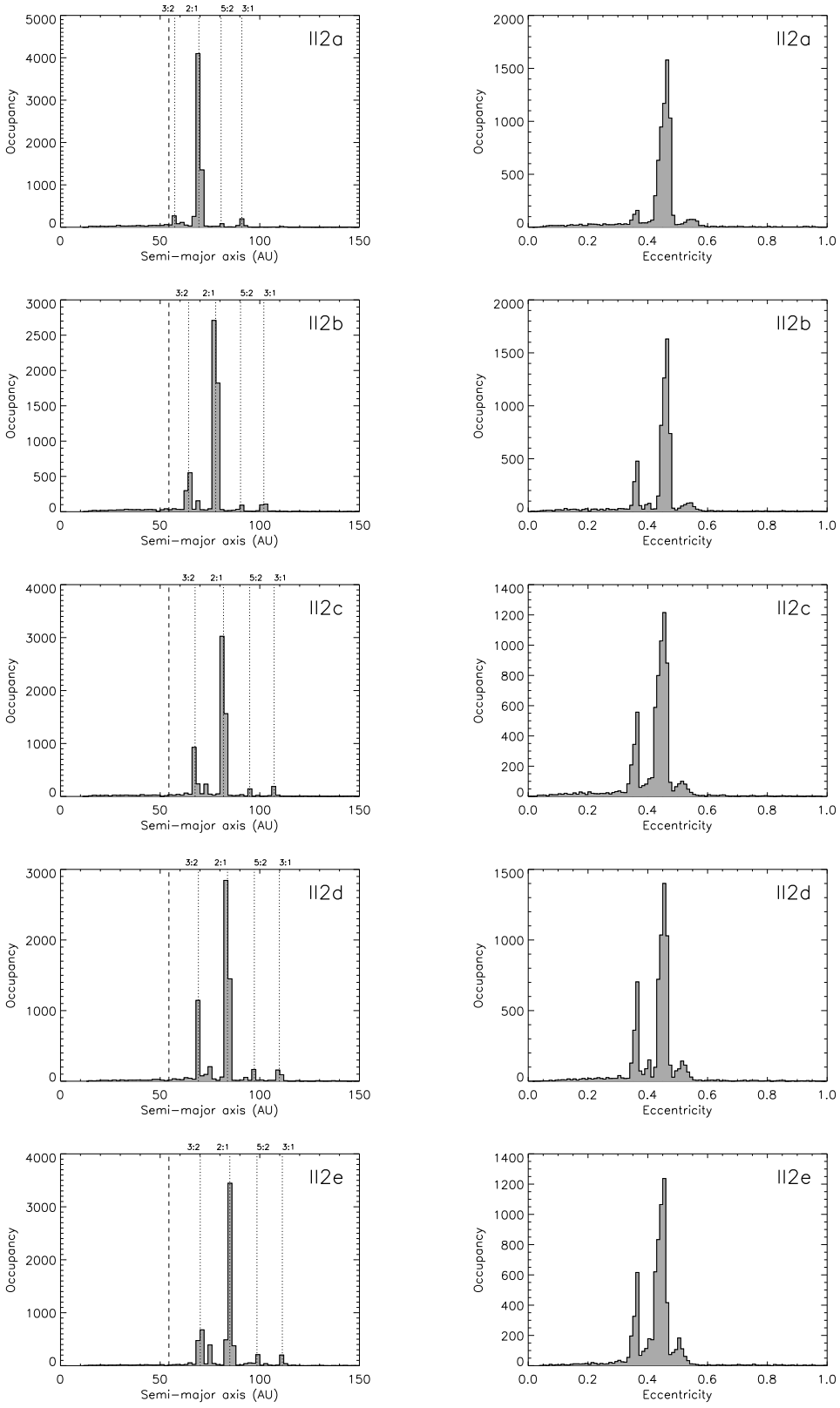

Figure 4.29. Distribution of semi-major axes and eccentricities for the model family II-2.

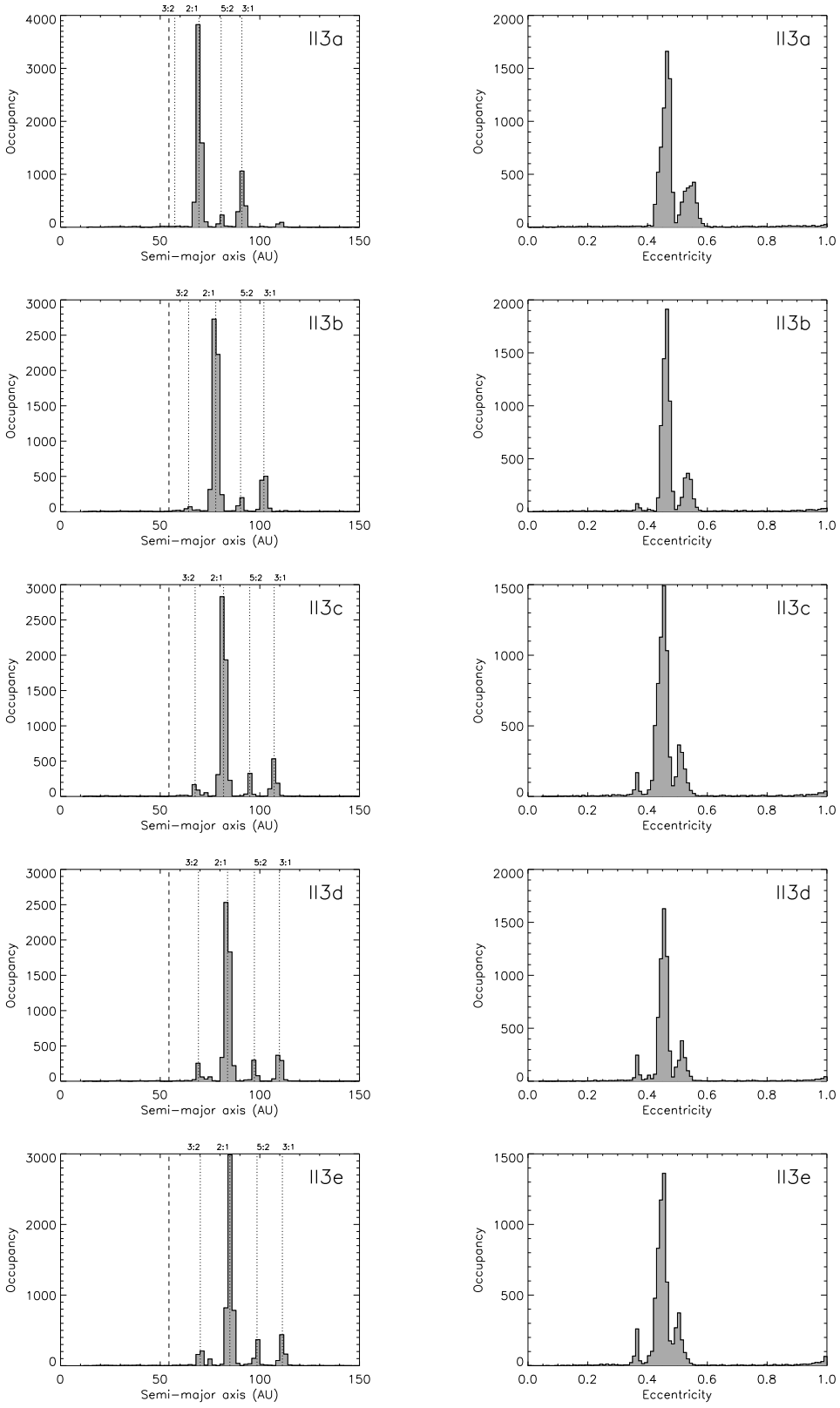

Figure 4.30. Distribution of semi-major axes and eccentricities for the model family II-3.

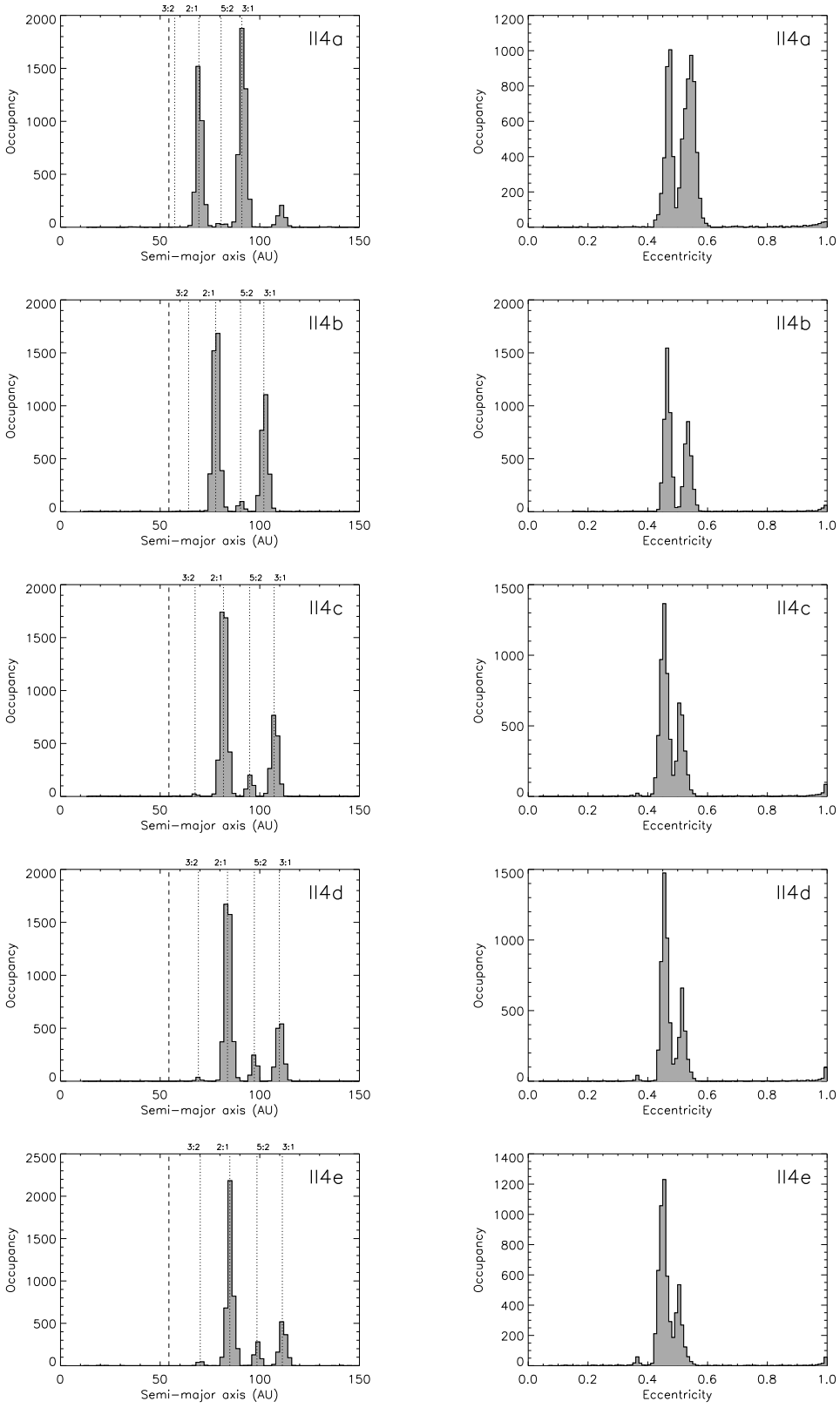

Figure 4.31. Distribution of semi-major axes and eccentricities for the model family II-4.

4.5.5 Simulated scattered-light images

The comparison of the disk models with the actual HST/NICMOS observation of HD 181327 necessitates the simulation of synthetic scattered light images. Wolf (2005) modelled the appearance of the disks at 1.1 μm by single-grain scattering taking into account the inclination of the disk, the illumination from the central star, and the optical properties of the dust grains. A circular region $0.3''$ in radius, corresponding to 15 AU at 50 pc, was cut from the scattered-light images, thereby mimicking the obscuration by the coronagraphic mask. Finally, the images were convolved with the 1.1-μm NICMOS point spread function in order to degrade the synthetic images to the HST resolution. The scattered light images are shown in Figure 4.32 and 4.33. The intensity scale has been stretched nonlinearly to enhance faint disk features.

For a direct comparison between the observation and various disk models a linear intensity scaling is more appropriate, presented in Figure 4.34 and 4.35. In the NICMOS image, the flux density inside $r \approx 1.2''$ (corresponding to $\lesssim 60$ AU) is dominated by residual noise from the PSF subtraction. This part of the image contains little useful information, and only disk structures outside of this region should be considered. We relied on visual judgement to assess the agreement between disk features seen in the observation and in the synthetic images.

The models of family II do not match the observations. The intensity of scattered light at the ring location ($r_{\rm ring} = 86.3$ AU) is very low. The faint arcs towards the observer seen in the high-mass, low-β models, (e. g. II-3d/e and II-4d/e) are primarily caused by anisotropic scattering on the diffuse disk edge. In addition, almost all resonant disk structures are well within the PSF-noise region.

Certain scattered-light images of the type-I models, however, seem to fit the observational features of the circumstellar ring quite well. The best agreement between the radial intensity distribution of the scattered light and the ring location is found for high planetary masses and small β parameters, i. e. larger dust grains. In particular, the model images I-4d and I-4e are consistent with the most salient features of the PSF-subtracted observation. A slight ambiguity, however, is introduced by the unknown position of the suspected planet with respect to the line of sight. We conclude that the ring of circumstellar debris observed around the HD 181327 can be interpreted as large dust particles locked in the 1:1 resonance with a 1 to 3 M_J planet on a circular orbit with radius 86.3 AU.

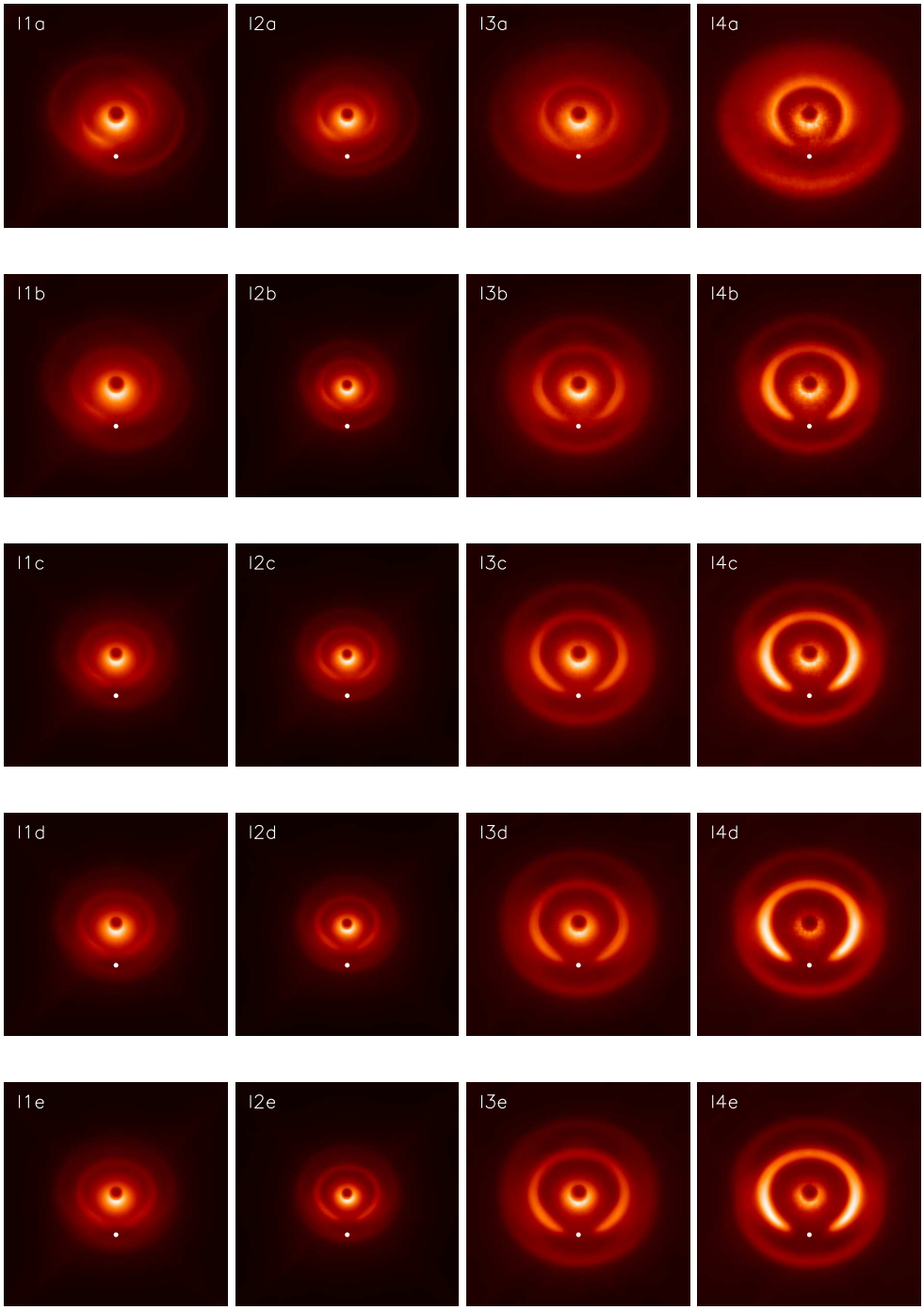

Figure 4.32. Simulated scattered-light images for debris disk model of type I. The intensity has been scaled as the cubic root of the flux density (in Jy/pixel). The position of the planet is marked by a white dot. Note that the side of the inner rim oriented towards the observer appears brighter due to anisotropic scattering.

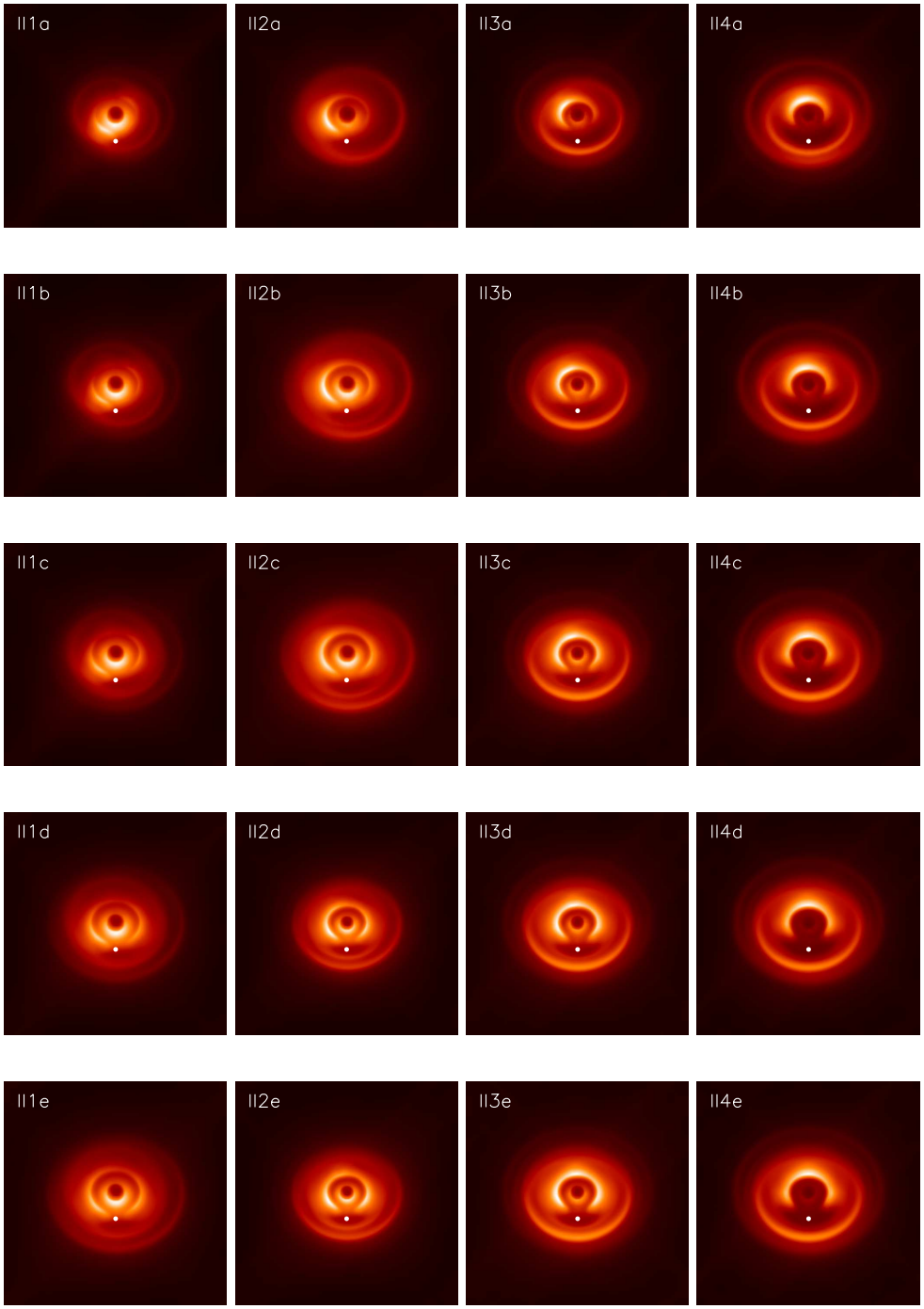

Figure 4.33. Simulated scattered-light images for debris disk model of type II. The intensity has been scaled as the cubic root of the flux density (in Jy/pixel). Each image has 513×513 pixels covering 400 by 400 AU.

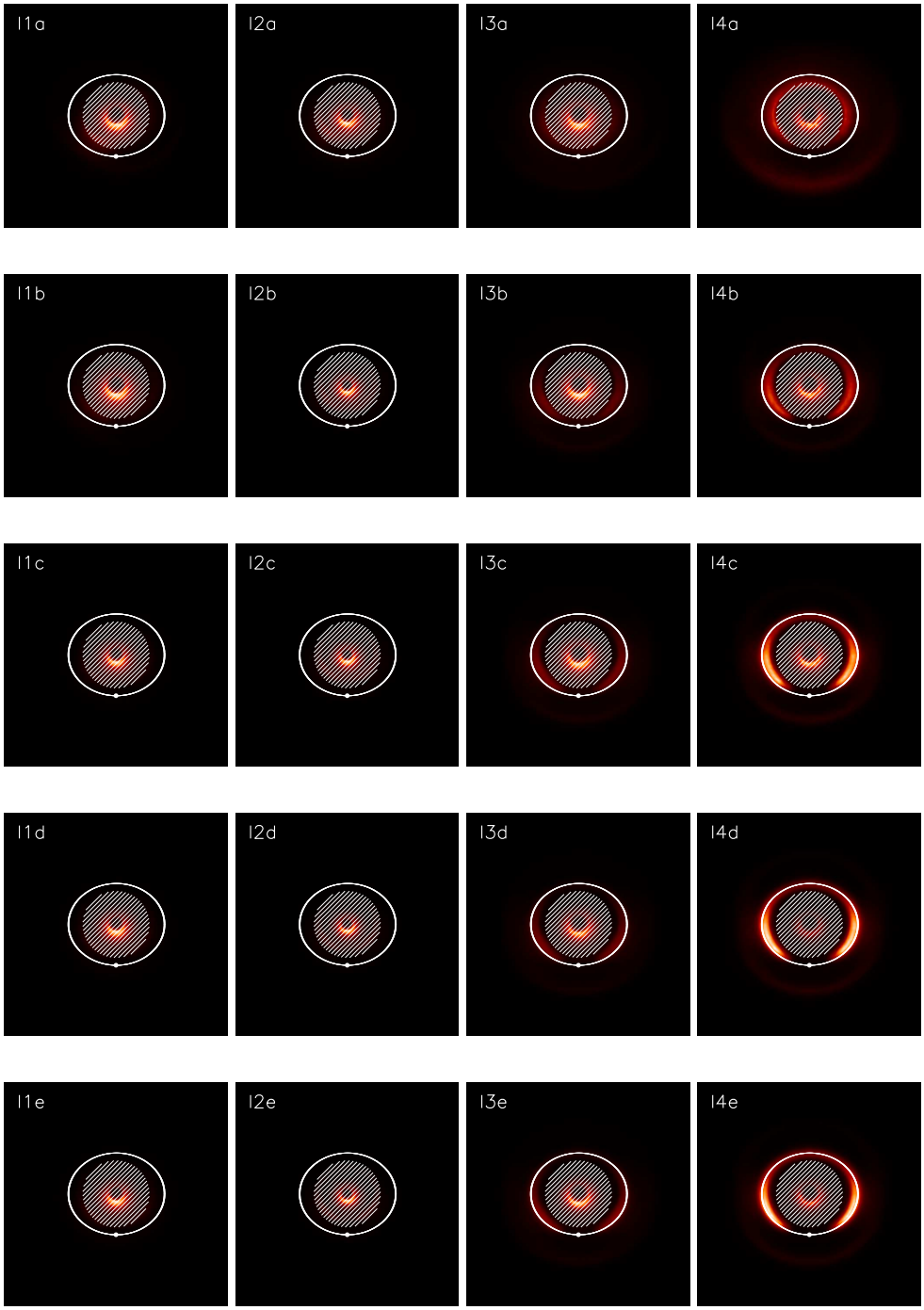

Figure 4.34. Comparison of the type-I scattered-light images with the location of the debris ring observed around HD 181327. The flux density of the image is scaled linearly. The ellipse shows a ring at 86.3 AU inclined by 31.7°; the position of the planet is marked by the white dot. The inner 60 AU dominated by residual noise are marked by the hatched circle.

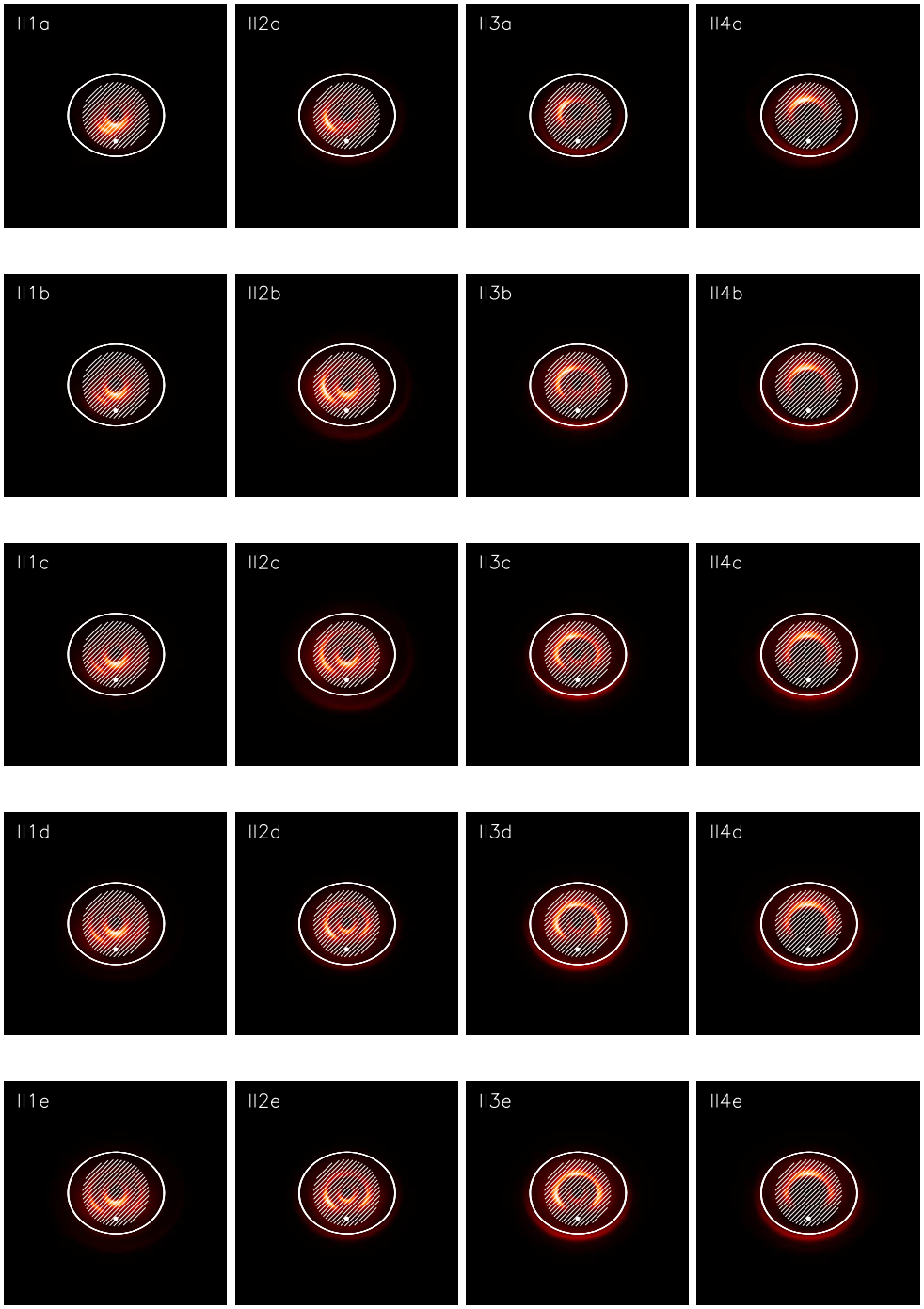

Figure 4.35. Comparison of the type-II scattered-light images with the location of the debris ring observed around HD 181327. Note that the planet ($a_{\rm pl} = 54.4$ AU), along with most of the resonance features, is located inside the excluded region shown by the hatched circle.

Chapter 5
Conclusions

These are the four that are never content:
that have never been filled since the dews began—
Jacala's mouth, and the glut of the kite,
and the hands of the ape, and the eyes of Man.

RUDYARD KIPLING, The Jungle Books

Science is like a giant jigsaw puzzle with countless players and an unknown number of pieces. Constantly pieces are added, made to fit, and removed. Progress on the big picture is made by accumulating the work of individual players whose solutions to a particular problem can establish links to adjacent fields. In the long run, an overarching framework is emerging. In this spirit, the studies presented here are aimed at obtaining a better understanding of the evolution of circumstellar disks by investigating the size and spatial distribution of dust in these systems.

Observing dust particle growth in disks around T Tauri stars A large sample of low-mass pre-main-sequence stars located in the Taurus-Auriga star-forming region has been investigated for signs of dust particle growth by means of 7-mm continuum observations obtained at the Very Large Array. Cold circumstellar material could be spatially resolved for 10 of the 14 targets. Two sources have insufficient signal-to-noise ratio for beam deconvolution, while another disk appears to be unresolved. GG Tau has been excluded on grounds of its complicated annular disk geometry. The disk sizes determined for the remaining 10 objects are in the range of 100–200 AU, effectively ruling out the possibility that the 7-mm emission originates from small, optically thick disks containing submicron-sized dust particles.

Knowing that the dust emission is mostly optically thin at 7 mm, the slopes of the millimetre spectral energy distributions could be directly translated into the frequency dependence of the dust opacity. After accounting for contributions from free-free emission and slight corrections for optical depth, dust opacity indices β between 0.5 and 1.6 were computed. Numerical values smaller than $\beta = 2$ are indicative for the presence of millimetre- to centimetre-sized dust aggregates in the bulk of the circumstellar disks. Four sources have $\beta > 1$, which could also be the result of submicron-sized dust with peculiar shape, composition, and/or porosity. Nevertheless, particle size remains the most influential parameter on the opacity indices, and the majority of sources show clear evidence for pebble-sized dust particles.

Table 5.1. Compilation of pre-main-sequence stars investigated for dust grain growth. The sample of Natta et al. (2004) is mainly composed of intermediate-mass pre-main-sequence stars (Herbig Ae objects), while the sources targeted in the present work are T Tauri stars. Disks resolved at millimetre wavelengths, i. e. where an unambiguous interpretation of shallow millimetre SEDs towards particle growth can be made, are shown in boldface.

Star	Spectral type	$T_\star$ (K)	$L_\star$ ($L_\odot$)	D (pc)	$M_\star$ ($M_\odot$)	Age (Myr)	$\lambda_{\max}$ (mm)	$\alpha_{\rm mm}$	β	$M_{\rm disk}$ ($M_\odot$)	Reference
HD 34282	A0	9800	36	400	2.3	3	3.2	3.0	1.3	0.09	Natta et al. (2004)
HD 150193	A1	9500	21	160	2.3	6	7.0	4.0	1.6	0.02	Natta et al. (2004)
HD 163296	A1	9500	36	122	2.3	5	7.0	2.6	0.8	0.05	Natta et al. (2004)
HD 35187	A2	9100	34	150	2.2	5	3.6	2.6	0.7	0.003	Natta et al. (2004)
UX Ori	A3	8600	42	450	2.2	3	7.0	2.0	0.0	0.03	Natta et al. (2004)
HD 142666	A8	7600	8	116	1.6	$>$10	7.0	2.2	0.4	0.01	Natta et al. (2004)
CQ Tau	F2	6900	4	100	1.5	$>$10	7.0	2.4	0.5	0.03	Testi et al. (2003)
HD 143006	G6	5770	0.8	82	1	$>$10	3.1	2.5	0.8	0.005	Natta et al. (2004)
TW Hya	K8	4000	0.23	55	0.6	10	7.0	2.3	0.7	0.03	Calvet et al. (2002)
RY Tau	K1	5080	7.60	140	1.69	0.2	7.0	2.5	0.8	0.04	This work
FT Tau	cont.	3890		140			7.0	2.6	0.9	0.03	This work
DG Tau B				140			7.0	2.9	1.4	0.14	This work
DG Tau	M	3890	1.7	140	0.56	0.3	7.0	2.5	0.7	0.06	This work
HL Tau	K7–M2	4060	0.9	140	0.55	1.0	7.0	2.9	1.3	0.12	This work
UZ Tau E	M1–3	3680	2.94	140	0.44	$<$0.1	7.0	2.6	0.8	0.02	This work
DL Tau	K7	4060	0.77	140	0.56	1.2	7.0	2.7	1.0	0.05	This work
CI Tau	K7	4060	0.87	140	0.70	0.8	7.0	3.0	1.3	0.03	This work
DO Tau	M0	3850	1.20	140	0.72	0.6	7.0	2.3	0.5	0.02	This work
GM Aur	K3	4730	0.83	140	0.72	1.8	7.0	3.2	1.6	0.04	This work
CY Tau	M1	3720	0.47	140	0.48	0.7	7.0	2.8	1.1	0.04	This work
GG Tau	K7	4060	1.50	140	0.65	0.3	7.0	2.9	1.2	0.11	This work
DM Tau	M1	3720	0.25	140	0.62	3.2	7.0	3.0	1.3	0.04	This work
LkCa 15	K5	4350	0.74	140		1.0	7.0	3.4	1.8	0.05	This work

These findings demonstrate that coagulation processes operate in the outer disks around T Tauri stars, and grain growth to millimetre- to centimetre-sized particles is completed within less than 1 Myr. The 10 T Tauri stars for which grain size information could be obtained constitute the largest sample of low-mass pre-main-sequence stars currently investigated for signs of dust particle growth to millimetre/centimetre dimensions. Together with similar results for TW Hya, CQ Tau, and two Herbig Ae stars, a picture of grain growth to pebble-sized particles in disks around low- to intermediate-mass pre-main-sequence stars is emerging (Table 5.1). Further investigations of grain growth with existing and upcoming millimetre interferometers are needed to study where and how fast the building blocks of planetesimals are formed. A publication reporting the results of this work is currently in press (Rodmann et al. 2006).

Analysis of infrared SEDs of debris disks based on Spitzer observations A fitting tool has been developed to model the infrared spectral energy distributions of main-sequence stars observed by the Spitzer Space Telescope in the framework of the Spitzer Legacy Science Program "Formation and Evolution of Planetary Systems"(FEPS). The Spitzer observations comprise photometry as well as low-resolution spectroscopy of a sample of 328 solar-type stars from 3 to 70 μm (up to 160 μm for a selected subsample) over a wide range of stellar ages (3 Myr–3 Gyr). A detailed modelling of the infrared excess emission for a number of stars allowed to derive physical properties of the circumstellar debris disks and of the constituent dust particles.

All of the debris disk systems modelled show evidence for large inner gaps (10–40 AU). The absence of circumstellar material in the inner disk is most likely the result of dust clearing by large planets, combined with an apparent lack of dust-producing minor bodies inside this region. One object (HD 12039) features an unusual ring-like debris disk, located at approximately 5 AU from the star and only $\sim$ 2 AU wide. This system is one of the few examples of debris material in the "terrestrial zone", and may be considered as an analogue of the solar system's asteroid belt. By comparing different stars with similar ages, it has been found that debris disk systems around solar-type stars display a great variety as a result of different initial conditions and/or divergent evolutionary paths. Several articles about FEPS sources appeared in the Astrophysical Journal (Meyer et al. 2004; Hollenbach et al. 2005; Kim et al. 2005) or are in press (Hines et al. 2005).

Dynamical models of debris disks with planets A Fortran code has been written to simulate the dynamical evolution of dust particles in debris disks. Based on a 'toy code', the relevant physics of a gas-free and collision-less system has been implemented. The model includes the gravitational perturbations of one or more planets, radiation pressure, and dissipative forces like Poynting-Robertson effect and stellar-wind drag. The loss of dust particles by ejection following close encounters with planets as well as sublimation in the vicinity of the star are treated correctly.

The Hermite integration scheme was found to be a suitable method to model the long-term evolution of massless test particles. The accuracy of the computation depends linearly on the integration time, and is proportional to the number of planets. The orbital eccentricities of the perturbing bodies have a relatively large impact on the accuracy. Systems with a planet on a moderately eccentric orbit are more expensive in terms of CPU power. The implementation of block time steps greatly economised computing time, and will enable the parallelisation of the code. The orbital evolution of, typically, $\sim 10^4$ dust particles can be followed for 10^6 orbits or more. The trapping of dust particles in mean motion resonances with a planet has been studied. Confirming the results of other works, only exterior resonances can compensate the dissipative effects of Poynting-Robertson drag and stellar wind to hold particles in quasi-stationary orbits.

Particles in interior resonances do not receive energy from repeated resonant encounters with the planet. Rather, the orbital decay is accelerated upon passage through interior commensurabilities, leading to an inner zone depleted in dust particles.

The debris disk model has been applied to reproduce the prominent structural features of a ring of circumstellar material recently discovered around the main-sequence star HD 181327. A set of 40 systems has been computed, varying the mass of the suspected planet, its distance to the star, and the dust grain size. A near-infrared scattered-light image has been generated for each model in order to match it to the actual HST/NICMOS coronagraphic image. The best agreement has been achieved for dust grains a few tens of microns in size locked in the 1:1 resonance with a Jupiter-mass (or more massive) planet on a circular orbit.

Appendix A
Astronomical and Physical Constants

Astronomical constants[1]

Astronomical unit	$1\ \mathrm{AU} = 1.495\,978\,7066 \times 10^{11}\ \mathrm{m}$
Parsec	$1\ \mathrm{pc} = 3.085\,6776 \times 10^{16}\ \mathrm{m}$
	$= 206\,264.806\ \mathrm{AU}$
Solar mass	$M_\odot = 1.9891 \times 10^{30}\ \mathrm{kg}$
Solar luminosity	$L_\odot = (3.845 \pm 0.008) \times 10^{26}\ \mathrm{W}$
Solar radius	$R_\odot = (6.955\,08 \pm 0.000\,26) \times 10^{8}\ \mathrm{m}$
Jupiter mass	$M_\mathrm{J} = 1.8987 \times 10^{27}\ \mathrm{kg}$
	$= 9.5455 \times 10^{-4}\ \mathrm{M}_\odot\ (1/1047.6\ \mathrm{M}_\odot)$
Earth mass	$M_\oplus = 5.9742 \times 10^{24}\ \mathrm{kg}$
	$= 3.1465 \times 10^{-3}\ \mathrm{M}_\mathrm{J}\ (1/317.82\ \mathrm{M}_\mathrm{J})$
Moon mass	$M_\mathrm{M} = 7.353 \times 10^{22}\ \mathrm{kg}$
	$= 12.3079 \times 10^{-3}\ \mathrm{M}_\oplus\ (1/81.248\ \mathrm{M}_\oplus)$

Physical constants[2]

Gravitational constant	$G = (6.6742 \pm 0.0010) \times 10^{-11}\ \mathrm{m^3\ kg^{-1}\ s^{-2}}$
Speed of light in vacuum	$c_0 = 299\,792\,458\ \mathrm{m\ s^{-1}}$ (exact value)
Boltzmann constant	$k_\mathrm{B} = (1.380\,6505 \pm 0.000\,0024) \times 10^{-23}\ \mathrm{J\ K^{-1}}$
Stefan-Boltzmann constant	$\sigma = (5.670\,400 \pm 0.000\,040) \times 10^{-8}\ \mathrm{W\ m^{-2}\ K^{-4}}$

[1] Taken from Cox (2000).

[2] 2002 CODATA recommended values of the fundamental physical constants; maintained at the Physics Laboratory of the National Institute of Standards and Technology (`http://physics.nist.gov/cuu/Constants/`).

Appendix B
List of Acronyms

ACS	Advanced Camera for Surveys
AO	Adaptive optics
AU	Astronomical unit
CPU	Central Processing Unit
CTA	Cryogenic telescope assembly
DDS	Debris Disk Radiative Transfer Simulation Tool
DSF	Debris Disk SED and Spectrum Fitting Tool
HPBW	Half-power beam width
HST	Hubble Space Telescope
IRAC	Infrared Array Camera
IRAS	Infrared Astronomical Satellite
IRS	Infrared Spectrograph
IRU	Inertial reference unit
ISM	Interstellar medium
ISO	Infrared Space Observatory
MIDI	Mid-Infrared Interferometric Instrument
MIPS	Multiband Infrared Photometer for Spitzer
MMR	Mean motion resonance
MODUST	Modelling of Dusty Stars
NICMOS	Near Infrared Camera and Multi-Object Spectrometer
PCRS	Pointing calibration reference sensors
PSF	Point spread function
SCUBA	Submillimetre Common User Bolometer Array
SED	Spectral energy distribution
SEST	Swedish-European Submillimetre Telescope
TTS	T Tauri star
VLA	Very Large Array

Bibliography

S. J. Aarseth. *Gravitational N-Body Simulations*. pp. 430. Cambridge, UK: Cambridge University Press, November 2003.

F. C. Adams, J. P. Emerson, and G. A. Fuller. Submillimeter photometry and disk masses of T Tauri disk systems. *ApJ*, 357:606–620, July 1990.

F. C. Adams, C. J. Lada, and F. H. Shu. Spectral evolution of young stellar objects. *ApJ*, 312: 788–806, January 1987.

S. H. P. Alencar and G. Basri. Profiles of Strong Permitted Lines in Classical T Tauri Stars. *AJ*, 119:1881–1900, April 2000.

W. J. Altenhoff, C. Thum, and H. J. Wendker. Radio emission from stars: A survey at 250 GHz. *A&A*, 281:161–183, January 1994.

P. Artymowicz. Beta Pictoris: an Early Solar System? *Annual Review of Earth and Planetary Sciences*, 25:175, 1997.

J.-C. Augereau. Structures in Dusty Disks. In *ASP Conf. Ser. 321: Extrasolar Planets: Today and Tomorrow*, page 305, December 2004.

J. C. Augereau, A. M. Lagrange, D. Mouillet, and F. Ménard. HST/NICMOS2 observations of the HD 141569 A circumstellar disk. *A&A*, 350:L51–L54, October 1999.

J. C. Augereau and J. C. B. Papaloizou. Structuring the HD 141569 A circumstellar dust disk. Impact of eccentric bound stellar companions. *A&A*, 414:1153–1164, February 2004.

H. H. Aumann, C. A. Beichman, F. C. Gillett, T. de Jong, J. R. Houck, F. J. Low, G. Neugebauer, R. G. Walker, and P. R. Wesselius. Discovery of a shell around Alpha Lyrae. *ApJL*, 278: L23–L27, March 1984.

Y. Avni. Energy spectra of X-ray clusters of galaxies. *ApJ*, 210:642–646, December 1976.

D. E. Backman and F. Paresce. Main-sequence stars with circumstellar solid material - The VEGA phenomenon. In *Protostars and Planets III*, pages 1253–1304, 1993.

M. E. Bailey, V. V. Emel'Yanenko, G. Hahn, N. W. Harris, K. A. Hughes, K. Muinonen, and J. V. Scotti. Oribital evolution of Comet 1995 O1 Hale-Bopp. *MNRAS*, 281:916–924, August 1996.

J. Bally, L. Testi, A. Sargent, and J. Carlstrom. Disk Mass Limits and Lifetimes of Externally Irradiated Young Stellar Objects Embedded in the Orion Nebula. *AJ*, 116:854–859, August 1998.

A. Balogh, R. G. Marsden, and E. J. Smith. *The heliosphere near solar minimum. The Ulysses perspective*. The heliosphere near solar minimum. The Ulysses perspective / André Balogh, Richard G. Marsden and Edward J. Smith (eds.). Springer-Praxis Books in Astrophysics and Astronomy. London: Springer. ISBN 1-85233-204-2, 2001, XXV + 411 pp., 2001.

E. E. Barnard. *Catalogue of 349 dark objects in the sky*. Chicago: University of Chicago Press, 1927, 1927.

D. Barrado y Navascués, J. R. Stauffer, I. Song, and J.-P. Caillault. The Age of beta Pictoris. *ApJL*, 520:L123–L126, August 1999.

C. Beauge and S. Ferraz-Mello. Resonance trapping in the primordial solar nebula - The case of a Stokes drag dissipation. *Icarus*, 103:301–318, June 1993.

C. Beauge and S. Ferraz-Mello. Capture in exterior mean-motion resonances due to Poynting-Robertson drag. *Icarus*, 110:239–260, August 1994.

S. V. W. Beckwith. Circumstellar Disks. In *NATO ASIC Proc. 540: The Origin of Stars and Planetary Systems*, page 579, 1999.

S. V. W. Beckwith, T. Henning, and Y. Nakagawa. Dust Properties and Assembly of Large Particles in Protoplanetary Disks. *Protostars and Planets IV*, page 533, May 2000.

S. V. W. Beckwith and A. I. Sargent. Particle emissivity in circumstellar disks. *ApJ*, 381:250–258, November 1991.

S. V. W. Beckwith, A. I. Sargent, R. S. Chini, and R. Güsten. A survey for circumstellar disks around young stellar objects. *AJ*, 99:924–945, March 1990.

C. Bertout. T Tauri stars - Wild as dust. *ARA&A*, 27:351–395, 1989.

H. Beust, A.-M. Lagrange, I. A. Crawford, C. Goudard, J. Spyromilio, and A. Vidal-Madjar. The beta Pictoris circumstellar disk. XXV. The Ca Ii absorption lines and the Falling Evaporating Bodies model revisited using UHRF observations. *A&A*, 338:1015–1030, October 1998.

J. Binney and M. Merrifield. *Galactic astronomy*. Princeton University Press, 1998.

R. P. Binzel. Planetary science: Spin control for asteroids. *Nature*, 425:131–132, September 2003.

C. F. Bohren and D. R. Huffman. *Absorption and scattering of light by small particles*. New York: Wiley, 1983, 1983.

J. Bouwman, G. Meeus, A. de Koter, S. Hony, C. Dominik, and L. B. F. M. Waters. Processing of silicate dust grains in Herbig Ae/Be systems. *A&A*, 375:950–962, September 2001.

R. E. Briggs. Symposium: Astrometry I: The steady-state space distribution of meteoric particles under the operation of the Poynting-Robertson Effect. *AJ*, 67:710, December 1962.

J. A. Burns, P. L. Lamy, and S. Soter. Radiation forces on small particles in the solar system. *Icarus*, 40:1–48, October 1979.

N. Calvet, P. D'Alessio, L. Hartmann, D. Wilner, A. Walsh, and M. Sitko. Evidence for a Developing Gap in a 10 Myr Old Protoplanetary Disk. *ApJ*, 568:1008–1016, April 2002.

N. Calvet and L. Hartmann. Balmer line profiles for infalling T Tauri envelopes. *ApJ*, 386:239–247, February 1992.

N. Calvet, L. Hartmann, and S. E. Strom. Evolution of Disk Accretion. *Protostars and Planets IV*, page 377, May 2000.

C. L. Carilli, J. E. Carlstrom, and M. A. Holdaway. Millimeter Interferometry. In *ASP Conf. Ser. 180: Synthesis Imaging in Radio Astronomy II*, page 565, 1999.

J. M. Carpenter. *private communication*, 2004.

J. M. Carpenter, S. Wolf, K. Schreyer, R. Launhardt, and T. Henning. Evolution of Cold Circumstellar Dust around Solar-type Stars. *AJ*, 129:1049–1062, February 2005.

J. Cernicharo, R. Bachiller, and G. Duvert. The Taurus-Auriga-Perseus complex of dark clouds. I - Density structure. *A&A*, 149:273–282, August 1985.

M. Clampin, J. E. Krist, D. R. Ardila, D. A. Golimowski, G. F. Hartig, H. C. Ford, G. D. Illingworth, F. Bartko, N. Benítez, J. P. Blakeslee, R. J. Bouwens, T. J. Broadhurst, R. A. Brown, C. J. Burrows, E. S. Cheng, N. J. G. Cross, P. D. Feldman, M. Franx, C. Gronwall, L. Infante, R. A. Kimble, M. P. Lesser, A. R. Martel, F. Menanteau, G. R. Meurer, G. K. Miley, M. Postman, P. Rosati, M. Sirianni, W. B. Sparks, H. D. Tran, Z. I. Tsvetanov, R. L. White, and W. Zheng. Hubble Space Telescope ACS Coronagraphic Imaging of the Circumstellar Disk around HD 141569A. *AJ*, 126:385–392, July 2003.

M. Cohen. The case for anisotropic mass loss from T Tauri stars. *PASP*, 94:266–270, April 1982.

M. Cohen. HL Tauri and its circumstellar disk. *ApJL*, 270:L69–L71, July 1983.

M. Cohen and J. H. Bieging. Radio variability and structure of T Tauri stars. *AJ*, 92:1396–1402, December 1986.

M. Cohen, J. H. Bieging, and P. R. Schwartz. VLA observations of mass loss from T Tauri stars. *ApJ*, 253:707–715, February 1982.

M. Cohen, S. T. Megeath, P. L. Hammersley, F. Martín-Luis, and J. Stauffer. Spectral Irradiance Calibration in the Infrared. XIII. "Supertemplates" and On-Orbit Calibrators for the SIRTF Infrared Array Camera. *AJ*, 125:2645–2663, May 2003.

A. N. Cox. *Allen's astrophysical quantities, 4th ed.* Springer, AIP Press, New York, 2000.

G. Cutispoto, L. Pastori, L. Pasquini, J. R. de Medeiros, G. Tagliaferri, and J. Andersen. Fast-rotating nearby solar-type stars, Li abundances and X-ray luminosities. I. Spectral classification, v sin i, Li abundances and X-ray luminosities. *A&A*, 384:491–503, March 2002.

G. Decin, C. Dominik, L. B. F. M. Waters, and C. Waelkens. Age Dependence of the Vega Phenomenon: Observations. *ApJ*, 598:636–644, November 2003.

A. T. Deller and S. T. Maddison. Numerical Modeling of Dusty Debris Disks. *ApJ*, 625:398–413, May 2005.

W. R. F. Dent, J. S. Greaves, V. Mannings, I. M. Coulson, and D. M. Walther. A search for molecular gas components in prototypal Vega-excess systems. *MNRAS*, 277:L25–L29, November 1995.

W. R. F. Dent, H. J. Walker, W. S. Holland, and J. S. Greaves. Models of the dust structures around Vega-excess stars. *MNRAS*, 314:702–712, June 2000.

S. F. Dermott, S. Jayaraman, Y. L. Xu, B. A. S. Gustafson, and J. C. Liou. A circumsolar ring of asteroidal dust in resonant lock with the Earth. *Nature*, 369:719–723, June 1994.

J. S. Dohnanyi. Collisional model of asteroids and their debris. *J. Geophys. Res.*, 74:2431–2554, 1969.

J. S. Dohnanyi. *Particle dynamics*, pages 527–605. Cosmic Dust, 1978.

C. Dominik and G. Decin. Age Dependence of the Vega Phenomenon: Theory. *ApJ*, 598:626–635, November 2003.

J. Dorschner. Infrared Spectra of Silicate Grains. *Astronomische Nachrichten*, 293:53, July 1971.

B. T. Draine. On the Submillimeter Opacity of Protoplanetary Disks. astro-ph/0507292 (ApJ submitted), 2005.

B. T. Draine and H. M. Lee. Optical properties of interstellar graphite and silicate grains. *ApJ*, 285:89–108, October 1984.

A. Duquennoy and M. Mayor. Duplicity in the solar neighbourhood. III - New spectroscopic elements for nine solar-type binary stars. *A&A*, 195:129–147, April 1988.

A. Dutrey, S. Guilloteau, G. Duvert, L. Prato, M. Simon, K. Schuster, and F. Menard. Dust and gas distribution around T Tauri stars in Taurus-Auriga. I. Interferometric 2.7mm continuum and ˆ13ˆCO J=1-0 observations. *A&A*, 309:493–504, May 1996.

A. Dutrey, S. Guilloteau, and M. Simon. Images of the GG Tauri rotating ring. *A&A*, 286:149–159, June 1994.

G. Duvert, S. Guilloteau, F. Ménard, M. Simon, and A. Dutrey. A search for extended disks around weak-lined T Tauri stars. *A&A*, 355:165–170, March 2000.

J. H. Elias. A study of the Taurus dark cloud complex. *ApJ*, 224:857–872, September 1978.

S. B. Fajardo-Acosta, R. E. Stencel, and D. E. Backman. Infrared Space Observatory Mapping of 60 MU M Dust Emission Around Vega-type Systems. *ApJL*, 487:L151, October 1997.

G. G. Fazio, J. L. Hora, L. E. Allen, M. L. N. Ashby, P. Barmby, L. K. Deutsch, J.-S. Huang, S. Kleiner, M. Marengo, S. T. Megeath, G. J. Melnick, M. A. Pahre, B. M. Patten, J. Polizotti, H. A. Smith, R. S. Taylor, Z. Wang, S. P. Willner, W. F. Hoffmann, J. L. Pipher, W. J. Forrest, C. W. McMurty, C. R. McCreight, M. E. McKelvey, R. E. McMurray, D. G. Koch, S. H. Moseley, R. G. Arendt, J. E. Mentzell, C. T. Marx, P. Losch, P. Mayman, W. Eichhorn, D. Krebs, M. Jhabvala, D. Y. Gezari, D. J. Fixsen, J. Flores, K. Shakoorzadeh, R. Jungo, C. Hakun, L. Workman, G. Karpati, R. Kichak, R. Whitley, S. Mann, E. V. Tollestrup, P. Eisenhardt, D. Stern, V. Gorjian, B. Bhattacharya, S. Carey, B. O. Nelson, W. J. Glaccum, M. Lacy, P. J. Lowrance, S. Laine, W. T. Reach, J. A. Stauffer, J. A. Surace, G. Wilson, E. L. Wright, A. Hoffman, G. Domingo, and M. Cohen. The Infrared Array Camera (IRAC) for the Spitzer Space Telescope. *ApJS*, 154:10–17, September 2004.

E. D. Feigelson and T. Montmerle. High-Energy Processes in Young Stellar Objects. *ARA&A*, 37: 363–408, 1999.

G. J. Flynn. Sources of 10 Micron Interplanetary Dust: the Contribution from the Kuiper Belt. In *ASP Conf. Ser. 104: IAU Colloq. 150: Physics, Chemistry, and Dynamics of Interplanetary Dust*, page 171, 1996.

A. Fujiwara, P. Cerroni, D. Davis, E. Ryan, and M. di Martino. Experiments and scaling laws for catastrophic collisions. In *Asteroids II*, pages 240–265, 1989.

M. Güdel. Stellar Radio Astronomy: Probing Stellar Atmospheres from Protostars to Giants. *ARA&A*, 40:217–261, 2002.

P. R. Gazis. Long-term enhancements in solar wind speed. *J. Geophys. Res.*, 101:415–424, January 1996.

N. Gershenfeld. *The nature of mathematical modeling*. Cambridge ; New York: Cambridge University Press, 1999., 1999.

A. M. Ghez, G. Neugebauer, and K. Matthews. The multiplicity of T Tauri stars in the star forming regions Taurus-Auriga and Ophiuchus-Scorpius: A 2.2 micron speckle imaging survey. *AJ*, 106: 2005–2023, November 1993.

C. K. Goertz. Dusty plasmas in the solar system. *Reviews of Geophysics*, 27:271–292, May 1989.

N. N. Gor'kavyi, L. M. Ozernoy, J. C. Mather, and T. Taidakova. Quasi-Stationary States of Dust Flows under Poynting-Robertson Drag: New Analytical and Numerical Solutions. *ApJ*, 488: 268, October 1997.

J. S. Greaves, W. S. Holland, G. Moriarty-Schieven, T. Jenness, W. R. F. Dent, B. Zuckerman, C. McCarthy, R. A. Webb, H. M. Butner, W. K. Gear, and H. J. Walker. A Dust Ring around epsilon Eridani: Analog to the Young Solar System. *ApJL*, 506:L133–L137, October 1998.

J. S. Greaves, V. Mannings, and W. S. Holland. The Dust and Gas Content of a Disk around the Young Star HR 4796A. *Icarus*, 143:155–158, January 2000.

E. Grün. Interplanetry Dust and the Zodiacal Cloud. In *Encyclopedia of the Solar System*, pages 673–696, 1999.

E. Grün, B. A. S. Gustafson, S. Dermott, and H. Fechtig. *Interplanetary dust*. Berlin : Springer, 2001. / (Astronomy and astrophysics library, 2001.

E. Grün, H. A. Zook, H. Fechtig, and R. H. Giese. Collisional balance of the meteoritic complex. *Icarus*, 62:244–272, May 1985.

A. W. Guess. Poynting-Robertson effect for a spherical source of radiation. *ApJ*, 135:855–866, May 1962.

S. Guilloteau, A. Dutrey, and M. Simon. GG Tauri: the ring world. *A&A*, 348:570–578, August 1999.

B. A. S. Gustafson. Physics of Zodiacal Dust. *Annual Review of Earth and Planetary Sciences*, 22:553–595, 1994.

H. J. Habing, C. Dominik, M. Jourdain de Muizon, R. J. Laureijs, M. F. Kessler, K. Leech, L. Metcalfe, A. Salama, R. Siebenmorgen, N. Trams, and P. Bouchet. Incidence and survival of remnant disks around main-sequence stars. *A&A*, 365:545–561, January 2001.

K. E. Haisch, E. A. Lada, and C. J. Lada. Disk Frequencies and Lifetimes in Young Clusters. *ApJL*, 553:L153–L156, June 2001.

T. Handa, S. M. Miyama, T. Yamashita, T. Omodaka, Y. Kitamura, M. Hayashi, T. Onishi, R. L. Snell, S. E. Strom, K. M. Strom, M. F. Skrutskie, S. Edwards, N. Ohashi, K. Sunada, M. Saito, Y. Fukui, A. Mizuno, J. Watanabe, and H. Kataza. Detection of a Circumstellar Gas around DM Tauri: A Protoplanetary Disk around a Single Star? *ApJ*, 449:894, August 1995.

D. A. Harper, R. F. Loewenstein, and J. A. Davidson. On the nature of the material surrounding VEGA. *ApJ*, 285:808–812, October 1984.

L. Hartmann. Flows, Fragmentation, and Star Formation. I. Low-Mass Stars in Taurus. *ApJ*, 578: 914–924, October 2002.

P. M. Harvey, B. J. Smith, J. Difrancesco, C. Colome, and F. J. Low. Far-Infrared Constraints on Dust Shells around Vega-like Stars. *ApJ*, 471:973, November 1996.

M. Harwit. Origins of the Zodiacal Dust Cloud. *J. Geophys. Res.*, 68:2171, April 1963.

A. P. Hatzes, W. D. Cochran, B. McArthur, S. L. Baliunas, G. A. H. Walker, B. Campbell, A. W. Irwin, S. Yang, M. Kürster, M. Endl, S. Els, R. P. Butler, and G. W. Marcy. Evidence for a Long-Period Planet Orbiting ϵ Eridani. *ApJL*, 544:L145–L148, December 2000.

S. R. Heap, D. J. Lindler, T. M. Lanz, R. H. Cornett, I. Hubeny, S. P. Maran, and B. Woodgate. Space Telescope Imaging Spectrograph Coronagraphic Observations of β Pictoris. *ApJ*, 539: 435–444, August 2000.

W. J. Henney and C. R. O'Dell. A Keck High-Resolution Spectroscopic Study of the Orion Nebula Pro plyds. *AJ*, 118:2350–2368, November 1999.

T. Henning, B. Michel, and R. Stognienko. Dust opacities in dense regions. *PNSS*, 43:1333–1343, February 1995.

T. Henning and H. Mutschke. Low-temperature infrared properties of cosmic dust analogues. *A&A*, 327:743–754, November 1997.

L. C. Henyey and J. L. Greenstein. Diffuse radiation in the Galaxy. *ApJ*, 93:70–83, January 1941.

G. H. Herbig. Radial velocities and spectral types of T Tauri stars. *ApJ*, 214:747–758, June 1977.

G. H. Herbig and K. R. Bell. Emission-Line Stars of the Orion Population. *Lick Obs. Bull.*, 1111, 1988.

W. Herbst, D. K. Herbst, E. J. Grossman, and D. Weinstein. Catalogue of UBVRI photometry of T Tauri stars and analysis of the causes of their variability. *AJ*, 108:1906–1923, November 1994.

R. H. Hildebrand. The Determination of Cloud Masses and Dust Characteristics from Submillimetre Thermal Emission. *Q. J. R. Astron. Soc.*, 24:267, September 1983.

D. C. Hines, D. E. Backman, J. Bouwman, L. A. Hillenbrand, J. M. Carpenter, M. R. Meyer, J. S. Kim, M. D. Silverstone, J. Rodmann, S. Wolf, E. E. Mamajek, T. Y. Brooke, D. L. Padgett, T. Henning, A. Moro-Martin, E. Stobie, K. D. Gordon, J. E. Morrison, J. Muzerolle, and K.Y.L. Su. The formation and evolution of planetary systems (feps): Discovery of an unusual debris disk system associated with HD 12039. *ApJ*, in press (astro-ph/0510294), 2005.

G. A. Hirth, R. Mundt, and J. Solf. Spatial and kinematic properties of the forbidden emission line region of T Tauri stars. 126:437–469, December 1997.

W. S. Holland, J. S. Greaves, W. R. F. Dent, M. C. Wyatt, B. Zuckerman, R. A. Webb, C. McCarthy, I. M. Coulson, E. I. Robson, and W. K. Gear. Submillimeter Observations of an Asymmetric Dust Disk around Fomalhaut. *ApJ*, 582:1141–1146, January 2003.

W. S. Holland, J. S. Greaves, B. Zuckerman, R. A. Webb, C. McCarthy, I. M. Coulson, D. M. Walther, W. R. F. Dent, W. K. Gear, and I. Robson. Submillimetre images of dusty debris around nearby stars. *Nature*, 392:788–790, 1998.

D. Hollenbach, U. Gorti, M. Meyer, J. S. Kim, P. Morris, J. Najita, I. Pascucci, J. Carpenter, J. Rodmann, T. Brooke, L. Hillenbrand, E. Mamajek, D. Padgett, D. Soderblom, S. Wolf, and J. Lunine. Formation and Evolution of Planetary Systems: Upper Limits to the Gas Mass in HD 105. *ApJ*, 631:1180–1190, October 2005.

E. K. Holmes, S. F. Dermott, B. Å. S. Gustafson, and K. Grogan. Resonant Structure in the Kuiper Disk: An Asymmetric Plutino Disk. *ApJ*, 597:1211–1236, November 2003.

M. Honda, H. Kataza, Y. K. Okamoto, T. Miyata, T. Yamashita, S. Sako, S. Takubo, and T. Onaka. Detection of Crystalline Silicates around the T Tauri Star Hen 3-600A. *ApJL*, 585:L59–L63, March 2003.

J. R. Houck, T. L. Roellig, J. van Cleve, W. J. Forrest, T. Herter, C. R. Lawrence, K. Matthews, H. J. Reitsema, B. T. Soifer, D. M. Watson, D. Weedman, M. Huisjen, J. Troeltzsch, D. J. Barry, J. Bernard-Salas, C. E. Blacken, B. R. Brandl, V. Charmandaris, D. Devost, G. E. Gull, P. Hall, C. P. Henderson, S. J. U. Higdon, B. E. Pirger, J. Schoenwald, G. C. Sloan, K. I. Uchida, P. N. Appleton, L. Armus, M. J. Burgdorf, S. B. Fajardo-Acosta, C. J. Grillmair, J. G. Ingalls, P. W. Morris, and H. I. Teplitz. The Infrared Spectrograph (IRS) on the Spitzer Space Telescope. *ApJS*, 154:18–24, September 2004.

C. A. Hummel, J. T. Armstrong, D. F. Buscher, D. Mozurkewich, A. Quirrenbach, and M. Vivekanand. Orbits of Small Angular Scale Binaries Resolved with the Mark III Interferometer. *AJ*, 110:376, July 1995.

R. Jayawardhana, S. Fisher, L. Hartmann, C. Telesco, R. Pina, and G. Fazio. A Dust Disk Surrounding the Young A Star HR 4796A. *ApJL*, 503:L79, August 1998.

E. L. N. Jensen, D. W. Koerner, and R. D. Mathieu. High-Resolution Imaging of Circumstellar Gas and Dust in UZ Tauri: Comparing Binary and Single-Star Disk Properties. *AJ*, 111:2431, June 1996.

D. Jewitt and J. Luu. Discovery of the candidate Kuiper belt object 1992 QB1. *Nature*, 362: 730–732, April 1993.

D. Jewitt, J. Luu, and J. Chen. The Mauna Kea-Cerro-Tololo (MKCT) Kuiper Belt and Centaur Survey. *AJ*, 112:1225, September 1996.

D. C. Jewitt and J. X. Luu. Physical Nature of the Kuiper Belt. *Protostars and Planets IV*, page 1201, May 2000.

C. M. Johns-Krull, J. A. Valenti, A. P. Hatzes, and A. Kanaan. Spectropolarimetry of Magnetospheric Accretion on the Classical T Tauri Star BP Tauri. *ApJL*, 510:L41–L44, January 1999.

C. M. Johns-Krull, J. A. Valenti, N. E. Piskunov, S. H. Saar, and A. P. Hatzes. New Measurements of T Tauri Magnetic Fields: Testing Magnetospheric Accretion. In *ASP Conf. Ser. 248: Magnetic Fields Across the Hertzsprung-Russell Diagram*, page 527, 2001.

B. F. Jones and G. H. Herbig. Proper motions of T Tauri variables and other stars associated with the Taurus-Auriga dark clouds. *AJ*, 84:1872–1889, December 1979.

A. H. Joy. Spectral Criteria in the Classification of Variable Stars. *PASP*, 54:15, February 1942.

A. H. Joy. T Tauri Variable Stars. *ApJ*, 102:168, September 1945.

A. H. Joy. Bright-Line Stars among the Taurus Dark Clouds. *ApJ*, 110:424, November 1949.

M. Jura, M. Malkan, R. White, C. Telesco, R. Pina, and R. S. Fisher. A Protocometary Cloud around HR 4796A? *ApJ*, 505:897–902, October 1998.

P. Kalas and D. Jewitt. Asymmetries in the Beta Pictoris Dust Disk. *AJ*, 110:794, August 1995.

M.-B. Kallenrode. *Space Physics*. Springer-Verlag Berlin Heidelberg New York, 1998.

S. J. Kenyon and B. C. Bromley. Dusty Rings: Signposts of Recent Planet Formation. *ApJL*, 577: L35–L38, September 2002.

S. J. Kenyon, D. Dobrzycka, and L. Hartmann. A new optical extinction law and distance estimate for the Taurus-Auriga molecular cloud. *AJ*, 108:1872–1880, November 1994.

S. J. Kenyon and L. Hartmann. Pre-Main-Sequence Evolution in the Taurus-Auriga Molecular Cloud. *ApJS*, 101:117, November 1995.

J. S. Kim, D. C. Hines, D. E. Backman, L. A. Hillenbrand, M. R. Meyer, J. Rodmann, A. Moro-Martín, J. M. Carpenter, M. D. Silverstone, J. Bouwman, E. E. Mamajek, S. Wolf, R. Malhotra, I. Pascucci, J. Najita, D. L. Padgett, T. Henning, T. Y. Brooke, M. Cohen, S. E. Strom, E. B. Stobie, C. W. Engelbracht, K. D. Gordon, K. Misselt, J. E. Morrison, J. Muzerolle, and K. Y. L. Su. Formation and Evolution of Planetary Systems: Cold Outer Disks Associated with Sun-like Stars. *ApJ*, 632:659–669, October 2005.

D. Kirkwood. *Meteoric astronomy: a treatise on shooting-stars, fireballs, and aerolites.* Philadelphia, J. B. Lippincott & co., 1867.

Y. Kitamura, M. Momose, S. Yokogawa, R. Kawabe, M. Tamura, and S. Ida. Investigation of the Physical Properties of Protoplanetary Disks around T Tauri Stars by a 1 Arcsecond Imaging Survey: Evolution and Diversity of the Disks in Their Accretion Stage. *ApJ*, 581:357–380, December 2002.

J. Klačka. Poynting-Robertson effect. I - Equation of motion. *Earth Moon and Planets*, 59:41–59, October 1992.

R. F. Knacke. Extinction by Interstellar Silica Grains. *Nature*, 217:44, 1968.

R. F. Knacke, S. B. Fajardo-Acosta, C. M. Telesco, J. A. Hackwell, D. K. Lynch, and R. W. Russell. The Silicates in the Disk of beta Pictoris. *ApJ*, 418:440, November 1993.

D. W. Koerner, C. J. Chandler, and A. I. Sargent. Aperture Synthesis Imaging of the Circumstellar Dust Disk around DO Tauri. *ApJL*, 452:L69, October 1995.

D. W. Koerner, M. E. Ressler, M. W. Werner, and D. E. Backman. Mid-Infrared Imaging of a Circumstellar Disk around HR 4796: Mapping the Debris of Planetary Formation. *ApJL*, 503: L83, August 1998.

D. W. Koerner and A. I. Sargent. Imaging the Small-Scale Circumstellar Gas Around T Tauri Stars. *AJ*, 109:2138, May 1995.

D. W. Koerner, A. I. Sargent, and S. V. W. Beckwith. A rotating gaseous disk around the T Tauri star GM Aurigae. *Icarus*, 106:2, November 1993.

M. Kojima and T. Kakinuma. Solar cycle dependence of global distribution of solar wind speed. *Space Science Reviews*, 53:173–222, August 1990.

O. Krauss and G. Wurm. Photophoresis and the Pile-up of Dust in Young Circumstellar Disks. *ApJ*, 630:1088–1092, September 2005.

J. E. Krist, K. R. Stapelfeldt, C. J. Burrows, J. J. Hester, A. M. Watson, G. E. Ballester, J. T. Clarke, D. Crisp, R. W. Evans, J. S. Gallagher, R. E. Griffiths, J. G. Hoessel, J. A. Holtzman, J. R. Mould, P. A. Scowen, and J. T. Trauger. Hubble Space Telescope WFPC2 Imaging of XZ Tauri:Time Evolution of a Herbig-Haro Bow Shock. *ApJL*, 515:L35–L38, April 1999.

A. V. Krivov, I. Mann, and N. A. Krivova. Size distributions of dust in circumstellar debris discs. *A&A*, 362:1127–1137, October 2000.

E. Krügel. *The physics of interstellar dust*. IoP Series in astronomy and astrophysics, Bristol, UK: The Institute of Physics, 2003., 2003.

E. A. Lada, K. M. Strom, and P. C. Myers. Environments of star formation - Relationship between molecular clouds, dense cores and young stars. In *Protostars and Planets III*, pages 245–277, 1993.

P. O. Lagage and E. Pantin. Dust Depletion in the Inner Disk of Beta-Pictoris as a Possible Indicator of Planets. *Nature*, 369:628, June 1994.

A.-M. Lagrange, D. E. Backman, and P. Artymowicz. Planetary Material around Main-Sequence Stars. *Protostars and Planets IV*, page 639, May 2000.

P. L. Lamy. On the dynamics of interplanetary dust grains. *Ph.D. Thesis*, 1975.

A. Laor and B. T. Draine. Spectroscopic constraints on the properties of dust in active galactic nuclei. *ApJ*, 402:441–468, January 1993.

D. Lazzaro, B. Sicardy, F. Roques, and R. Greenberg. Is there a planet around beta Pictoris? Perturbations of a planet circumstellar dust disk. 2: The analytical model. *Icarus*, 108:59–80, March 1994.

C. Leinert, S. Roser, and J. Buitrago. How to maintain the spatial distribution of interplanetary dust. *A&A*, 118:345–357, February 1983.

C. Leinert, H. Zinnecker, N. Weitzel, J. Christou, S. T. Ridgway, R. Jameson, M. Haas, and R. Lenzen. A systematic approach for young binaries in Taurus. *A&A*, 278:129–149, October 1993.

K. Levenberg. A Method for the Solution of Certain Non-Linear Problems in Least-Squares. *Quart. Appl. Math.*, 2:164–168, September 1944.

A. Li and J. I. Lunine. Modeling the Infrared Emission from the HD 141569A Disk. *ApJ*, 594: 987–1010, September 2003.

J.-C. Liou and H. A. Zook. Evolution of Interplanetary Dust Particles in Mean Motion Resonances with Planets. *Icarus*, 128:354–367, August 1997.

J.-C. Liou and H. A. Zook. Signatures of the Giant Planets Imprinted on the Edgeworth-Kuiper Belt Dust Disk. *AJ*, 118:580–590, July 1999.

J.-C. Liou, H. A. Zook, and S. F. Dermott. Kuiper Belt Dust Grains as a Source of Interplanetary Dust Particles. *Icarus*, 124:429–440, December 1996.

J.-C. Liou, H. A. Zook, J. S. Greaves, and W. S. Holland. Does Planet Exist in Epsilon Eridani? A Comparison Between Observations Numerical Simulations. In *Lunar and Planetary Institute Conference Abstracts*, page 1416, March 2000.

J.-C. Liou, H. A. Zook, and A. A. Jackson. Radiation pressure, Poynting-Robertson drag, and solar wind drag in the restricted three-body problem. *Icarus*, 116:186–201, July 1995.

R. Liseau. Molecular line observations of southern main-sequence stars with dust disks: alpha PS A, beta Pic, epsilon ERI and HR 4796 A. Does the low gas content of the beta PIC and varepsilon ERI disks hint of planets? *A&A*, 348:133–138, August 1999.

M. C. Liu. Substructure in the Circumstellar Disk Around the Young Star AU Microscopii. *Science*, 305:1442–1444, September 2004.

M. C. Liu, B. C. Matthews, J. P. Williams, and P. G. Kalas. A Submillimeter Search of Nearby Young Stars for Cold Dust: Discovery of Debris Disks around Two Low-Mass Stars. *ApJ*, 608: 526–532, June 2004.

L. Loinard, A. J. Mioduszewski, L. F. Rodríguez, R. A. González, M. I. Rodríguez, and R. M. Torres. Multiepoch VLBA Observations of T Tauri South. *ApJL*, 619:L179–L182, February 2005.

L. W. Looney, L. G. Mundy, and W. J. Welch. Unveiling the Circumstellar Envelope and Disk: A Subarcsecond Survey of Circumstellar Structures. *ApJ*, 529:477–498, January 2000.

J. Makino. Optimal order and time-step criterion for Aarseth-type N-body integrators. *ApJ*, 369: 200–212, March 1991.

J. Makino and S. J. Aarseth. On a Hermite integrator with Ahmad-Cohen scheme for gravitational many-body problems. *Publ. Astron. Soc. Jpn.*, 44:141–151, April 1992.

J. Makino and P. Hut. Performance analysis of direct N-body calculations. *ApJS*, 68:833–856, December 1988.

K. Malfait, C. Waelkens, L. B. F. M. Waters, B. Vandenbussche, E. Huygen, and M. S. de Graauw. The spectrum of the young star HD 100546 observed with the Infrared Space Observatory. *A&A*, 332:L25–L28, April 1998.

E. E. Mamajek, M. R. Meyer, P. M. Hinz, W. F. Hoffmann, M. Cohen, and J. L. Hora. Constraining the Lifetime of Circumstellar Disks in the Terrestrial Planet Zone: A Mid-Infrared Survey of the 30 Myr old Tucana-Horologium Association. *ApJ*, 612:496–510, September 2004.

V. Mannings and J. P. Emerson. Dust in discs around T Tauri stars: Grain growth? *MNRAS*, 267: 361–378, March 1994.

D. W. Marquardt. An Algorithm for Least-Squares Estimation of Non-Linear Parameters. *J. Soc. Ind. Appl. Math.*, 11:431–441, September 1963.

R. D. Mathieu, A. M. Ghez, E. L. N. Jensen, and M. Simon. Young Binary Stars and Associated Disks. *Protostars and Planets IV*, page 703, May 2000.

R. D. Mathieu, E. L. Martin, and A. Magazzu. UZ Tau E: A New Classical T Tauri Spectroscopic Binary. *Bulletin of the American Astronomical Society*, 28:920, May 1996.

J. S. Mathis and G. Whiffen. Composite interstellar grains. *ApJ*, 341:808–822, June 1989.

S. L. W. McMillan. The Vectorization of Small-N Integrators. *LNP Vol. 267: The Use of Supercomputers in Stellar Dynamics*, 267:156, 1986.

G. Meeus, M. Sterzik, J. Bouwman, and A. Natta. Mid-IR spectroscopy of T Tauri stars in Chamealeon I: Evidence for processed dust at the earliest stages. *A&A*, 409:L25–L29, October 2003.

M. R. Meyer, D. Backman, S. V. W. Beckwith, T. Y. Brooke, J. M. Carpenter, M. Cohen, U. Gorti, T. Henning, L. A. Hillenbrand, D. Hines, D. Hollenbach, J. Lunine, R. Malhotra, E. Mamajek, P. Morris, J. Najita, D. L. Padgett, D. Soderblom, J. Stauffer, S. E. Strom, D. Watson, S. Weidenschilling, and E. Young. The Formation and Evolution of Planetary Systems: SIRTF Legacy Science in the VLT Era. In *The Origins of Stars and Planets: The VLT View. Proceedings of the ESO Workshop held in Garching, Germany, 24-27 April 2001, p. 463.*, page 463, 2002.

M. R. Meyer, L. A. Hillenbrand, D. E. Backman, S. V. W. Beckwith, J. Bouwman, T. Y. Brooke, J. M. Carpenter, M. Cohen, U. Gorti, T. Henning, D. C. Hines, D. Hollenbach, J. S. Kim, J. Lunine, R. Malhotra, E. E. Mamajek, S. Metchev, A. Moro-Martin, P. Morris, J. Najita, D. L. Padgett, J. Rodmann, M. D. Silverstone, D. R. Soderblom, J. R. Stauffer, E. B. Stobie, S. E. Strom, D. M. Watson, S. J. Weidenschilling, S. Wolf, E. Young, C. W. Engelbracht, K. D. Gordon, K. Misselt, J. Morrison, J. Muzerolle, and K. Su. The Formation and Evolution of Planetary Systems: First Results from a Spitzer Legacy Science Program. *ApJS*, 154:422–427, September 2004.

T. Minato, M. Köhler, H. Kimura, I. Mann, and T. Yamamoto. Momentum transfer to interplanetary dust from the solar wind. *A&A*, 424:L13–L16, September 2004.

G. F. Mitchell, A. I. Sargent, and V. Mannings. DG Tau B: The Interaction of an Atomic Jet with Ambient Molecular Gas. *ApJL*, 483:L127, July 1997.

A. Mizuno, T. Onishi, Y. Yonekura, T. Nagahama, H. Ogawa, and Y. Fukui. Overall distribution of dense molecular gas and star formation in the the Taurus cloud complex. *ApJL*, 445:L161–L165, June 1995.

F. J. Molster and L. B. F. M. Waters. The Mineralogy of Interstellar and Circumstellar Dust. *LNP Vol. 609: Astromineralogy*, 609:121–170, 2003.

A. Moro-Martín and R. Malhotra. A Study of the Dynamics of Dust from the Kuiper Belt: Spatial Distribution and Spectral Energy Distribution. *AJ*, 124:2305–2321, October 2002.

A. Moro-Martín, S. Wolf, and R. Malhotra. Signatures of Planets in Spatially Unresolved Debris Disks. *ApJ*, 621:1079–1097, March 2005.

R. Mundt, T. Bührke, and T. P. Ray. A close association of five jet and outflow sources in the HL Tauri region. *ApJL*, 333:L69–L72, October 1988.

C. D. Murray and S. F. Dermott. *Solar system dynamics*. Cambridge University Press, 1999.

H. Mutschke, B. Begemann, J. Dorschner, J. Gürtler, B. Gustafson, T. Henning, and R. Stognienko. Steps toward interstellar silicate mineralogy. III. The role of aluminium in circumstellar amorphous silicates. *A&A*, 333:188–198, May 1998.

J. Najita, J. S. Carr, and R. D. Mathieu. Gas in the Terrestrial Planet Region of Disks: CO Fundamental Emission from T Tauri Stars. *ApJ*, 589:931–952, June 2003.

A. Natta, L. Testi, R. Neri, D. S. Shepherd, and D. J. Wilner. A search for evolved dust in Herbig Ae stars. *A&A*, 416:179–186, March 2004.

R. Neuhäuser, M. F. Sterzik, J. H. M. M. Schmitt, R. Wichmann, and J. Krautter. ROSAT survey observation of T Tauri stars in Taurus. *A&A*, 297:391, May 1995.

B. Nordström, M. Mayor, J. Andersen, J. Holmberg, F. Pont, B. R. Jørgensen, E. H. Olsen, S. Udry, and N. Mowlavi. The Geneva-Copenhagen survey of the Solar neighbourhood. Ages, metallicities, and kinematic properties of about 14 000 F and G dwarfs. *A&A*, 418:989–1019, May 2004.

C. R. O'Dell and Z. Wen. Postrefurbishment mission Hubble Space Telescope images of the core of the Orion Nebula: Proplyds, Herbig-Haro objects, and measurements of a circumstellar disk. *ApJ*, 436:194–202, November 1994.

N. Ohashi, M. Hayashi, R. Kawabe, and M. Ishiguro. The Nobeyama Millimeter Array Survey of Young Stellar Objects Associated with the Taurus Molecular Cloud. *ApJ*, 466:317, July 1996.

F. M. Olnon. Thermal Bremsstrahlung radiospectra for inhomogeneous objects, with an application to MWC 349 . *A&A*, 39:217–223, March 1975.

E. J. Öpik. Collision probability with the planets and the distribution of planetary matter. *Proc. R. Irish Acad. Sect. A, vol. 54, p. 165-199 (1951).*, 54:165–199, 1951.

V. G. Ortega, R. de la Reza, E. Jilinski, and B. Bazzanella. The Origin of the β Pictoris Moving Group. *ApJL*, 575:L75–L78, August 2002.

V. Ossenkopf and T. Henning. Dust opacities for protostellar cores. *A&A*, 291:943–959, November 1994.

L. M. Ozernoy, N. N. Gorkavyi, J. C. Mather, and T. A. Taidakova. Signatures of Exosolar Planets in Dust Debris Disks. *ApJL*, 537:L147–L151, July 2000.

N. Panagia and M. Felli. The spectrum of the free-free radiation from extended envelopes. *A&A*, 39:1–5, February 1975.

E. Pantin, P. O. Lagage, and P. Artymowicz. Mid-infrared images and models of the beta Pictoris dust disk. *A&A*, 327:1123–1136, November 1997.

E. N. Parker. Dynamics of the Interplanetary Gas and Magnetic Fields. *ApJ*, 128:664, November 1958.

P. Plavchan, M. Jura, and S. J. Lipscy. Where Are the M Dwarf Disks Older Than 10 Million Years? *ApJ*, 631:1161–1169, October 2005.

D. E. Potter. *private communication*, 2005.

J. H. Poynting. Radiation in the solar system : its effect on temperature and its pressure on small bodies. *MNRAS*, 64:A1s, November 1903.

L. Prato, M. Simon, T. Mazeh, S. Zucker, and I. S. McLean. Component Masses of the Young Spectroscopic Binary UZ Tau E. *ApJL*, 579:L99–L102, November 2002.

T. Preibisch and M. D. Smith. The distance to the T Tauri stars in Taurus determined from their rotational properties. *A&A*, 322:825–834, June 1997.

W. H. Press, S. A. Teukolsky, W. T. Vetterling, and B. P. Flannery. *Numerical recipes in C. The art of scientific computing*. Cambridge: University Press, 2nd ed., 1992.

F. Przygodda, R. van Boekel, P. Ábrahám, S. Y. Melnikov, L. B. F. M. Waters, and C. Leinert. Evidence for grain growth in T Tauri disks. *A&A*, 412:L43–L46, December 2003.

A. C. Quillen and S. Thorndike. Structure in the ϵ Eridani Dusty Disk Caused by Mean Motion Resonances with a 0.3 Eccentricity Planet at Periastron. *ApJL*, 578:L149–L152, October 2002.

G. H. Rieke, E. T. Young, C. W. Engelbracht, D. M. Kelly, F. J. Low, E. E. Haller, J. W. Beeman, K. D. Gordon, J. A. Stansberry, K. A. Misselt, J. Cadien, J. E. Morrison, G. Rivlis, W. B. Latter, A. Noriega-Crespo, D. L. Padgett, K. R. Stapelfeldt, D. C. Hines, E. Egami, J. Muzerolle, A. Alonso-Herrero, M. Blaylock, H. Dole, J. L. Hinz, E. Le Floc'h, C. Papovich, P. G. Pérez-González, P. S. Smith, K. Y. L. Su, L. Bennett, D. T. Frayer, D. Henderson, N. Lu, F. Masci, M. Pesenson, L. Rebull, J. Rho, J. Keene, S. Stolovy, S. Wachter, W. Wheaton, M. W. Werner, and P. L. Richards. The Multiband Imaging Photometer for Spitzer (MIPS). *ApJS*, 154:25–29, September 2004.

H. P. Robertson. Dynamical effects of radiation in the solar system. *MNRAS*, 97:423, April 1937.

J. Rodmann, T. Henning, C. J. Chandler, L. G. Mundy, and D. J. Wilner. Large dust particles in disks around t tauri stars. *A&A*, in press (astro-ph/0509555), 2006.

L. F. Rodriguez, J. Canto, J. M. Torrelles, J. F. Gomez, G. Anglada, and P. T. P. Ho. Subarcsecond VLA maps of the disk and the jet in HL Tauri. *ApJL*, 427:L103–L106, June 1994.

S. M. Rucinski. IRAS observations of T Tauri and post-T Tauri stars. *AJ*, 90:2321–2330, November 1985.

Th. Schmidt-Kaler. Interplanetry Dust and the Zodiacal Cloud. In *Landolt-Börnstein Numerical Data and Functional Relationships and Technology, Vol. 2*, 1982.

Schneider. The Extrasolar Planets Encyclopaedia. `www.obspm.fr/planets`, 2005.

G. Schneider, B. A. Smith, E. E. Becklin, D. W. Koerner, R. Meier, D. C. Hines, P. J. Lowrance, R. J. Terrile, R. I. Thompson, and M. Rieke. NICMOS Imaging of the HR 4796A Circumstellar Disk. *ApJL*, 513:L127–L130, March 1999.

G. Schneider et al. HD 181327 – HR 4796 A's older and bigger brother. *in preparation*, 2006.

H. Scholl, F. Roques, and B. Sicardy. Resonance trapping of circumstellar dust particles by an alleged planet. *Celestial Mechanics and Dynamical Astronomy*, 56:381–393, June 1993.

O. Schütz, M. Nielbock, S. Wolf, T. Henning, and S. Els. SIMBA's view of the ε Eri disk. *A&A*, 414:L9–L12, January 2004.

R. Schwenn and E. Marsch. *Physics of the Inner Heliosphere I. Large-Scale Phenomena.* Physics of the Inner Heliosphere I, 1990.

H. Shang, S. Lizano, A. Glassgold, and F. Shu. Free-free Radio Emission from Young Stellar Objects. *ApJL*, 612:L69–L72, September 2004.

B. Sicardy, C. Beauge, S. Ferraz-Mello, D. Lazzaro, and F. Roques. Capture of grains into resonances through Poynting-Robertson drag. *Celestial Mechanics and Dynamical Astronomy*, 57: 373–390, October 1993.

M. D. Silverstone. The Vega Phenomenon: Evolution and multiplicity. *Ph.D. Thesis*, August 2000.

M. Simon, A. M. Ghez, C. Leinert, L. Cassar, W. P. Chen, R. R. Howell, R. F. Jameson, K. Matthews, G. Neugebauer, and A. Richichi. A lunar occultation and direct imaging survey of multiplicity in the Ophiuchus and Taurus star-forming regions. *ApJ*, 443:625–637, April 1995.

B. A. Smith and R. J. Terrile. A circumstellar disk around Beta Pictoris. *Science*, 226:1421–1424, December 1984.

C. Spangler, A. I. Sargent, M. D. Silverstone, E. E. Becklin, and B. Zuckerman. Dusty Debris around Solar-Type Stars: Temporal Disk Evolution. *ApJ*, 555:932–944, July 2001.

R. Spurzem. Direct N-body Simulations. *Journal of Computational and Applied Mathematics*, 109:407–432, September 1999.

S. W. Stahler and F. Palla. *The formation of stars*. The formation of stars, by S.W. Stahler and F. Palla. New York, NY: Wiley, 2004, 2004.

K. R. Stapelfeldt, E. K. Holmes, C. Chen, G. H. Rieke, K. Y. L. Su, D. C. Hines, M. W. Werner, C. A. Beichman, M. Jura, D. L. Padgett, J. A. Stansberry, G. Bendo, J. Cadien, M. Marengo, T. Thompson, T. Velusamy, C. Backus, M. Blaylock, E. Egami, C. W. Engelbracht, D. T. Frayer, K. D. Gordon, J. Keene, W. B. Latter, T. Megeath, K. Misselt, J. E. Morrison, J. Muzerolle, A. Noriega-Crespo, J. Van Cleve, and E. T. Young. First Look at the Fomalhaut Debris Disk with the Spitzer Space Telescope. *ApJS*, 154:458–462, September 2004.

K. M. Strom, S. E. Strom, S. Edwards, S. Cabrit, and M. F. Skrutskie. Circumstellar material associated with solar-type pre-main-sequence stars - A possible constraint on the timescale for planet building. *AJ*, 97:1451–1470, May 1989.

R. J. Sylvester and V. Mannings. Optical, infrared and millimetre-wave properties of Vega-like systems - IV. Observations of a new sample of candidate Vega-like sources. *MNRAS*, 313: 73–86, March 2000.

T. Takeuchi and P. Artymowicz. Dust Migration and Morphology in Optically Thin Circumstellar Gas Disks. *ApJ*, 557:990–1006, August 2001.

H. Tanaka, S. Inaba, and K. Nakazawa. Steady-State Size Distribution for the Self-Similar Collision Cascade. *Icarus*, 123:450–455, October 1996.

L. Testi, A. Natta, D. S. Shepherd, and D. J. Wilner. Large grains in the disk of CQ Tau. *A&A*, 403:323–328, May 2003.

P. Thebault and J.-C. Augereau. Upper limit on the gas density in the beta-pictoris system: On the effect of gas drag on the dust dynamics. *A&A*, in press (astro-ph/0502450), 2005.

H. Ungerechts and P. Thaddeus. A co survey of the dark nebulae in perseus, taurus, and auriga. *A&AS*, 63:645–660, March 1987.

R. van Boekel, M. Min, C. Leinert, L. B. F. M. Waters, A. Richichi, O. Chesneau, C. Dominik, W. Jaffe, A. Dutrey, U. Graser, T. Henning, J. de Jong, R. Köhler, A. de Koter, B. Lopez, F. Malbet, S. Morel, F. Paresce, G. Perrin, T. Preibisch, F. Przygodda, M. Schöller, and M. Wittkowski. The building blocks of planets within the 'terrestrial' region of protoplanetary disks. *Nature*, 432:479–482, November 2004.

M. E. van den Ancker, D. de Winter, and H. R. E. Tjin A Djie. HIPPARCOS photometry of Herbig Ae/Be stars. *A&A*, 330:145–154, February 1998.

W. B. Weaver and G. Jones. A catalog of co-added IRAS fluxes of Orion population stars. *ApJS*, 78:239–266, January 1992.

S. J. Weidenschilling. The distribution of mass in the planetary system and solar nebula. *Astrophys. Space. Sci.*, 51:153–158, September 1977.

S. J. Weidenschilling and A. A. Jackson. Orbital resonances and Poynting-Robertson drag. *Icarus*, 104:244–254, August 1993.

A. J. Weinberger, E. E. Becklin, G. Schneider, B. A. Smith, P. J. Lowrance, M. D. Silverstone, B. Zuckerman, and R. J. Terrile. The Circumstellar Disk of HD 141569 Imaged with NICMOS. *ApJL*, 525:L53–L56, November 1999.

J. C. Weingartner and B. T. Draine. Dust Grain-Size Distributions and Extinction in the Milky Way, Large Magellanic Cloud, and Small Magellanic Cloud. *ApJ*, 548:296–309, February 2001.

M. W. Werner, T. L. Roellig, F. J. Low, G. H. Rieke, M. Rieke, W. F. Hoffmann, E. Young, J. R. Houck, B. Brandl, G. G. Fazio, J. L. Hora, R. D. Gehrz, G. Helou, B. T. Soifer, J. Stauffer, J. Keene, P. Eisenhardt, D. Gallagher, T. N. Gautier, W. Irace, C. R. Lawrence, L. Simmons, J. E. Van Cleve, M. Jura, E. L. Wright, and D. P. Cruikshank. The Spitzer Space Telescope Mission. *ApJS*, 154:1–9, September 2004.

S. M. White, R. Pallavicini, and M. R. Kundu. Radio flares and magnetic fields on weak-line T Tauri stars. *A&A*, 259:149–154, June 1992.

R. Wichmann, J. H. M. M. Schmitt, and S. Hubrig. Nearby young stars. *A&A*, 399:983–994, March 2003.

D. R. Williams and G. W. Wetherill. Size distribution of collisionally evolved asteroidal populations - Analytical solution for self-similar collision cascades. *Icarus*, 107:117, January 1994.

J. P. Williams, J. Najita, M. C. Liu, S. Bottinelli, J. M. Carpenter, L. A. Hillenbrand, M. R. Meyer, and D. R. Soderblom. Detection of Cool Dust around the G2 V Star HD 107146. *ApJ*, 604: 414–419, March 2004.

D. J. Wilner. unpublished data, 1998.

D. J. Wilner, P. D'Alessio, N. Calvet, M. J. Claussen, and L. Hartmann. Toward Planetesimals in the Disk around TW Hydrae: 3.5 Centimeter Dust Emission. *ApJL*, 626:L109–L112, June 2005.

D. J. Wilner, P. T. P. Ho, J. H. Kastner, and L. F. Rodríguez. VLA Imaging of the Disk Surrounding the Nearby Young Star TW Hydrae. *ApJL*, 534:L101–L104, May 2000.

D. J. Wilner, P. T. P. Ho, and L. F. Rodriguez. Subarcsecond VLA Observations of HL Tauri: Imaging the Circumstellar Disk. *ApJL*, 470:L117, October 1996.

D. J. Wilner, M. J. Holman, M. J. Kuchner, and P. T. P. Ho. Structure in the Dusty Debris around Vega. *ApJL*, 569:L115–L119, April 2002.

D. J. Wilner and O. P. Lay. Subarcsecond Millimeter and Submillimeter Observations of Circumstellar Disks. *Protostars and Planets IV*, page 509, May 2000.

S. Wolf. *private communication*, 2005.

S. Wolf and L. A. Hillenbrand. Model Spectral Energy Distributions of Circumstellar Debris Disks. I. Analytic Disk Density Distributions. *ApJ*, 596:603–620, October 2003.

S. Wolf and N. V. Voshchinnikov. Mie scattering by ensembles of particles with very large size parameters. *Computer Physics Communications*, 162:113–123, September 2004.

B. E. Wood, H.-R. Müller, G. P. Zank, J. L. Linsky, and S. Redfield. New Mass-Loss Measurements from Astrospheric Lyα Absorption. *ApJL*, 628:L143–L146, August 2005.

N. J. Woolf and E. P. Ney. Circumstellar Infrared Emission from Cool Stars. *ApJL*, 155:L181, March 1969.

A. E. Wright and M. J. Barlow. The radio and infrared spectrum of early-type stars undergoing mass loss. *MNRAS*, 170:41–51, January 1975.

J. T. Wright, G. W. Marcy, R. P. Butler, and S. S. Vogt. Chromospheric Ca II Emission in Nearby F, G, K, and M Stars. *ApJS*, 152:261–295, June 2004.

M. C. Wyatt. Resonant Trapping of Planetesimals by Planet Migration: Debris Disk Clumps and Vega's Similarity to the Solar System. *ApJ*, 598:1321–1340, December 2003.

M. C. Wyatt. The insignificance of P-R drag in detectable extrasolar planetesimal belts. *A&A*, 433:1007–1012, April 2005.

M. C. Wyatt and W. R. F. Dent. Collisional processes in extrasolar planetesimal discs - dust clumps in Fomalhaut's debris disc. *MNRAS*, 334:589–607, August 2002.

M. C. Wyatt, S. F. Dermott, C. M. Telesco, R. S. Fisher, K. Grogan, E. K. Holmes, and R. K. Piña. How Observations of Circumstellar Disk Asymmetries Can Reveal Hidden Planets: Pericenter Glow and Its Application to the HR 4796 Disk. *ApJ*, 527:918–944, December 1999.

S. P. Wyatt and F. L. Whipple. The Poynting-Robertson effect on meteor orbits. *ApJ*, 111:134–141, January 1950.

S. Yamamoto and T. Mukai. Dust production by impacts of interstellar dust on Edgeworth-Kuiper Belt objects. *A&A*, 329:785–791, January 1998.

H. A. Zook. Hyperbolic cosmic dust - Its origin and its astrophysical significance. 23:1391–1397, October 1975.

H. A. Zook and O. E. Berg. A source for hyperbolic cosmic dust particles. 23:183–203, January 1975.

B. Zuckerman. Dusty Circumstellar Disks. *ARA&A*, 39:549–580, 2001.

B. Zuckerman and E. E. Becklin. Submillimeter studies of main-sequence stars. *ApJ*, 414:793–802, September 1993.

B. Zuckerman, T. Forveille, and J. H. Kastner. Inhibition of Giant Planet Formation by Rapid Gas Depletion around Young Stars. *Nature*, 373:494, February 1995.

B. Zuckerman and I. Song. Dusty Debris Disks as Signposts of Planets: Implications for Spitzer Space Telescope. *ApJ*, 603:738–743, March 2004.

I am verily like the cat sitting on the edge of an ocean of milk,
hoping to lap it all up.

KAMBAN, 11th-century Tamil poet

Acknowledgements

It was the best of times,
it was the worst of times.

CHARLES DICKENS, A Tale of Two Cities

There is, unfortunately, the least time available for that part of the thesis that is dearest to my heart. Many contributed to the fruition of this work with advice, help and encouragement of various kinds. To those missing here, either because of short time or poor memory – both excusable weaknesses after the toil and trouble of a dissertation –, I would like to express my gratitude.

It is a long-standing tradition to thank those people first that bear most of the responsibility for the success of a doctoral thesis. I dutifully follow this custom by thanking my supervisor Thomas Henning. He has been an authoritative source of new ideas and directions. Working under him gave me the opportunity to enter diverse fields in planet and star formation research and to enlarge my scientific horizon.

With the Doktorvater, as often as not, busy or away, I have benefited from the kind assistance given by the rest of the institute family. First and foremost, I am deeply thankful to Sebastian Wolf for his unflagging support, understanding, and cordial hospitality. I also gratefully acknowledge the help of Jeroen Bouwman in all Spitzer matters. It has been a great pleasure to work with Johny Setiawan on radial-velocity searches for substellar companions. He took me along to Chile as his apprentice, and without him I would not have the chance to visit this fascinating country every so often. Furthermore, his outstanding culinary skills offered me a weekly relief from the monotony of the canteen.

With the professionalism, openness, and humour of the people there, the Astronomisches Rechen-Institut has become somewhat of a second home to me. Rainer Spurzem introduced me to the exciting field of dynamical simulations and graciously accepted the role of co-supervisor and co-referee. With his swift understanding of the N-body world, Patrick Glaschke gave me a hand more than once. Andreas Brunthaler (then at the Max Planck Institute for Radio Astronomy, Bonn) and Hendrik Linz watched my first steps in the strange realm of millimetre interferometry.

Together with Udo Neumann, Stefan Hanke, Kerstin Geißler, Siegfried Falter and Wolfgang Gässler, I discovered the magic of free climbing and mountaineering. Countless walls and summits are waiting out there, and hopefully we will tackle some of them in the future. I am also glad to have been one of the lucky few to work in Room 216, where laughter is plenty and good tea is served. Unforgotten are many delightful moments from our after-lunch coffee break. My warmest thanks are reserved for Jessica, my strength and best friend.